



Orthogonal Frequency Division Multiplexing for Optical Access Networks

A thesis submitted for the degree of Doctor of Philosophy in
Electronic and Electrical Engineering

Oluyemi Omololu Omomukuyo

Department of Electronic and Electrical Engineering
University College London

April 2013

Statement of Originality

I declare that this thesis is entirely my own work and no portion of the thesis has been submitted in any form in support of an application for another degree or qualification of this or any other University or Institution of Higher Learning. Information obtained from external sources has been duly acknowledged and referenced.

Oluyemi Omomukuyo

April 16, 2013

Abstract

Orthogonal Frequency Division Multiplexing (OFDM) is a modulation scheme with numerous advantages that has for years been employed as the leading physical interface in many wired and wireless communication systems. Recently, with advancements made in digital signal processing, there has been a surge of interest in applying OFDM techniques for optical communications.

This thesis presents extensive research on optical OFDM and how it is being applied in access networks. With the aid of theoretical analysis, simulations and experiments, it is shown that the system performance of direct-detection optical OFDM (DD-OOOFDM) in the presence of MZM non-linear distortion can be improved by proper biasing and selection of appropriate drive to the MZM. Investigations are conducted to illustrate how a variation in the number of subcarriers and the modulation format influences the sensitivity of the DD-OOOFDM system to the MZM non-linear distortion. The possibility of improving the spectral efficiency by reduction of the width of the guard band is also investigated.

This thesis also looks into the radio-over-fibre (RoF) transmission of Multiband OFDM UWB as a transparent and low-cost solution for distributing multi-Gbit/s data to end-users in FTTH networks. Due to relaxed regulatory requirements and the wide bandwidth available, UWB operation in the 60-GHz band is also considered for this FTTH application scenario. Four techniques for enabling MB-OFDM UWB RoF operation in the 60-GHz band are experimentally demonstrated. The impacts of various parameters on the performance of the techniques as well as the limitations imposed by fibre distribution are illustrated.

Finally, a digital pre-distorter is proposed for compensating for the MZM non-linearity. Experimental demonstration of this digital pre-distortion in an UWB

over fibre transmission system shows an increased tolerance to the amplitude of the driving OFDM signal as well as an increase in the optimum modulation index of the OFDM signal.

Acknowledgements

I would like to express my sincere gratitude to my supervisor Dr. John E. Mitchell for his invaluable guidance, patience, support, suggestions, advice, and time spent during various consultations throughout the course of this study. Without him, I definitely would have found it extremely difficult to complete my programme. In addition, I am also grateful that through him, I have significantly improved my technical writing ability, as well as gained the right attitude to solve research problems.

I would also like to thank Dr. Manoj Thakur for pointing me in the right direction several times when I ran completely out of ideas and was beginning to panic. I am also grateful to him for the long hours spent with me in the lab, assisting me and offering valuable advice on how to carry out my experiments.

Many thanks also to the past and present members of the Communications and Information Systems Group led by Prof. Izzat Darwazeh including Dr. Bowen Cao, Dr. Fei Qin, Dr. Darminder Ghataoura, Dr. Davide Anastasia, Dujdow Buranapanichkit, George Smart, Yu Chen, Russell Anam, Ryan Grammenos and George Konstantinou for their friendship, the wonderful memories, and for creating a most enjoyable research environment.

I would also like to thank Prince Eludoyin who has been so influential in making the acquisition of this Ph.D. degree a reality. I truly appreciate your support.

Finally, I would like to thank my loving parents, my siblings and my friends for their moral, spiritual and financial support, and encouragement throughout my years of education.

Table of contents

Statement of originality.....	2
Abstract	3
Acknowledgements	5
Table of contents.....	6
List of Figures.....	9
List of Tables	13
List of Abbreviations and Acronyms	14
Chapter 1. Introduction	21
1.1 Thesis organisation	25
1.2 Contributions and publications	28
Chapter 2. Optical OFDM-based access networks	31
2.1 Introduction.....	31
2.2 Next-generation broadband access networks and technologies	33
2.2.1 Fibre access network architectures	36
2.2.2 Passive optical networks.....	38
2.2.2.1 TDMA-PONs.....	39
2.2.2.2 WDMA-PONs.....	40
2.2.2.3 SCMA-PONs	40
2.2.2.4 OCDMA-PONs.....	41
2.3 Radio-over-fibre (RoF) techniques.....	41
2.3.1 Direct modulation	43
2.3.2 External modulation	47
2.3.3 Benefits and limitations of RoF technology	56
2.3.4 RF power degradation due to chromatic dispersion in IM-DD systems with DSB-C modulation.....	59
2.3.5 Applications of RoF technology	63
2.3.5.1 Distributed antenna systems.....	63
2.3.5.2 Antenna array beamforming.....	65
2.3.5.3 Enhancement of cable television networks.....	66
2.4 OFDM review	68
2.4.1 Single-carrier and multi-carrier modulation systems	68
2.4.2 OFDM principles	72

2.4.3	Mathematical representation of an OFDM signal	73
2.4.4	OFDM system implementations	74
2.4.5	OFDM disadvantages	82
2.4.5.1	Peak-to-average power ratio of OFDM signals	82
2.4.5.2	Phase noise sensitivity.....	83
2.5	Optical OFDM flavours.....	84
2.5.1	DD-OFDM systems	85
2.5.1.1	Hermitian symmetry design	87
2.5.1.2	RF up-conversion design.....	88
2.5.1.3	Hilbert transform design.....	89
2.5.2	CO-OFDM systems	90
2.5.2.1	Direct up/down design	92
2.5.2.2	IF design	93
2.6	OFDM applications in optical access networks.....	94
2.6.1	OFDM in PONs	95
2.6.2	OFDM for UWB radio communications	99
2.6.3	60-GHz radio technology	109
2.6.3.1	Characteristics of the 60-GHz band.....	110
2.6.3.2	Frequency allocation and worldwide regulation	113
2.6.3.3	International 60-GHz standards	114
2.6.3.4	Potential MB-OFDM UWB 60-GHz applications.....	115
2.7	The OptSim™ simulation platform.....	115
2.8	Summary	119
Chapter 3. System performance of direct-detection optical OFDM in the presence of MZM non-linear distortion		
3.1	Introduction	121
3.2	Theoretical analysis.....	122
3.3	Simulation setup	126
3.4	Experimental setup	130
3.5	System performance tests	136
3.6	System parameter variation tests.....	141
3.7	Spectral efficiency tests	148
3.8	Summary	150
Chapter 4. Ultra-wideband (UWB) radio-over-fibre in FTTH access networks		
4.1	Introduction.....	152
4.2	Simulation evaluation and experimental demonstration of MB-OFDM UWB RoF transmission	153

4.2.1	Impact of MZM non-linearity on sytem performance	159
4.2.2	Impact of fibre transmission on sytem performance	166
4.2.3	Impact of received optical power on sytem performance	169
4.3	Summary	170
Chapter 5. MB-OFDM UWB RoF operation in the 60-GHz band.....		173
5.1	Introduction	173
5.2	60-GHz MB-OFDM UWB generation by IM-DD	175
5.2.1	Technique #1 (DFB laser+MZM).....	178
5.2.1.1	Impact of laser non-linearity	185
5.2.1.2	Impact of laser bias current.....	186
5.2.1.3	Impact of operating temperature	188
5.2.1.4	Impact of LO power	189
5.2.1.5	Impacts of received optical power and fibre transmission	190
5.2.2	Technique #2 (Cascaded MZMs)	194
5.2.2.1	Impact of MZM non-linearity	199
5.2.2.2	Impact of LO power	201
5.2.2.3	Impacts of received optical power and fibre transmission	202
5.2.3	Technique #3 (Electrical frequency up-conversion using mixer)	204
5.2.3.1	Impact of IF power.....	212
5.2.3.2	Impact of LO power	214
5.2.3.3	Impacts of received optical power and fibre transmission	215
5.3	Comparison of the IM-DD transmission techniques	217
5.4	60-GHz MB-OFDM UWB generation by OHD	222
5.4.1	Impacts of received optical power and fibre transmission.....	230
5.4.2	Impact of wireless transmission.....	231
5.5	MZM non-linearity compensation using pre-distortion	233
5.5.1	Digital pre-distorter model	235
5.5.2	Experimental setup and results for digital pre-distortion.....	238
5.6	Summary	242
Chapter 6 Concluding remarks and future work.....		245
6.1	Thesis summary	245
6.2	Main contributions of this thesis	246
6.3	Future work.....	249
References		250

List of Figures

FIGURE 2.1 THE ACCESS NETWORK.....	34
FIGURE 2.2 FIBRE ACCESS NETWORK ARCHITECTURES: (A) POINT-TO-POINT. (B) ACTIVE STAR. (C) PASSIVE STAR	37
FIGURE 2.3 PON ARCHITECTURE	38
FIGURE 2.4 TRANSMITTING RF SIGNALS BY IM-DD USING: (A) DIRECT MODULATION OF A LASER (B) EXTERNAL MODULATION USING AN MZM	42
FIGURE 2.5 LASER DIODE L-I CURVE.....	43
FIGURE 2.6 (A) OPTICAL SPECTRUM AT OUTPUT OF DIRECTLY-MODULATED LASER. (B) PHOTODETECTED ELECTRICAL SPECTRUM.....	46
FIGURE 2.7 DUAL-ELECTRODE MZM.....	47
FIGURE 2.8 (A) DSB-C SIGNAL AT OUTPUT OF DE-MZM SHOWING OPTICAL CARRIER WITH EVEN-ORDER AND ODD-ORDER SIDEBANDS (B) SYSTEM CONFIGURATION FOR GENERATING DSB-C SIGNALS.....	50
FIGURE 2.9 OPTICAL SPECTRUM OF AND SYSTEM CONFIGURATION FOR GENERATING: (A) DSB-C SIGNALS (B) DSB-SC SIGNALS (C)&(D) OSSB SIGNALS.....	51
FIGURE 2.10 PHOTODETECTED ELECTRICAL SPECTRUM FOR: (A) DSB-C SIGNALS (B) DSB-SC SIGNALS (C) OSSB SIGNALS	55
FIGURE 2.11 ATTENUATION LOSS IN SILICA AS A FUNCTION OF WAVELENGTH.....	56
FIGURE 2.12 RF POWER DEGRADATION FOR DSB-C AND OSSB TRANSMISSIONS	63
FIGURE 2.13 A SCHEMATIC OF ANDREW CORPORATION'S (COMMScope INC.) INTELLIGENT OPTICAL NETWORK (ION) FAMILY OF OPTICAL DISTRIBUTED ANTENNA SYSTEMS.....	65
FIGURE 2.14 HYBRID FIBRE COAXIAL NETWORK ARCHITECTURE.....	67
FIGURE 2.15 SERIAL-TO-PARALLEL CONVERSION IN FDM SYSTEMS	70
FIGURE 2.16 FDM TRANSMITTER	70
FIGURE 2.17 SINGLE-CARRIER AND MULTI-CARRIER MODULATION: (A) SINGLE-CARRIER TECHNIQUE, (B) CONVENTIONAL MULTICARRIER TECHNIQUE (FDM), AND (C) OFDM MULTICARRIER MODULATION TECHNIQUE	71
FIGURE 2.18 THREE TIME-DOMAIN SUBCARRIERS WITHIN AN OFDM SYMBOL OF DURATION T	73
FIGURE 2.19 OFDM OVERLAPPING SPECTRUM FOR 8 SUBCARRIERS	75
FIGURE 2.20 OSCILLATOR-BASED OFDM IMPLEMENTATION	75
FIGURE 2.21 DFT-BASED OFDM IMPLEMENTATION	78
FIGURE 2.22 CYCLIC PREFIX INSERTION.....	79
FIGURE 2.23 OVERSAMPLING FOR SHIFTING THE ALIASES FROM THE OFDM SIGNAL, THEREBY SIMPLIFYING FILTERING.....	80
FIGURE 2.24 DD-OFDM RECEIVED OPTICAL SPECTRUM (LEFT), ITS COMPONENTS (MIDDLE) AND THE RESULTS (RIGHT) OF PHOTODETECTION IN THE ELECTRICAL DOMAIN	86
FIGURE 2.25 HERMITIAN SYMMETRY TRANSMITTER DESIGN	88
FIGURE 2.26 RF UP-CONVERSION TRANSMITTER DESIGN	89
FIGURE 2.27 HILBERT TRANSFORM TRANSMITTER DESIGN	90
FIGURE 2.28 DIRECT UP/DOWN ARCHITECTURE FOR CO-OFDM	92
FIGURE 2.29 IF ARCHITECTURE FOR CO-OFDM	94
FIGURE 2.30 OPTICAL OFDMA VARIANTS	96
FIGURE 2.31 OFDMA-PON ARCHITECTURE	97
FIGURE 2.32 ACCORDANCE NETWORK ARCHITECTURE	99
FIGURE 2.33 FCC SPECTRAL MASK FOR LICENSE-FREE APPLICATIONS IN INDOOR ENVIRONMENTS	100
FIGURE 2.34 CO-EXISTENCE NATURE OF UWB WITH OTHER WIRELESS SERVICES	101
FIGURE 2.35 WIRELESS RANGE OF UWB IN COMPARISON WITH OTHER WIRELESS SERVICES	102
FIGURE 2.36 SCHEMATIC DIAGRAM OF UWB RoF DISTRIBUTION IN FTTH ACCESS NETWORKS	103
FIGURE 2.37 SIMULATION OF CHANNEL CAPACITY VARIATION WITH SNR FOR DIFFERENT CHANNEL BANDWIDTHS	104

FIGURE 2.38 MB-OFDM UWB CHANNELIZATION ACCORDING TO THE ECMA-368 STANDARD	105
FIGURE 2.39 MB-OFDM UWB TONE ASSIGNMENT AND OFDM SYMBOL STRUCTURE	107
FIGURE 2.40 CCM THEORY OF OPERATION	117
FIGURE 2.41 RECEIVED CONSTELLATIONS: (A) UNEQUALISED (B) EQUALISED	118
FIGURE 3.1 (A) DE-MZM WITH HYBRID COUPLER (B) DE-MZM OPTICAL POWER TRANSFER CHARACTERISTICS.....	123
FIGURE 3.2 DD-OOOFDM SIMULATION SETUP ILLUSTRATING THE CCM THEORY OF OPERATION.....	127
FIGURE 3.3 VISUALISATION OF EVM IN THE I-Q PLANE.....	129
FIGURE 3.4 DD-OOOFDM EXPERIMENTAL SETUP.....	131
FIGURE 3.5 ELECTRICAL AND OPTICAL SPECTRA AT CORRESPONDING POINTS IN THE EXPERIMENTAL SETUP SHOWN IN FIGURE 3.4.....	132
FIGURE 3.6 TIMING METRIC USED FOR OFDM SYMBOL SYNCHRONISATION (A) SCHMIDL AND COX (B) MINN-ZENG MODIFICATION.....	135
FIGURE 3.7 SNAPSHOT OF THE DD-OOOFDM EXPERIMENTAL SETUP.....	135
FIGURE 3.8 EXPERIMENTAL EQUALISED 4-QAM CONSTELLATIONS FOR DIFFERENT NORMALISED BIAS LEVELS: (A) 0.27 (B) 0.5 (C) 0.69.....	136
FIGURE 3.9 EVM VS. NORMALISED MZM BIAS VOLTAGE USING BOTH SIMULATION AND EXPERIMENTAL SETUPS.....	137
FIGURE 3.10 SIMULATED VALUES OF EVM VS. NORMALISED BIAS FOR DIFFERENT VALUES OF NORMALISED DRIVE LEVEL.....	139
FIGURE 3.11 SIMULATED VALUES OF EVM VS. NORMALISED DRIVE LEVELS FOR A NORMALISED BIAS OF 0.5.....	139
FIGURE 3.12 SIMULATED OSSB SEPCTRUM AT OUTPUT OF MZM FOR (A) $\alpha=0.02$ (B) $\alpha=0.13$	140
FIGURE 3.13 EVM VS ε FOR DIFFERENT NUMBER OF SUBCARRIERS.....	142
FIGURE 3.14 SIMULATED PAPR DISTRIBUTION FOR DIFFERENT NUMBER OF SUBCARRIERS AND DIFFERENT MODULATION FORMATS.....	143
FIGURE 3.15 SIMULATED PAPR AS A FUNCTION OF THE NUMBER OF SUBCARRIERS.....	144
FIGURE 3.16 EVM DEGRADATION WITH SSMF LEGTH FOR DIFFERENT NUMBER OF SUBCARRIERS.....	145
FIGURE 3.17 EVM VS ε FOR DIFFERENT MODULATION FORMATS, USING BOTH SIMULATION AND EXPERIMENTAL SETUPS.....	147
FIGURE 3.18 EXPERIMENTAL EQUALISED CONSTELLATIONS FOR DIFFERENT MODULATION FORMATS.....	147
FIGURE 3.19 SIMULATED RECEIVED ELECTRICAL SPECTRUM WITH $\alpha=0.11$ FOR: (A) $\varepsilon=0.5$ (B) $\varepsilon=0.9$	148
FIGURE 3.20 BER VS $\frac{B_{gap}}{B_{sc}}$ FOR $\alpha=0.11$ S AND FOR DIFFERENT VALUES OF ε	149
FIGURE 4.1 SIMULATION SCHEMATIC OF THE MB-OFDM UWB TRANSMISSION SYSTEM.....	154
FIGURE 4.2 (A)-(C) ELECTRICAL AND OPTICAL SPECTRA AT CORRESPONDING POINTS IN THE SIMULATION SCHEMATIC SHOWN IN FIGURE 4.8. (D) EQUALISED CONSTELLATION DIAGRAMS AT -7 dBm UWB DRIVE POWER AND 1 dBm RECEIVED OPTICAL POWER FOR 26-KM SSMF TRANSMISSION	156
FIGURE 4.3 EXPERIMENTAL SETUP OF THE MB-OFDM UWB RoF SYSTEM	158
FIGURE 4.4 EXPERIMENTAL AND SIMULATED VALUES OF EVM OF THE THREE UWB SUB-BANDS VS. UWB DRIVE POWER FOR 26-KM SSMF TRANSMISSION	159
FIGURE 4.5 SIMULATION SETUP FOR THE TWO-TONE TEST	160
FIGURE 4.6 TWO-TONE TEST FOR 26-KM SSMF TRANSMISSION SHOWING THE FUNDAMENTAL COMPONENTS (1 AND 1.004 GHz) AND THE IMD3 COMPONENTS (0.996 AND 1.008 GHz) FOR: (A) RF TONE AMPLITUDE OF 1. (B) RF TONE AMPLITUDE OF 3.2	161
FIGURE 4.7 ANALYTICAL APPROXIMATION SHOWING VARIATION OF FUNDAMENTAL AND IMD3 POWERS WITH MODULATION INDEX	163
FIGURE 4.8 SIMULATION SHOWING VARIATION OF FUNDAMENTAL AND IMD3 POWERS WITH MODULATION INDEX	164
FIGURE 4.9 EVM OF THE THREE UWB SUB-BANDS VS. MODULATION INDEX FOR 26-KM SSMF TRANSMISSION (SIMULATION)	165

FIGURE 4.10 BER OF THE THREE UWB SUB-BANDS AS A FUNCTION OF LAUNCH POWER FOR DIFFERENT SSMF LENGTHS (SIMULATION)	166
FIGURE 4.11 EVM_{opt} VS. FIBRE LENGTH FOR THE THREE UWB SUB-BANDS.....	168
FIGURE 4.12 SUB-BAND 2 EQUALISED CONSTELLATION FOR DIFFERENT FIBRE LENGTHS	168
FIGURE 4.13 EVM OF THE THREE UWB SUB-BANDS VS. RECEIVED OPTICAL POWER.....	169
FIGURE 5.1 HIGH-LEVEL DIAGRAM SHOWING THE THREE IM-DD TECHNIQUES FOR 60-GHZ MB-OFDM UWB GENERATION.....	177
FIGURE 5.2 SCHEMATIC LAYOUT OF TECHNIQUE #1.....	179
FIGURE 5.3 EXPERIMENTAL SETUP FOR TECHNIQUE #1. INSETS (A) – (C): ELECTRICAL AND OPTICAL SPECTRA AT CORRESPONDING POINTS IN THE EXPERIMENTAL SETUP. INSET (D): EQUALISED BACK-TO-BACK CONSTELLATION DIAGRAMS AT 1 DBM RECEIVED OPTICAL POWER.....	183
FIGURE 5.4 EVM VS. UWB DRIVE POWER FOR DIFFERENT BIAS CURRENTS FOR THE THREE UWB SUB-BANDS.....	186
FIGURE 5.5 EVM VS. LASER BIAS CURRENT FOR THE THREE UWB SUB-BANDS.....	187
FIGURE 5.6 DFB LASER WAVELENGTH DRIFT WITH BIAS CURRENT	188
FIGURE 5.7 (A) EVM DEGRADATION WITH INCREASE IN OPERATING TEMPERATURE (B) LASER OUTPUT OPTICAL POWER VS. BIAS CURRENT FOR DIFFERENT OPERATING TEMPERATURES.....	189
FIGURE 5.8 EVM VS. LO POWER FOR THE THREE UWB SUB-BANDS	190
FIGURE 5.9 SUB-BAND #2 EVM VS. RECEIVED OPTICAL POWER FOR DIFFERENT SSMF LENGTHS.....	191
FIGURE 5.10 PHOTODETECTED SPECTRUM FOR TECHNIQUE #1. INSET: MAGNIFIED VIEW OF THE OPTICAL SPECTRUM AT THE OUTPUT OF THE DE-MZM, CONSIDERING ONLY THE FIRST-ORDER OPTICAL SIDEBANDS.....	192
FIGURE 5.11 DOWN-CONVERTED UWB SIGNAL SPECTRA, SHOWING SIGNAL DETERIORATION AT LONGER SSMF LENGTHS.....	193
FIGURE 5.12 SIMULATION OF EVM DEGRADATION OF SUB-BAND#2 AND RF POWER DEGRADATION OF A 1.75 GHz SIGNAL WITH INCREASING FIBRE LENGTHS.....	193
FIGURE 5.13 SCHEMATIC LAYOUT OF TECHNIQUE #2.....	194
FIGURE 5.14 EXPERIMENTAL SETUP FOR THE CASCADED MZMS TECHNIQUE.....	198
FIGURE 5.15 EVM VS. UWB DRIVE POWER FOR THE THREE UWB SUB-BANDS.....	200
FIGURE 5.16 EVM VS. NORMALISED BIAS VOLTAGE OF DE-MZM1.....	201
FIGURE 5.17 EVM VS. LO POWER FOR THE THREE UWB SUB-BANDS.....	202
FIGURE 5.18 SUB-BAND #2 EVM VS. RECEIVED OPTICAL POWER FOR DIFFERENT SSMF LENGTHS.....	203
FIGURE 5.19 PHOTODETECTED SPECTRUM FOR TECHNIQUE #2.....	203
FIGURE 5.20 DOWN-CONVERTED UWB SIGNAL SPECTRA, SHOWING ROBUSTNESS TO CHROMATIC DISPERSION.....	204
FIGURE 5.21 SCHEMATIC LAYOUT OF TECHNIQUE #3.....	205
FIGURE 5.22 EXPERIMENTAL SETUP OF TECHNIQUE #3.....	208
FIGURE 5.23 (A) SINGLE-DIODE MIXER. I-V CHARACTERISTICS FOR (B) IDEAL DIODE (C) PRACTICAL SCHOTTKY DIODE.....	210
FIGURE 5.24 SINGLE-BALANCED DIODE MIXER.....	211
FIGURE 5.25 SPURIOUS IMAGE TERM OVERLAPPING WITH DESIRED RF SIGNAL.....	212
FIGURE 5.26 SUB-BAND #2 EVM VS. IF POWER.....	213
FIGURE 5.27 SUB-BAND #2 EVM VS. LO POWER.....	215
FIGURE 5.28 SUB-BAND #2 EVM VS. RECEIVED OPTICAL POWER FOR DIFFERENT SSMF LENGTHS.....	216
FIGURE 5.29 EVM DEGRADATION FOR UWB SIGNAL AND RF POWER DEGRADATION FOR A 61.75 GHz SIGNAL AT 1 DBM RECEIVED OPTICAL POWER WHEN OPTICAL DSB-C TRANSMISSION IS USED.....	217
FIGURE 5.30 SCHEMATIC LAYOUT OF OHD TECHNIQUE.....	223
FIGURE 5.31 EXPERIMENTAL SETUP OF OHD TECHNIQUE.....	227
FIGURE 5.32 (A)-(C) ELECTRICAL AND OPTICAL SPECTRA AT CORRESPONDING POINTS IN EXPERIMENTAL SETUP SHOWN IN FIGURE 5.21. (D) EQUALIZED CONSTELLATION DIAGRAMS AT 1 DBM RECEIVED OPTICAL POWER FOR 26 KM SSMF AND 2 M WIRELESS TRANSMISSION.....	228

FIGURE 5.33 EVM OF THE THREE UWB SUB-BANDS AS A FUNCTION OF RECEIVED OPTICAL POWER FOR A FIXED WIRELESS DISTANCE OF 2.4 M AND DIFFERENT SSMF LENGTHS.....	231
FIGURE 5.34 WIRELESS EXPERIMENTAL SETUP	232
FIGURE 5.35 EVM AS A FUNCTION OF RECEIVED OPTICAL POWER FOR A FIXED SSMF LENGTH OF 26 KM AND DIFFERENT WIRELESS DISTANCES (DIRECT COAXIAL LINK ALSO INCLUDED).....	233
FIGURE 5.36 (A) MZM POWER TRANSFER CHARACTERISTICS (B) PRE-DISTORTER TRANSFER CHARACTERISTICS (C) COMPENSATED TRANSFER CHARACTERISTICS FOR DIFFERENT VALUES OF V_{on} AND V_{π} : 1.2 V AND 1 V; 2.1 V AND 1.7 V; 3.9 V AND 3.1 V; 4.8 V AND 2.6 V; 5 V AND 4 V.....	238
FIGURE 5.37 EXPERIMENTAL SETUP FOR DIGITAL PRE-DISTORTION.....	240
FIGURE 5.38 EVM vs. UWB DRIVE POWER: WITH/WITHOUT DIGITAL PRE-DISTORTION COMPENSATION.....	241

List of Tables

TABLE 2.1 xDSL BANDWIDTH VS. DISTANCE CAPABILITY	35
TABLE 2.2 MAXIMUM EIRP LEVELS AS STATED BY FCC FOR UWB EMISSIONS.....	100
TABLE 2.3 FREQUENCY DETAILS OF MB-OFDM UWB SUB-BANDS IN THE MANDATORY BAND GROUP #1.....	105
TABLE 2.4 TIME-FREQUENCY CODES FOR BAND GROUP #1	107
TABLE 2.5 SPECTRAL EFFICIENCY COMPARISON BETWEEN TYPICAL 60-GHz AND IEEE 802.11N SYSTEMS.....	110
TABLE 2.6 FREQUENCY PLAN, MAXIMUM EIRP AND MAXIMUM TRANSIT POWER IN THE 60-GHz BAND FOR VARIOUS COUNTRIES	113
TABLE 2.7 SUMMARY OF WIRELESS 60-GHz STANDARDS	114
TABLE 3.1 OFDM SYSTEM PARAMETERS.....	127
TABLE 4.1 MB-OFDM UWB SYSTEM PARAMETERS ACCORDING TO THE ECMA-368 STANDARD	155
TABLE 5.1 60-GHz MB-OFDM UWB SYSTEM PARAMETERS.....	182
TABLE 5.2 COMPARISONS OF THE THREE IM-DD TRANSMISSION TECHNIQUES.....	219

List of Abbreviations and Acronyms

ADC	-	Analogue-to-Digital Converter
ADSL	-	Asymmetric Digital Subscriber Line
AO-OFDM	-	All Optical Orthogonal Frequency Division
AP	-	Access Point
ASCII	-	American Standard Code for Information Interchange
ASE	-	Amplified Spontaneous Emission
ATM	-	Asynchronous Transfer Mode
AWG(1)	-	Arbitrary Waveform Generator
AWG(2)	-	Arrayed Waveguide Grating
BER	-	Bit Error Rate
BG	-	Band Group
BPF	-	Band-Pass Filter
BPSK	-	Binary Phase Shift Keying
CATV	-	Cable Television
CCDF	-	Complementary Cumulative Distribution Function
CCM	-	Custom Component for MATLAB
CNR	-	Carrier-to-Noise Ratio
CO	-	Central Office
CO-OFDM Multiplexing	-	Coherent Optical Orthogonal Frequency Division
CPE	-	Customer-Premise Equipment
CPS	-	Common Phase Shift

CW	-	Continuous Wave
DAB	-	Digital Audio Broadcast
DAC	-	Digital-to-Analogue Converter
DAS	-	Distributed Antenna Systems
D.C.	-	Direct Current
D.C.M	-	Dual-Carrier Modulation
DD-OOFDM Division Multiplexing	-	Direct-Detection Optical Orthogonal Frequency
DE-MZM	-	Dual-Electrode Mach-Zehnder Modulator
DFB	-	Distributed Feedback
DFT	-	Discrete Fourier Transform
DP	-	Distribution Point
DSB-C	-	Double Sideband with Carrier
DSB-SC	-	Double Sideband Suppressed Carrier
DSL	-	Digital Subscriber Line
DSP	-	Digital Signal Processing
DVB	-	Digital Video Broadcast
DWDM	-	Dense Wavelength Division Multiplexing
ECMA	-	European Computer Manufacturers Association
EDFA	-	Erbium-Doped Fibre Amplifier
EIRP	-	Equivalent Isotropic Radiated Power
EMI	-	Electromagnetic Interference
EVM	-	Error Vector Magnitude

FBG	-	Fibre Bragg Grating
FCC	-	Federal Communications Commission
FDM	-	Frequency Division Multiplexing
FEC	-	Forward Error Correction
FFI	-	Fixed Frequency Interleaving
FFT	-	Fast Fourier Transform
FSPL	-	Free-Space Path Loss
FTTB	-	Fibre-To-The-Building
FTTCab	-	Fibre-To-The-Cabinet
FTTH	-	Fibre-To-The-Home
FWM	-	Four-Wave Mixing
GEM	-	GPON Encapsulation Method
GVD	-	Group Velocity Dispersion
HD	-	High-Definition
HDMI	-	High-Definition Multimedia Interface
HDTV	-	High-Definition Television
HFC	-	Hybrid Fibre Coaxial
HIPERLAN/2	-	High Performance Radio Local Area Network Version 2
HPA	-	High-Power Amplifier
I/Q	-	In-Phase/Quadrature-Phase
ICI	-	Inter-Carrier Interference
IDFT	-	Inverse Discrete Fourier Transform
IEEE	-	Institute of Electrical and Electronics Engineers

IF	-	Intermediate Frequency
IFFT	-	Inverse Fast Fourier Transform
IM-DD	-	Intensity Modulation with Direct Detection
ION	-	Intelligent Optical Network
IR-UWB	-	Impulse-Radio Ultra Wideband
ISI	-	Inter-Symbol Interference
ITU-T	-	International Telecommunication Union – Telecommunications Unit
LAN	-	Local Area Network
LiNbO ₃	-	Lithium Niobate
LNA	-	Low-Noise Amplifier
LO	-	Local Oscillator
LPF	-	Low-Pass Filter
LSB	-	Lower Sideband
LTE	-	Long-Term Evolution
MAC	-	Media Access Control
MB-OFDM Multiplexing	-	Multi Band Orthogonal Frequency Division
MIMO	-	Multiple-Input Multiple-Output
MTU	-	Mobile Terminal Unit
MZM	-	Mach-Zehnder Modulator
NLOS	-	Non-Line-Of-Sight
OBPF	-	Optical Band-Pass Filter

OCDMA	-	Optical Code Division Multiple Access
OFDM	-	Orthogonal Frequency Division Multiplexing
OFDMA	-	Orthogonal Frequency Division Multiple Access
OHD	-	Optical Heterodyne Detection
OIDFT	-	Optical Inverse Discrete Fourier Transform
OLT	-	Optical Line Terminal
ONT	-	Optical Network Terminal
ONU	-	Optical Network Unit
OSNR	-	Optical Signal-to-Noise Ratio
OSSB	-	Optical Single Sideband
OTDM	-	Optical Time-Division Multiplexing
PAN	-	Personal Area Network
PAPR	-	Peak-to-Average Power Ratio
PDA	-	Personal Digital Assistant
PIN	-	Positive-Intrinsic-Negative
PMD	-	Polarisation Mode Dispersion
PON	-	Passive Optical Network
PSK	-	Phase Shift Keying
QAM	-	Quadrature Amplitude Modulation
RAU	-	Remote Antenna Unit
RF	-	Radio Frequency
RGI	-	Reduced-Guard-Interval
RIN	-	Relative Intensity Noise

R.M.S	-	Root Mean Square
RoF	-	Radio-over-Fibre
RTT	-	Round-Trip Time
RVA	-	Radio Frequency Variable Attenuator
SCM	-	Subcarrier Multiplexing
SCMA	-	Subcarrier Multiple Access
SDH	-	Synchronous Digital Hierarchy
SLM	-	Selected Mapping
SNR	-	Signal-to-Noise Ratio
SONET	-	Synchronous Optical Networking
SSMF	-	Standard Single-Mode Fibre
TDMA	-	Time Division Multiple Access
TEC	-	Thermo-Electric Cooler
TFC	-	Time-Frequency Code
TFI	-	Time-Frequency Interleaving
USB	-	Upper Sideband
UWB	-	Ultra-Wideband
VCSEL	-	Vertical-Cavity Surface-Emitting Laser
VDSL	-	Very-high-bit-rate Digital Subscriber Line
VISA-GPIB Purpose Interface Bus	-	Virtual Instrument Standard Architecture - General
VOA	-	Variable Optical Attenuator
VoD	-	Video on Demand

WDM	-	Wavelength-Division Multiplexing
WDMA	-	Wavelength-Division Multiple Access
WiMax	-	Worldwide Interoperability for Microwave Access
WLAN	-	Wireless Local Area Network
WPAN	-	Wireless Personal Area Network

Chapter 1. Introduction

Orthogonal frequency division multiplexing (OFDM), an efficient multi-carrier modulation scheme with numerous advantages, has for years been employed in a wide variety of wired and wireless communication standards including wireless LAN networks (HIPERLAN/2, IEEE 802.11a, IEEE 802.11g); Worldwide Interoperability for Microwave Access (WiMax - IEEE 802.16); Digital Subscriber Line (DSL) and Digital Audio and Video Broadcast (DAB, DVB).

OFDM, having been established as the physical interface of choice for these communication standards, has only recently made a transition to the optical communications community [1], [2]. A major hindrance to this transition has been the differences between conventional OFDM systems and conventional optical systems. In conventional OFDM systems, the signal is bipolar and the information is carried on the electrical field while in a typical optical system, the signal is unipolar and the information is carried on the intensity of the optical signal.

However, advancements in silicon technology supported by Moore's law, together with increased demand for higher data rates across long fibre distances have facilitated the emergence of OFDM in optical communications [3].

For optical communications, OFDM has demonstrated resilience to transmission impairments arising from fibre polarisation mode dispersion and chromatic dispersion. It has been shown that provided the delay spread caused by chromatic dispersion is less than the cyclic prefix interval, OFDM can easily compensate for dispersion-induced impairments [4]. This is no trivial advantage when one considers the fact that as data rates increase, chromatic dispersion increases with the square of the data rate while polarisation mode dispersion (PMD)

increases linearly with the data rate [5]. Consequently, at such high data rates, the computational requirements involved in electronic dispersion compensation for serial modulation formats may become impractical, particularly in access networks [6]. Another important advantage of OFDM worthy of note is the increase in spectral efficiency that can be obtained from using higher modulation formats [7].

By being able to apply the afore-mentioned advantages of OFDM into the optical domain, OFDM has demonstrated research potential for a wide variety of applications in the core, metro and access networks.

There are two types of existing optical OFDM systems. The first type typically requires electronic fast Fourier Transform (FFT) processors and digital-to-analogue converters (DACs) to generate an electrical OFDM signal. This electrical OFDM signal is then converted into an optical signal by either by direct modulation of a laser or by using an external modulator [1]-[4]. Despite these systems being disadvantaged by the transmission data rate limitations set by the throughput of electronics, there is a lot of flexibility in the generation and detection of the OFDM signal. In particular, functions like advanced modulation formats, subcarrier equalisation and adaptive filtering can be implemented [8]. Throughout this work, the term “optical OFDM” specifically refers to these type of optical OFDM systems.

In the second type of optical OFDM systems, the OFDM subcarriers are generated optically and modulated as single-carrier signals. These systems are the so-called all-optical OFDM (AO-OFDM) systems. Various variants of AO-OFDM systems have been proposed. In the scheme proposed by Yonenaga *et al.* [9], an optical subcarrier generator is used to generate OFDM subcarriers which are then simultaneously fed into an integrated optical modulator. Each subcarrier is modulated by a duobinary signal and each modulated subcarrier is coupled and the

output transmitted over fibre. Another variant of AO-OFDM systems utilises optical Inverse Discrete Fourier Transforms (OIDFTs) [10]-[13]. In these systems, the OIDFTs are designed using phase modulators and optical delay lines. Yet another AO-OFDM variant utilises a multiple subcarrier laser source with a carrier separation equal to the baud rate of the signal [14], [15]. Each laser output is then optically demultiplexed using an arrayed waveguide grating (AWG), with an array of I/Q optical modulators used to individually modulate each subcarrier. After the parallel modulation, the subcarriers are multiplexed using another AWG and then transmitted over fibre. While AO-OFDM systems typically avoid the transmission data rate limitations suffered by the first type of optical OFDM systems, their overall complexity, especially on the receiver side, is currently prohibitive for optical access [16].

For access network applications, optical OFDM has been applied in ultra-wideband (UWB) systems for the distribution of high-definition (HD) multimedia content [17]. UWB, or multiband-OFDM UWB (MB-OFDM UWB) as it is often referred to, is a radio technology occupying regulated spectrum from 3.1 to 10.6 GHz [18]. Applications of UWB include short-range, high-throughput indoor data communications with the potential to exceed 1 Gbit/s [19], radar sensors [20] and automobile short-range communications [21]. Current interest in UWB, both from industry and academia, is fuelled by its intrinsic properties including its ability to co-exist with other systems, low power consumption, wide bandwidth, low latency, low probability of interception and high data rate.

However, a combination of the fundamental limits of thermal noise and Shannon limits, together with the restrictions placed by the FCC on the maximum UWB equivalent isotropic radiated power (EIRP) spectral density restricts the

wireless range of UWB systems to a few meters. Since the broad bandwidth limits coaxial cable distribution [22], a transparent and low-cost solution is to employ transmission over fibre. This enables the advantages of UWB to be combined with the advantages optical fibre offers in terms of wide bandwidth and low attenuation loss to increase the wireless coverage of UWB systems to hundreds of meters, distributing UWB signals to multiple simplified remote antenna units (RAUs).

Although UWB systems are capable of supporting multi-Gbit/s communications, the UWB capacity is restricted worldwide, with different regulations in different countries. This makes it difficult to support bandwidth-intensive applications that require multi-Gbit/s data rates such as uncompressed HD video streaming, video-on-demand and wireless high-speed file transfer. This regulation constraint makes the 60-GHz band quite interesting for UWB operation because of the huge bandwidth and relaxed regulation requirements. Furthermore, 60-GHz regulation permits much higher EIRP than existing wireless local area network (WLAN) and wireless personal area network (WPAN) systems [23]. In addition, the small size of 60-GHz antennas permits multiple-antenna solutions at the user terminal that would have been near-impossible at lower frequencies. This permits UWB to be introduced in devices like mobile phones which have space restrictions. Because of the high density of RAUs required for 60-GHz operation, using RoF technology for distribution of the 60-GHz MB-OFDM UWB signals would result in simplified operation and maintenance which would eventually translate to cost savings.

The main technical objective of this thesis is the proposal, analysis, simulation and experimental demonstration of various OFDM-based radio-over-fibre (RoF) architectures in different frequency bands, ranging from baseband to millimetre-

wave systems for multi-Gbit/s communications. In this work, the term “RoF” refers to the transport and distribution of analogue electrical signals (which could be at baseband, intermediate-frequency (IF) or RF frequencies) over an optical fibre link; with the electrical signal used to modulate the lightwave.

For the various architectures, our investigations are concerned with, but not limited to, proof-of-concept demonstrations and evaluation of the effect of parameters such as modulator non-linearity, drive power, bias current, fibre dispersion and the received optical power on the system performance.

For majority of the experimental work considered in this thesis, the OFDM signals modulate the lightwave using Mach-Zehnder modulators (MZMs) which are inherently non-linear devices. In this thesis, we also carry out MZM non-linearity impairment compensation by digital pre-distortion to improve the system performance of the optical OFDM systems at high modulation indexes.

The details of the thesis structure and the contributions of this work are presented in the following sub-sections.

1.1 Thesis organisation

A common structure is used throughout this thesis. Each chapter begins with an introduction where the aims and contents of the chapter are highlighted, and is concluded with a summary of the main contributions of the chapter. The thesis is organised as follows:

Chapter 2 provides an overview of optical access networks, covering state-of-the-art technologies, principles, recent progress and different application scenarios. In this chapter, various optical fibre topologies and technologies for shared fibre multiple are first discussed. RoF is then introduced as a hybrid technology that

combines the advantages of optical fibre and wireless access. The benefits, limitations and latest applications of RoF technology are also discussed. Next, OFDM is introduced as a solution to chromatic dispersion compensation in optical communication networks. In order to provide fundamental understanding of how an OFDM system works, we talk about the background, history, basic mathematical principles, system implementations, advantages and disadvantages of OFDM. We also briefly review some important optical communication concepts. The two broad flavours of optical OFDM that are currently in use – coherent optical OFDM (CO-OFDM) and direct-detection optical OFDM (DD-OOOFDM) are discussed. Then, we illustrate how OFDM has been used in PONs and UWB communications for optical access applications. Finally, a brief introduction of the OptSim™ simulation platform is given.

Chapter 3 focuses on how the non-linearity of the MZM affects the performance of the DD-OOOFDM system. This chapter shows how, because of the MZM non-linearity, system performance is dependent on the MZM drive and bias levels. The chapter follows this up with an investigation into how a variation in system parameters such as the modulation format and number of subcarriers influences the MZM non-linear distortion and consequently, the system performance. Finally, the possibility of optimising the spectral efficiency of the DD-OOOFDM system by employing a reduced frequency guard band is investigated by simulation.

Chapter 4 looks at MB-OFDM UWB transmission over standard single mode fibre (SSMF) in fibre-to-the-home (FTTH) access networks. In particular, we demonstrate with the aid of simulations and experiments, how the UWB range can be extended by using SSMF to optically distribute the MB-OFDM UWB signal in its native format from a central office to the customer's premises. This access technique

is a flexible, transparent and low-cost solution, permitting the delivery of multi-Gbit/s UWB signals for HD audio and video contents. To prevent chromatic dispersion-induced fading, optical single sideband (OSSB) architectures are employed. Using error vector magnitude (EVM) and bit error rate (BER) measurements as figures of merit, we carry out investigations into how the transmission performance is affected by various impairments including the MZM non-linearity, fibre transmission and received optical power variation.

Chapter 5 explores MB-OFDM UWB operation in the 60-GHz radio band as a means to further improving the range and flexibility of UWB. This chapter illustrates and experimentally demonstrates four techniques for enabling MB-OFDM UWB RoF operation in the 60-GHz band. These techniques are classified in terms of the underlying modulation/detection principles employed, namely Intensity Modulation with Direct Detection (IM-DD) and optical heterodyne detection (OHD). For the first three techniques (based on IM-DD), we experimentally demonstrate that the system performance of the various techniques is limited by the first major non-linear component encountered by the driving UWB signal. We also illustrate the limitations imposed on the three techniques by fibre distribution. We then demonstrate analytically and experimentally that the OHD technique is robust to laser phase noise. The final part of Chapter 5 is concerned with applying digital pre-distortion as a linearisation technique to compensate for the MZM non-linearity and improve system performance at high modulation indexes. In this regard, a digital pre-distorter with a transfer function which is the inverse of the MZM power transfer function is proposed and experimentally demonstrated. The proposed digital pre-distortion technique is valid for any single-electrode MZM. EVM results are presented in this chapter to evaluate the performance improvement brought about by pre-distortion.

Chapter 6 concludes the thesis and proposes potential future work planned for further research.

1.2 Contributions and publications

The major contributions of the work herein presented can be summarised as follows:

- Proposed a simple 60-GHz radio-over-fibre system employing a combination of uncorrelated optical heterodyning and envelope detection. Analytically demonstrated that the proposed system is capable of avoiding the laser phase noise effects at baseband. Carried out proof-of-concept experimental demonstration of the proposed system for the successful transmission of a 3.84 Gbit/s, 16-QAM MB-OFDM UWB signal over up to 48-km standard single-mode fibre and a further 4-m wireless channel. The experimental results therefore confirm that photonic millimetre-wave signal generation and detection can be achieved without the need for complex optical phase-locked loops and high-frequency microwave sources.
- Carried out comprehensive analytical studies and experimental demonstrations of three techniques for millimetre-wave MB-OFDM UWB generation. In each of these three techniques, the modulating MB-OFDM UWB signal drives a different type of non-linear component – a laser, a MZM and a mixer. Experimentally demonstrated that the system performance of the various techniques is limited by the first major non-linear component encountered by the driving UWB signal. The three techniques are also compared in terms of transmission performance, fibre distribution, cost and complexity.
- Proposed a novel digital pre-distortion technique to compensate for the MZM non-linearity in DD-OFDM systems and improve system performance at high modulation indexes. The proposed digital pre-distorter has a transfer characteristic which is the inverse of the MZM power transfer characteristic. The digital pre-distortion function is also valid for any single-electrode MZM. Carried out proof-of-concept experimental demonstration of the proposed pre-

distortion technique in an MB-OFDM UWB RoF system where performance analysis showed an increased tolerance to the amplitude of the applied UWB signal as well as increase in the optimum drive power when pre-distortion is employed. For drive powers up to 18 dBm, the EVM is still less than -15 dB when digital pre-distortion is applied, almost a 9 dB improvement when compared to the uncompensated case.

- Demonstrated, with the aid of experiments and simulations, the performance of a DD-OFDM system with respect to the non-linearity of the MZM. Clearly illustrated that the system performance can be improved by proper selection of the bias point and appropriate drive to the MZM. Showed that to obtain an EVM penalty (due to the MZM non-linear distortion) of < 2 dB, the normalised MZM drive level has to be ≤ 0.11 ; and the normalised MZM bias needs to be within 0.06 of the normalised quadrature bias voltage value of 0.5.
- Demonstrated how a variation in system parameters such as the number of subcarriers and the modulation format influenced the non-linear distortion caused by the MZM and consequently, the performance of the DD-OFDM system. Showed that the impact of the MZM non-linearity on the system performance can be reduced by reducing the number of subcarriers. This improvement is however, only seen for short fibre lengths (< 50 km). Also experimentally demonstrated that as higher level modulation formats are employed, the system performance gets more affected by the MZM non-linearity because the interference due to the MZM non-linear distortion becomes more severe.
- Demonstrated that with a quadrature bias to the MZM, a very low level of intermodulation distortion products is obtained which results in the system BER remaining largely unchanged for at least a 50% reduction in the guard band. For a quadrature bias, a system BER of 2.6×10^{-9} is obtained when the width of the guard band is 80% of the OFDM bandwidth. When the guard band is reduced to 50% of the OFDM bandwidth, the BER is still around 2.6×10^{-9} . Thus, the spectral efficiency in DD-OFDM systems can be improved by reduction of the width of the guard band by at least 50% if a quadrature bias is used.

The research work has resulted in the following publications listed below:

- O. Omomukuyo, M. P. Thakur and J. E. Mitchell, "Simple 60-GHz MB-OFDM ultra-wideband RoF system based on remote heterodyning," *IEEE Photon. Technol. Lett.*, vol. 25, no. 3, pp. 268-271, Feb. 2013.
- O. Omomukuyo, M. P. Thakur and J. E. Mitchell, "Experimental demonstration of digital predistortion for linearisation of Mach-Zehnder modulators in direct-detection MB-OFDM ultra-wideband over fiber systems," in *Proc. Asia Communications and Photonics Conference (ACP'12)*, Nov. 7–10, 2012, paper ATh1C.4.
- O. Omomukuyo, M. P. Thakur and J. E. Mitchell, "Experimental performance analysis of MB-OFDM ultra-wideband radio-over-fiber signals in the 60-GHz band using a commercially-available DFB laser," in *Proc. International Conference on Transparent Optical Networks (ICTON'12)*, July. 2–5, 2012, paper Mo.C3.4.
- O. Omomukuyo, M. P. Thakur and J. E. Mitchell, "Experimental demonstration of the impact of MZM non-linearity on direct-detection optical OFDM," in *Proc. IEEE International Wireless Communications and Networking Conference Workshop on Hybrid Optical Wireless Access Networks (WCNC/HOWAN'12)*, pp. 419-423, Apr. 1-4, 2012.
- O. Omomukuyo and J. E. Mitchell, "Performance evaluation of a 60-GHz multi-band OFDM (MB-OFDM) ultra-wideband radio-over-fibre system," in *Proc. London Communications Symposium (LCS'11)*, London, UK, Sep. 8, 2011.
- O. Omomukuyo and J. E. Mitchell, "Impact of Mach-Zehnder non-linearity on the receiver sensitivity of direct-detection optical OFDM", in *Proc. London Communications Symposium (LCS'10)*, London, UK, Sep. 10, 2010.

Chapter 2. Optical OFDM-based access networks

2.1 Introduction

As stated in Chapter 1, an increase in demand for high data rates has been an important factor in the emergence of OFDM in the optical domain, with a wide variety of solutions developed for different applications both in the core and access networks. This emergence has been facilitated by the intrinsic advantages of OFDM such as its high spectral efficiency, ease of channel and phase estimation; and robustness against delay. In this chapter, an overview of optical access networks is presented, covering state-of-the-art technologies, principles, recent progress and different application scenarios. We also present OFDM as an effective solution to the major problems of today's optical access networks and describe how OFDM has been applied in the access network in the form of passive optical networks (PONs) and through UWB systems.

The structure of this chapter is as follows: section 2.2 provides an overview of next-generation broadband access networks. In this section, we highlight optical fibre as probably the most viable means of meeting the ever-increasing bandwidth demand of subscribers. Various optical fibre topologies such as point-to-point and point-to-multipoint are illustrated, together with their respective advantages and disadvantages. The various state-of-the-art optical technologies currently being deployed for shared fibre multiple access such as time division multiple access (TDMA), wavelength division multiple access (WDMA), subcarrier multiple access (SCMA), and optical code division multiple access (OCDMA) are also briefly discussed.

In section 2.3, RoF is introduced as a hybrid access technology that combines the wide bandwidth and low loss merits of optical fibre with the mobility advantages of radio access. In this section, the key optical components used in contemporary RoF systems, as well as some basic RoF concepts are described in order to provide a foundation on which the simulations and experiments in the succeeding chapters are built on. This will also make it easier to understand the results presented in those chapters. The latest RoF applications are also presented in this section.

Section 2.4 introduces OFDM as a candidate technology for next-generation, high-speed optical access networks. This section provides a review of some fundamental OFDM principles including the background, basic mathematical representation, system implementations, cyclic prefix use, advantages and disadvantages of OFDM. This literature review is essential in order to appreciate the motivation behind applying OFDM techniques in optical communication systems.

In section 2.5, the two optical OFDM variants that have been introduced – coherent optical OFDM (CO-OFDM) and direct-detection optical OFDM (DD-OOFDM) are examined with a focus on their corresponding transmitter and receiver side architectures. The respective advantages and disadvantages of these two variants are also highlighted, with emphasis placed on implementation aspects that are of importance in optical access networks.

Section 2.6 looks at how OFDM has been applied in access networks in PONs and for UWB systems communications. We briefly look at the multi-user version of OFDM i.e. orthogonal frequency division multiple access (OFDMA), and review the reasons why it has been advocated for application in next-generation PONs. The principles and latest advances of OFDMA-PONs are also discussed. Next, the motivation behind the transition to RoF for the distribution of MB-OFDM

UWB signals for home networks is discussed. The final part of section 2.6 talks about the feasibility of utilising the 60-GHz band for MB-OFDM UWB RoF operation.

In section 2.7, the OptSim™ platform which is the software package used throughout this thesis for design and simulation of the different optical OFDM systems is introduced. Finally, the conclusions are drawn in section 2.8.

2.2 Next-generation broadband access networks and technologies

The access network is the link between the service provider's central office and the customer's premises. It is also called the last mile (from the service provider's perspective), or the first mile (from the customer's perspective) and provides the connection to and from the user network as shown in Figure 2.1. In the core network, optical fibre is used, with technologies such as synchronous optical networking (SONET)/synchronous digital hierarchy (SDH) employed.

Typical data rates in the core network are between 10 Gbit/s and 1 Tbit/s over long distances. However, these high data rates are not available to end users in many of today's networks because of what is referred to as the "last-mile bottleneck". This bottleneck arises because access networks based on legacy infrastructure like twisted pair were never intended to carry data and are now reaching their capacity limits.

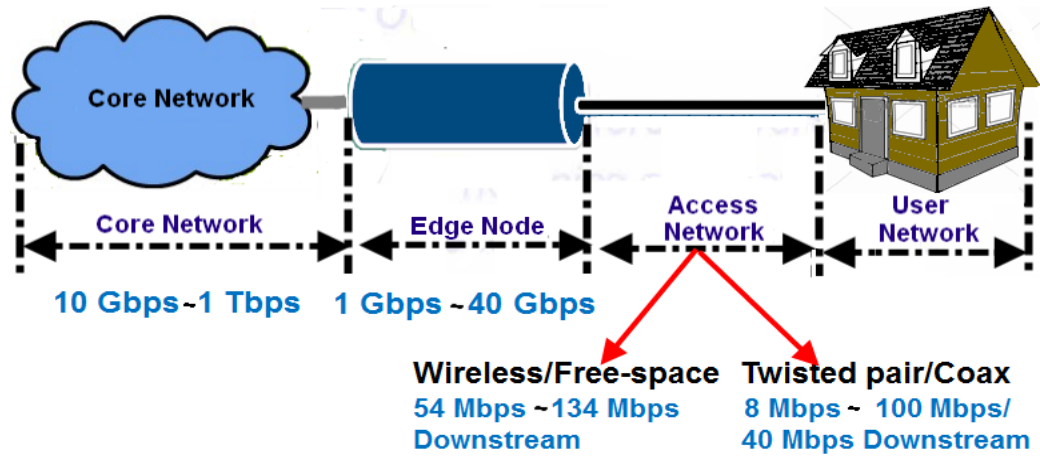


Figure 2.1. The access network.

In recent years, the demand of customers has evolved from simply voice and broadcast services to bandwidth-intensive applications such as Video on Demand (VoD), HD multimedia, online gaming, peer-to-peer file sharing, teleworking, and cloud storage. Consequently, the existing access infrastructures based on copper and coaxial cable are seriously struggling with the pressure of the bandwidth provisioning and cannot keep up.

For instance, xDSL technologies which utilise the existing copper telephone infrastructure to transmit data are distance-sensitive. Hence, the longer the distance from the local exchange to the subscriber is, the lower the available downstream data rate. In the same vein, coaxial cable is disadvantaged by its huge loss and limited bandwidth. Since VoD requires at least 3 Mbit/s of downstream bandwidth while High-definition television (HDTV) alone requires around 20 Mbit/s of downstream bandwidth, it is obvious that the capabilities of these legacy infrastructures are being tested to their limits.

As a result of this, some of the afore-mentioned technologies, typically the xDSL family, have evolved to accommodate higher bitrates for larger number of users. However, these modifications have come at the cost of a shorter reach.

For example, as shown in Table 2.1, asymmetric digital subscriber line (ADSL) typically has a maximum downstream data rate of around 12 Mbit/s at 0.3 km from the local exchange, with a maximum reach of 5.4 km. ADSL 2+ which extends the capability of basic ADSL by doubling the number of downstream channels has a maximum downstream data rate of around 26 Mbit/s at 0.3 km but has a reduced maximum reach of 3.6 km. On the other hand, very-high-bit-rate digital subscriber line (VDSL) can support downstream data rates of up to 52 Mbit/s at a distance of 0.3 km but has a much shorter maximum reach of 1.3 km, where the downstream capacity has degraded to 13 Mbit/s. This implies that for VDSL, the data has to be carried from the local exchange to a point closer to the customer.

As a result of the capacity challenges encountered by legacy infrastructure, optical fibre with its wide bandwidth and low-loss advantages, having already been adopted in core networks, has been seen as a suitable alternative and is now being increasingly deployed in access networks.

Technology	Max. Upstream Capacity (Mbit/s)	Max. Downstream Capacity	Max. Distance (km)	Downstream Capacity at Max. Distance (Mbit/s)
ADSL	0.64	12 (0.3 km)	5.4	1.5
ADSL 2+	1	26 (0.3 km)	3.6	4
VDSL	16	52 (0.3 km)	1.3	13

Table 2.1. xDSL bandwidth vs. distance capability [24]. ADSL: Asymmetric digital subscriber line. VDSL: (Very high bit rate digital subscriber line).

2.2.1 Fibre access network architectures

There are three fibre access network architectures that may be deployed. These are shown in Figure 2.2 and explained below:

- i). Point-to-point (home-run) architecture: In this architecture, individual fibres are run from the local exchange to each subscriber's premises. The advantage of this architecture is that it provides high bandwidth to each subscriber, together with high flexibility in upgrading that particular subscriber. However, since individual fibres need to be connected for each subscriber, both high installation and termination costs, as well as limited floor space in the local exchange to house large amount of equipment are disadvantages for deployment of this architecture.
- ii). Active star architecture: In this architecture, a single fibre is run from the local exchange to an active node near the subscribers. From this active node, the connection to the subscriber's premises could be made through a variety of ways as shown in Figure 2.2 (b). In fibre-to-the-cabinet (FTTCab) architecture, short spans of optical fibre are run from the active node to cabinets in the street. From these cabinets, the connection to the subscriber's premises can be made using twisted pair cables or coaxial cable lines. In the fibre-to-the-building (FTTB) architecture, optical fibre is run from the active node to an optical network terminal (ONT) usually located in the basement of a large building e.g. a block of flats. From this ONT, the communication traffic can be run throughout the building to various subscribers using coaxial cable or twisted pair cables. In the case of the FTTH architecture, optical fibre is run from the active node to an ONT located at a subscriber's home. The advantage of the active star architecture is that it requires only a single feeder fibre from the local exchange which helps reduce costs in comparison with the point-to-point architecture. However, it is disadvantaged by the need for appropriate power

supply to, and proper maintenance of the active node. Since the active node is placed outside on the street, it also needs to be able to withstand a wider range of temperature variation than in-door equipment.

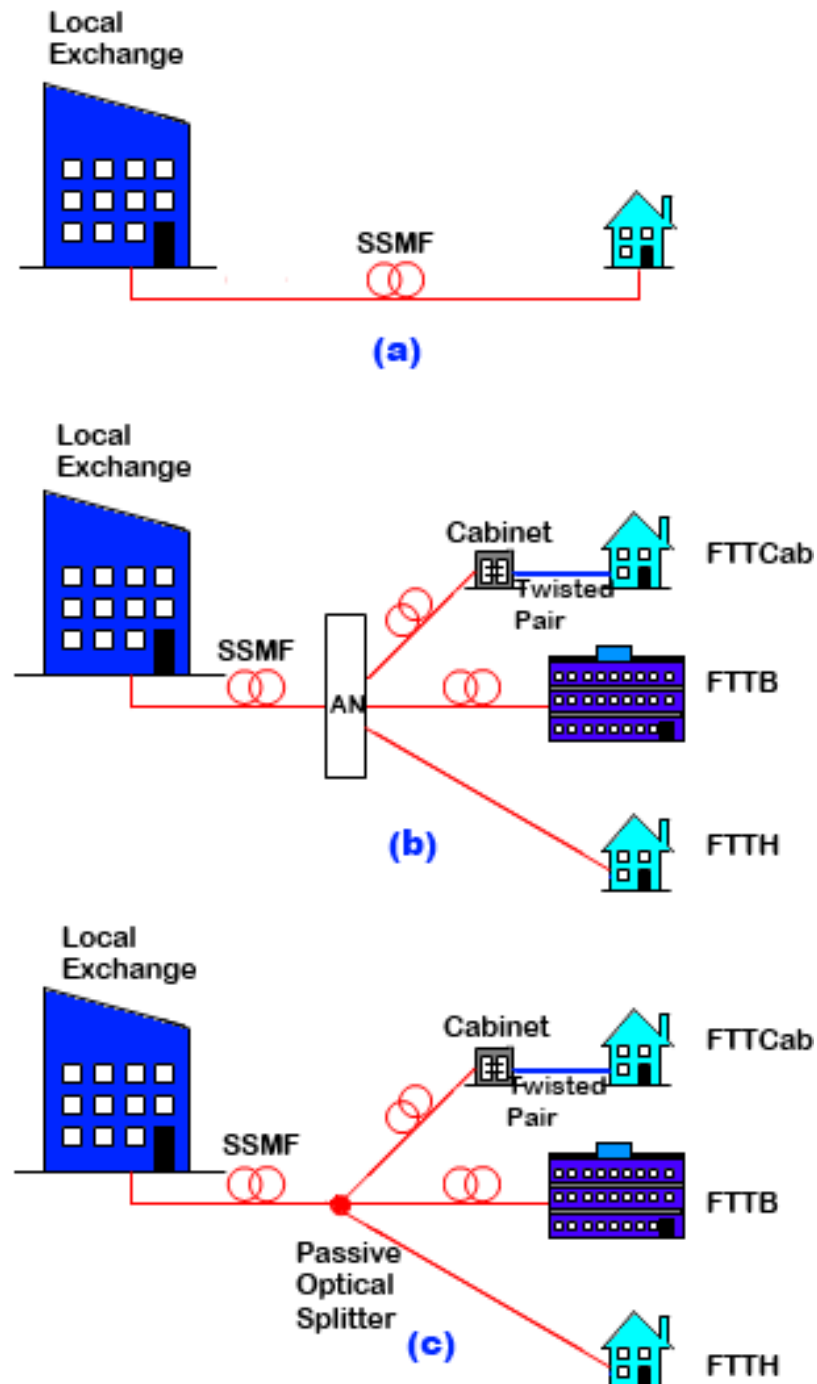


Figure 2.2. Fibre access network architectures: (a) Point-to-point. (b) Active star. (c) Passive star. SSMF: Standard single-mode fibre. AN: Active node. FTTCab: Fibre-to-the-cabinet. FTTB: Fibre-to-the-building. FTTH: Fibre-to-the-home.

iii). Passive star architecture: This architecture is essentially the same as the active star architecture with the active node replaced by a passive node (typically a passive optical splitter/combiner), and is the architecture employed in PONs. As a result of having no active electronics on the field, the maintenance and powering requirements of the active star architecture are avoided. However since in this architecture, the traffic multiplexing in the upstream direction is achieved optically by combining the individual data streams at the passive optical combiner, adequate multiple access techniques are required in order to avoid collision of the individual data streams.

2.2.2 Passive optical networks

As stated in the previous sub-section, in a PON architecture, a single fibre originates from a central location, typically an optical line terminal (OLT) in a local exchange as shown in Figure 2.3. At a point close to the customers, a passive optical splitter on the street divides the fibre between a number of optical network units (ONUs), where there is usually one ONU per customer premises.

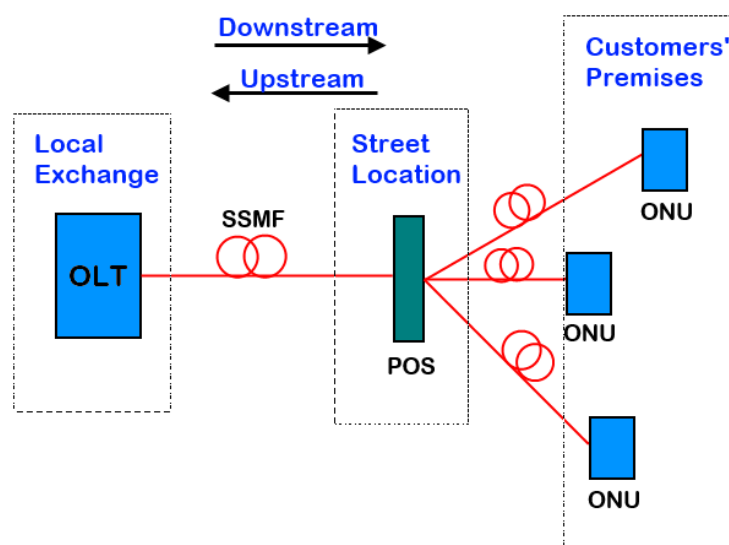


Figure 2.3. PON architecture. OLT: Optical line terminal. SSMF: Standard single-mode fibre. POS: Passive optical splitter. ONU: Optical network unit.

In order for the individual ONUs to be able to send traffic upstream to the OLT without collisions, it is necessary to have an appropriate multiple access scheme. In this regard, several multiple access techniques have been developed for PON operation. These include TDMA, WDMA, SCMA, and OCDMA.

2.2.2.1 TDMA-PONs

In TDMA-PONs, a round-robin time-domain algorithm is utilised which ensures that during each time slot, only one ONU can transmit or receive. Since the ONUs are typically at different distances from the OLT, ranging protocols are used to ensure that each ONU sends its data at the right time instant. These ranging protocols measure the round-trip time (RTT) from each ONU to the OLT and then offset each RTT to the highest RTT. For TDMA-PONs, a burst mode receiver which can handle different amplitude levels of packets is also needed at the OLT.

Initially with TDMA-PONs, the bandwidth of each ONU was assigned during ranging. This implies that the capacity of each ONU would decrease with an increase in the number of ONUs. However, TDMA-PONs can now dynamically adjust the bandwidth of each ONU depending on customer need.

Several TMDA-PONs have been standardised. These include broadband PON (BPON) defined by the ITU-T G.983 standard, the gigabit PON (GPON) defined by the ITU-T G.984 standard, and the Ethernet PON (EPON) defined by the IEEE 802.3ah standard.

BPON uses only asynchronous transfer mode (ATM) cells to carry data. It also uses a maximum of 32 ONUs with a maximum reach of 20 km. Data rates of 155/622 Mbit/s (up- and downstream) are achievable. GPON can use ATM cells, GPON encapsulation method (GEM) frames, or a mixture of both to carry data. In

GPON, the maximum ONU split size is 64 with a maximum reach of 20 km, while data rates as high as 1.244/2.488 Gbit/s (up-and downstream) are achievable. GPON also uses reed-Solomon (255,239) forward error correction (FEC). EPONs carry variable-length packets up to 1518 bytes in length, which are transported at 1.25 Gbit/s using the IEEE 802.3 Ethernet protocol [25]. The maximum ONU split size for EPON is 32; with a maximum reach of 20 km. FEC is also included as an option in the EPON standard.

2.2.2.2 *WDMA-PONs*

Typically in WDMA-PONs, each ONU uses a dedicated wavelength to transmit data to the OLT, implying there is no need for time synchronisation. This multiple wavelength arrangement requires multiple transceivers; hence AWGs or optical filters are needed to correctly distribute the wavelengths. Moreover, having each ONU operating at a dedicated wavelength might be impractical because of the cost and complexity involved for network operators in managing the inventory of lasers. To avoid this, colourless ONUs such as those utilising reflective modulators [26], spectral slicing approaches [27], or Fabry–Pérot lasers [28] have been developed and can bring down the cost of WDMA-PONs.

2.2.2.3 *SCMA-PONs*

In the upstream direction in SCMA-PONs, each ONU uses a different electrical frequency to modulate its data. Since each ONU data stream is in a different frequency band, no time synchronisation is needed. However, the need for different frequency bands puts high requirement on the frequency range of the user

equipment. In addition, if the wavelengths of the lasers used at the ONUs are very close to each other, optical beat interference products at the receiver could arise.

2.2.2.4 *OCDMA-PONs*

In OCDMA-PONs, different ONUs are assigned unique orthogonal optical codes. Each ONU could use a different sequence of short optical pulses which are on-off modulated with the data to be transmitted (time-slicing) or different combination of spectral slices from a broadband optical source (spectral-slicing). The disadvantage of OCDMA-PONs is that they require expensive optical encoders and decoders, limiting their use to special applications for e.g. where network security is a major concern.

2.3 *Radio-over-fibre techniques*

Although FTTH access technologies can provide huge bandwidth to subscribers, they are not flexible enough to permit user mobility. On the other hand, while wireless networks are typically quick and easy to deploy, and also permit user mobility, they require increased cell density to provide Gbit/s data rates. Consequently, in order to support multi-Gbit/s communications, next-generation access networks are featuring the integration of optical fibre and wireless networks in the form of RoF architectures so as to harness the respective advantages of both propagation media. Such a convergence of the two networks will enable network penetration to be boosted and will result in capital and operational cost savings.

RoF techniques are involved with transmitting RF signals from a central station, via optical fibre, to multiple remote antenna units. Out of the different

methods used to achieve this, in this work we are most concerned with intensity modulation with direct detection (IM-DD).

In IM-DD, an intensity-modulated optical signal is obtained either by directly applying a real-valued RF signal to a laser diode to manipulate its bias current (direct modulation) as shown in Figure 2.4 (a); or indirectly, by using an external modulator like a Mach-Zehnder modulator (MZM) to modulate the intensity of light from the laser diode operating in continuous wave mode as shown in Figure 2.4 (b).

The resulting optical signal travels along the fibre where it is directly detected by a photodetector and converted back to an electrical signal for onward wireless transmission to mobile terminal units (MTUs).

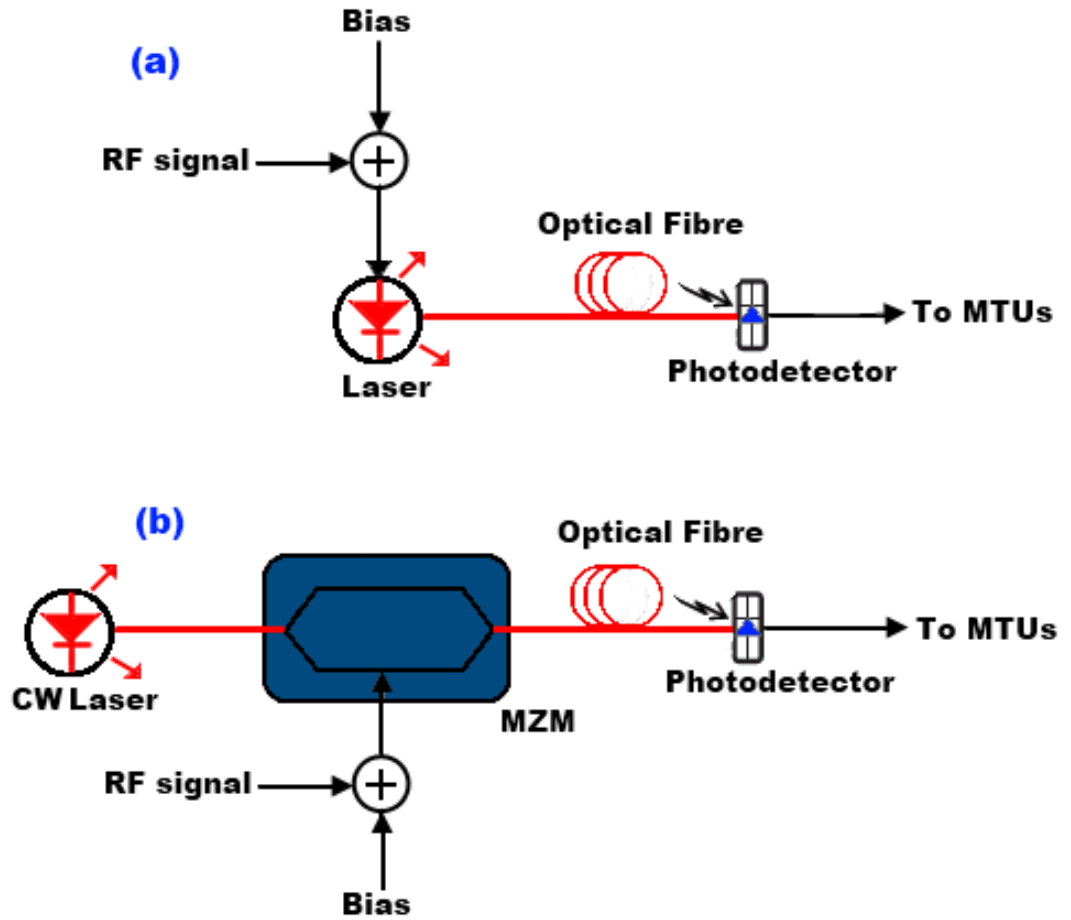


Figure 2.4. Transmitting RF Signals by IM-DD using: (a) Direct modulation of a laser (b) External Modulation using an MZM. CW: Continuous-wave. MZM: Mach-Zehnder modulator. MTU: Mobile Terminal Unit

2.3.1 Direct modulation

A laser diode can easily be modulated by controlling its current. The degree to which the laser emits light when current is injected into it is aptly illustrated on its L-I curve, as shown in Figure 2.5. As the injected current is increased, the laser emits spontaneously, until it gets to the threshold current I_{th} , where stimulated emission starts. The slope $\frac{\Delta P}{\Delta I}$ of the linear portion of this L-I curve is an indication of the efficiency of the laser diode in carrying out electro-optical conversion. The lower the value of I_{th} , the more efficient the laser is.

In directly modulated lasers, the modulation current causes transient fluctuations in the laser wavelength. This is because the frequency of the laser output changes in response to the modulation current (about 100 MHz frequency shift per mA of drive current [5]), effectively adding some frequency modulation to the signal. This phenomenon is referred to as laser chirp.

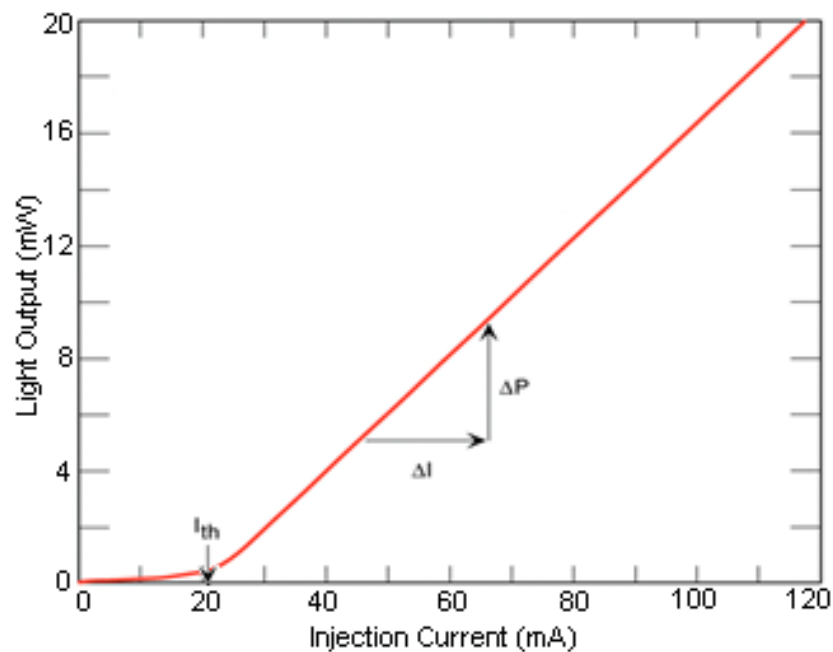


Figure 2.5. Laser diode L-I curve.

The output pulse of the laser is made of different optical wavelengths, and since the refractive index of the fibre is dependent on the wavelength, different wavelengths of the pulse propagate at different speeds. Typically, longer wavelengths travel faster than shorter wavelengths. This effect is referred to as group velocity dispersion (GVD) and results in a spreading out of the pulse as it propagates along the fibre. The variation of dispersion with wavelength is not linear so the wavelength fluctuations caused by laser chirp result in a change in the dispersion level. The effect of this interaction of the laser chirp with dispersion is more pulse broadening.

The transfer function of the fibre, $H(\omega)$ in the presence of GVD is given by:

$$H(\omega) = e^{-j\omega^2 \frac{\beta_2}{2} L} \quad (2.1)$$

where β_2 and L represent the fibre GVD parameter and fibre length respectively.

The GVD parameter can also be related to the chromatic dispersion parameter, D of the optical fibre by [29]:

$$\beta_2 = -\frac{\lambda_o^2}{2\pi c} D \quad (2.2)$$

where c is the speed of light and λ_o is the corresponding wavelength.

If the modulating RF signal has amplitude A and angular frequency ω_{RF} , ignoring the chirp of the laser, the output optical field of the laser, $E_o(t)$ can be expressed as:

$$E_o(t) = \left\{ \sqrt{2P_o} \left(\sqrt{(1 + m A \sin(\omega_{RF} t))} \right) \right\} \cdot e^{j\omega_c t} \quad (2.3)$$

where P_o , ω_c , and m are the optical power of the laser, the centre emission wavelength of the laser, and the modulation index respectively.

Expanding (2.3) into a Taylor series yields:

$$E_o(t) = \left\{ \sqrt{2P_o} \left(\sum_{n=0}^{\infty} \frac{(-1)^n (2n)! (mA \sin(\omega_{RF}t))^n}{(1-2n)n!^2 4^n} \right) \right\} \cdot e^{j\omega_c t} \quad (2.4)$$

Ignoring the higher-order terms in (2.4), the output optical field can be approximated as:

$$E_o(t) \approx \left\{ \sqrt{2P_o} \left(1 + \frac{mA}{2} \sin(\omega_{RF}t) - \frac{m^2 A^2}{8} \sin^2(\omega_{RF}t) + \frac{m^3 A^3}{16} \sin^3(\omega_{RF}t) \right) \right\} \cdot e^{j\omega_c t} \quad (2.5)$$

$$E_o(t) \approx \left\{ \sqrt{2P_o} \left(1 + \frac{mA}{2} \sin(\omega_{RF}t) - \frac{m^2 A^2}{16} [1 - \cos(2\omega_{RF}t)] + \frac{m^3 A^3}{64} [3\sin(\omega_{RF}t) - \sin(3\omega_{RF}t)] \right) \cdot e^{j\omega_c t} \right\} \quad (2.6)$$

$$\approx \left\{ \sqrt{2P_o} \left(\left(1 - \frac{m^2 A^2}{16} \right) + \left(\frac{mA}{2} + \frac{3m^3 A^3}{64} \right) \sin(\omega_{RF}t) + \frac{m^2 A^2}{16} \cos(2\omega_{RF}t) - \frac{m^3 A^3}{64} [\sin(3\omega_{RF}t)] \right) \cdot e^{j\omega_c t} \right\} \quad (2.7)$$

Equation (2.7) shows that the optical spectrum at the output of the directly-modulated laser is composed of an optical carrier at a frequency of ω_c , and several sidebands; each sideband separated at a distance of ω_{RF} from the next sideband as shown in Figure 2.6 (a). This optical signal is called a double-sideband with carrier (DSB-C) signal.

Equation (2.7) also shows that since m is generally less than 1, the amplitudes of the sidebands of the DSB-C signal decrease with increase in the harmonic order.

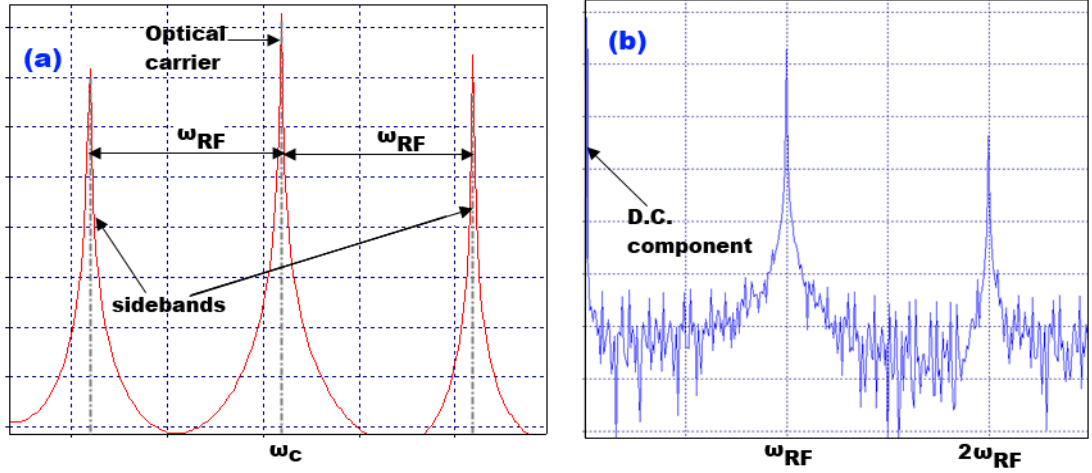


Figure 2.6. (a) Optical spectrum at output of directly-modulated laser. (b) Photodetected electrical spectrum.

Considering only the optical carrier and the first-order optical sidebands as shown in Figure 2.6 (a), and neglecting the fibre channel, the photocurrent, $I_o(t)$, generated when the optical DSB-C signal impinges on a photodetector is given by:

$$I_o(t) = \mathcal{R}\{|E_o(t)|^2\} \quad (2.8)$$

where \mathcal{R} is the responsivity of the photodetector. It is easy to show, after some algebraic manipulation, that (2.8) can be expressed as:

$$I_o(t) = 2\mathcal{R}P_o \left\{ \left[\left(1 - \frac{m^2 A^2}{16} \right)^2 + \frac{1}{2} \left(\left(\frac{mA}{2} + \frac{3m^3 A^3}{64} \right)^2 \right) \right] \right. \\ \left. + \left[\left(\frac{16 - m^2 A^2}{8} \right) \left(\frac{mA}{2} + \frac{3m^3 A^3}{64} \right) \sin(\omega_{RF} t) \right] \right. \\ \left. - \left[\frac{1}{2} \left(\left(\frac{mA}{2} + \frac{3m^3 A^3}{64} \right)^2 \right) \cos(2\omega_{RF} t) \right] \right\} \quad (2.9)$$

The first term in (2.9) is a D.C. component; the second term, centred at ω_{RF} is formed from the superimposition of the mixing products arising from the beating of each first-order optical sideband with the optical carrier. The last term, centred at $2\omega_{RF}$ is obtained from the beating of the first-order optical sidebands with

themselves. These terms are all depicted in the photodetected electrical spectrum shown in Figure 2.6 (b).

2.3.2 External modulation

For high transmission data rates, external modulation provides a better optical modulation solution than direct modulation. This is because as data rates increase, the bit durations become smaller and the impact of the pulse broadening caused by laser chirp becomes more severe.

The external modulator used for all simulations and experiments in this thesis is the MZM. A typical dual-electrode MZM (DE-MZM), as shown schematically in Figure 2.7, is made of Lithium Niobate ($LiNbO_3$) and comprises two Y-junctions. Light in the waveguide on getting to the first Y-junction is split into two halves. The electro-optical properties of $LiNbO_3$ enable a phase modulation of the light in both arms depending on whether or not an electrical field is applied to the electrodes. The light in the two arms is then recombined at the second Y-junction to produce the optical output.

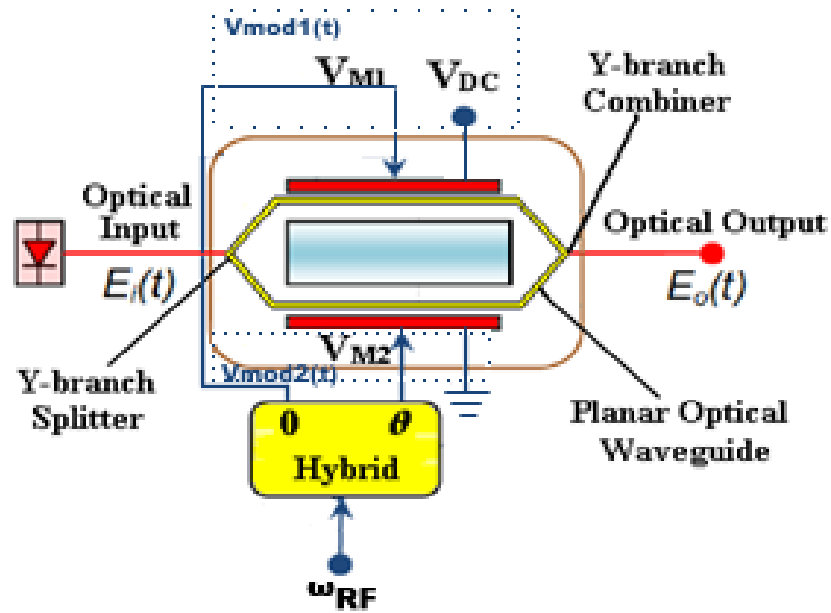


Figure 2.7. Dual-electrode MZM

With no electrical field applied, there is no phase difference between the two arms and the light combines to give an intensity maximum at the output of the DE-MZM. An application of an electrical field results in a phase difference, which could result in constructive or destructive interference.

If the phase difference is π , there's total destructive interference, corresponding to the "off" state for the DE-MZM. An MZM where only one of the arms is modulated with a voltage is referred to as a single-electrode MZM.

With an ideal extinction ratio assumed, and ignoring the insertion loss of the MZM; if the D.C. offset voltage at which maximum transmission is obtained is assumed to be 0, the output and input optical fields of the MZM are related by the following equation:

$$E_o(t) = \frac{E_i(t)}{2} \cdot [e^{j\varphi_1(t)} + e^{j\varphi_2(t)}] \quad (2.10)$$

where $E_o(t)$, $E_i(t)$, $\varphi_1(t)$ and $\varphi_2(t)$ are the MZM output and input optical fields, and the phase shifts in the upper and lower MZM arms respectively. The drive voltages $V_{mod1}(t)$ and $V_{mod2}(t)$ applied to the top and bottom electrodes are related to the phase shifts by:

$$\varphi_1(t) = \frac{\pi V_{mod1}(t)}{V_\pi}, \varphi_2(t) = \frac{\pi V_{mod2}(t)}{V_\pi} \quad (2.11)$$

Using (2.11) in (2.10), the output optical field becomes:

$$E_o(t) = \frac{E_i(t)}{2} \cdot \left[e^{j\frac{\pi V_{mod1}(t)}{V_\pi}} + e^{j\frac{\pi V_{mod2}(t)}{V_\pi}} \right] \quad (2.12)$$

where V_π is the voltage at which there's complete suppression of the MZM output.

If a D.C. bias voltage is applied to one of the electrodes of the MZM while the other D.C. terminal is grounded, the drive voltages can be expressed as:

$$V_{mod1}(t) = V_{M1}(t) + V_{DC} \quad (2.13)$$

$$V_{mod2}(t) = V_{M2}(t) \quad (2.14)$$

where $V_{M1}(t)$ and $V_{M2}(t)$ are the two outputs of the electrical hybrid coupler used to split the modulating sinusoidal RF signal with amplitude A and angular frequency ω_{RF} .

$V_{M1}(t)$ and $V_{M2}(t)$ are applied to the top and bottom electrode respectively and are given by:

$$V_{M1}(t) = A \sin(\omega_{RF}t) \quad (2.15)$$

$$V_{M2}(t) = A \sin(\omega_{RF}t + \theta) \quad (2.16)$$

where θ is the phase angle of the electrical hybrid coupler.

Making use of (2.13) – (2.16), (2.12) can be re-written as:

$$E_o(t) = \frac{E_i(t)}{2} \cdot [e^{j\pi(\varepsilon + \alpha \sin(\omega_{RF}t))} + e^{j\pi(\alpha \sin(\omega_{RF}t + \theta))}] \quad (2.17)$$

where $\varepsilon = \frac{V_{DC}}{V_\pi}$ and $\alpha = \frac{A}{V_\pi}$ are the normalised bias and drive levels respectively. If we take $E_i(t)$ to be a CW signal from a laser with amplitude B and centre emission frequency f_c , (2.17) reduces to:

$$E_o(t) = \frac{B}{2} \{ e^{j\alpha\pi \sin(\omega_{RF}t + \theta)} + e^{j\alpha\pi \sin(\omega_{RF}t)} \cdot e^{j\varepsilon\pi} \} \cdot e^{j\omega_c t} \quad (2.18)$$

Equation (2.18) can be further expanded using Bessel functions as:

$$E_o(t) = \frac{B}{2} \left\{ \left(\sum_{n=-\infty}^{\infty} J_n(\alpha\pi) \cdot e^{j[(\omega_c + n\omega_{RF})t + n\theta]} \right) + \left(e^{j\varepsilon\pi} \cdot \sum_{n=-\infty}^{\infty} J_n(\alpha\pi) \cdot e^{j[(\omega_c + n\omega_{RF})t]} \right) \right\} \quad (2.19)$$

$$E_o(t) = \frac{B}{2} \left\{ \sum_{n=-\infty}^{\infty} J_n(\alpha\pi) e^{j\left((\omega_c + n\omega_{RF})t + \frac{n\theta}{2}\right)} \left(e^{j\left(\frac{n\theta}{2}\right)} + e^{j\left(\varepsilon\pi - \frac{n\theta}{2}\right)} \right) \right\} \quad (2.20)$$

where $J_n(x)$ is the Bessel function of the first kind of order n . Equation (2.20) indicates that the optical signal at the output of the MZM is also a DSB-C signal,

made up of the optical carrier at the laser centre emission frequency ω_c , and several sidebands, located at multiples of the frequency of the modulating RF signal ω_{RF} as shown in Figure 2.8 (a). To generate this DSB-C signal, the two arms of the MZM are driven by two RF signals with equal amplitude but out of phase by π .

The MZM also has to be biased at its most linear point, the quadrature point as shown in Figure 2.8 (b). At the quadrature point, the value of the D.C. bias voltage to the MZM is $\frac{V_\pi}{2}$. However, it is important to note that depending on the value of the D.C. bias voltage, we can end up suppressing the optical carrier and the even-order optical sidebands, or the odd-order optical sidebands.

If the MZM is biased at the maximum point of the optical intensity transfer function (0 in this case), and the two arms of the MZM are driven by two RF signals with equal amplitude and out of phase by π , we obtain a special case of a DSB-C signal with its odd-order optical sidebands suppressed as shown in Figure 2.9 (a).

For this DSB-C scheme, $\theta = \pi$ and $\varepsilon = 0$. Consequently, (2.20) reduces to:

$$E_{o_DSBC}(t) = B \left\{ \sum_{n=-\infty}^{\infty} J_n(\alpha\pi) e^{j\left((\omega_c+n\omega_{RF})t+\frac{n\pi}{2}\right)} \left(\cos\left(\frac{n\pi}{2}\right) \right) \right\} \quad (2.21)$$

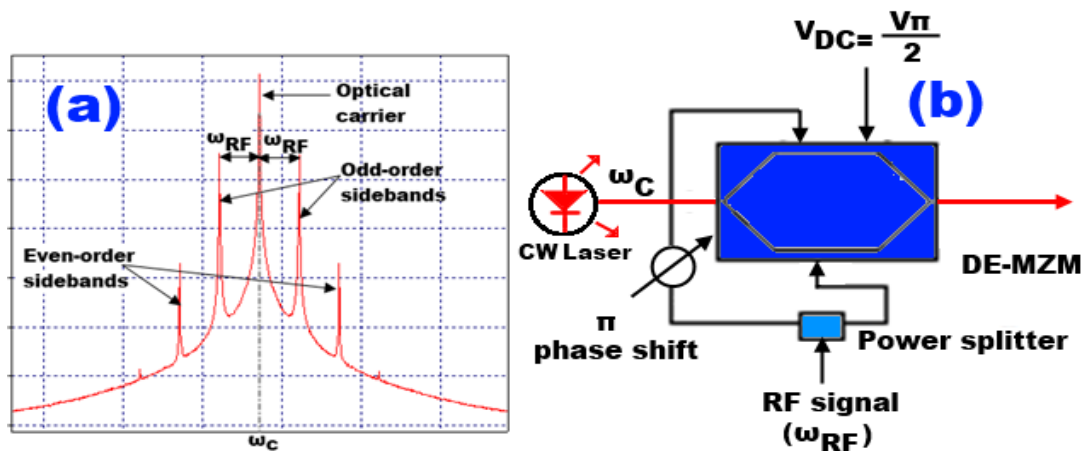


Figure 2.8. (a) DSB-C signal at output of DE-MZM showing optical carrier with even-order and odd-order sidebands (b) System configuration for generating DSB-C signals. CW: Continuous wave. DE-MZM: Dual-electrode Mach-Zehnder modulator

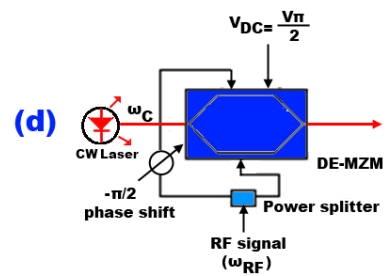
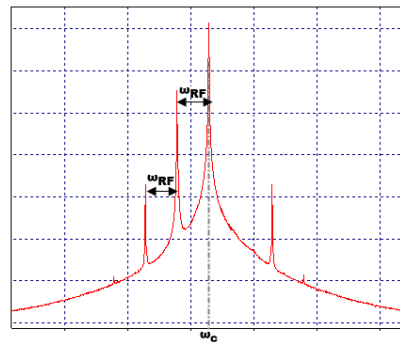
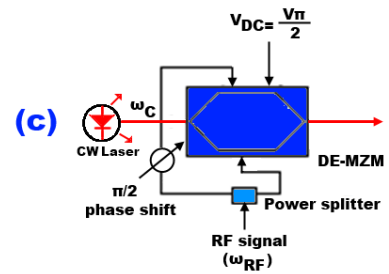
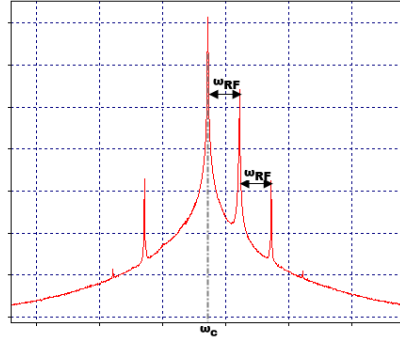
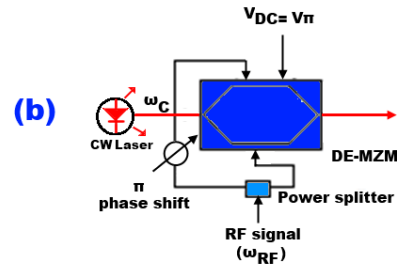
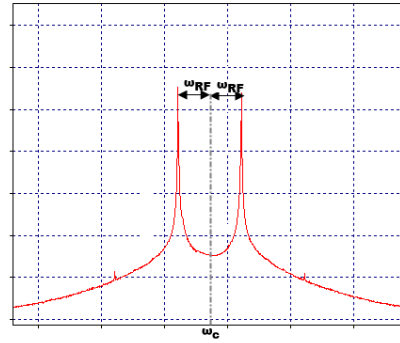
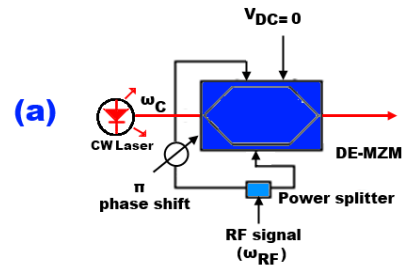
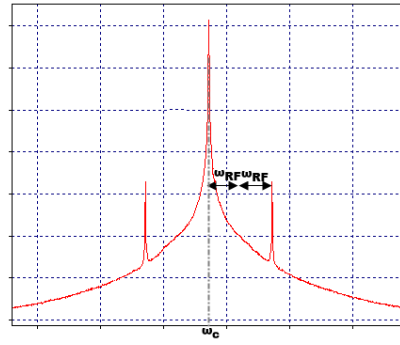


Figure 2.9. Optical spectrum of and system configuration for generating: (a) DSB-C signals (odd-order optical sidebands suppressed). (b) DSB-SC signals. (c) OSSB signals (lower first-order optical sideband suppressed). (d) OSSB signals (upper first-order optical sideband suppressed). CW: Continuous wave. DE-MZM: Dual-electrode Mach-Zehnder modulator.

A close inspection of (2.21) shows that because $\cos\left(\frac{n\pi}{2}\right) = 0$ for all odd values of n , with this DSB-C scheme, all the odd-order optical sidebands are eliminated, leaving the optical carrier and the even-order optical sidebands.

In a similar vein as in (2.8), considering only the optical carrier and the second-order optical sidebands, and neglecting the fibre channel, the generated photocurrent for this optical DSB-C signal is:

$$I_{o_DSBC}(t) = \Re\{|E_{o_DSBC}(t)|^2\} \quad (2.22)$$

Equation (2.22) can be simplified as:

$$I_{o_DSBC}(t) \approx \Re B^2 \left\{ [J_0^2(\alpha\pi) + 2J_2^2(\alpha\pi)] - 4[J_0(\alpha\pi)J_2(\alpha\pi)\cos(2\omega_{RF}t + \pi)] + 2[J_0(\alpha\pi)J_2(\alpha\pi)\cos(4\omega_{RF}t + 2\pi)] \right\} \quad (2.23)$$

It is obvious from (2.23) that for this DSB-C scheme, the output photocurrent contains the D.C. component (the first term in (2.23)), a component at $2\omega_{RF}$ (the second term in (2.23)) which is formed from the beating of the second-order optical sidebands with the optical carrier, and a component at $4\omega_{RF}$ (the last term in (2.23)) which is formed from the beating of the second-order optical sidebands with themselves. All these terms are depicted in the photodetected spectrum shown in Figure 2.10 (a).

If the D.C bias voltage is set at V_π , and the two arms of the MZM are driven by two RF signals with equal amplitude and out of phase by π , we end up suppressing the optical carrier and the even-order sidebands, leaving only the odd-order sidebands. This is a double-sideband suppressed carrier (DSB-SC) signal as

shown in Figure 2.9 (b). For the DSB-SC scheme, $\theta = \pi$ and $\varepsilon = 1$. Consequently, (2.20) reduces to:

$$E_{o_DSBSC}(t) = jB \left\{ \sum_{n=-\infty}^{\infty} J_n(\alpha\pi) e^{j\left((\omega_c + n\omega_{RF})t + \frac{n\pi}{2}\right)} \left(\sin\left(\frac{n\pi}{2}\right) \right) \right\} \quad (2.24)$$

Equation (2.24) confirms that because $\sin\left(\frac{n\pi}{2}\right) = 0$ for $n = 0$ and for all even values of n , with the DSB-SC scheme, the output of the DE-MZM is carrier-suppressed, and all the even-order optical sidebands are eliminated, leaving only the odd-order optical sidebands.

Considering only the first-order optical sidebands and neglecting the fibre channel, the generated photocurrent for this optical DSB-SC signal is:

$$I_{o_DSBSC}(t) = \mathcal{R} \left\{ |E_{o_DSBSC}(t)|^2 \right\} \quad (2.25)$$

Equation (2.25) can be simplified as:

$$I_{o_DSBSC}(t) \approx 2\mathcal{R}B^2 \left\{ J_1^2(\alpha\pi) [1 - \cos(2\omega_{RF}t + \pi)] \right\} \quad (2.26)$$

Equation (2.26) shows that for the DSB-SC scheme, the output photocurrent as shown in Figure 2.10 (b) consists of a D.C. component and a component centred at $2\omega_{RF}$, formed from the beating of the first-order optical sidebands with themselves. The DSB-SC scheme is widely used in many optical communications systems to generate a microwave signal with an angular frequency, ω_o which is double the angular frequency of the modulating RF signal (i.e $\omega_o = 2\omega_{RF}$).

Biassing the MZM at $\frac{V_\pi}{2}$ with the two arms of the MZM driven by two RF signals with equal amplitudes and a $\pm \frac{\pi}{2}$ phase shift between them yields an optical single sideband signal (OSSB). The lower sideband is suppressed if the phase shift

is $\frac{\pi}{2}$, as shown in Figure 2.9 (c) while the upper sideband is suppressed if the phase shift is $-\frac{\pi}{2}$, as shown in Figure 2.9 (d). For the OSSB scheme, $\theta = \pm \frac{\pi}{2}$ and $\varepsilon = \frac{1}{2}$.

Consequently, for this scheme, (2.20) reduces to:

$$E_{o_OSSB}(t) = \begin{cases} \frac{B}{2} \left\{ \sum_{n=-\infty}^{\infty} J_n(\alpha\pi) e^{j((\omega_c + n\omega_{RF})t + \frac{n\pi}{4})} \left(e^{j(\frac{n\pi}{4})} + j e^{-j(\frac{n\pi}{4})} \right) \right\}, & \text{if } \theta = +\frac{\pi}{2} \\ \frac{B}{2} \left\{ \sum_{n=-\infty}^{\infty} J_n(\alpha\pi) e^{j((\omega_c + n\omega_{RF})t - \frac{n\pi}{4})} \left(e^{-j(\frac{n\pi}{4})} + j e^{j(\frac{n\pi}{4})} \right) \right\}, & \text{if } \theta = -\frac{\pi}{2} \end{cases} \quad (2.27)$$

In (2.27), only the lower first-order optical sideband ($n = -1$) is suppressed if $\theta = +\frac{\pi}{2}$, while only the upper first-order optical sideband ($n = 1$) is suppressed if $\theta = -\frac{\pi}{2}$.

Considering the case where the lower first-order optical sideband is suppressed, and neglecting the second-order optical sidebands as well as the fibre channel, the generated photocurrent for this OSSB signal is:

$$I_{o_OSSB}(t) = \mathcal{R} \left\{ |E_{o_OSSB}(t)|^2 \right\} \quad (2.28)$$

Equation (2.28) can be simplified as:

$$I_{o_OSSB}(t) \approx \mathcal{R} \frac{B^2}{2} \left\{ [J_0^2(\alpha\pi) + 2J_1^2(\alpha\pi)] + 2\sqrt{2} \left[J_0(\alpha\pi)J_1(\alpha\pi) \cos \left(\omega_{RF}t + \frac{\pi}{4} \right) \right] \right\} \quad (2.29)$$

Equation (2.29) shows that for the OSSB scheme, the output photocurrent as illustrated in Figure 2.10 (c) consists of a D.C. component and a component centred at ω_{RF} which is formed from the beating of the upper first-order optical sideband with the optical carrier.

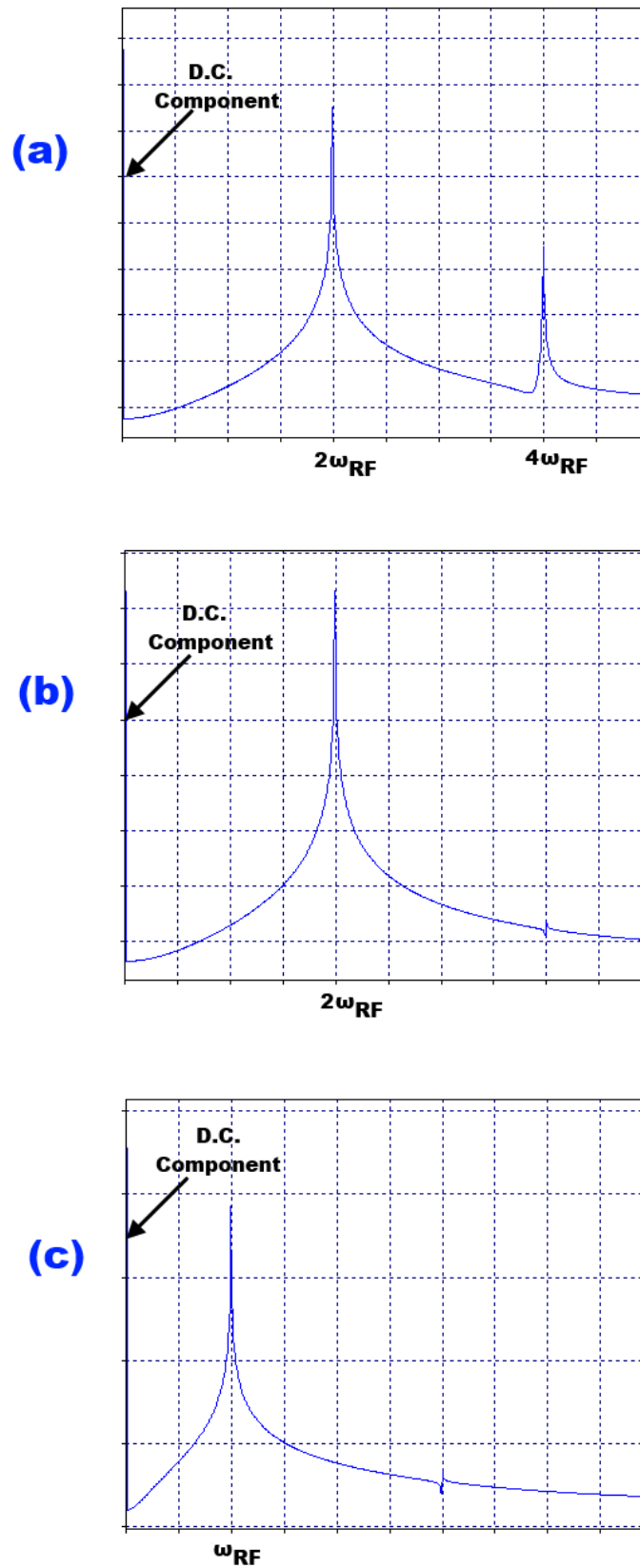


Figure 2.10. Photodetected electrical spectrum for: (a) DSB-C signals (odd-order optical sidebands suppressed). (b) DSB-SC signals. (c) OSSB signals.

2.3.3 Benefits and limitations of RoF technology

Some commonly expressed benefits of RoF technology stem from the intrinsic advantages of utilising optical fibre as a transmission medium with regards to its low attenuation loss and large bandwidth. In today's commercially-available standard single-mode fibres (SSMFs) made from silica, the reduction of the loss due to absorption by the impurities in the silica has been successful up to the point where the loss due to Rayleigh scattering is the dominant component [29]. Consequently, the attenuation losses in the three wavelength windows used for optical communication: 800 nm, 1300 nm, and 1550 nm are typically 2.5 dB/km, 0.4 dB/km, and 0.25 dB/km as shown in Figure 2.11.

These losses are much lower than that of coaxial cable, where the losses are higher by three orders of magnitude at higher frequencies [30]. For example, for frequencies above 5 GHz, the attenuation of a 0.5 inch coaxial cable is more than 500 dB/km [31]. Alternative transmission of high-frequency electrical signals through free space is also problematic because the free-space path loss increases with the square of the frequency in accordance with Friis transmission formula [32]:

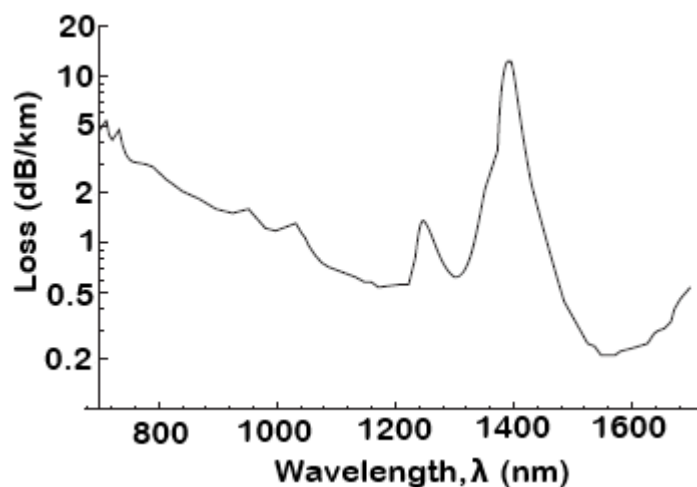


Figure 2.11. Attenuation loss in silica as a function of wavelength [29].

$$FSPL = \left(\frac{4\pi Rf}{c} \right)^2 \quad (2.30)$$

where FSPL, R, f and c represent the free-space path loss, distance between the transmitting and receiving antennas, the transmitted frequency and the speed of light respectively. This high FSPL would necessitate the use of expensive regenerative/amplification equipment in order to distribute the high-frequency electrical signals over long distances. Therefore, by transmitting these electrical signals in optical form over SSMF which has relatively low loss, the transmission distances (before the signals need to be amplified or regenerated again) are increased.

Another benefit of using RoF technology is the large bandwidth that optical fibre offers. The available bandwidth can be measured in terms of either wavelength or frequency by using the equation:

$$\Delta f \approx \frac{\Delta \lambda \cdot c}{\lambda^2} \quad (2.31)$$

where c is the speed of light, λ is the corresponding wavelength, and Δf and $\Delta \lambda$ represent the bandwidth expressed in terms of frequency and wavelength respectively. Considering the 1300 and 1550 nm transmission windows, and taking the usable bandwidth in these bands to be the bandwidth over which the loss in dB/km is within a factor of 2 of its minimum, from (2.31) the available usable bandwidth is about 35 THz [29]. However, the usable optical fibre bandwidth in today's state-of-the-art commercial networks is limited by the bandwidth of the Erbium-Doped Fibre Amplifiers (EDFAs) which are widely used. Conventional EDFAs typically operate in the 1530 to 1570 nm frequency band. Substituting $\Delta \lambda = 40$ nm in (2.31) yields a usable bandwidth of around 5 THz.

In addition to the bandwidth limitation of EDFAs, the limited bandwidth of the electronic devices used to transmit and receive the electrical signals also restricts

the utilisation of the large bandwidth offered by optical fibre. Multiplexing techniques such as optical time-division multiplexing (OTDM), wavelength-division multiplexing (WDM), as well as subcarrier multiplexing (SCM) have however been used in optical systems as solutions around this problem [30].

With the explosive multimedia-driven growth of internet traffic, current global communication systems are rapidly approaching the information capacity of current optical fibre transmission technologies. Consequently, there has also been research in recent years to address this issue, for example the UNLOC research programme currently being undertaken by researchers at UCL and Aston University which is focused on “unlocking” the capacity of optical communications by combining photonic concepts, information theory techniques, digital signal processing, and advanced modulation formats [33].

Another of the major benefits of RoF technology is that of centralisation. In RoF systems, the higher layer and signal processing functions (e.g. frequency up-conversion, carrier modulation, and multiplexing) occur only at the central station. This makes the RAUs simpler and lighter, and a single central station can be used to serve a number of RAUs. In addition, it is possible to have multiple central stations located in the same central site. Consequently, this centralisation results in easier installation and maintenance which would then lead to operational cost savings. Also, since the RAUs are simple, there will be reduced power consumption which is beneficial in situations where the RAUs are located in remote places not fed by the power grid. Having lighter RAUs is also important in specific applications scenarios like deployment of RoF in aircrafts.

Other advantages of RoF technology include its immunity to electromagnetic interference (EMI) since the signals are transmitted in the form of light; and its transparency to modulation and signal formats.

The principal disadvantage of the RoF concept as it is presented in this work is that being an analogue transmission system (since it involves analogue modulation and detection of light), it is susceptible to noise from various sources and distortion. The possible noise sources in RoF systems are the laser's relative intensity noise (RIN), the laser's phase noise, the photodiode's shot noise, the RF amplifier's thermal noise, and the optical amplifier's amplified spontaneous emission (ASE). Distortion typically arises from the non-linearity of devices (lasers, modulators), and the fibre chromatic dispersion.

When noise is added to the optical signal, it results in bit errors at the decision gate in the receiver side, while distortion could result in inter-symbol interference (ISI) due to the induced changes in the optical pulse shapes. This also results in BER degradation. The distortion brought about by the non-linearity of the external modulator will be extensively discussed in chapter 3. In section 2.3.4, we illustrate the kind of signal degradation that can occur in a RoF system because of fibre chromatic dispersion.

2.3.4 RF power degradation due to chromatic dispersion in IM-DD systems with DSB-C modulation

In this sub-section, the impact the fibre chromatic dispersion has on a RoF system employing IM-DD with DSB-C modulation, as shown in Figure 2.8 (b), is examined. In IM-DD systems with DSB-C modulation, when the optical signal impinges on the square-law photodiode, each sideband beats with the optical carrier to yield a beat signal with a frequency (and phase) equal to the difference in

frequency (and phase) of the beating components. As shown in Figures 2.6 (b) and 2.10 (a), these two beat signals add up to yield a single component at the RF frequency at the output [34].

However, due to fibre chromatic dispersion, each spectral component experiences different phase shifts depending on the chromatic dispersion parameter, the modulating RF frequency and the length of the fibre [34]. This produces a phase difference in the two beat signals at the RF frequency which results in destructive interference of the beat signals, which in turn causes a reduction of the power of the recovered RF signal, and hence a reduction in its carrier-to-noise ratio (CNR) [35].

If the phase difference between the beat signals is π , there will be total destructive interference resulting in complete power cancellation of the RF signal. To avoid this, either one of the sidebands in a DSB-C optical signal must be suppressed before transmission over fibre, or OSSB modulation implemented so there is only one beat signal at the photodiode (as shown in Figures 2.9 (c) and 2.10 (c)). Alternatively, DSB-SC transmission can be employed (as shown in Figure 2.9 (b) and 2.10 (b)).

To evaluate the dispersion-induced RF power degradation in DSB-C transmission, the optical fibre can be modelled as a BPF with flat amplitude response and linear group delay [35]. The transfer function of the fibre, $H(\omega)$ of the fibre can be obtained from (2.1) and (2.2) as:

$$H(\omega) = e^{j\frac{\pi LD\lambda_o^2 f^2}{c}} \quad (2.32)$$

where f is the frequency of the RF signal and all other terms are as defined previously in (2.1) and (2.2).

The RF power P_{RF} of the generated RF signal will vary approximately as [34]:

$$P_{RF} \propto \cos \left[\frac{\pi LD}{c} \lambda_o^{-2} f^2 \right] \quad (2.33)$$

Complete power cancellation of the RF signal occurs when the argument of the cosine function in (2.33) equals $\frac{n\pi}{2}$, for all odd values of n . This indicates that for a fixed radio frequency f , the lengths L of fibre at which power cancellation of the RF signal occur is given by:

$$L = \frac{nc}{2D\lambda_o^{-2}f^2}, \quad n = 1, 3, 5, \dots \quad (2.34)$$

Equation (2.34) indicates that as the RF frequency increases, the effect of the chromatic dispersion becomes more severe, and the power-cancellation cycle becomes smaller, limiting the fibre-link distance.

In a similar vein, for a fixed length of fibre L , the frequencies f at which power cancellation of the RF signal occur can be obtained from (2.34) as:

$$f = \left(\frac{nc}{2D\lambda_o^{-2}L} \right)^{\frac{1}{2}} \quad (2.35)$$

In order to demonstrate the RF power degradation in a DSB-C transmission, the schematic shown in Figure 2.8 (b) has been implemented in OptSim™ to yield a DSB-C signal with no sidebands suppressed. A CW laser with output power of 0 dBm and centre emission wavelength of 1550 nm acts as the optical source to the MZM which has an extinction ratio of 20 dB and a V_π of 5 V. The electrical drive to the MZM is a sinusoidal RF signal.

The value of the frequency, f of the modulating RF signal is varied from 2 to 20 GHz. The optical DSB-C signal is transmitted over an optical back-to-back link, and directly-detected by a photodiode with a responsivity of 0.6 A/W.

For each value of f , the received RF power is measured with an electrical power meter attached to the output of the photodiode. The simulations are then

repeated for 20 km of SSF with an attenuation of 0.2 dB/km and a chromatic dispersion parameter D of 16ps/nm/km. The attenuation loss brought about by fibre transmission is compensated by an optical amplifier to ensure that the received optical power at the photodiode is the same as in the back-to-back transmission.

The RF power degradation is then computed to be the difference between the measured RF power at 20 km and the measured RF power for optical back-to-back transmission.

A plot of this RF power degradation against the frequency of the signal as depicted in Figure 2.12 shows a periodic degradation of the RF power, with power nulls obtained at 5.1, 9.1, 11.6, 14, 15.8, 17.5 and 19 GHz where there is complete power cancellation of the RF signal. A maximum RF power degradation of around 25 dB is obtained with the DSB-C transmission.

Using (2.35), the power nulls are computed to occur at the following frequencies: 5.28, 9.14, 11.81, 13.97, 15.84, 17.51 and 19.04 GHz, showing very good agreement with the results obtained through simulation.

In a likewise manner, the OSSB schematic as shown in Figure 2.9 (c) has also been implemented in OptSim™ with the same simulation parameters as in the DSB-C case.

The RF power degradation has also been plotted against the RF frequency in Figure 2.12, where it can be seen that with OSSB transmission, the received RF power remains fairly constant with RF frequency with a maximum RF power degradation of only around 1.5 dB obtained.

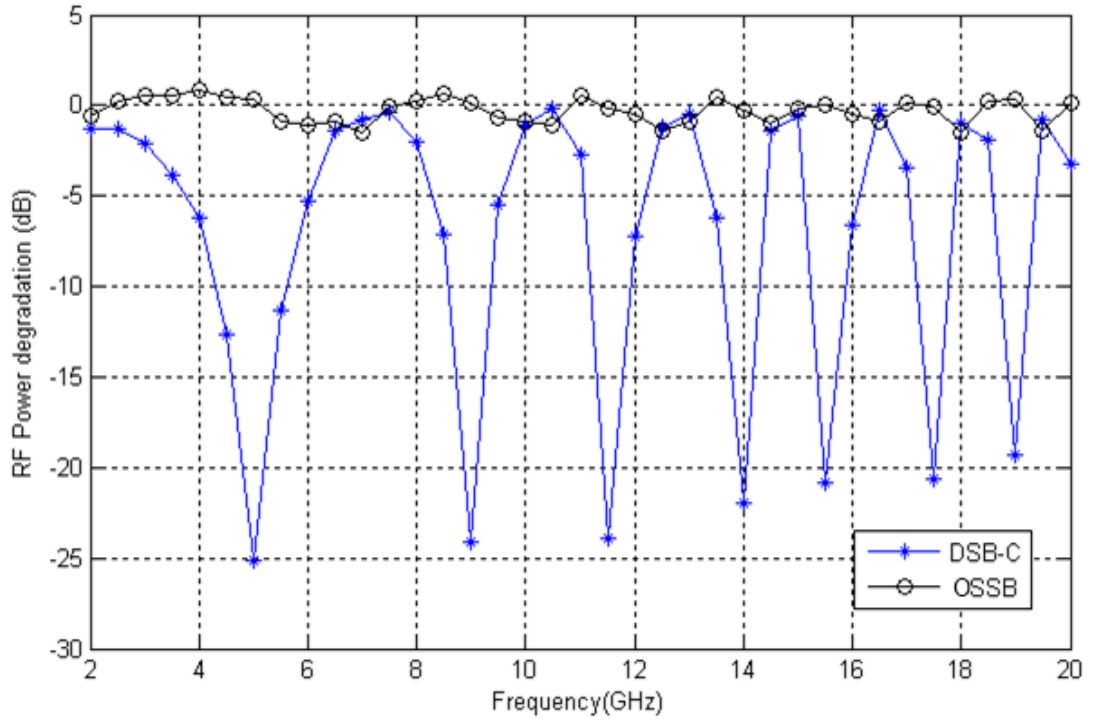


Figure 2.12. RF power degradation for DSB-C and OSSB transmissions.

2.3.5 Applications of RoF technology

Over the past couple of years, RoF techniques have been the subject of extensive research and investigation; and find application in distributed antenna systems (DAS), millimetre-wave and THz generation systems, enhancement of cable television (CATV) systems, antenna array beamforming, imaging and spectroscopy, and radar processing [36], [37]. Some of these applications are discussed below.

2.3.5.1 Distributed antenna systems

One of the most dominant markets for RoF technology today is the distribution of wireless standards over optical fibre in centralised architectures for both indoor and outdoor applications; the so-called DAS. A DAS is a network of spatially separated antennas connected by coaxial cable and optical fibre. DAS

installations have been used to extend the range and capacity of radio systems in situations where strong coverage is difficult; and are being increasingly used in a wide variety of locations including corporate office buildings, airports, shopping centres, stadiums, and underground stations.

An example of a commercially-available DAS architecture manufactured by Andrew Corporation (now owned by CommScope Inc.) for indoor wireless signal distribution [38] is shown in Figure 2.13. This DAS architecture is capable of transporting radio signals in the frequency range between 800 and 2500 MHz for cellular and WLAN applications. In this DAS architecture, the so-called equipment hotel is the central office which contains the base transceiver stations (BTSs) where the signal processing functions are carried out before the radio signals are transmitted via coaxial cable to an intelligent optical network (ION)-M master unit. The ION-M master unit is responsible for controlling the entire ION-M system and for transmitting and receiving RF signals via coaxial cable to/from the operator base stations. Optical fibre cables then connect up to 124 ION-M or ION-B remote units to the ION-M master unit. The remote units convert and amplify the RF signals from optical signals for transport over coaxial cable to the antenna for wireless coverage. The remote units also convert the RF signals from the antenna to optical signals for transport over optical fibre back towards the central office.

This particular system has been deployed at a number of important sporting events such as the Olympic Games in Sydney (2000), Beijing (2008), and London (2012); and the FIFA World Cups in Germany (2006), and South Africa (2010). It has also been deployed in the world's tallest building in Dubai, and the world's largest indoor stadium (Dallas Cowboys stadium, USA) [39].

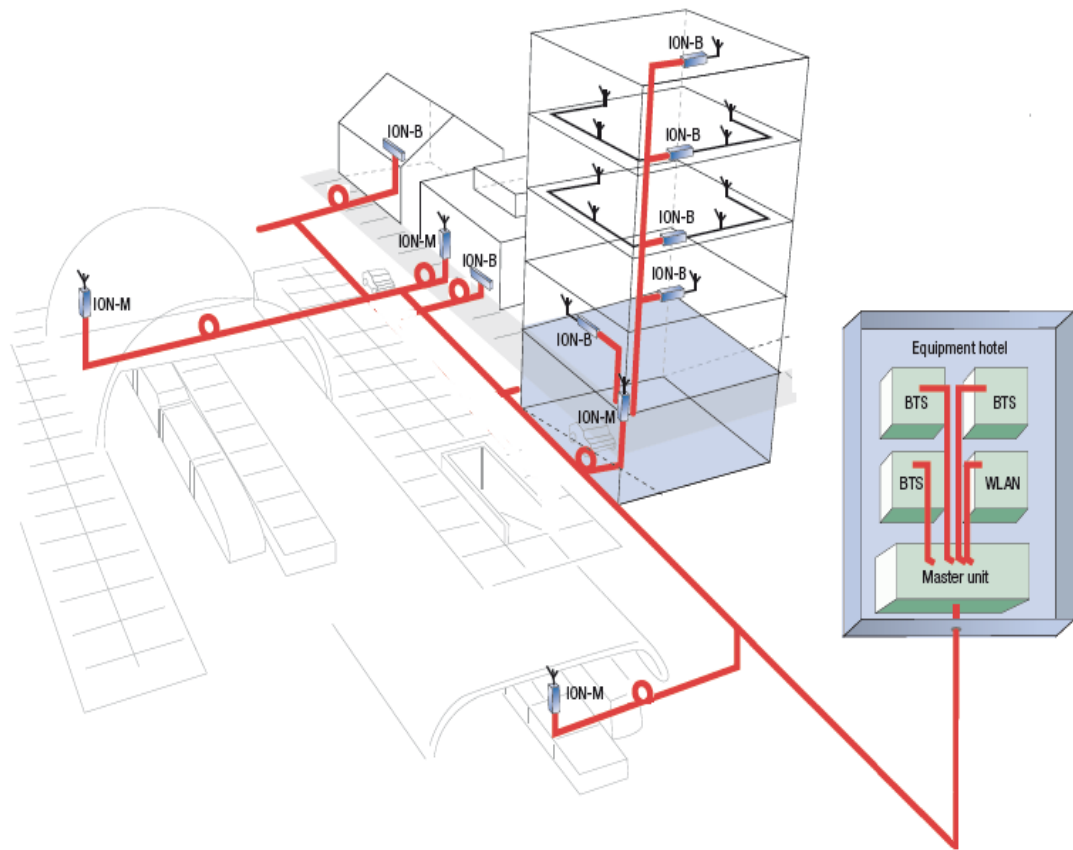


Figure 2.13. A schematic of Andrew Corporation's (CommScope Inc.) intelligent optical network (ION) family of optical distributed antenna systems [37]. BTS: Base transceiver station. WLAN: Wireless local area network.

2.3.5.2 Antenna array beamforming

Beamforming is a signal processing technique used in phased arrays which has been implemented in some mobile communication systems as a means of sharing the time and frequency resources among users who are spatially separated [40]. Over the last decade, it has become increasingly necessary to have “true time delays” in phased array antennas, especially as radar systems are required to achieve higher resolution, longer distances and wider scan angles [41]. In classic phased arrays, the phase of the transmitted/received wave is controlled by a transmit/receive module on the antenna element. For a system with narrow RF bandwidth, a classic phased array works well. However, for a system with wide RF bandwidth, the main beam direction varies with frequency, a phenomenon referred to as “squint”. Squint results

in temporarily distorted pulses, loss of gain, as well as spatial and temporal resolutions, rendering phased arrays unsuitable for many applications [41].

By replacing the phase delays with true time delays, squint can be eliminated. True time delays have been implemented using the Rotman lens, which uses RF guided waves in a special structure to produce the delays [42]. However, the Rotman lens is disadvantaged by the smaller volume and lower weight requirements of true time delays. RoF offers an alternative solution in the form of optical components that can provide lightweight delay modules. Optical true time delays have been demonstrated using optical path switching [43], [44], and dispersive components that provide different delays at different optical wavelengths [45], [46].

2.3.5.3 *Enhancement of cable television networks*

CATV networks are usually laid out over large geographical areas, and are designed for downstream broadcasting of a combination of digital and analogue channels which are frequency division multiplexed in a carrier frequency grid extending up to 1 GHz [25]. Coaxial cables are used to carry the CATV signals into subscribers' residences. In traditional CATV networks, trunk amplifiers were usually required every 600 m, with around 30 amplifiers in cascade. Consequently, the CATV signals suffered degradation from the thermal noise as well as the non-linear intermodulation distortion of the amplifiers.

The RoF concept has been applied to the enhancements of CATV networks through the so-called hybrid fibre coaxial (HFC) network. In the feeder network in HFC systems, optical fibre is used as the trunk lines that carry the CATV signals from the central office to the local neighbourhoods. In comparison with coaxial cable, the use of optical fibre ensures greater downstream bandwidth and extra

capacity for future expansion. The relatively low loss of optical fibre also means trunk amplifiers are eliminated.

At the central office in an HFC network, the CATV signals are remodulated into specific frequency grids, modulated on a light beam and sent through fibre to distribution centres. If a laser diode with low RIN or linearised external modulator is used at the central office, the signals can be transmitted without much loss of quality. The distribution centres serve around 2000 homes. From the distribution centres, optical fibre is run to several fibre nodes, with each fibre node serving about 500 homes.

At each fibre node, opto-electronic conversion takes place, and the electrical signal is carried in a tree and branch coaxial distribution network to various subscriber residences as shown in Figure 2.14. Nowadays, HFC networks carry not only CATV signals but also voice and data signals as well.

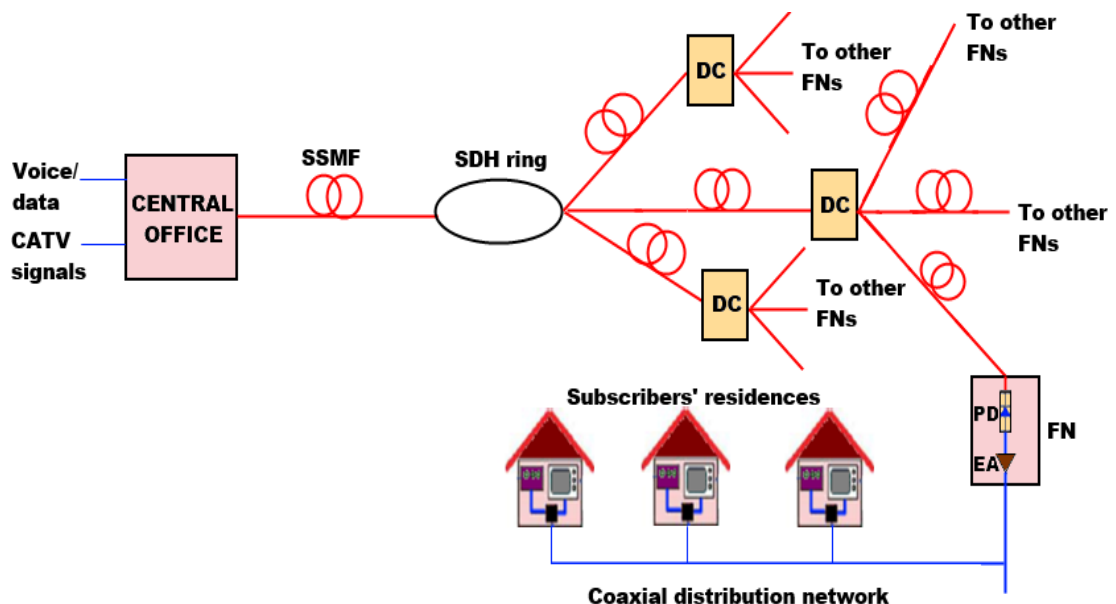


Figure 2.14. Hybrid fibre coaxial network architecture. CATV: Cable television. SSMF: Standard single-mode fibre. SDH: Synchronous digital hierarchy. DC: Distribution centre. FN: Fibre node. PD: Photodetector. EA: Electrical amplifier.

2.4 OFDM review

In RoF systems, system designers have to deal with the inherent linear distortions that exist in the fibre link (in the form of chromatic dispersion and PMD) as well as in the wireless link (in the form of multipath fading). Despite optical fibre being historically thought to be a virtually inexhaustible resource and with transmission rates being low enough to render linear distortion effects negligible [16], this is not the norm in the context of next-generation optical access. This is because as stated in section 2.2, there has been an explosion of demand of subscribers for bandwidth-intensive applications that require multi-Gbit/s data rates to support them. As data rates increase, both chromatic dispersion increases quadratically with the data rate while PMD increases linearly with the data rate [5]. In addition, recent research has shown that the optical fibre channel itself imposes some fundamental capacity limits [47].

Considering all these, OFDM, a modulation format advantaged by its spectral efficiency, robustness against delay, and ease of channel and phase estimation, made the transition into the optical communications world where it was applied for long-haul fibre transmission at high data rates of up to 100 Gbit/s [48]-[50] and is now being used for optical access applications.

In this section, a review of general OFDM principles is provided to appreciate the motivation behind applying OFDM techniques in optical communication systems.

2.4.1 Single-carrier and multi-carrier modulation systems

There are two modulation techniques that are employed in modern communication systems. These are single-carrier modulation and multi-carrier

modulation. In single-carrier modulation, the information is modulated onto one carrier by varying the amplitude, frequency or the phase of the carrier. For digital systems, this information is in the form of bits or symbols (collection of bits). The signalling interval for a single-carrier modulation system equals the symbol duration and the entire bandwidth is occupied by the modulated carrier. As data rates increase, the symbol duration T_s becomes smaller. If T_s is smaller than the channel delay spread τ , there will be significant ISI due to the memory of the dispersive channel [51] and an error floor quickly develops. Consequently, the system becomes more susceptible to loss of information from adverse conditions such as frequency selective fading due to multipath, interference from other sources, and impulse noise.

On the other hand, in multi-carrier modulation systems such as frequency division multiplexing (FDM) systems, the modulated carrier occupies only a fraction of the total bandwidth. In such systems, the transmitted information at a high data rate is divided into N lower-rate parallel streams, each of these streams simultaneously modulating a different subcarrier. If the total data rate is R_s , each parallel stream would have a data rate equal to R_s/N . This implies that the symbol duration of each parallel stream is $N \times T_s$, N times longer than that the serial symbol duration; and much greater than the channel delay spread τ . These systems are thus tolerant to ISI and are increasingly being employed in modern communication systems where high data rates are used and saving of limited spectrum is of utmost importance.

As an illustration on the serial-to-parallel conversion process that occurs in multi-carrier modulation systems, let us assume we have four subcarriers labelled C_0 to C_3 , and our input bit stream is 1 0 1 1 0 0 1. Using BPSK modulation for example to map the bits to symbols, we represent bit 1 with 1, and bit 0 with -1.

Thus, our BPSK symbols are: 1 -1 1 1 -1 -1 -1 1 . The serial-to-parallel converter converts the serial bit stream into parallel streams and assigns the data to the four subcarrier channels as shown in Figure 2.15.

Figure 2.16 shows a conventional FDM transmitter incorporating a serial-to-parallel converter. As can be seen from the figure, to maintain the data rate of R_s/N for each parallel stream, the parallel symbol duration is N times as long as that of the serial symbol duration T_s . The summation of these parallel information symbols will form one FDM symbol.

	C_0	C_1	C_2	C_3
Symbol 1	1	-1	1	1
Symbol 2	-1	-1	-1	1

Figure 2.15. Serial-to-parallel conversion in FDM systems.

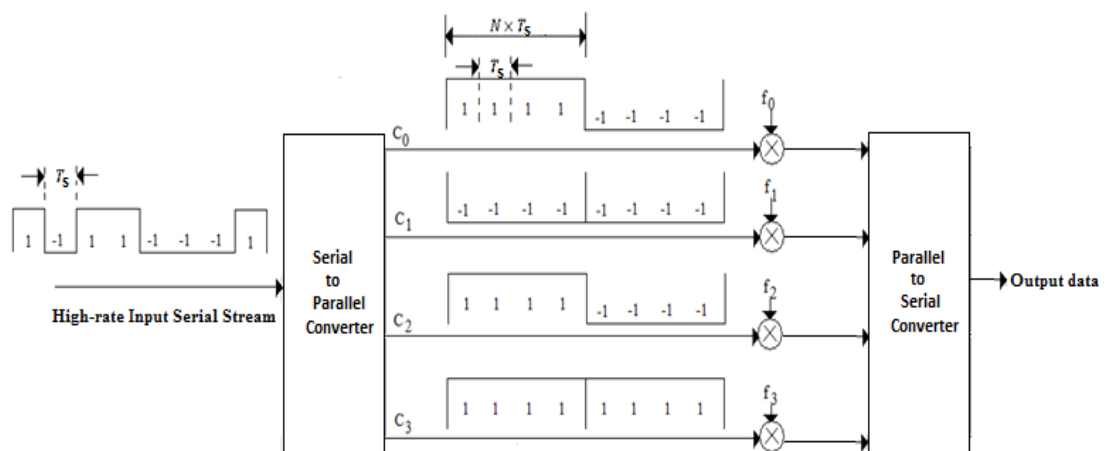


Figure 2.16. FDM transmitter.

In order to prevent one subcarrier's spectrum from interfering with another, and to ensure accurate individual demodulation of subcarriers using filters, FDM systems require guard bands between the modulated subcarriers, as shown in Figure 2.17 (b). The use of these guard bands results in poor spectral efficiency [52]. OFDM is a special case of FDM which makes use of orthogonal subcarriers. The OFDM signal in the frequency domain is shown in Figure 2.17 (c).

As we can see from Figure 2.17 (c), in OFDM, the spectra of the subcarriers overlap, resulting in saving of bandwidth. The spectrum of each subcarrier is sinc-shaped and the peak of each subcarrier corresponds to the zero-crossings of the other subcarriers. As long as the orthogonality between the subcarriers is maintained, there is no ICI because the energy from one subcarrier does not contribute to the energy of the adjacent subcarriers [52].

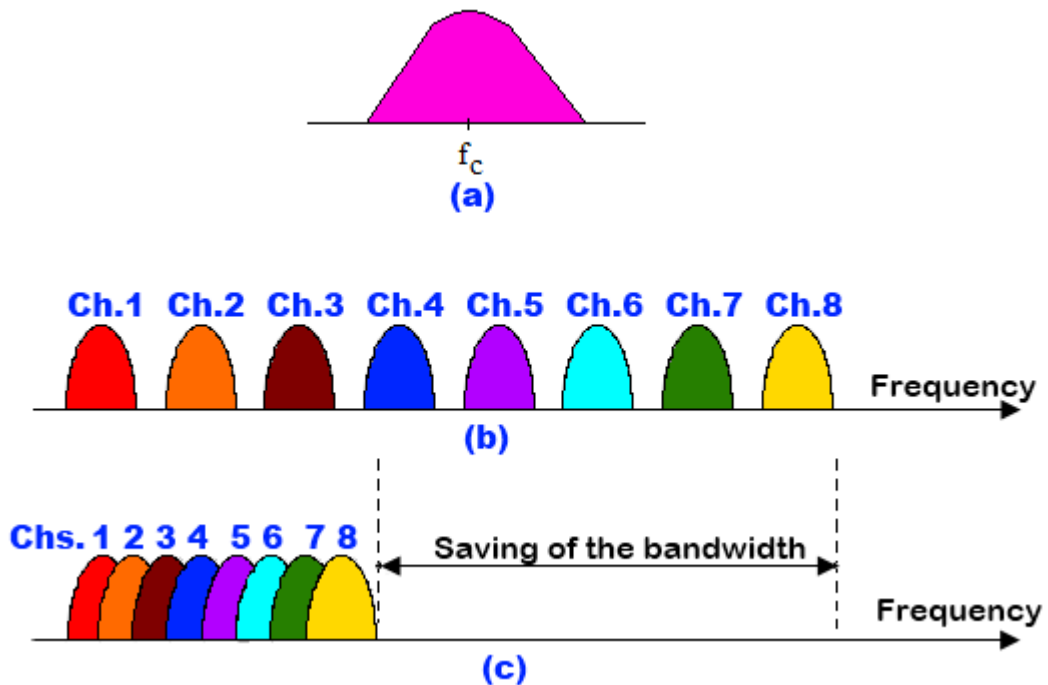


Figure 2.17. Single-carrier and multi-carrier modulation: (a) Single-carrier technique, (b) Conventional multicarrier technique (FDM), and (c) OFDM multicarrier modulation technique [52].

2.4.2 OFDM principles

The principles of OFDM have been around for several years, being introduced by Chang in a seminal paper as far back as 1966 [53]. The fundamental concept of OFDM is the orthogonality of the subcarriers. A set of subcarriers, given by $s_n(t) = e^{j(2\pi f_n t)}$ where $n = \frac{-N}{2} + 1, \dots, \frac{N}{2}$ and $0 \leq t \leq T$ are said to be orthogonal in the time domain if the following equation holds:

$$\begin{aligned} \langle s_k(t), s_l(t) \rangle &= \int_0^T s_k(t) s_l^*(t) dt \\ &= \int_0^T e^{j2\pi(f_k - f_l)t} dt \\ &= \int_0^T e^{j2\pi(k-l)\Delta f t} dt \\ &= T\delta_{k,l} \end{aligned} \quad (2.36)$$

where $\delta_{k,l}$ is the Kronecker delta symbol defined by:

$$\delta_{k,l} = \begin{cases} 1, & \text{if } k = l \\ 0, & \text{if } k \neq l \end{cases} \quad (2.37)$$

In order for the orthogonality to exist between the subcarriers, the following conditions are necessary:

- The frequency of each subcarrier must be chosen such that each subcarrier has an integer number of cycles within the OFDM symbol duration.
- The difference in the number of cycles per OFDM symbol for adjacent subcarriers must be one.

For these two conditions to be met, the frequency separation between adjacent subcarriers has to be the inverse of the OFDM symbol duration T .

Figure 2.18 shows three time-domain subcarriers within an OFDM symbol, clearly showing that the conditions for orthogonality are met.

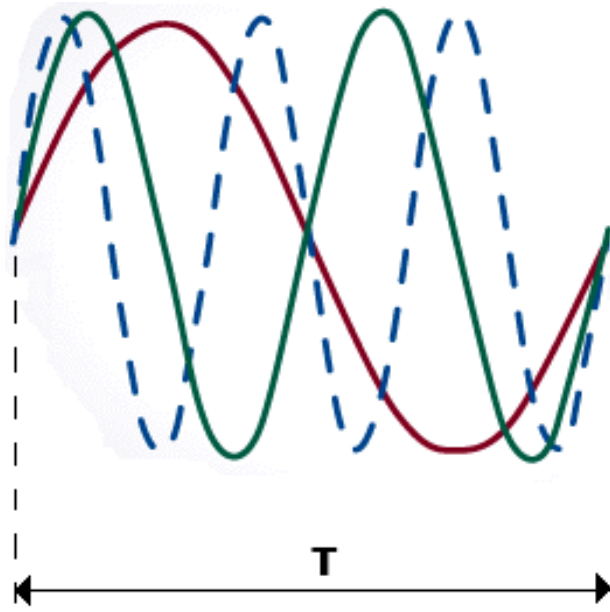


Figure 2.18. Three time-domain subcarriers within an OFDM symbol of duration T

As we can see, all subcarriers (shown here to have the same amplitude and phase) have an integer number of cycles within the OFDM symbol period T .

2.4.3 Mathematical representation of an OFDM signal

The complex envelope of an OFDM signal, ignoring the cyclic prefix, can be represented mathematically as:

$$s(t) = \sum_{k=-\infty}^{+\infty} \sum_{n=-\frac{N_{sc}}{2}}^{\frac{N_{sc}}{2}} a_{n,k} g_n(t - kT) \quad (2.38)$$

$$g_n(t) = \frac{1}{\sqrt{T}} e^{j\frac{2\pi n t}{T}}, t \in [0, T] \quad (2.39)$$

where $a_{n,k}$ is the complex symbol transmitted on the n th OFDM subcarrier at the k th signalling interval, $g_n(t - kT)$ is the complex subcarrier, T is the OFDM symbol period, and N_{sc} is the total number of OFDM subcarriers.

2.4.4 OFDM system implementations

An OFDM system can be implemented both in continuous time and discrete time. The continuous-time implementation of OFDM makes use of a bank of oscillators, one oscillator for each subcarrier. At the transmitter, the incoming information stream is mapped into symbols depending on the modulation format used (n-PSK or n-QAM) and then fed into a serial-to-parallel conversion block. Each parallel stream at the output of the serial-to-parallel conversion block is used to modulate the corresponding subcarrier simply by multiplication with that particular subcarrier. As stated in section 2.4.2, the frequencies of adjacent subcarriers must differ by $1/T$ to maintain orthogonality. At the receiver, the received signal is correlated by the same subcarriers to give the original transmitted symbols. The spectrum of a BPSK-modulated OFDM signal comprising 8 subcarriers is simulated in MATLAB in Figure 2.19 using the continuous-time implementation shown in Figure 2.20.

As we can see in Figure 2.19, the spectra of the subcarriers are sinc-shaped and overlap, where the sinc function is defined as:

$$\text{sinc}(x) = \frac{\sin(\pi x)}{\pi x} \quad (2.40)$$

For the MATLAB simulation, the incoming symbols have a symbol duration of 2.5 ms. This implies that the OFDM symbol duration, as illustrated in Figure 2.16 will be $T = 8 \times 2.5 \text{ ms} = 0.02 \text{ s}$. Consequently, the frequency spacing between the subcarriers is $1/T = 50 \text{ Hz}$, as we can clearly see in Figure 2.19. At the peak of each subcarriers spectrum, the spectra of the other subcarriers are zero, hence the subcarriers are orthogonal.

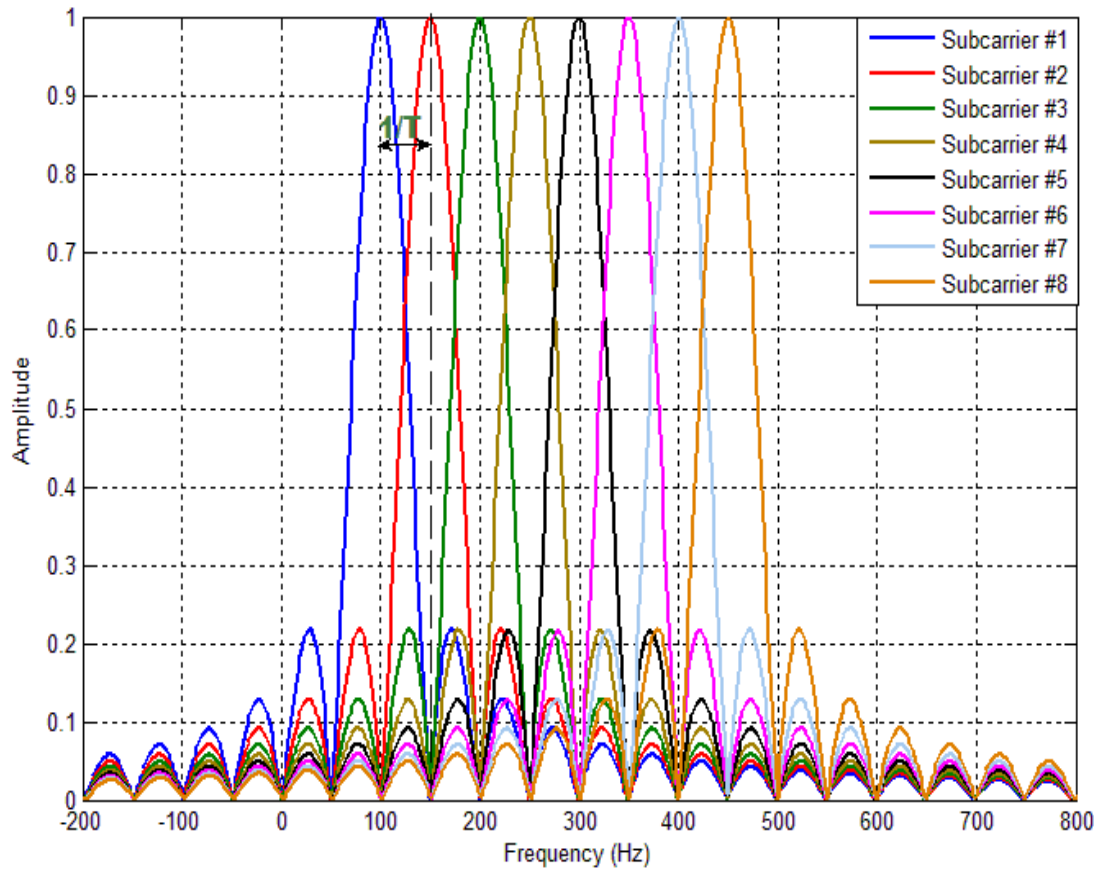


Figure 2.19. OFDM overlapping spectrum for 8 subcarriers.

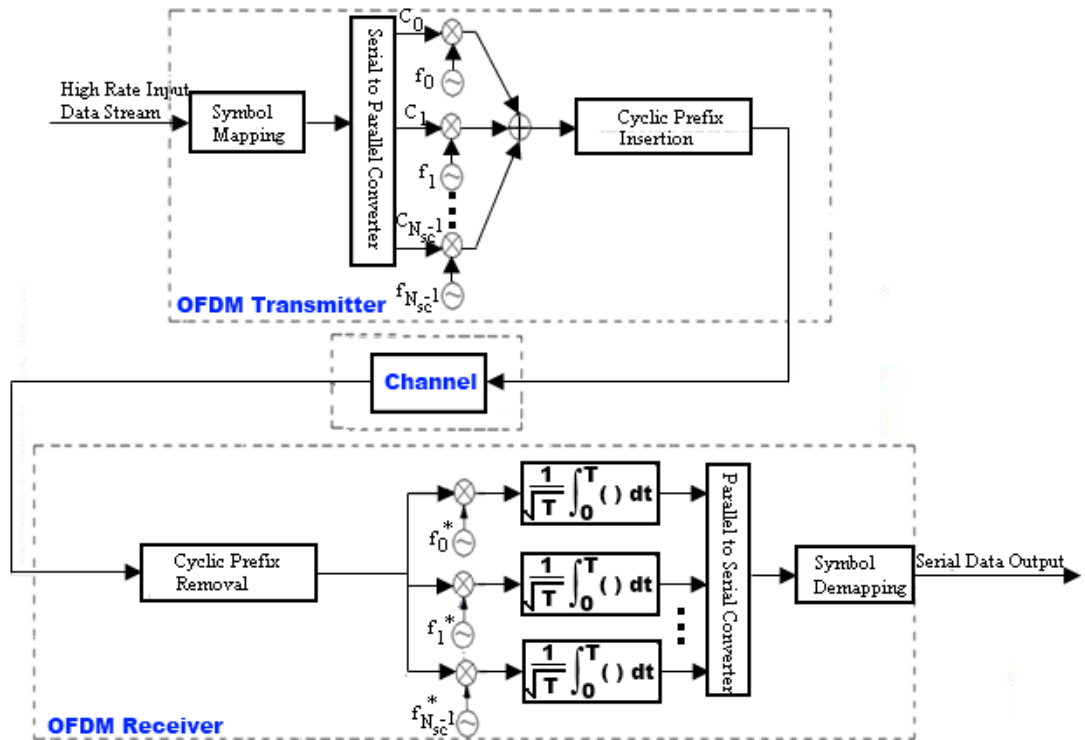


Figure 2.20. Oscillator-based OFDM implementation.

To ensure that the transmission channel affects each subcarrier as a flat channel, OFDM requires a large number of subcarriers [3]. This implies that for this implementation, a large number of oscillators would be required at the transmitter and receiver, giving rise to a considerably complex, cost-ineffective and consequently, impractical architecture.

For each OFDM symbol, the n th recovered complex symbol, $\hat{a}_{n,k}$ at the k th signalling interval is given by:

$$\begin{aligned} \hat{a}_{n,k} \\ = \frac{1}{\sqrt{T}} \int_0^T r(t) \cdot g_n^*(t - kT) dt \end{aligned} \quad (2.41)$$

where $r(t)$ is the received OFDM signal, the superscript "*" carries out the complex conjugation operation, and all other terms are as defined in section 2.4.3. Equation (2.41) shows that each complex symbol is recovered by multiplying the OFDM symbol by the complex conjugate of the particular subcarrier and integrating over the signalling interval.

On the other hand, the discrete-time OFDM implementation extends the ideas introduced by the continuous-time model into the digital domain by making use of the Discrete Fourier Transform (DFT) and the Inverse Discrete Fourier Transform (IDFT). The concept of using the IDFT and DFT to carry out OFDM modulation and demodulation was first proposed by Weinstein and Ebert in 1971 [54].

The DFT is defined on the N -long complex sequence $x = (x_j, 0 \leq j < N)$ as [55]:

$$F_k(x) = \frac{1}{\sqrt{N}} \sum_{n=0}^{N-1} x_n e^{-\frac{2\pi i}{N}nk} \quad 0 \leq k < N \quad (2.42)$$

The IDFT is defined as:

$$F_k^{-1}(x) = \frac{1}{\sqrt{N}} \sum_{n=0}^{N-1} x_n e^{\frac{2\pi i}{N}nk} \quad 0 \leq k < N \quad (2.43)$$

Thus, it can be said that the discrete value of the transmitted OFDM signal, $s(t)$ is merely a simple N -point IDFT of the information symbol, x_n . In reality, due to the large number of complex multiplications involved in computing the DFT and the IDFT, OFDM modulation and demodulation are accomplished more efficiently with the Inverse Fast Fourier Transform (IFFT) and the FFT. By using the IFFT and FFT, the number of complex multiplications is reduced from N^2 to $\left(\frac{N}{2}\right) \cdot \log_2(N)$ using a radix-2 algorithm and from N^2 to $\left(\frac{3}{8}\right) \cdot N \cdot \log_2(N-2)$ using a radix-4 algorithm [52].

Compared to the oscillator-based OFDM implementation, the discrete-time implementation is less complex because a large number of orthogonal subcarriers can be easily modulated and demodulated by using the IFFT and FFT without having to resort to having a huge bank of oscillators. The discrete-time OFDM architecture is shown in Figure 2.21.

At the transmitter, the incoming serial bit stream at a high data rate, after coding and interleaving, is converted into several low-rate parallel streams, each mapped onto corresponding information symbols for the subcarriers within one OFDM symbol. The DFT-based OFDM system treats the information symbols as if they were in the frequency domain. These symbols, denoted as X_0, X_1, \dots, X_{N-1} in Figure 2.21 are used as the inputs to an IFFT block which converts them to the time domain samples x_0, x_1, \dots, x_{N-1} . A cyclic prefix, obtained by copying a number of samples from the end of each time-domain OFDM symbol, is appended to the start of that OFDM symbol.

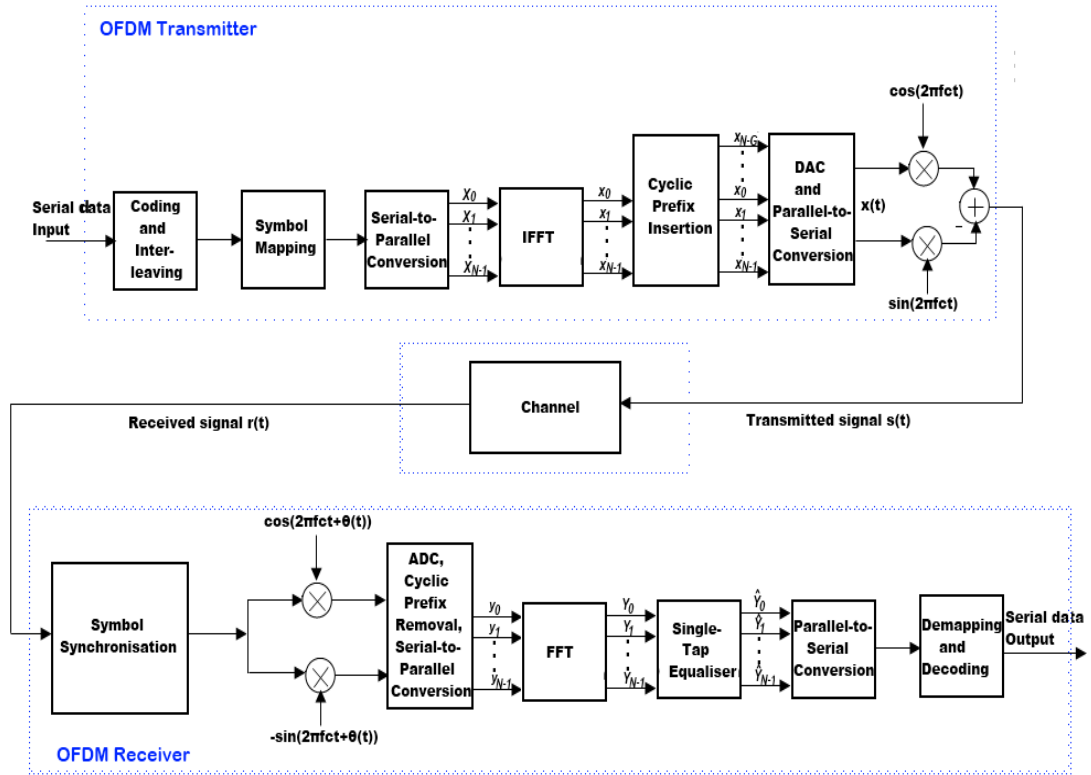


Figure 2.21. DFT-based OFDM implementation. IFFT: Inverse Fast Fourier Transform. DAC: Digital-to-analogue converter. ADC: Analogue-to-digital converter. FFT: Fast Fourier Transform.

Although this process introduces some amount of redundancy, it is through the use of the cyclic prefix that OFDM is resilient not only to ISI but also ICI that arises from multipath in time-dispersive environments. This is because provided the length of the multipath delay is less than the length of the cyclic prefix, the cyclic prefix ensures that the attenuated and delayed copies of the OFDM symbol due to multipath still have an integer number of cycles within the OFDM period. If phase transitions of any of the delayed paths do occur, they occur within the cyclic prefix interval [52]. Also, it is because of this cyclic prefix that OFDM equalisation can be easily carried out in the receiver using a one-tap equaliser.

If an ordinary guard interval with a length greater than the length of the multipath delay were to be used, the sum of the multipath replicas would not yield a

continuous wave. There will no longer be an integer number of cycles within the FFT interval, resulting in loss of orthogonality between the subcarriers, and ICI at the receiver. However, the use of the cyclic prefix ensures that the OFDM signal and its replicas are all continuous. Consequently, the sequence of received samples in one OFDM symbol is equivalent to one period of a cyclic convolution between the transmitted OFDM symbol and the samples of the channel impulse response. In the frequency domain, this corresponds to the multiplication of a particular subcarrier by its corresponding sample of the channel frequency response. This allows a one-tap equaliser to be used on that particular subcarrier to correct for any amplitude or phase distortions introduced by the channel. Figure 2.22 illustrates the cyclic prefix insertion process.

It should be noted that the use of the cyclic prefix reduces the bandwidth efficiency of OFDM transmissions by the factor $\frac{T}{(T+T_g)}$ [51], where T_g is the cyclic prefix duration. This is because some of the bandwidth is used for the guard interval without carrying information. Also, the use of the cyclic prefix results in a reduction of the SNR since the cyclic prefix samples are discarded at the receiver. After cyclic prefix insertion, the discrete time-domain baseband signal is passed through a DAC which converts the discrete signal into an analogue signal in readiness for up-conversion and subsequent transmission over the analogue channel.

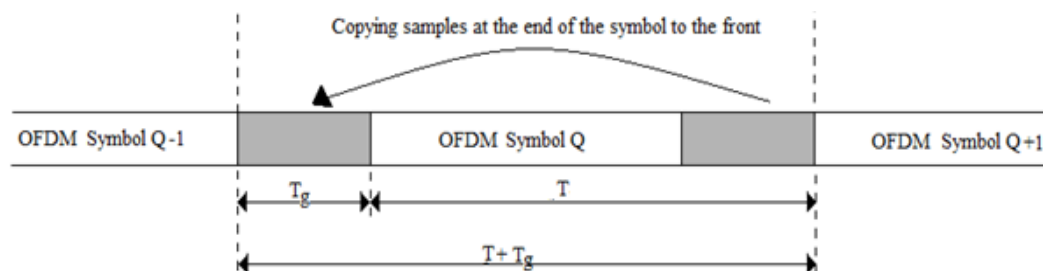


Figure 2.22. Cyclic prefix insertion. T: Active OFDM symbol duration. T_g: Cyclic prefix duration.

Ideally, this digital-to-analogue conversion should convolve each OFDM time-domain sample with a sinc function. When the DAC samples the time-domain OFDM signal at a sampling rate of f_s , aliases at multiples of the sampling rate are produced. If all the subcarriers are modulated (i.e. all the inputs to the IFFT are used to carry data), these aliases would be located right next to the main OFDM signal, meaning it would be very difficult to use any practical filter to separate them.

This problem is circumvented by oversampling using zero padding. Here, zero-valued subcarriers are placed at specific positions (around the Nyquist term) in the IFFT input sequence. Consequently, the aliases are shifted away from the main OFDM signal, thus simplifying the analogue filtering requirements at the transmitter.

As we can see in Figure 2.23, with oversampling, the zeros are mapped onto frequencies around the Nyquist term which is located at the centre of the IFFT. These frequencies correspond to the lowest negative and the highest positive frequencies of the signal.

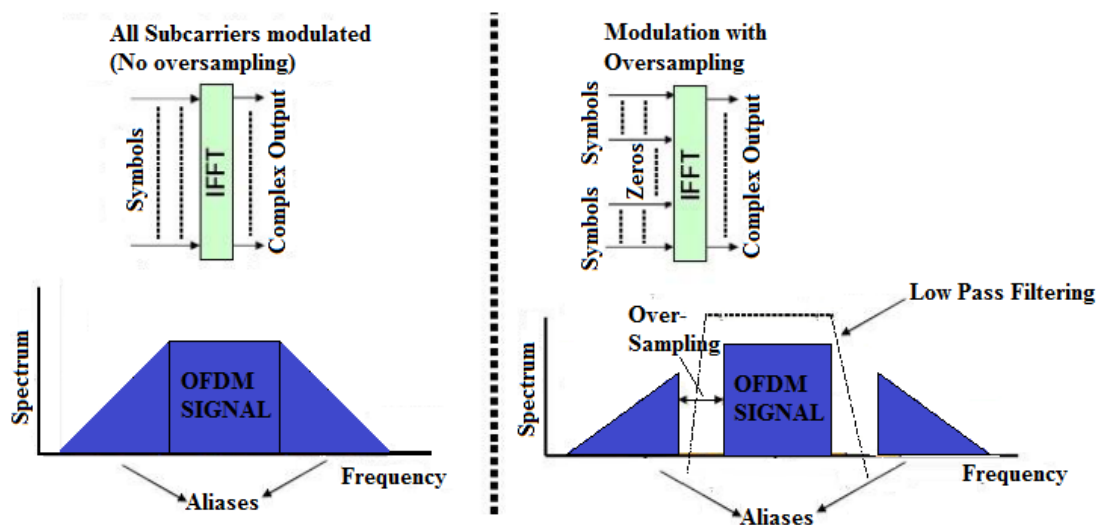


Figure 2.23. Oversampling for shifting the aliases from the OFDM signal, thereby simplifying filtering.

Consequently, the zero-carrying subcarriers become guard bands at either side of the main OFDM signal, with the resultant effect that the spectral replicas are much further apart from the main OFDM signal than in the case of no oversampling. Thus, a reconstruction filter to filter off the aliases is much easier to design.

After the DAC, the baseband analogue OFDM signal is then up-converted to an RF passband using an electrical IQ mixer. With reference to Figure 2.21, the up-converted passband signal $s(t)$ is:

$$s(t) = \text{Re}(x(t)) \cdot \cos(2\pi f_c t) - \text{Im}(x(t)) \cdot \sin(2\pi f_c t) \quad (2.44)$$

$$s(t) = \text{Re}(x(t) \cdot e^{j2\pi f_c t}) \quad (2.45)$$

where $\text{Re}(x(t))$ and $\text{Im}(x(t))$ denote the real and imaginary parts of the baseband signal $x(t)$ respectively, and f_c is the passband carrier frequency. From (2.45), it can be seen that the up-conversion process converts the complex-valued baseband OFDM signal to a real-valued signal.

At the receiver, the received OFDM signal is fed into a symbol synchronisation block whose function is to determine the precise moment where the OFDM symbol starts and ends in the received frame. The continuous-time OFDM signal is then down-converted back to baseband and passed to an ADC for conversion to the digital domain. The cyclic prefix samples are then discarded before the discrete-time samples, y_0, y_1, \dots, y_{N-1} are passed to the FFT block for demodulation. Equalisation follows next before de-interleaving, demapping and decoding to recover the data.

2.4.5 OFDM disadvantages

Despite its numerous advantages, OFDM has a number of disadvantages. Out of the various disadvantages, we will consider its high Peak-to-Average Power Ratio (PAPR) and its sensitivity to phase noise because of the significant challenges these disadvantages present for optical fibre communications

2.4.5.1 *Peak-to-average power ratio of OFDM signals*

Since OFDM has a multicarrier nature, the various subcarriers that make up the OFDM signal combine constructively. Consequently, since we are summing several sinusoids, the OFDM signal in the time domain has a high PAPR. Because of this high PAPR, any transmitter nonlinearities would translate into out-of-band power and in-band distortion. Despite the OFDM signal having relatively infrequently occurring high peaks, these peaks can still cause sufficient out-of-band power when there is saturation of the output power amplifier or when there is even the slightest amplifier non-linearity [56]. The PAPR is defined as:

$$PAPR = \frac{\max\{|s(t)|^2\}}{E\{|s(t)|^2\}}, \quad t \in [0, T] \quad (2.46)$$

where $E\{\cdot\}$ denotes the expectation operator.

In optical communications, EDFAs are employed. These amplifiers are characterised by a slow response time, making them linear regardless of the input signal power. Nevertheless, the high PAPR of OFDM is still a challenge because of the non-linearity of the external modulator, the ADC and the optical fibre [3]. When the OFDM signal is transmitted over fibre, the Kerr effect gives rise to four-wave mixing (FWM) distortion products. The strength of these FWM products depends on the signal's PAPR [57]. Techniques such as signal clipping, Selected Mapping and

Trellis Shaping (SLM) as well as signal scrambling have been proposed as solutions to the high PAPR of OFDM [3], [57].

2.4.5.2 Phase noise sensitivity

OFDM signals are quite sensitive to phase noise. The received OFDM signal with laser phase noise can be modelled mathematically as:

$$r(t) = \sum_{k=-\infty}^{+\infty} \sum_{n=\frac{-N_{sc}}{2}+1}^{\frac{N_{sc}}{2}} a_{n,k} p_n(t - kT) \quad (2.47)$$

$$p_n(t) = \frac{1}{\sqrt{T}} e^{j\left(\frac{2\pi n t}{T} + \phi(t)\right)}, t \in [0, T] \quad (2.48)$$

where $\phi(t)$ is the laser phase noise and all other terms are as defined in section 2.4.3.

The adverse effects of phase noise are two-fold:

- A rotation of the phase of all the subcarriers in the frequency domain by the same angle due to the common phase shift (CPS). This CPS results in the entire OFDM constellation being shifted by the same angle. Phase noise causes BER degradation because the constellation points could rotate beyond the symbol decision regions. This skewed rotation can be corrected by using frequency-domain equalisation.
- ICI and consequent BER degradation.

In optical OFDM systems, the laser phase noise is usually relatively large and becomes more of a problem as higher order modulation formats are employed to achieve high spectral efficiency modulation [3]. This is because the phase noise penalty is proportional to the SNR, and higher order modulation formats require higher SNR.

This sensitivity to laser phase noise has necessitated, as we will later find out in section 2.5, the requirement for narrow linewidth lasers and small FFT sizes in the CO-OFDM flavour of optical OFDM.

2.5 Optical OFDM flavours

In the previous sections, we have succeeded in gaining a fundamental understanding of some OFDM and optical communications principles which will serve as the foundation for the simulations and experiments on optical OFDM that will be carried out in succeeding chapters.

Optical OFDM solutions can be classified into two broad groups based on the techniques used for detection at the receiver. These groups are direct-detection optical OFDM (DD-OOFDM) and coherent optical OFDM (CO-OFDM). These two detection techniques have their respective advantages and disadvantages. CO-OFDM has shown superior performance than DD-OOFDM in terms of spectral efficiency and receiver sensitivity [58]. It is possible, in the context of optical access, for this increase in receiver sensitivity to be exploited in PONs to increase the ONU splitting ratio or the PON reach. However, CO-OFDM systems require a coherent receiver, meaning the optical carrier has to be generated locally by a laser before photodetection. They are thus sensitive to laser phase noise, and conventional CO-OFDM systems would require narrow linewidth lasers and small FFT sizes to reduce the influence of this phase noise. This is disadvantageous because narrow linewidth lasers are quite expensive and small FFT sizes increase the overhead of cyclic prefix [59].

CO-OFDM systems also have a higher degree of complexity and cost than DD-OOFDM systems because they require extra polarisation controllers, an optical

hybrid and dual photodiodes. This increased complexity is practically prominent in the receiver side and may pose a challenge in deploying cost-effective PONs.

Consequently, in terms of optical access, the advantages DD-OOFDM systems offer over CO-OFDM systems as regards simplicity and cost savings [60] render it the more attractive option. Hence, the simulations and experiments in this thesis will be focused entirely on DD-OOFDM.

2.5.1 DD-OOFDM systems

In DD-OOFDM systems, the transmitted optical OFDM signal is detected at the receiver using just a single photodiode. Since no laser is required at the receiver, the optical carrier has to be transmitted together with the OFDM signal. In order to ensure that the OFDM signal is unipolar, a sufficiently large D.C. bias has to be added to it. As a result, a significant portion of the total transmitted power is contained in the transmitted optical carrier, rather than in the OFDM signal. This increases the vulnerability of the optical OFDM signal to OSNR degradation [16]. It has however been shown that the DD-OOFDM performance can be optimised by equally dividing the optical power between the optical carrier and the OFDM sideband [1], [60].

As explained in section 2.3.4, because the optical carrier is present in the signal to be transmitted, to avoid power cancellation due to fibre chromatic dispersion in a DSB-C transmission, either one of the sidebands in the DSB-C optical signal must be suppressed before transmission over fibre, or OSSB modulation implemented.

When this single-sideband optical OFDM signal impinges on the square-law photodiode, intermodulation distortion products due to mixing of pairs of OFDM

subcarriers with themselves are produced. These unwanted tones occur close to D.C. Consequently, DD-OFDM systems require a spectrally-inefficient guard band between the optical carrier and the OFDM band so that these unwanted tones fall within the guard band and do not cause significant in-band distortion [60], [61]. The width of this guard band must be at least equal to the OFDM bandwidth. Thus, the required optical bandwidth is determined not only by the OFDM bandwidth but also by the bandwidth of the guard band.

Figure 2.24 shows the mixing products obtainable when the optical carrier, subcarriers and ASE intermix upon photodetection. The ASE is assumed to be band-limited by an optical filter.

In Figure 2.24, although the various components that make up the photodetected electrical signal are indistinguishable in the actual signal, they have been separated for the purpose of analysis.

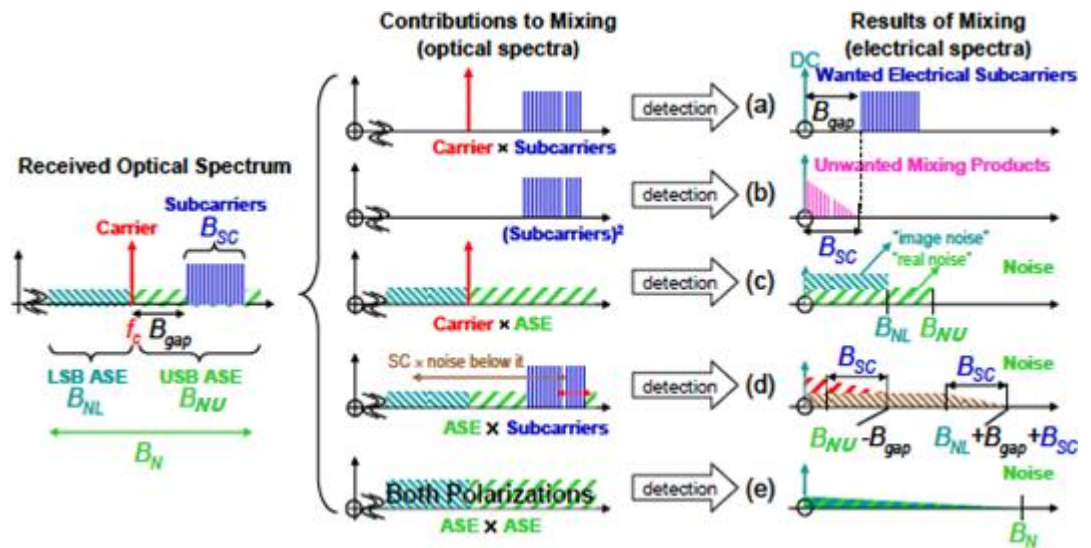


Figure 2.24. DD-OFDM received optical spectrum (left), its components (middle) and the results (right) of photodetection in the electrical domain [61]. LSB: Lower sideband. USB: Upper sideband. ASE: Amplified spontaneous emission. SC: Subcarrier. B_{NL} : Bandwidth of the LSB ASE. B_{NU} : Bandwidth of the USB ASE. B_N : Total ASE bandwidth. B_{SC} : OFDM bandwidth. B_{gap} : Bandwidth of the guard band.

The mixing of the OFDM sideband with the optical carrier yields the wanted OFDM signal with bandwidth B_{sc} . The mixing of the subcarriers with themselves yields the unwanted out-of-band noise with bandwidth B_{sc} which falls within the guard band. The unwanted in-band noise is due to products resulting from $Carrier \times ASE$, $ASE \times Subcarriers$, and $ASE \times ASE$ mixing.

In the subsequent sub-sections, three DD-OOFDM transmitter designs as introduced by Schmidt, Lowery and Armstrong in [60] are reviewed. These three designs vary in their levels of complexity but all generate the required real-valued signal required to carry out intensity modulation [56], and also all use a single photodetector at the receiver for direct-detection.

2.5.1.1 *Hermitian symmetry design*

In this design, to generate the real-valued OFDM signal, the input vector to the IFFT is constrained to have Hermitian symmetry. For Hermitian symmetry, the positive half of the N -size IFFT contains the baseband modulated symbols while the negative half contains the complex conjugates of these symbols as shown in Figure 2.25.

The width of the guard band B_{gap} is determined by the number of inputs to the IFFT that are set to zero. In the case where $B_{gap} = B_{sc}$, only $\frac{N}{4}$ complex values can be transmitted in each OFDM symbol [60].

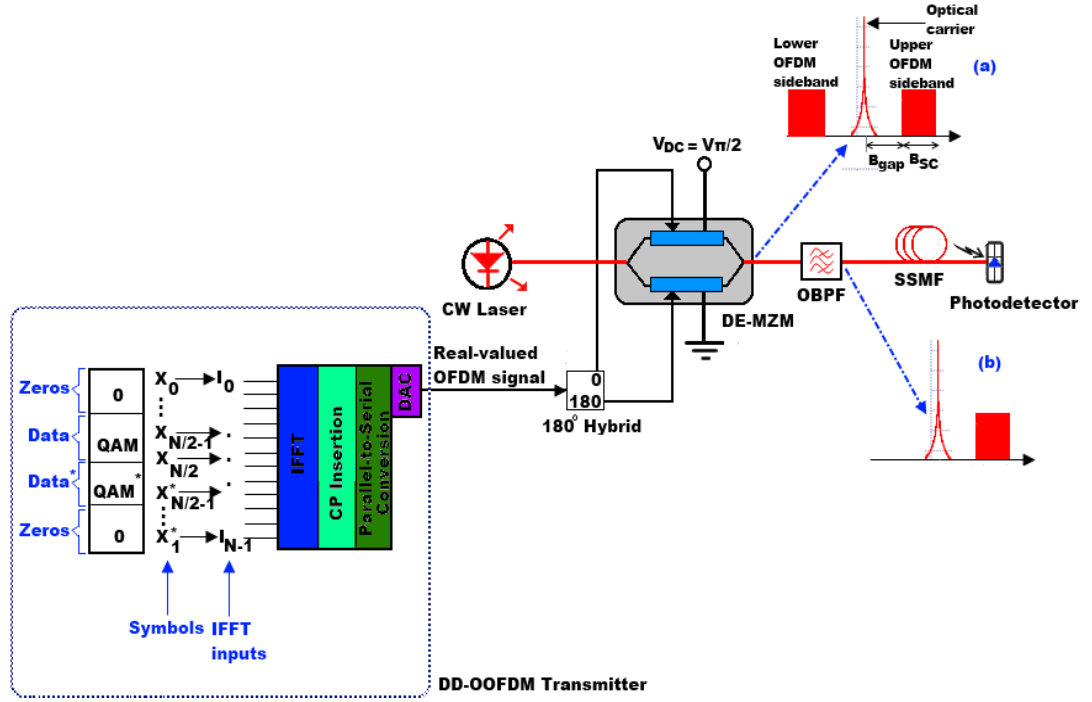


Figure 2.25. Hermitian symmetry transmitter design. QAM: Quadrature amplitude modulation. IFFT: Inverse Fast Fourier Transform. CP: Cyclic prefix. DAC: Digital-to-analogue converter. CW: Continuous wave. DE-MZM: Dual-electrode Mach Zehnder modulator. OBPF: Optical band-pass filter. SSMF: Standard single-mode fibre. Inset (a): DSB-C signal obtained at output of DE-MZM. Inset (b): OSSB signal obtained by filtering off lower OFDM sideband of DSB-C signal.

The generated real-valued OFDM signal is then fed into a 180° electrical hybrid, whose outputs drive the DE-MZM biased at the quadrature point to yield a DSB-C signal as shown in inset (a) of Figure 2.25. One of the sidebands of this DSB-C signal has to be filtered by an OBPF (inset (b) of Figure 2.25) before transmission over fibre so as to avoid the chromatic dispersion-induced power fading.

2.5.1.2 RF up-conversion design

In this design, the real-valued OFDM signal is generated by up-converting the complex baseband OFDM signal by mixing it with a sinusoidal RF signal as shown in Figure 2.26.

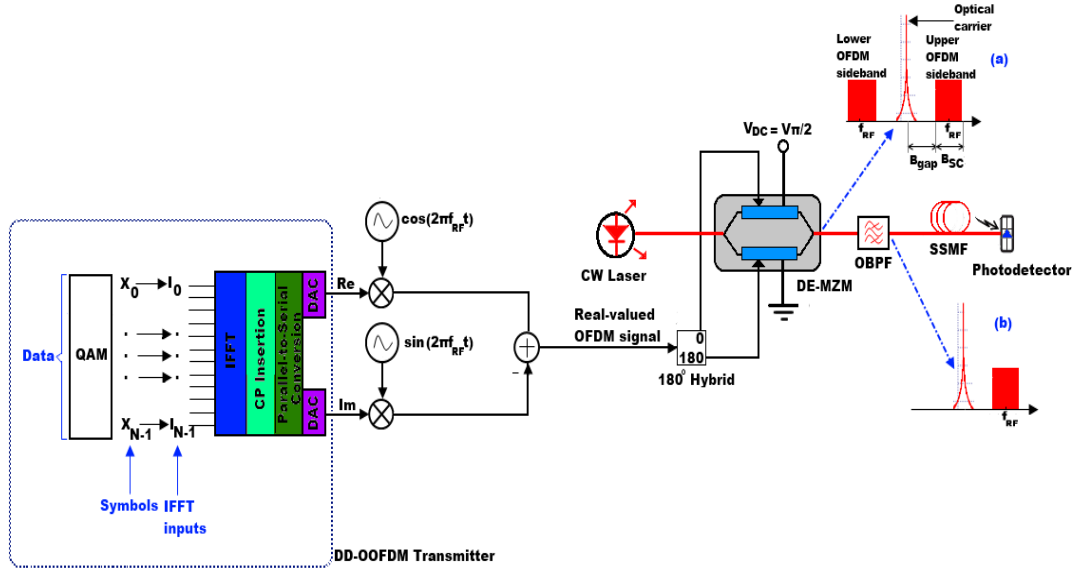


Figure 2.26. RF up-conversion transmitter design. QAM: Quadrature amplitude modulation. IFFT: Inverse Fast Fourier Transform. CP: Cyclic prefix. DAC: Digital-to-analogue converter. Re: Real. Im: Imaginary. CW: Continuous wave. DE-MZM: Dual-electrode Mach Zehnder modulator. OBPF: Optical band-pass filter. SSMF: Standard single-mode fibre. Inset (a): DSB-C signal obtained at output of DE-MZM. Inset (b): OSSB signal obtained by filtering off lower OFDM sideband of DSB-C signal.

In this case, the width of the required guard band B_{gap} will be determined by the value of the RF frequency, f_{RF} . This implies that all the OFDM subcarriers apart from the D.C. subcarrier can be used to carry data [60]. In a similar manner as in the Hermitian symmetry design, one of the sidebands of the DSB-C signal generated at the output of the DE-MZM has to be suppressed before transmission over fibre.

2.5.1.3 Hilbert transform design

This design circumvents the need for an optical filter to carry out sideband filtering of the generated optical OFDM signal. To achieve this, the concept of generating an OSSB signal as shown previously in Figures 2.9 (c) and 2.9 (d) is employed with the difference being that the required 90° phase difference between the dual driving signals is obtained using the frequency-domain Hilbert transform. Hence, the quadrature-biased MZM is driven by a real-valued OFDM signal and its Hilbert transform as shown in Figure 2.27.

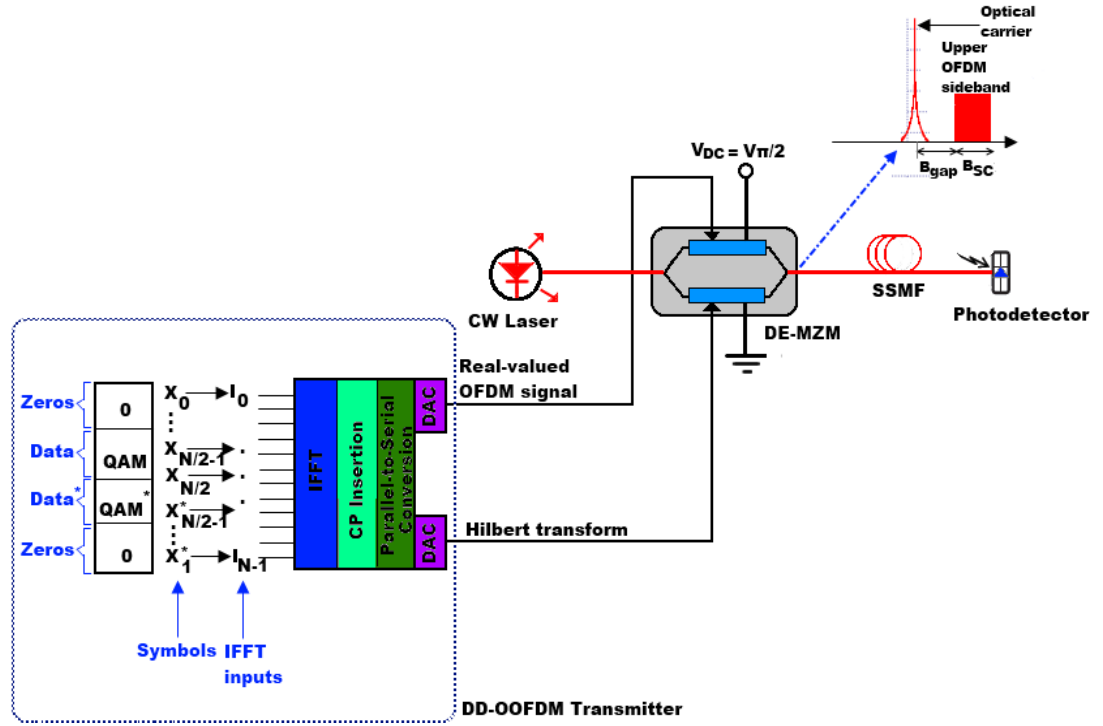


Figure 2.27. Hilbert transform transmitter design. QAM: Quadrature amplitude modulation. IFFT: Inverse Fast Fourier Transform. CP: Cyclic prefix. DAC: Digital-to-analogue converter. CW: Continuous wave. DE-MZM: Dual-electrode Mach Zehnder modulator. SSMF: Standard single-mode fibre. Inset: OSSB signal obtained at output of DE-MZM.

The real-valued OFDM signal is obtained by utilising Hermitian symmetry. The Hilbert transform is preferred to using a 90° electrical hybrid for OSSB generation because electrical hybrids are limited by the range of frequencies they can operate at. Consequently, if the modulating OFDM signal is at an IF frequency which is out of the operating range of the 90° hybrid, it would be impossible to carry out OSSB modulation. Using the Hilbert transform resolves this issue. The inset of Figure 2.27 shows that an OSSB signal is produced at the output of the DE-MZM.

2.5.2 CO-OFDM systems

The concept of CO-OFDM was first proposed by Shieh and Athaudage [62], and early CO-OFDM experiments included 1000-km SSMF transmission at 8 Gbit/s [4], and 4160-km SSMF transmission at 20 Gbit/s [59]. Subsequent CO-OFDM

experiments have successfully used a variety of per-channel multi-Gbit/s data rates, from 400 Gbit/s [63] to 1 Tbit/s [64], [65] and higher [66].

In CO-OFDM systems, the optical carrier is not transmitted together with the OFDM sideband. This implies that unlike in DD-OFDM systems, more optical power can be allocated to the OFDM sideband. In addition, since CO-OFDM utilises coherent detection, the full optical field is linearly captured [67]. Consequently, in CO-OFDM systems, the need for a frequency guard band between the optical carrier and the OFDM sideband to isolate IMD effects is obviated.

However, as previously stated, in CO-OFDM systems, the optical carrier is generated locally by a laser before photodetection. As a result, laser phase noise is an important issue which should be taken into account when designing such systems, and is especially detrimental in uncompensated links where the equaliser has to first compensate for the receive phase noise, then the channel distortions, and then the transmit phase noise [68]. The phase noise upon the OFDM signal reception comprises two components: a random noise term, and a common deterministic term originating from the laser phase drift that affects all the OFDM subcarriers uniformly [69]. This laser phase drift results in ICI. Effective digital signal processing (DSP) algorithms for phase noise correction are thus a key requirement in the design of CO-OFDM systems.

Initially, because of the laser phase drift, CO-OFDM systems required sophisticated phase tracking mechanisms to guarantee accurate symbol decision. However, recent proposals of reduced-guard-interval (RGI) CO-OFDM systems [63], [64], [70] which require a lower cyclic prefix overhead, have, in comparison with conventional CO-OFDM systems, demonstrated a significant reduction in the laser-phase-noise-induced ICI [71], [72]. The use of an interferometric device

together with very simple processing has also been proposed for reducing the phase noise of transmit or receive lasers [68].

In the subsequent sub-sections, the architecture choices for a generic CO-OFDM system as introduced by Shieh *et al.* [58] are presented.

2.5.2.1 Direct up/down design

In this design, a complex baseband OFDM signal is generated by the CO-OFDM transmitter. This baseband OFDM signal is converted to an optical signal by using an optical I/Q modulator as shown in Figure 2.28.

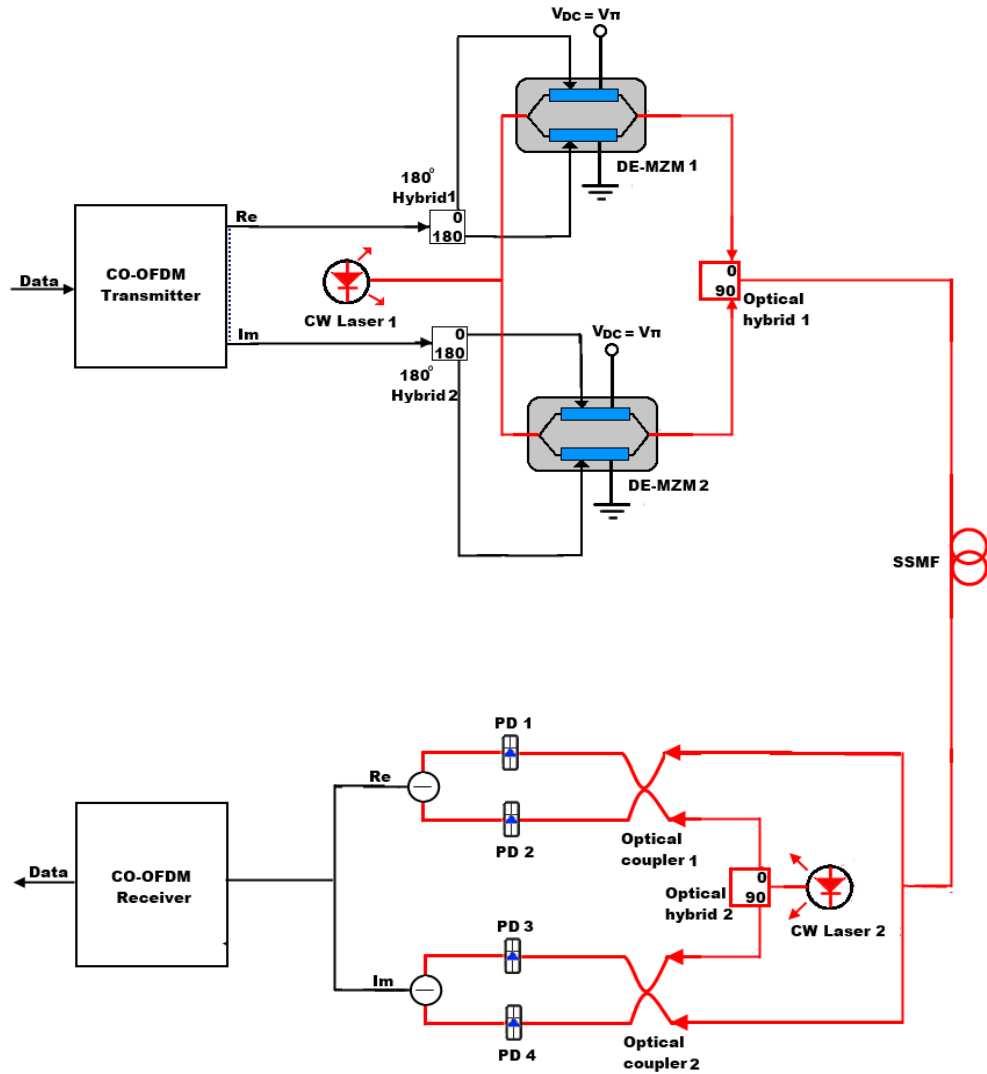


Figure 2.28. Direct up/down architecture for CO-OFDM. CO-OFDM: Coherent optical OFDM. Re: Real. Im: Imaginary. CW: Continuous wave. DE-MZM: Dual-electrode Mach Zehnder modulator. SSMF: Standard single-mode fibre.

The optical I/Q modulator is made up of two MZMs, both biased at the null-point, with an optical 90° hybrid at the output of the bottom MZM. The real and imaginary parts of the complex baseband OFDM signal are used to drive the top and bottom MZMs respectively.

With a null-point bias, the optical carrier in the generated optical signal at the output of the optical I/Q modulator is suppressed. This implies that CO-OFDM systems do not run the risk of sideband cancellation due to fibre chromatic dispersion. This generated DSB-SC OFDM signal is transmitted over the optical fibre link and then fed to the optical receiver.

In the direct up/down design, the optical receiver carries out optical I/Q detection using two pairs of balanced receivers and an optical 90° hybrid. This design obviates the need for an image rejection filter in both transmitter and receiver [58].

2.5.2.2 IF design

The transmitter for this design is quite similar to the transmitter for the DD-OFDM RF up-conversion design with the only difference being that the MZM is biased at the null point to enable suppression of the optical carrier. The optical carrier is reintroduced locally at the receiver side as shown in Figure 2.29. The OBPF shown in Figure 2.29 is used to filter off the image OFDM band obtained at the output of the DE-MZM so as to improve the spectral efficiency and power efficiency of the design.

In the IF down-conversion system, the electrical OFDM signal is first down-converted back to baseband after which electrical I/Q detection is carried out using a pair of balanced receivers.

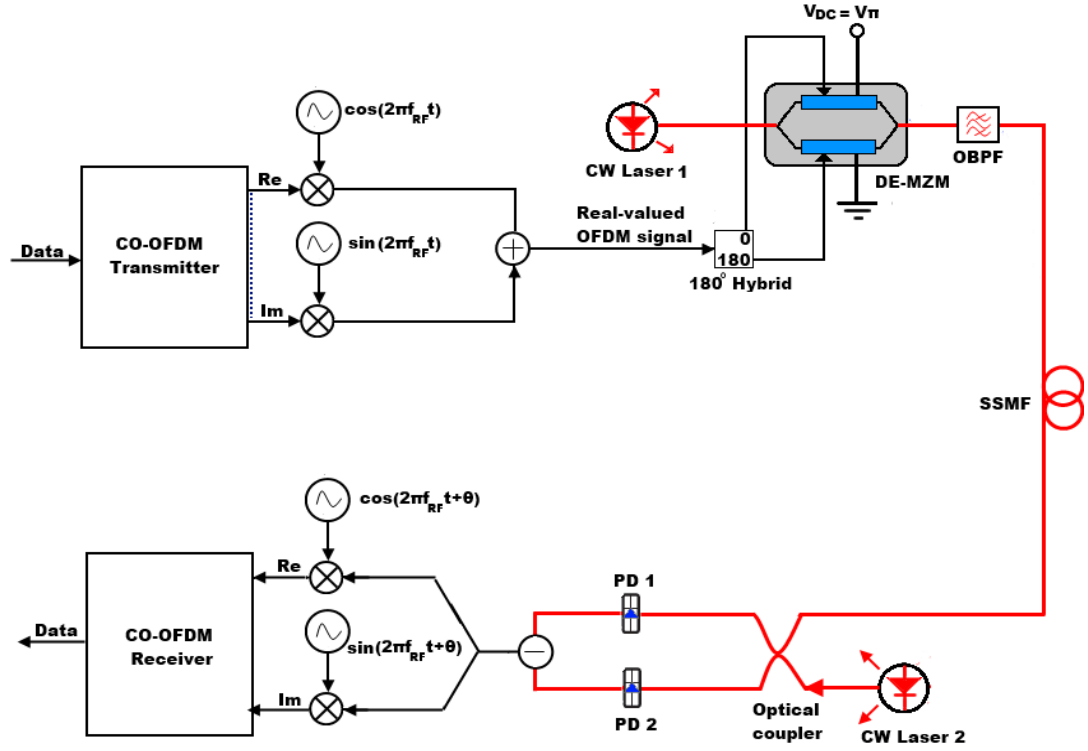


Figure 2.29. IF architecture for CO-OFDM. CO-OFDM: Coherent optical OFDM. Re: Real. Im: Imaginary. CW: Continuous wave. DE-MZM: Dual-electrode Mach Zehnder modulator. OBPF: Optical band-pass filter. SSMF: Standard single-mode fibre.

It is important to note that since the transmitter/receiver can be of either direct or IF up/down architectures, there are four design choices for CO-OFDM systems.

Although CO-OFDM systems offer many attractive advantages, they come at the expense of increased cost and complexity when compared to DD-OFDM systems. This increased complexity, which is more obvious at the receiver side, may render CO-OFDM systems unsuitable for future cost-effective, short reach access applications.

2.6 OFDM applications in optical access networks

Having described OFDM and how it has made its way into the optics world, in this section, we briefly describe the use of OFDM in PONs and UWB communications for optical access applications.

2.6.1 OFDM in PONs

Present-day PON solutions do not seem to adequately address the stringent requirements of next-generation optical access networks. Together with dynamic bandwidth assignment, next generation PON systems are expected to transparently deliver multiple services over a common architecture. This architecture should be able to support multi-stage splitting at low power consumption, with up to 1000 ONUs serviced by a given optical distribution network. In addition, it is envisioned that aggregate data rates of up to 40 Gbit/s and 10 Gbit/s downstream/upstream over up to 100 km reach would be offered by such systems [73] – [76].

The performance of current standardised TDMA-PONs as introduced in section 2.2.2.1 is affected by packet latency and not transparent to other traffic flowing simultaneously through the same link. In addition, the complexity of burst-mode TDM receivers at high data rates makes it quite a challenge to scale up TDMA-PONs to multi-Gbit/s aggregate data rates [73].

On the other hand, although WDMA-PONs as introduced in section 2.2.2.2 can transparently deliver multiple services by utilising a dedicated wavelength for each ONU, they are still currently quite expensive to deploy. Moreover, WDMA-PONs demonstrate limitations in terms of bandwidth granularity and flexibility in dynamic bandwidth allocation.

It does seem that the current PON solutions used today are not able to meet the requirements of next-generation optical access. To combat the disadvantages suffered by the other PON technologies, OFDMA-PON has been introduced [77], [78] for the delivery of heterogeneous services. OFDMA is a multi-user version of OFDM whereby instead of assigning all the subcarriers to one user, subsets of subcarriers are assigned to different users.

There are three optical OFDMA variants as shown in Figure 2.30. In the first variant, referred to as 1-D OFDMA, different subcarriers from the same OFDM band are assigned to different users. The second variant is called 2-D OFDMA, where different users are assigned different OFDM subcarriers and TDM time-slots. It is therefore a combination of 1-D OFDMA with TDMA. The final variant, called 3-D OFDMA features different users being assigned different OFDM subcarriers and TDM time slots on different WDM wavelengths. The dynamic bandwidth allocation, TDM slot scheduling, as well as the wavelength assignment can all be implemented in DSP [16].

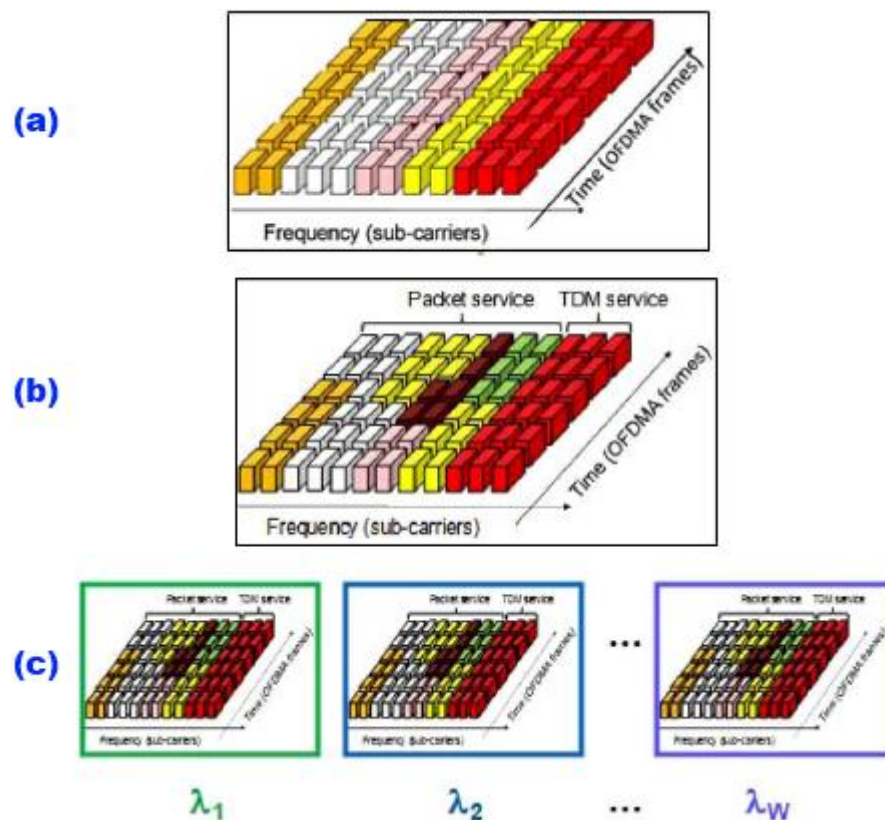


Figure 2.30. Optical OFDMA variants [16]: (a) 1-D OFDMA. (b) 2-D OFDMA. (c) 3-D OFDMA.

The OFDMA-PON principle is illustrated in Figure 2.31. The OLT assigns a sub-channel with one or more subcarriers to each ONU. Some dedicated subcarriers are reserved as transparent pipes for delivery of arbitrary analogue or digital signals. In the case that one ONU does not have enough traffic to fill up its assigned bandwidth, several ONUs can share the same sub channel using TDM. The OLT receiver is capable of receiving multiple signals from different wavelengths simultaneously and is also able to allow multiple transmitters to operate within the same time slot.

The advantages of OFDMA-PON over the other PON technologies can be summarised as follows [3]:

1. It has improved spectral efficiency, implying that low bandwidth optical components can be used.
2. It requires fewer receivers in the OLT, translating to cheaper costs than in WDM-PON.
3. It demonstrates service transparency since the reserved subcarriers that act as transparent pipes can support both digital and analogue signals.
4. It is a scalable architecture and can coexist with WDM-PON and TDM-PON.

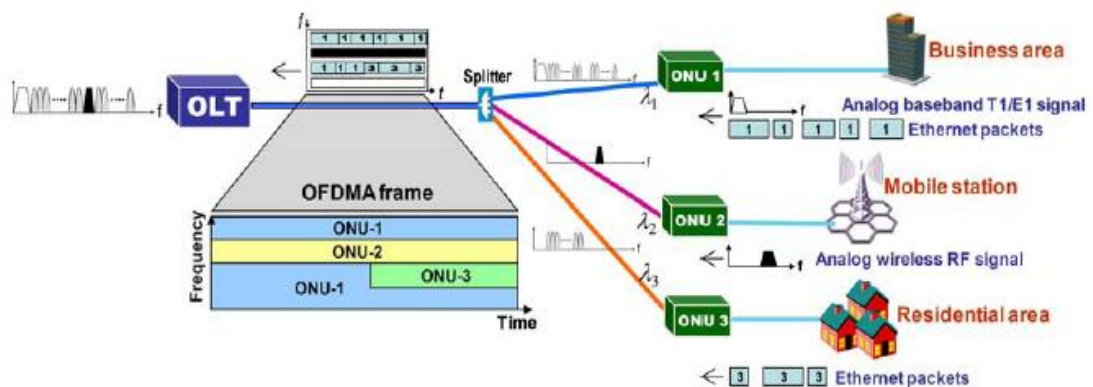


Figure 2.31. OFDMA-PON architecture [78].

To date, a number of research groups have proposed and experimentally demonstrated a wide variety of OFDMA-PON architectures to support various services. Some of these proposals include: an OFDMA-PON architecture with source-free ONUs where direct-detection is used for the downstream transmission and coherent detection is used for the upstream transmission [79]; an extended-reach OFDMA-WDM-PON with a split ratio of 256 [80]; a multiple-input multiple-output (MIMO) OFDMA-PON which utilises polarisation multiplexing [81]; and an OFDMA-PON architecture that makes use of adaptively-modulated OFDM format [82].

In terms of the Media Access Control (MAC) layer, two of the current proposals for MAC protocols for OFDMA-PONs include PONIARD [83] and ACCORDANCE [84], [85]. PONIARD uses OFDMA/TDMA bandwidth allocation only at inter-slice levels, with pure TDMA used elsewhere [83], so we will focus more on ACCORDANCE, whose MAC protocol operates at both inter-segment and intra-segment levels (where slices/segments are groups of subcarriers).

The EU FP7 Project ACCORDANCE [84] addresses both the physical and MAC layers in OFDMA-PONs, with emphasis placed on the convergence of the optical infrastructure with existing standard wireless solutions [85]. This permits a seamless OFDMA-based access network which can support various types of connectivity. The ACCORDANCE architecture is depicted in Figure 2.32.

In the ACCORDANCE architecture, a single fibre originates from the OLT in the central office to a Level 1 remote node (RN) where it is split into many fibre branches. The Level 1 RN could either be a power splitter or an AWG. If a power splitter is used, the OLT can dynamically distribute different spectral segments of different widths among different parts of the network.

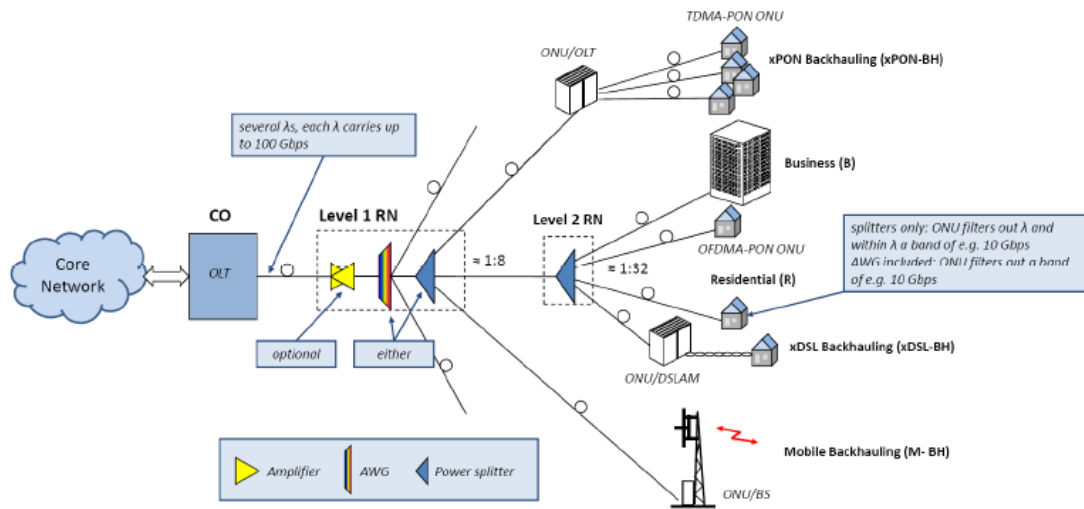


Figure 2.32. ACCORDANCE network architecture [85]. OLT: Optical line terminal. CO: Central office. RN: Remote node. ONU: Optical network unit. DSLAM: Digital subscriber line access multiplexer. BH: Backhauling. AWG: Arrayed waveguide grating. BS: Base station.

The use of a power splitter however increases the splitting loss. On the other hand, using an AWG means segment assignment would be static but there is no splitting loss and no need for optical filtering to remove unwanted spectral components at each ONU.

From the Level 1 RN, fibre branches span out to various ONUs (or to a Level 2 RN for further splitting) for various types of services including xDSL backhauling, mobile backhauling, xPON backhauling, as well as for residential and corporate FTTH customers. One of the main benefits expected to emerge from ACCORDANCE is node consolidation, enabling centralisation of network functions, resulting in reduction in operating costs for network operators.

2.6.2 OFDM for UWB radio communications

UWB radio communications have in recent years attracted growing attention both in academia and in industry due to the advantages they offer including low

power consumption, low cost, low latency, wide bandwidth and low probability of interference [86].

In 2002, the Federal Communications Commission (FCC) permitted unlicensed operation in the 3.1 GHz to 10.6 GHz band for use of UWB communication devices [18]. The maximum equivalent isotropic radiated power (EIRP) of UWB, as defined by FCC Part 15 is -41.3 dBm/MHz as shown in Figure 2.33 and Table 2.2.

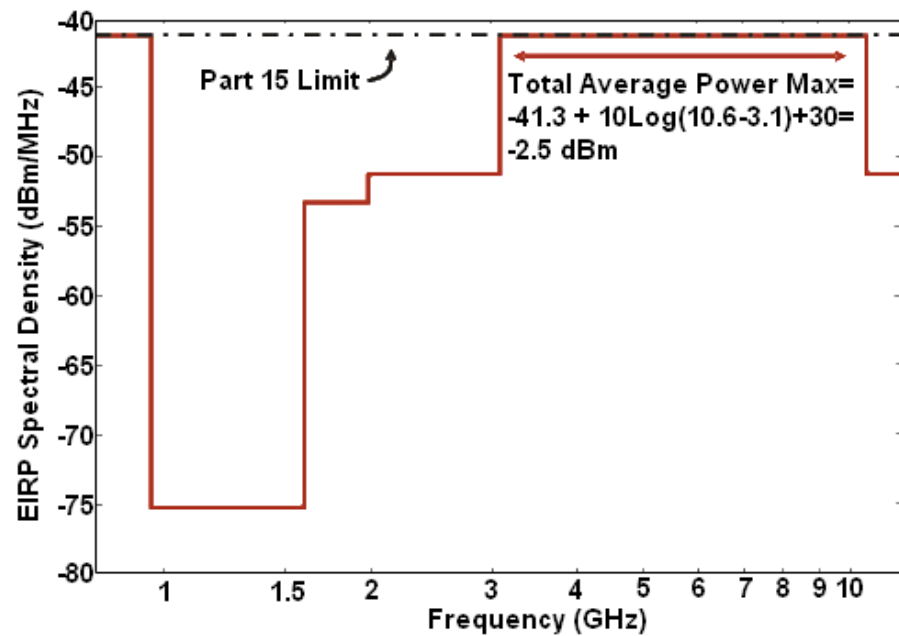


Figure 2.33. FCC spectral mask for license-free applications in indoor environments [18].

Frequency (MHz)	EIRP (dBm/MHz)
960-1610	-75.3
1610-1900	-53.3
1990-3100	-51.3
3100-10600	-41.3
Above 10600	-51.3

Table 2.2. Maximum EIRP levels as stated by FCC for UWB emissions [18].

The FCC restriction on the EIRP of UWB has enabled it to be designed to look like imperceptible random noise to conventional radios. On the one hand, this restriction has permitted UWB co-existence with other wireless services in the same frequency range (e.g. Long-Term Evolution (LTE), IEEE 802.16e and IEEE 802.11a) as shown in Figure 2.34, but on the other hand, has limited the wireless range of UWB systems to a few metres as shown in Figure 2.35.

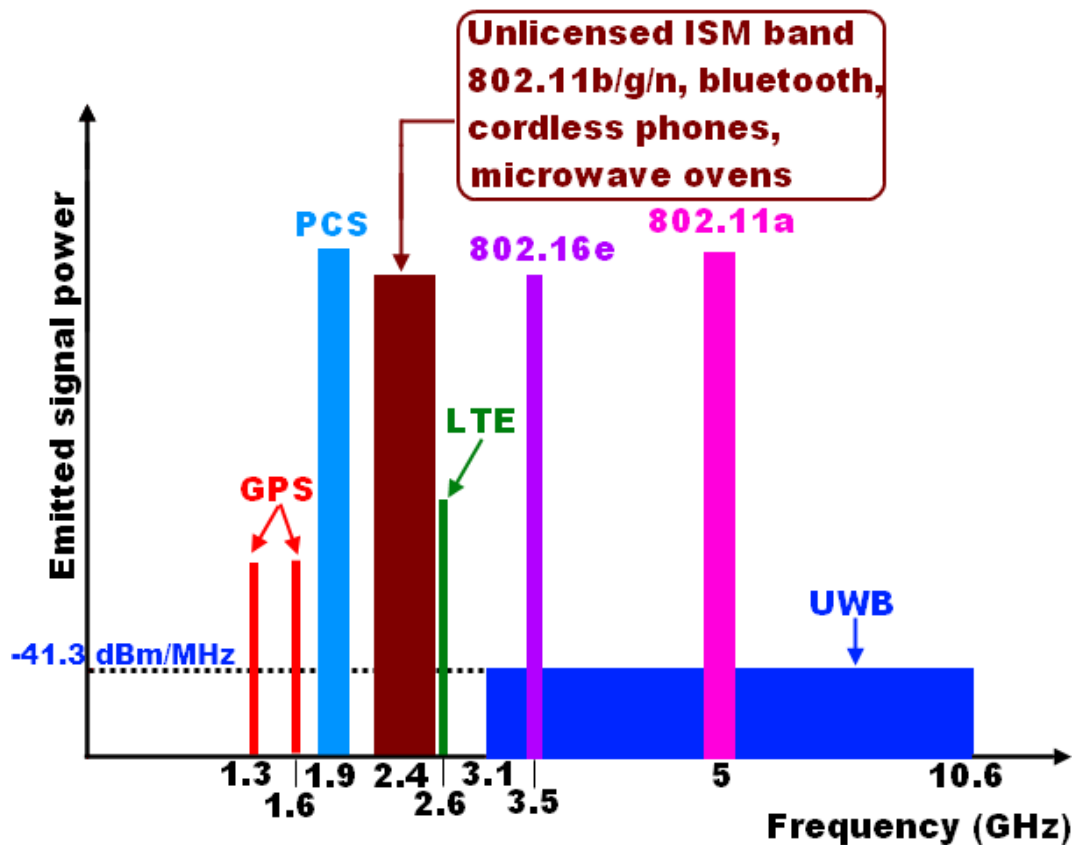


Figure 2.34. Co-existence nature of UWB with other wireless services. GPS: Global Positioning System. PCS: Personal Communications Service. ISM: Industrial, Scientific and Medical. LTE: Long-Term Evolution. (Note: Bandwidths and power are not drawn to scale).

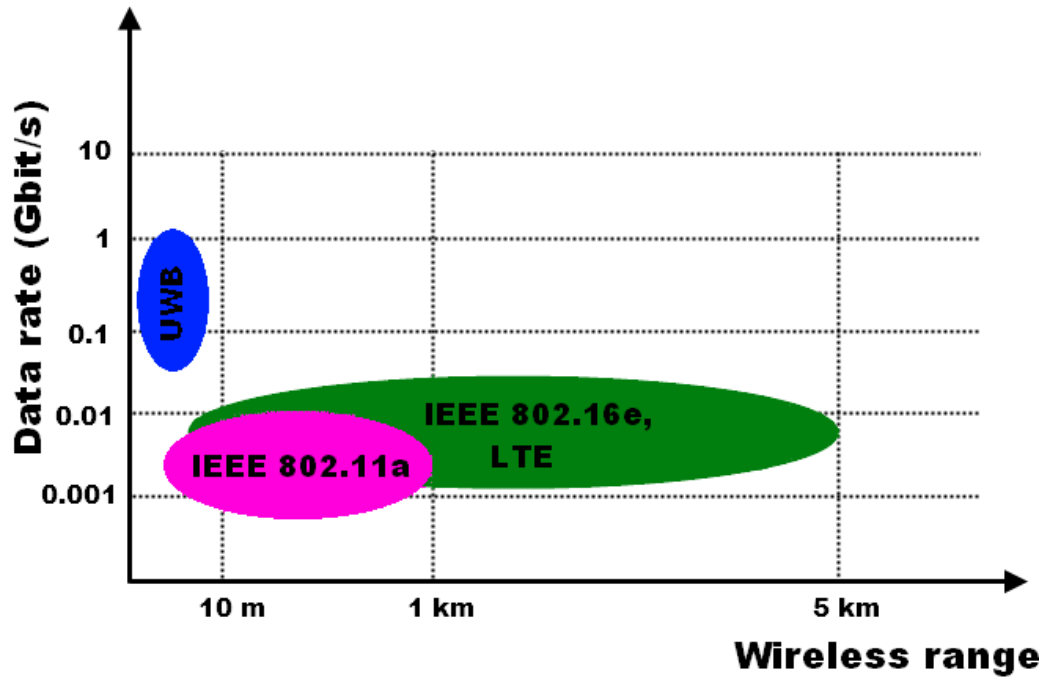


Figure 2.35. Wireless range of UWB in comparison with other wireless services like IEEE 802.11a, IEEE 802.16e and LTE. (Note: Wireless range not drawn to scale).

Since the use of coaxial cables to extend the wireless range of UWB has proven to be quite expensive because of its low power and broad bandwidth [22], transmission over fibre offers a transparent, practical and low-cost solution. RoF distribution of UWB signals over SSMF has been proposed in [87] for the delivery of HD audio and video content in FTTH networks.

In this approach, as shown in Figure 2.36 (assuming a point-to-point architecture), SSMFs are used to distribute the UWB signals in their native format from the central office of the core network operator, through an SSMF-based FTTH network, to several distribution points (DPs) in different customers' premises.

The DPs are further connected via short spans of optical fibre to various remote access points (APs) for further in-building wireless transmission to various UWB-enabled customer-premises equipment (CPE) such as laptops, computers, televisions and mobile phones.

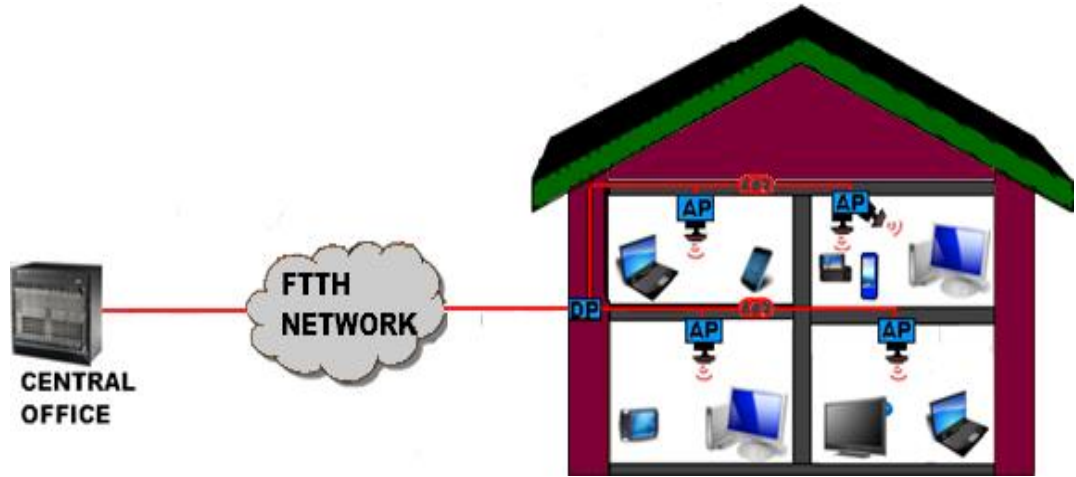


Figure 2.36. Schematic diagram of UWB RoF distribution in FTTH access networks. DP: Distribution Point. AP: Access Point.

The use of FTTH networks for UWB distribution in such a manner not only extends the UWB range but also enables the advantages of UWB to be combined with the advantages optical fibre offers in terms of wide bandwidth and low attenuation loss. In addition, no frequency up-conversion or trans-modulation is required at the customer's premises resulting in receivers that are agnostic with regards to the modulation scheme employed.

In addition to the afore-mentioned advantages of UWB, another major attraction of UWB is its potential to support high bitrates. This can be inferred from Shannon's capacity theorem that relates the maximum channel capacity, C in bit/s to both the channel bandwidth, B in Hz and the SNR.

$$C = B \times \log_2(1 + \text{SNR}) \quad (2.49)$$

Equation (2.49) shows that the capacity per channel can be increased by increasing the SNR and/or by increasing the channel bandwidth. This is confirmed in Figure 2.37 showing the plots of the channel capacity for channel bandwidths

ranging from 1 MHz to 1 GHz. Here, it can be seen that the increase in channel capacity with SNR becomes more pronounced as the channel bandwidth increases.

Currently, there are two major UWB implementations. The first one is called impulse-radio UWB (IR-UWB) and involves transmission of pulses with a very short duration of a few nanoseconds. The second implementation is based on OFDM and is called multi-band OFDM UWB (MB-OFDM UWB). The work in this thesis focuses entirely on the MB-OFDM UWB implementation. According to the draft IEEE 802.15.3a proposal [88], which was later adopted by the European Computer Manufacturers' Association (ECMA) in the ECMA-368 standard [89], for the MB-OFDM UWB implementation, the 7.5 GHz UWB spectrum is divided into 14 non-overlapping frequency sub-bands, each sub-band with a bandwidth of 528 MHz as shown in Figure 2.38.

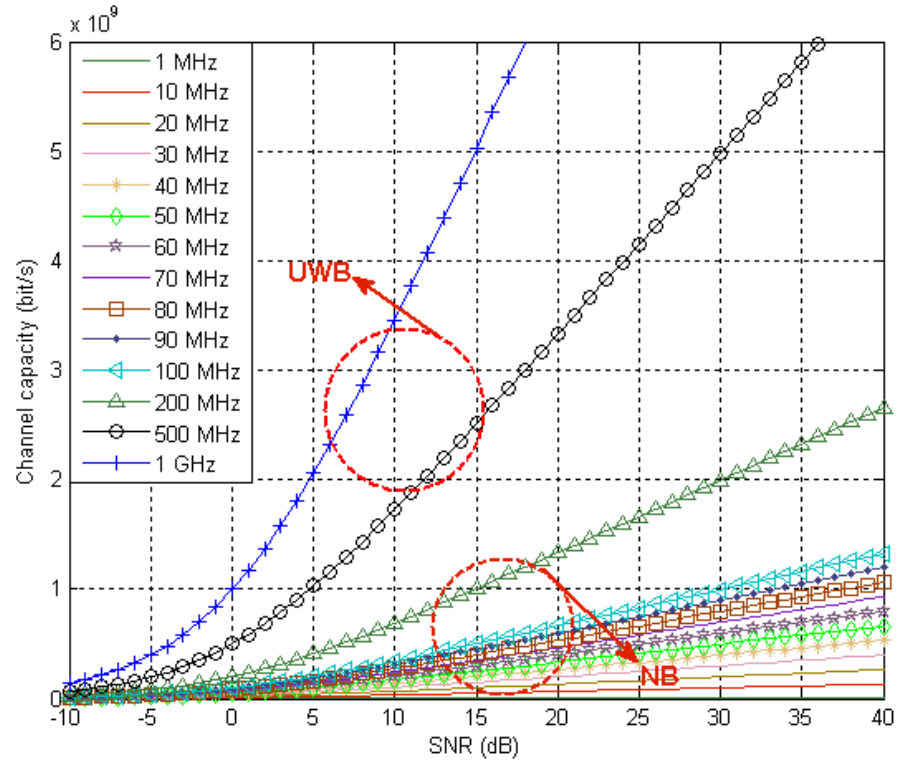


Figure 2.37. Simulation of channel capacity variation with SNR for different channel bandwidths using (2.49). NB: Narrow band.

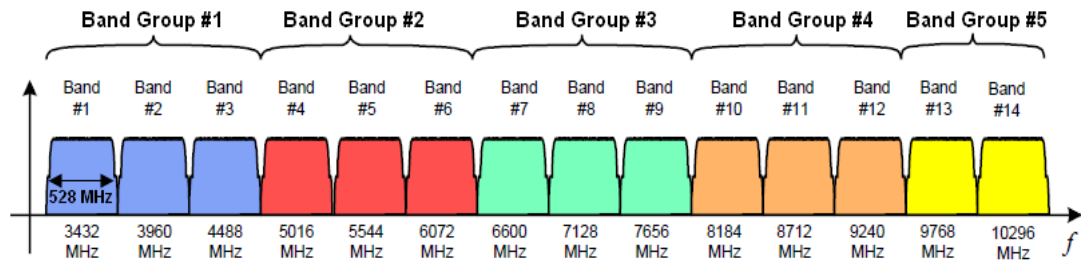


Figure 2.38. MB-OFDM UWB channelization according to the ECMA-368 standard [89].

These 14 sub-bands are further organised into 5 Band Groups (BGs). BGs #1 to #4 have 3 channels while BG #5 has only 2 channels. A variable data rate from 53.3 to 480 Mbit/s per sub-band is suggested in the ECMA-368 standard. BG #1, spanning from 3.168 GHz to 4.752 GHz, as depicted in Table 2.3, is mandatory while BGs #2 to #5 are optional. Most of the commercially-available UWB devices operate in BG #1

Time-frequency codes (TFCs) are used to determine which sub-band is occupied by the 528-MHz wide OFDM signal. There are three types of TFCs that have been defined.

Band Number	Lower Frequency (GHz)	Centre Frequency (GHz)	Upper Frequency (GHz)
1	3.168	3.432	3.696
2	3.696	3.960	4.224
3	4.224	4.488	4.752

Table 2.3. Frequency details of MB-OFDM UWB sub-bands in the mandatory Band Group #1

In the first TFC, referred to as Time-Frequency Interleaving (TFI), the information is interleaved over three sub-bands of a BG. The second TFC is referred to as TFI2, where the information is interleaved over two sub-bands of a BG. The final TFC is referred to as Fixed Frequency Interleaving (FFI) which follows a no-frequency hopping scheme where the information is transmitted on a single sub-band during all the time slots. BG #1 supports four TFI codes (TFCs 1-4), three FFI codes (TFCs 5-7) and three TFI2 codes (TFCs 8-10) as shown in Table 2.4.

Each MB-OFDM UWB sub-band has 128 subcarriers. Out of these, 100 are data tones, 12 are pilots for carrier and phase tracking, 10 are guard tones and the remaining 6 are null tones (used to relax the electrical filter requirements).

An FFT size of 128 samples and a cyclic prefix length of 32 samples are used for each sub-band. A guard interval length of 5 samples separates one sub-band from the next. The subcarrier frequency spacing is 4.125 MHz, resulting in an FFT/IFFT period of 242.42 ns, a cyclic prefix duration of 60.61 ns and an OFDM symbol duration of 312.5 ns, as shown in Figure 2.39.

Both QPSK and Dual Carrier Modulation (D.C.M) techniques could be used for modulating the subcarriers. Consequently, a maximum bit rate per sub-band of 480 Mbit/s and an aggregate bit rate of 6.72 Gbit/s per user (when all the fourteen sub-bands are combined) are achievable.

The data and pilot tones have indices from $[-56 \dots -1, +1 \dots +56]$. The guard tones are obtained by copying the edge data tones at indices $[-56 \dots -52, +52 \dots +56]$, and are assigned indices $[-61 \dots -57, +57 \dots +61]$.

TFC Number	BAND ID Sequence					
1	1	2	3	1	2	3
2	1	3	2	1	3	2
3	1	1	2	2	3	3
4	1	1	3	3	2	2
5	1	1	1	1	1	1
6	2	2	2	2	2	2
7	3	3	3	3	3	3
8	1	2	1	2	1	2
9	1	3	1	3	1	3
10	2	3	2	3	2	3

Table 2.4. Time-frequency codes for Band Group #1 [89].

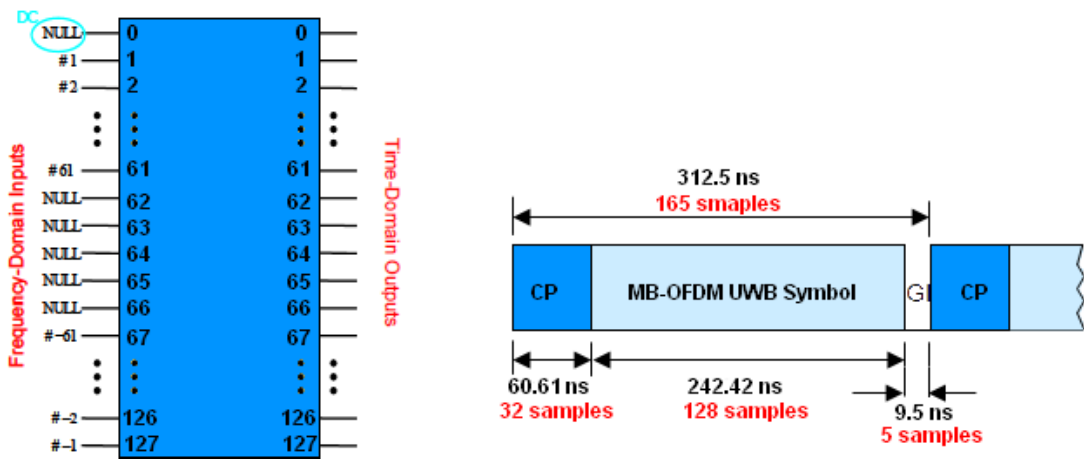


Figure 2.39. MB-OFDM UWB tone assignment and OFDM symbol structure. GI: Guard Interval. CP: Cyclic prefix.

As shown in Figure 2.39, the tones with the coefficients numbered 1 to 61 are mapped to IFFT inputs 1 to 61; while the tones with coefficients numbered -61 to -1 are mapped to IFFT inputs 67 to 127. This implies that the IFFT inputs from 62 to 66, as well as the 0 input (reserved for the D.C. term) are assigned to the zero-valued null tones.

The transmitted MB-OFDM UWB signal ($S_{MB}(t)$) can be expressed mathematically as [89]:

$$S_{MB}(t) = \text{Re} \left\{ \sum_{k=0}^{N-1} S_k(t - kT) e^{j(2\pi f_c t + \varphi(t))} \right\} \quad (2.50)$$

where $S_k(t)$ is the k th OFDM symbol of duration T , N is the number of OFDM symbols transmitted, and f_c and $\varphi(t)$ represent the carrier frequency and phase noise of the RF carrier local oscillator respectively.

In order to achieve even higher MB-OFDM UWB data rates, both spatial and multipath diversities via the use of MIMO can be exploited, as proposed in [90]-[93], since the channel capacity of UWB systems increases with the number of transmit/receive antennas [94]. In [90], the MIMO UWB proposal utilises band hopping in combination with joint coding across spatial, temporal and frequency domains to exploit all of the available spatial and frequency diversities inherent in UWB environments; while in [91], the use of MIMO techniques with linear precoded OFDM has been proposed for multi-Gbit/s home applications.

Incorporating the MIMO technique into UWB is also an interesting solution to the problem of the EIRP constraints imposed on UWB by the FCC. For instance, if space-time coding is utilised, although the overall transmitted power would still be the same as a single-transmit antenna system, the power for a specific transmitted symbol will be strengthened without violating the FCC spectral mask [94].

2.6.3 60-GHz radio technology

In section 2.6.2, it was stated that a maximum MB-OFDM UWB aggregate bit rate of 6.72 Gbit/s per user (when all the fourteen sub-bands are combined) is achievable. Due to spectral co-existence issues however, this UWB capacity is further restricted strictly outside the U.S, with different regulations in different countries [95]; resulting in an available effective UWB bandwidth of only 1.5 GHz [96]. This implies that the maximum available bit rate is limited to hundreds of Mbit/s, making it difficult to support bandwidth-intensive applications that require multi-Gbit/s data rates such as uncompressed HD video streaming, video-on-demand and wireless high-speed file transfer.

To overcome these limitations, the 60-GHz band has been considered for the RoF delivery of multi-Gbit/s MB-OFDM UWB signals to end-users in FTTH access networks. 60-GHz radio technology offers various operational advantages over current wireless communication systems operating at lower frequencies [97].

The unlicensed bandwidth regulated for generic 60-GHz radio worldwide spans up to 9 GHz. This huge unlicensed bandwidth can be exploited to offer potential multi-Gbit/s wireless connectivity. Operation in the 60-GHz band permits the use of antennas which do not only have high gain (up to 40 dBi) [23], but are also much smaller than those used in the lower frequency bands. This enables MIMO, beam forming and beam steering, which enhances the channel capacity and also supports non-line-of-sight (NLOS) communications [98]. It is therefore not surprising that there has been an explosion of interest in 60-GHz technology in recent times.

There have been a number of standardisation efforts and industry alliance formations including WirelessHD [99], ECMA-387 [100], IEEE 802.15.3c [101],

and WiGig [102] aimed at promoting 60-GHz technology to support multi-Gbit/s wireless communications. This has resulted in some consumer electronic products based on 60-GHz radio technology being introduced in the market. However, some challenges in achieving full-scale commercialisation remain, especially in providing robust 60-GHz products [23]. Some of these challenges are highlighted in subsection 2.6.3.1.

2.6.3.1 Characteristics of the 60-GHz band

The huge unlicensed bandwidth internationally available for 60-GHz systems not only has the potential to support high-throughput wireless communications but also simplifies the design of such systems. This is because low spectral efficiency can be used in such systems to achieve high data rates [23].

Table 2.5 shows a comparison of the spectral efficiency required to achieve 1 Gbit/s for both typical 60 GHz and IEEE 802.11n systems.

Technology	Bandwidth (MHz)	Efficiency @ 1 Gbit/s (bit/s/Hz)	Target data rate (Mbit/s)	Efficiency required (bit/s/Hz)
60 GHz	2000	0.5	4000	2
IEEE 802.11n	40	25.0	600	15.0

Table 2.5. Spectral efficiency comparison between typical 60-GHz and IEEE 802.11n systems [23].

Here, it can be seen that 60-GHz systems require a spectral efficiency of 0.5 bit/s/Hz to achieve 1 Gbit/s while the corresponding required spectral efficiency for IEEE 802.11n is as high as 25 bit/s/Hz, implying higher system design costs [23].

Unfortunately, there are a couple of challenges with operation at 60 GHz that have inhibited full-scale deployment of 60-GHz systems. One of the major challenges is the high free-space path loss in the 60-GHz band in accordance with (2.30). Consequently, the 60-GHz wireless channel demonstrates between 20 to 40 dB increased free-space path loss [103]. In addition, this band is plagued with high atmospheric absorption due to atmospheric oxygen which resonates at 60 GHz due to transitions between its three closely spaced rotational states [104]. This results in an attenuation of the 60 GHz signal by an additional 7-15.5 dB/km, depending on the atmospheric conditions [103], [105].

Another specific challenge with 60-GHz radio technology has to do with the difficulties in implementing power amplifiers at this frequency. This is because increase in the frequency of transistor operation in an amplifier results in a decrease in the effective gain per transistor [103]. In order for power amplifiers to generate enough power in transmit antennas, there has to be an increase in transistor size. Increase in transistor size however results in a corresponding decrease in gain. In addition, the high PAPR of the MB-OFDM UWB signals may in itself necessitate the use of expensive power amplifiers to enable operation at a higher average power.

The higher free-space path loss, although an apparent disadvantage, has enabled higher frequency reuse, resulting in a high throughput network. It is therefore possible to use multiple devices operating at the same frequency in a high density pattern without running the risk of interference between them. In addition, because of the high path loss, 60-GHz operation is confined to indoor environments,

implying less severe interference than that in the lower frequency bands. Also, in order to overcome the higher free-space path loss, 60-GHz radios utilise high-gain antennas (up to 40 dBi). These antennas, by virtue of the high frequency of operation, have very compact sizes, thus permitting multiple antenna solutions.

Therefore, wireless networking at 60 GHz is inherently made up of small radio cells of radius typically limited to less than 10 m [106]. This implies that the number of RAUs required in a given geographical deployment area will be quite high. To link the different RAUs together, and to a central station, some kind of backbone network must be deployed. This backbone network must not be cost-prohibitive, must be easy to deploy and must also be capable of transmitting multi-Gbit/s data over various distances.

The insufficient bandwidth and serious propagation loss of conventional coaxial cables render them inadequate for such a backbone network. Using RoF technology to distribute the 60-GHz signals from the central station to the RAUs would be an effective way to deal with the demands of the small radio cell 60-GHz network and result in a simplified overall system design. This is because as stated previously in section 2.3.3, in addition to the very wide bandwidth and low propagation loss advantages of optical fibre, RoF also makes it possible to centralise the RF signal processing functions in the central station, facilitating equipment sharing and significantly simplifying the RAUs which would only have to perform optoelectronic conversion and amplification functions.

Consequently, with a high density of RAUs being a necessity for 60-GHz radio deployment, using RoF technology for distribution of the 60-GHz signals would result in simplified operation and maintenance which would eventually translate to cost savings.

2.6.3.2 Frequency allocation and worldwide regulation

The 60-GHz unlicensed frequency range is subject to different regulations and frequency bands in different countries. In the US [107] and Canada [108], the FCC has allocated 7 GHz of bandwidth from 57 to 64 GHz for 60-GHz operation. In Europe [109] and in Australia (indoor use only) [110], 9 GHz of bandwidth, from 57 to 66 GHz is available, while the frequency range from 59 to 66 GHz (with a maximum allowed bandwidth of 2.5 GHz) is available in Japan [111] .

The 60-GHz frequency band-plan, limits on transmit power, and maximum EIRP for the various countries is shown in Table 2.6.

Region	Frequency Range (GHz)	Bandwidth (GHz)	Maximum EIRP (dBm)	Maximum Transmit Power (dBm)
US/ Canada	57-64	7.0	43.0 (peak) 40.0 (average)	27.0 (for bandwidth \geq 10 0 MHz)
Europe	57-66	9.0	40.0 (Indoor only) 25.0 (Indoor and outdoor)	Not Defined
Australia	57-66	9.0	43.0 (Indoor only)	13.0
Japan	59-66	7.0	57.0	10.0

Table 2.6. Frequency plan, maximum EIRP and maximum transit power in the 60-GHz band for various countries.

2.6.3.3 *International 60-GHz standards*

Interest in the 60-GHz band has fuelled the introduction of international standards by many industry alliances, consortiums and standards groups. Table 2.7 summarises the various international 60-GHz standardisation efforts, together with their associated modulation schemes and maximum data rates.

Standard	Modulation Scheme		Max. Data Rate (Gbit/s)
IEEE 802.15.3c	Single carrier (BPSK, MSK, QPSK, 8PSK, 16- QAM)	OFDM (QPSK, 16- QAM, 64- QAM)	5.28 (Single carrier) 5.775 (HSI OFDM) 3.8 (AV OFDM)
WirelessHD	OFDM		7 28 (MIMO)
ECMA-387	SCBT	OFDM	6.350 (SCBT – without channel bonding) 4.032 (OFDM – without channel bonding)
WiGig	Single carrier	OFDM	4.6 (Single carrier) 7 (OFDM)

Table 2.7. Summary of wireless 60-GHz standards. HSI: High-speed interface. AV: Audio video. SCBT: Single-carrier block transmission.

2.6.3.4 Potential MB-OFDM UWB 60-GHz applications

The severe attenuation suffered in the 60 GHz band renders it unsuitable for long-range communications but make it interesting for short-range wireless applications. Consequently, because of its simplified operation and maintenance benefits, it is envisaged that RoF technology can be utilised for the delivery of multi-Gbit/s UWB signals in the 60-GHz band to end-users in FTTH access networks for multiple in-building wireless PAN applications including, but not limited to [23]:

- i). High-speed wireless transfer of large data files;
- ii). Uncompressed HD video streaming;
- iii). Wireless gaming with low latency and high-quality performance;
- iv). Wireless docking stations for inter-connecting various electronic devices including laptops, PDAs and external monitors;
- v). Cable replacement of gigabit Ethernet, enabling bidirectional wireless multi-Gbit/s Ethernet traffic.

2.7 The OptSim™ simulation platform

OptSim™ is RSoft's software tool for optical communication systems design and simulation at the signal propagation level [112], giving the possibility to create multiple configurations for any given transmission scenario.

The OptSim™ simulation platform comprises a graphical user interface as well as electrical, electro-optical and optical components e.g. RF signal generators, amplifiers, optical modulators, laser diodes, photodetectors, optical fibres, optical filters, etc. which can be independently configured with parameters to model actual commercially-available components.

Certain component parameters (e.g. device non-linearities, fibre dispersion) can also be turned off to observe how a system would perform in an ideal transmission scenario. Each component is represented by an icon or model block, and OptSim™ represents the whole transmission system as a collection of interconnected blocks. The icons are connected together to represent the flow of signal data from one component to the other [113].

OptSim™ also comes with lab-like measurement instruments like optical spectrum analysers, oscilloscopes, power meters, electrical spectrum analysers, BER testers, etc. for performance monitoring (e.g. BER, Q value, OSNR) of a given system design.

OptSim™ has a co-simulation functionality which enables it to run co-simulations with 3rd party software like MATLAB, Cadence Spectre, Liekki Application Designer and Luna Optical Vector Analyzer. This functionality enables custom component for MATLAB modules (CCMs) to be created and used in OptSim™ to simulate any electrical, electro-optical or optical component in a given optical network architecture. The behaviour of a CCM during a simulation run is governed by an external MATLAB subroutine. This MATLAB subroutine fully interacts with the OptSim™ data structure either for pre-processing or post-processing [114]. It is this functionality that has been utilised in this thesis for simulating the various optical OFDM architectures.

In this thesis, the CCMs are customised to act as the optical OFDM transmitter and receiver, where the simulation parameters of these CCMs such as the number of transmitted bits, number of OFDM subcarriers, the modulation format and the IFFT/FFT size are defined during CCM creation and can be easily edited in any simulation run in order to conduct different system performance tests.

The CCMs interface with the OptSim™ simulator scheduler to run a particular MATLAB subroutine which generates the OFDM signal in the case of the transmitter. In the case of the receiver, the MATLAB subroutine is responsible for carrying out equalisation, demodulation, EVM computation and demapping of the received OFDM signal. The MATLAB subroutine writes the vector signal output and then the MATLAB subroutine for that CCM closes. When this happens, control of the simulation is passed back to the OpSim™ simulation environment and the rest of the project simulation continues. The CCM theory of operation is depicted in Figure 2.40.

After photodetection, the received OFDM signal is equalised by using a one-tap equaliser in the CCM that acts as the OFDM receiver. In this CCM, in order to carry out equalisation, a training symbol with a known bit sequence is inserted every 10 data symbols. Using the training symbols, a set of channel frequency responses corresponding to each subcarrier are obtained by comparing the received training symbols with the transmitted ones by carrying out a single complex division.

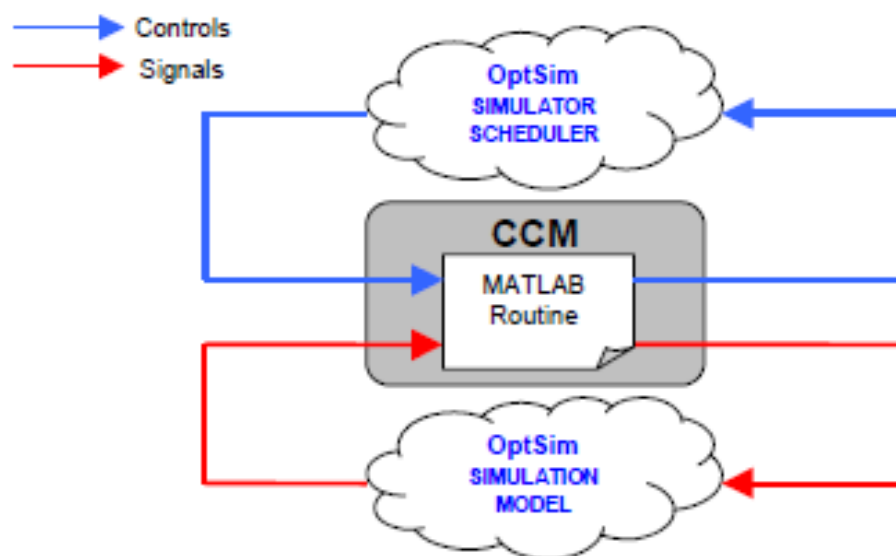


Figure 2.40. CCM theory of operation [114].

The channel estimate for each subcarrier is then obtained by averaging over the set of channel responses. These channel estimates are the coefficients of the so-called one-tap equaliser. Equalisation is then carried out by dividing the received OFDM symbols by the channel estimates.

Figure 2.41 shows an example of an overlaid received 4-QAM constellation before and after equalisation in the CCM that acts as the OFDM receiver. The overlaid unequalised constellation is shaped like a doughnut because of the effect of chromatic dispersion. Chromatic dispersion causes a phase delay for each OFDM subcarrier. This phase delay is expressed as [3]:

$$\Phi_D(f_k) = \pi \cdot c \cdot D \cdot L \cdot \frac{f_k^2}{f_o^2} \quad (2.51)$$

where $\Phi_D(f_k)$ is the phase delay due to chromatic dispersion for the k th OFDM subcarrier, f_k is the frequency of the k th subcarrier, f_o is the frequency of the optical carrier, c is the speed of light, D is the chromatic dispersion parameter and L is the length of the fibre. Chromatic dispersion causes a rotation of each constellation point around the origin.

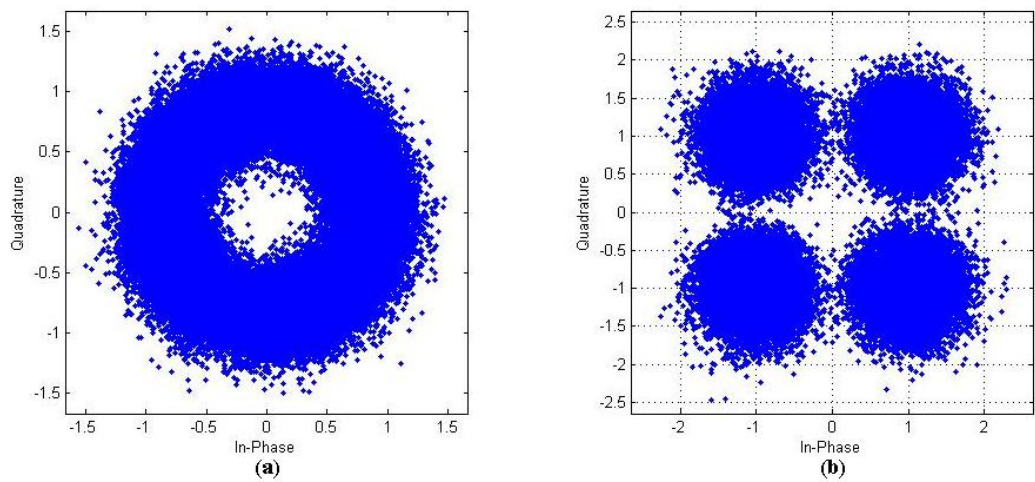


Figure 2.41. Received constellations: (a) unequalised (b) equalised.

From (2.51), it can be seen that the degree of rotation for each subcarrier's constellation is proportional to the frequency of the subcarrier relative to the optical carrier squared. So, the subcarriers furthest away from the optical carrier receive the most rotation.

The beauty of using MATLAB- OptSim™ co-simulations in such a manner is that the exact same MATLAB routines as used in the CCMs that act as the OFDM transmitter and receiver can also be used in experiments for generating the OFDM signal and for offline baseband digital signal processing. This, as we will find out in succeeding chapters, enables the simulation and experimental parameters to be matched as well as possible for the purpose of result comparison.

2.8 Summary

This chapter commenced with an overview of next-generation broadband access networks and state-of-the-art technologies where various optical fibre topologies such as point-to-point and point-to-multipoint; and fibre multiple access schemes have been discussed, together with their respective advantages and disadvantages.

Next, RoF technology has been introduced as a hybrid access technology that combines the benefits of both optical and wireless networks. The basic RoF techniques that will be made use of in the simulations and experiments that will be carried out in the succeeding chapters have been discussed. We have also shown, with the aid of mathematical analysis, how different optical signals – DSB-C, DSB-SC and OSSB signals can be produced by biasing the MZM at the maximum, null and quadrature points respectively. Some of the latest applications of RoF technology, as well as its benefits and limitations have also been presented. The

periodic RF power degradation due to chromatic dispersion in a DSB-C transmission has been illustrated, where the frequencies at which power nulls are obtained tallied for both simulations and numerical calculations. It has also been shown that with OSSB transmission, we can avoid the significant RF power degradation due to chromatic dispersion that occurs in DSB-C transmissions. As shown in Figure 2.12, with OSSB transmission employed a maximum RF power degradation of only around 1.5 dB obtained as compared to maximum power degradation of 25 dB obtained with the DSB-C transmission

We have also introduced single-carrier and multi-carrier modulation systems. This has provided an excellent backdrop for discussing the basics of OFDM and highlighting what has made it emerge as a suitable technology for optical communications. In particular, the principles of operation of OFDM, its mathematical representation, system implementations, advantages, and disadvantages have been discussed. In section 2.5, the two broad forms of optical OFDM – DD-OOFDM and CO-OFDM have been introduced. The various transmitter architectures that exist under these two variants have also been illustrated.

We have talked about how optical OFDM has been used in applications in the access network in the form of PONs and UWB systems, with some of the relevant proposals and latest projects discussed. Finally, the OptSim™ simulation platform, which is the simulation tool used throughout this thesis, has been introduced, and one-tap equalisation demonstrated.

Chapter 3. System performance of direct-detection optical OFDM in the presence of MZM non-linear distortion

3.1 Introduction

In section 2.5.1, it was shown that DD-OOFDM systems require a spectrally-inefficient guard band (with a bandwidth, B_{gap} at least equal to the OFDM signal bandwidth) between the optical carrier and the OFDM signal band. This is so that the second-order intermodulation distortion products, that arise when pairs of subcarriers mix with themselves, fall within this guard band and do not cause significant in-band distortion.

In this chapter, we show that the power transfer characteristic of an MZM is non-linear. Because of this non-linearity, the system performance degrades at high MZM drive and bias levels. We demonstrate, with the aid of theoretical analysis, simulations and experiments, how the system performance of DD-OOFDM in the presence of the MZM non-linear distortion can be improved by proper biasing and selection of appropriate drive to the MZM. Simulations and experiments are also conducted to investigate how a variation in system parameters such as the number of subcarriers and the modulation format influences the sensitivity of the DD-OOFDM system to the non-linear distortion from the MZM. Finally, simulations are conducted to examine the possibility of improving the spectral efficiency of DD-OOFDM systems by reduction of the width of the guard band B_{gap} .

The structure of this chapter is as follows: section 3.2 provides the theoretical analysis for the MZM non-linear distortion considering the DD-OOFDM system with OSSB modulation, which is the modulation technique that is extensively used

throughout this thesis. In this section, the power transfer function of the MZM is expressed as a Taylor series which includes the third-order and fifth-order non-linear distortion terms, and it is shown that there is a system performance trade-off with regards to the MZM non-linear distortion and the received SNR. In sections 3.3 and 3.4, the simulation and experimental setups used to conduct tests on the impact of the MZM non-linearity on the system performance are described respectively. Section 3.5 provides analysis of the simulation and experimental results of the system performance tests. This section illustrates the dependence of the system performance on the MZM bias point and the amplitude of the drive to the MZM. In section 3.6, the analysis of the system parameter variation tests is given with the aid of simulations and verified with experiments. This section looks at how the system performance is affected when the number of subcarriers and modulation format is varied. The system performance, making use of EVM measurements as the performance metric, is measured against the MZM bias level. Thereafter, the possibility of optimising the spectral efficiency of the DD-OOFDM system by employing a reduced frequency guard band is investigated by simulation in section 3.7. Finally, the conclusions are drawn in section 3.8.

3.2 Theoretical analysis

Figure 3.1 (a) shows a schematic of the DE- MZM used in this work. Following from (2.12), the optical power, $P_o(t)$ at the output of the DE-MZM can be obtained by taking the square of the modulus of the output optical field as follows:

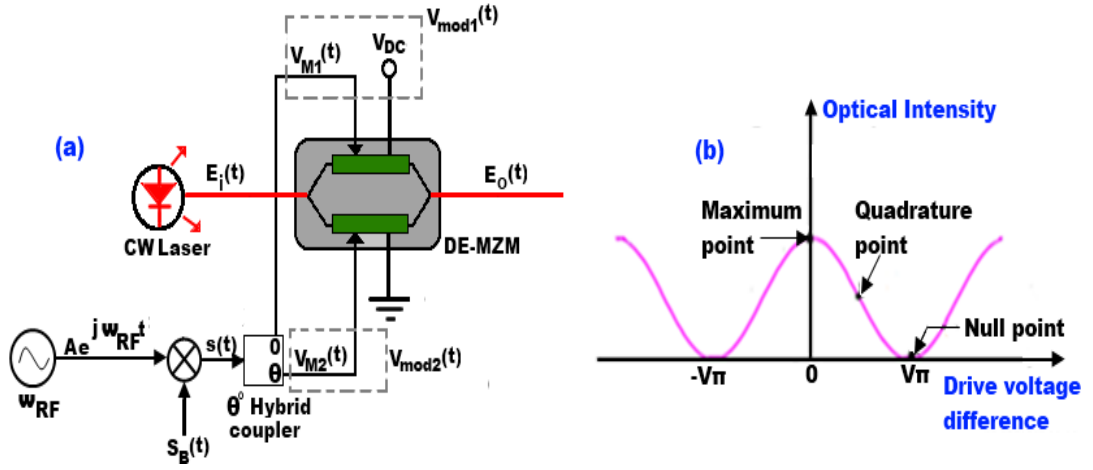


Figure 3.1. (a) DE-MZM with hybrid coupler (b) DE-MZM optical power transfer characteristics. CW: Continuous-wave. DE-MZM: Dual-electrode Mach-Zehnder modulator.

$$P_o(t) = \frac{|E_i|^2}{4} \cdot \left[\left(\cos\left(\frac{\pi V_{mod1}(t)}{V_\pi}\right) + \cos\left(\frac{\pi V_{mod2}(t)}{V_\pi}\right) \right)^2 + \left(\sin\left(\frac{\pi V_{mod1}(t)}{V_\pi}\right) + \sin\left(\frac{\pi V_{mod2}(t)}{V_\pi}\right) \right)^2 \right] \quad (3.1)$$

where $V_{mod1}(t)$ and $V_{mod2}(t)$ represent the drive voltages applied to the top and bottom electrodes of the MZM respectively and V_π is the half-wave switching voltage of the MZM.

In Figure 3.1 (a), in a similar fashion as in Figure 2.7, a D.C. bias voltage has been applied to the upper electrode of the MZM while the other D.C. terminal is grounded. Consequently, $V_{mod1}(t)$ and $V_{mod2}(t)$ are given by (2.13) and (2.14) respectively.

In this case, $V_{M1}(t)$ and $V_{M2}(t)$, which are the two outputs of the electrical hybrid coupler used to split the modulating real-valued passband OFDM signal $s(t)$, are given, respectively, by:

$$V_{M1}(t) = \text{Re}\{s_B(t) \cdot Ae^{j\omega_{RF}t}\} \quad (3.2)$$

$$V_{M2}(t) = \text{Re}\{s_B(t) \cdot A e^{j(\omega_{RF}t + \theta)}\} \quad (3.3)$$

$$\text{and } s_B(t) = \sum_{k=\frac{-N_{SC}}{2}+1}^{\frac{N_{SC}}{2}} C_k e^{j2\pi f_k t} \quad (3.4)$$

where $s_B(t)$, A , ω_{RF} and θ represent the baseband OFDM signal, the amplitude and the angular frequency of the LO used for up-converting the baseband OFDM signal, and the phase angle of the electrical hybrid coupler respectively. N_{SC} is the number of OFDM subcarriers, C_k is the k th subcarrier (either information or pilot symbol), and f_k is the frequency of the k th subcarrier. It should be noted that for the sake of simplicity, the baseband OFDM signal in (3.4) shows only one OFDM frame.

It is easy to show, after some algebraic manipulations that the power transfer function, $\left(\frac{P_o(t)}{P_i(t)}\right)$ of the MZM can be re-written as:

$$\frac{P_o(t)}{P_i(t)} = \frac{1}{2} \left[1 + \cos \left(\frac{\pi(V_{mod1}(t) - V_{mod2}(t))}{V_\pi} \right) \right] \quad (3.5)$$

$$\frac{P_o(t)}{P_i(t)} = \cos^2 \left(\frac{\pi}{2} \cdot \frac{(V_{mod1}(t) - V_{mod2}(t))}{V_\pi} \right) \quad (3.6)$$

Equation (3.6) confirms that the MZM power transfer function is non-linear due to the presence of the \cos^2 term and that the value of $\frac{P_o(t)}{P_i(t)}$ is dependent only on the drive voltage difference as shown in Figure 3.1 (b).

Using (3.2) and (3.3) in (3.6), the MZM power transfer function reduces to:

$$\frac{P_o(t)}{P_i(t)} = \cos^2 \left(\frac{\pi}{2} \cdot [\varepsilon + \alpha \text{Re}\{s_B(t) \cdot e^{j\omega_{RF}t} - s_B(t) \cdot e^{j(\omega_{RF}t + \theta)}\}] \right) \quad (3.7)$$

where $\varepsilon = \frac{V_{DC}}{V_\pi}$ and $\alpha = \frac{A}{V_\pi}$ are the normalised bias and drive levels respectively.

Equation (3.7) shows that for fixed values of α (with ω_{RF} and θ fixed), the value of $\frac{P_o(t)}{P_i(t)}$ will be solely determined by the value of the normalised bias, ε .

Similarly, for fixed values of ε (with ω_{RF} and θ also fixed), the system performance will be dependent on the value of the normalised drive, α .

Equation (3.7) can further be expressed as:

$$\frac{P_o(t)}{P_i(t)} = \frac{1}{2} \left\{ 1 + \sin \left(\frac{\pi}{2} - \varepsilon\pi + \alpha\pi \operatorname{Re} \{ s_B(t) \cdot e^{j(\omega_{RF}t + \theta)} - s_B(t) \cdot e^{j\omega_{RF}t} \} \right) \right\} \quad (3.8)$$

As illustrated earlier in section 2.3.2, for generating an OSSB signal, $\theta = \pm \frac{\pi}{2}$ and $\varepsilon = \frac{1}{2}$ for a quadrature MZM bias. Consequently, (3.8) reduces to:

$$\frac{P_o(t)}{P_i(t)} = \frac{1}{2} \{ 1 + \sin(\alpha\pi m(t)) \} \quad (3.9)$$

where

$$m(t) = \operatorname{Re} \{ s_B(t) \cdot e^{j(\omega_{RF}t \pm \frac{\pi}{2})} - s_B(t) \cdot e^{j\omega_{RF}t} \} \quad (3.10)$$

Expanding (3.9) into a Taylor series yields:

$$\frac{P_o(t)}{P_i(t)} = \frac{1}{2} \left\{ 1 + \sum_{n=0}^{\infty} \frac{(-1)^n}{(2n+1)!} [\alpha\pi m(t)]^{2n+1} \right\} \quad (3.11)$$

Ignoring the higher-order terms in (3.11), the MZM power transfer function for OSSB modulation can be approximated as:

$$\frac{P_o(t)}{P_i(t)} \approx \frac{1}{2} \left\{ 1 + \alpha\pi m(t) - \frac{1}{3!} [\alpha\pi m(t)]^3 + \frac{1}{5!} [\alpha\pi m(t)]^5 \right\} \quad (3.12)$$

The third and fifth-order non-linear distortion terms in (3.12) will generate inter-modulation products between the subcarriers in the OFDM signal band. For small normalised drive levels ($\alpha \ll 1$), the non-linear distortion terms are negligible. However, with such small levels of drive power, the power of the optical carrier is much higher than the power in the optical OFDM sideband, resulting in low received electrical SNR and consequently, poor system performance. Increase in the value of α results in improvement in the system performance due to an increase in the SNR. For very large values of α however, the non-linear distortion terms become

prominent and result in system performance degradation. Thus, there is a system performance trade-off with regards to the MZM non-linear distortion and the received SNR.

In the subsequent sub-sections, following on from the theoretical analysis, the dependence of the system performance on the drive conditions of the MZM (bias and drive level) will be illustrated both by simulations and experimentally using EVM measurements as the performance metric. Our investigations will aim to illustrate the optimum MZM drive conditions to yield the best system performance.

3.3 Simulation setup

Figure 3.2 shows the simulation setup for the DD-OOFDM system, utilising the OptSim™ platform as described previously in section 2.7. In order to generate an OSSB signal, the Hilbert transform design as explained in section 2.5.1.3 is utilised. Consequently, the CCM module that acts as the OFDM transmitter has two outputs. The first transmitter output is the generated real-valued OFDM signal; and to obtain the required 90-degree phase difference for OSSB generation, the second transmitter output is the frequency-domain Hilbert transform of the OFDM signal.

The OFDM signal has a bandwidth of 1.5 GHz and is generated using a 512-point IFFT with a cyclic prefix length of 128 samples. 64 data-carrying subcarriers have been used; each modulated using 4-QAM. This results in an OFDM symbol duration of 53.34 ns. Consequently, the gross data rate is 3 Gbit/s (1.5 Gbaud). The system parameters used are listed in Table 3.1.

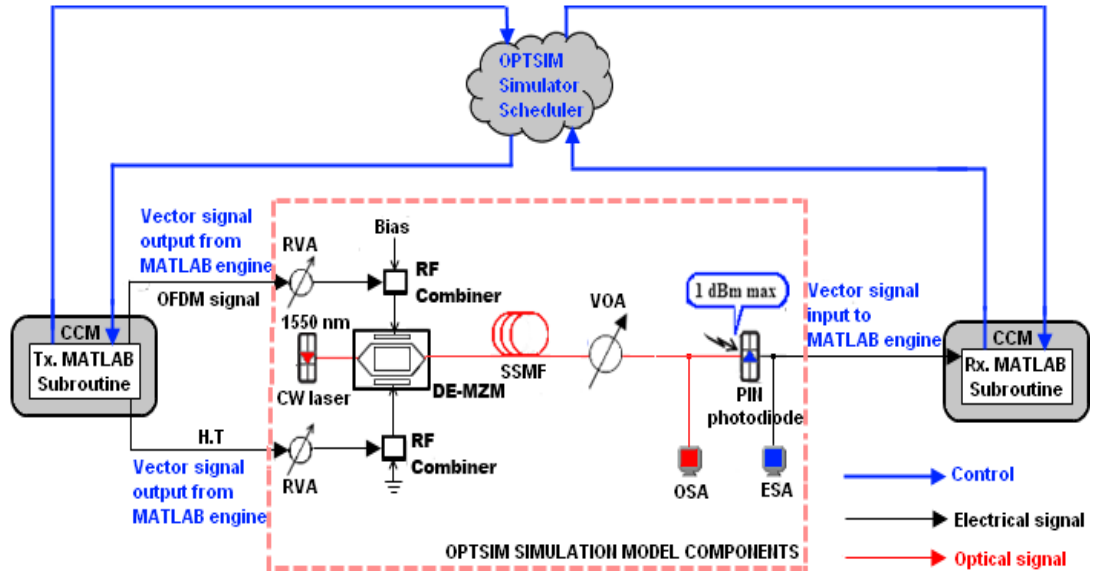


Figure 3.2. DD-OFDM simulation setup illustrating the CCM theory of operation. CCM: Custom component for MATLAB module. Tx.: Transmit. HT: Hilbert Transform. RVA: RF variable attenuator. CW: Continuous-wave. DE-MZM: Dual-electrode Mach-Zehnder modulator. VOA: Variable optical attenuator. SSMF: Standard single-mode fibre. OSA: Optical spectrum analyser. ESA: Electrical spectrum analyser. Rx.: Receive.

System parameter	Value
Subcarrier modulation format	4-QAM
FFT size	512
OFDM bandwidth	1.5 GHz
Number of data-carrying subcarriers	64
OFDM subcarrier frequency spacing	23.44 MHz
Information duration	42.67 ns
Cyclic prefix length (in samples)	128 (25%)
Cyclic prefix duration	10.67 ns
OFDM symbol duration	53.34 ns
Gross data rate	3 Gbit/s
Net data rate	2.4 Gbit/s

Table 3.1. OFDM system parameters.

Since the main purpose of this chapter is to analyse the influence of the MZM non-linear distortion on the system performance, the OFDM system parameters as shown in Table 3.1 do not conform to any particular existing standard. Rather, as stated in section 3.1, and as we will demonstrate in succeeding sections, the system parameters such as the number of subcarriers and the modulation format will be varied to see if trade-offs exist between fibre transmission distance and robustness to the MZM non-linear distortions.

After generation of the electrical OFDM signal and its Hilbert transform, the MATLAB subroutine closes, and control of the simulation is passed back to the OptSim™ simulation environment where the two transmitter outputs are used as the electrical drives to a DE-MZM ($V\pi = 3.1$ V, extinction ratio = 20 dB, insertion loss = 6 dB). A D.C. bias voltage is applied to one electrode of the MZM.

The electrical drive power to the MZM is varied by tuning the attenuation of the RF variable attenuators (RVAs). A CW laser with 9.47 dBm output power, a linewidth of 800 kHz and centre emission wavelength of 1550 nm is used as the laser source for the MZM. The OSSB signal is transmitted over SSMF with dispersion parameter, D of 16 ps/nm/km and attenuation of 0.2 dB/km. A PIN photodiode with a responsivity of 0.6 A/W is used as the photodetector. The attenuation provided by the VOA is adjusted as appropriate to set the maximum average power input to the photodiode at 1 dBm. It is important to stress at this point that the simulation parameter values have been so chosen so as to match the values of the actual components we will later use in the experiments. This will enable the simulation results to be matched with the experimental ones.

Once the photodetected signal reaches the CCM that acts as the OFDM receiver, the MATLAB engine starts again, passing the vector signal input and

launching the MATLAB subroutine for the OFDM receiver which in this case carries out the baseband digital signal processing including one-tap equalisation, demodulation, demapping, constellation plotting, as well as EVM and BER computation.

The EVM is a measure of the signal divergence from an ideal reference. The error vector is obtained by subtracting the n th received symbol S_n from an ideal reference symbol Z_n as shown in Figure 3.3.

For a total number of N OFDM symbols transmitted, the R.M.S value of the EVM (EVM_{rms}) can be expressed as:

$$EVM_{rms} = \sqrt{\frac{\frac{1}{N} \sum_{n=1}^N |Z_n - S_n|^2}{\frac{1}{N} \sum_{n=1}^N |Z_n|^2}} \quad (3.13)$$

In the case of M -ary square QAM, an appropriate expression for the BER is [115]:

$$BER \cong \frac{\sqrt{M} - 1}{\sqrt{M} \log_2 \sqrt{M}} \cdot \text{erfc} \left[\sqrt{\frac{3 \log_2 M \cdot \gamma}{2(M - 1)}} \right] \quad (3.14)$$

where $\text{erfc}(x)$ is the complementary error function and γ is the SNR.

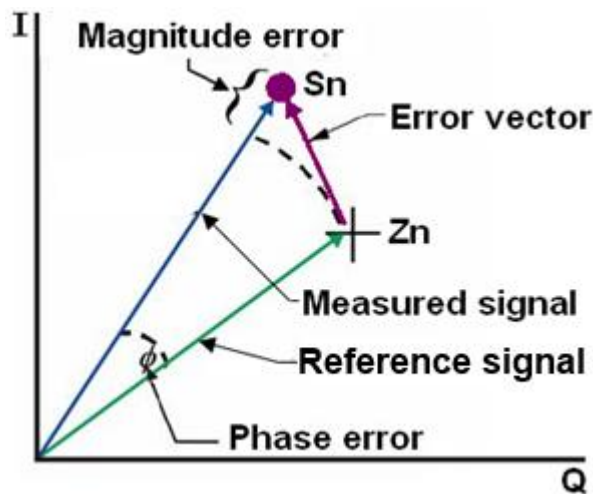


Figure 3.3. Visualisation of Error Vector Magnitude (EVM) in the I-Q plane.

The Q function, $Q(x)$ can be expressed as [116]:

$$Q(x) = \frac{1}{\sqrt{2\pi}} \int_x^{\infty} e^{-\frac{t^2}{2}} dt \quad (3.15)$$

where $Q(x)$ is related to $erfc(x)$ as follows:

$$Q(x) = 0.5erfc\left(\frac{x}{\sqrt{2}}\right) \quad (3.16)$$

The EVM can also be related to γ as follows [116]:

$$EVM \cong \frac{1}{\sqrt{\gamma}} \quad (3.17)$$

Making use of (3.16) and (3.17) in (3.14), the relationship between the EVM and BER for an M -ary square QAM is given by:

$$BER \cong \frac{2(\sqrt{M} - 1)}{\sqrt{M} \log_2 \sqrt{M}} \cdot Q \left[\frac{\sqrt{2}}{EVM} \sqrt{\frac{3 \log_2 M}{2(M - 1)}} \right] \quad (3.18)$$

Due to the memory limitations of our workstation and restrictions in MATLAB as regards the maximum size of a variable, error counting at Gbit/s data rates is not possible. Therefore, in this chapter and throughout this thesis, the BER is analytically obtained from the EVM using the expression given in (3.18). It is important to state at this point that (3.18) is obtained under the assumption that there is no optical amplification.

3.4 Experimental setup

The experimental system setup for the performance evaluation of the DD-OOFDM system is shown in Figure 3.4. Making use of the Hilbert Transform transmitter design and the same MATLAB routines and system parameters as used previously in section 3.3, the OFDM signal and its Hilbert Transform are saved as

single-column ASCII text files and then loaded into a Tektronix AWG7122B Arbitrary Waveform Generator (AWG). When both the mapping of the subcarriers to IFFT array and the size of the IFFT array are fixed, the sampling rate of the AWG is what determines the bandwidth of the generated OFDM signal. On the other hand, with a fixed sampling rate and IFFT size, the way the subcarriers are mapped to the IFFT determines the centre frequency of the OFDM signal.

The AWG is operated in dual-output mode. The first AWG output is the OFDM signal as shown in Figure 3.5 (a), while the second output is the Hilbert transform of the OFDM signal. These two outputs are used as the electrical drives to a Fujitsu FTM7921ER 10-Gbit/s DE-MZM. The peak-to-peak amplitudes of these driving signals are 1 V.

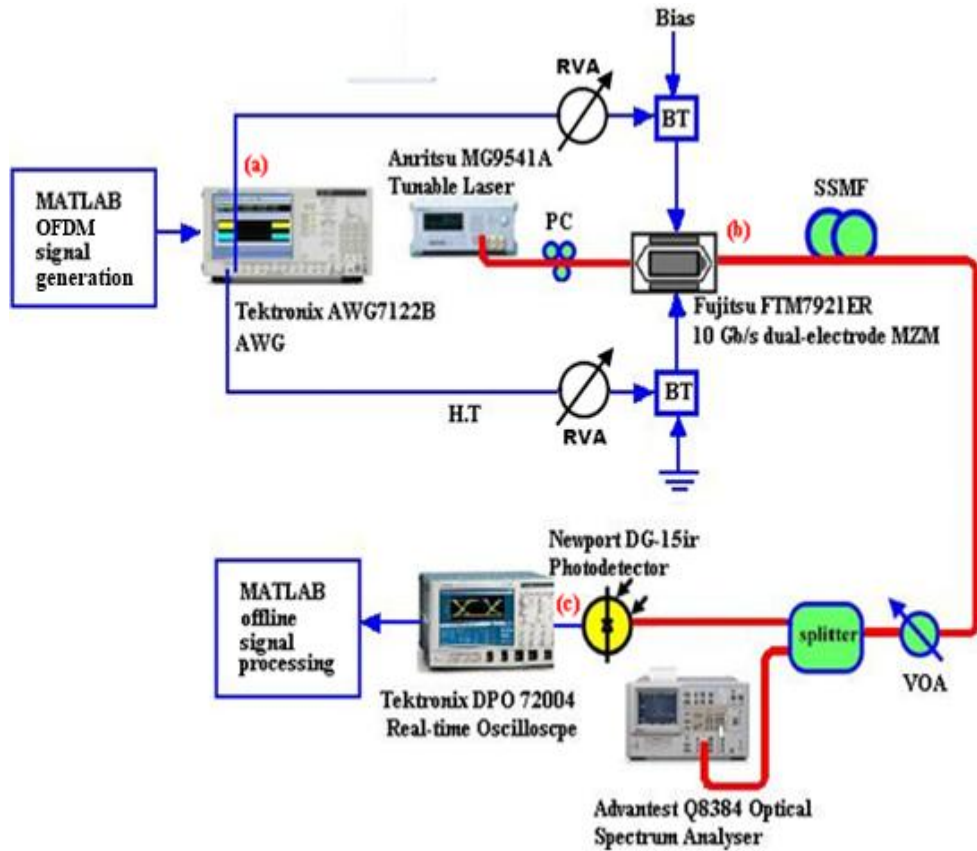


Figure 3.4. DD-OFDM experimental setup. AWG: Arbitrary waveform generator. RVA: RF variable attenuator. PC: Polarisation controller. BT: Bias tee. MZM: Mach-Zehnder modulator. SSMF: Standard single-mode fibre. VOA: Variable optical attenuator.

The MZM has a V_π of 3.1 V, an insertion loss of 6 dB and an extinction ratio of 20 dB. A D.C. bias voltage is applied via a bias-T to one arm of the MZM while the other bias-T is grounded. An Anritsu MG9541A tunable laser with centre emission wavelength of 1550 nm, linewidth of 800 kHz and 9.47 dBm output power is used as the CW laser source for the quadrature-biased MZM. The OSSB signal at the output of the MZM at point (b) in Figure 3.4 is shown in Figure 3.5 (b).

The modulated optical signal after the MZM is sent through 20-km SSMF with a chromatic dispersion parameter D of 16 ps/nm/km and attenuation loss of 0.2 dB/km before being directly detected by a Newport DG-15ir, 20-GHz photodiode. The spectrum of the photodetected OFDM signal is shown in Figure 3.5 (c).

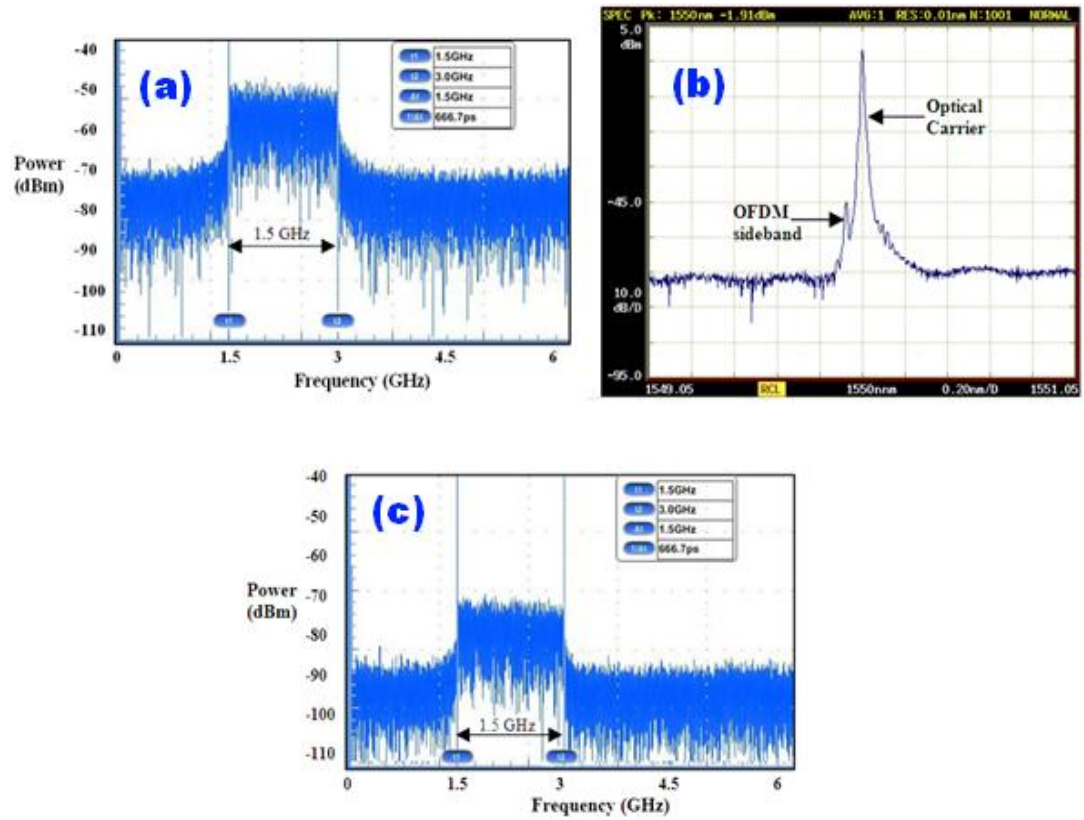


Figure 3.5 (a)-(c). Electrical and optical spectra at corresponding points in the experimental setup shown in Figure 3.4.

By varying the attenuation provided by the VOA placed before the photodiode, the received optical power and consequently the received SNR can be varied. After photodetection, the electrical OFDM signal is captured using a Tektronix DPO72004, 20-GHz, 50-GS/s real-time digital sampling oscilloscope.

The oscilloscope is operated at a sampling rate of 25 GS/s and has a large memory that can store about 200 million samples of the signal for processing. The baseband digital signal processing is performed offline in MATLAB.

In the MATLAB code for the OFDM receiver, a Virtual Instrument Standard Architecture-General Purpose Interface Bus (VISA-GPIB) object is created, which establishes a connection between the MATLAB workspace and the oscilloscope via its GPIB interface. At any instant the MATLAB code is run, this VISA-GPIB object enables the data from the oscilloscope to be easily captured and saved as a variable in the MATLAB code. Since the sampling rates of the AWG and the oscilloscope may differ, this captured data is then resampled at a rate which equals the ratio of the sampling rate of the AWG to the sampling rate of the oscilloscope.

Symbol synchronisation is then carried out on the resampled data in order to determine the start of the OFDM symbol. For the symbol synchronisation, Minn and Zeng's modification [117] to Schmidl and Cox's method for OFDM symbol synchronization [118] is employed.

In Schmidl and Cox's method, a training symbol with two identical halves in the time-domain is used to determine where the OFDM symbol starts in the received frame. Each half of the training symbol contains $L = \frac{N}{2}$ samples, where N is the IFFT/FFT size. A window of $2L$ samples slides across the received OFDM time-domain samples and a timing metric is computed. This timing metric is given by [118]:

$$M(d) = \frac{|P(d)|^2}{R^2(d)} \quad (3.19)$$

where d is a time index corresponding to the first sample in a window of $2L$ samples and

$$P(d) = \sum_{m=0}^{L-1} r^*(d+m) \cdot r(d+m+L) \quad (3.20)$$

$$R(d) = \sum_{m=0}^{L-1} |r(d+m+L)|^2 \quad (3.21)$$

where $P(d)$ is the autocorrelation function of the received signal, $R(d)$ is the power of the second half of the training symbol, and the superscript "*" carries out the complex conjugation operation.

The start of the OFDM symbol is determined by the value of d that maximises $M(d)$. $M(d)$ will be minimum at all other values of d . As an example, a plot of the timing metric against received samples is shown in Figure 3.6 (a) where it can be seen that the timing metric reaches a plateau with a length equal to the length of the cyclic prefix (128 samples). This introduces some uncertainty as to the exact start of the OFDM symbol.

This uncertainty is solved by Minn and Zeng's modification as shown in Figure 3.6 (b) which averages the timing metric over a window of the same length as the cyclic prefix. In this case, the start of the OFDM symbol is easily obtained from the received sample value that corresponds to the maximum value of the timing metric.

After synchronisation, the cyclic prefix is removed. This is followed by demodulation of the data, one-tap equalisation using dedicated training symbols, demapping, and EVM/BER computation using (3.13) and (3.18).

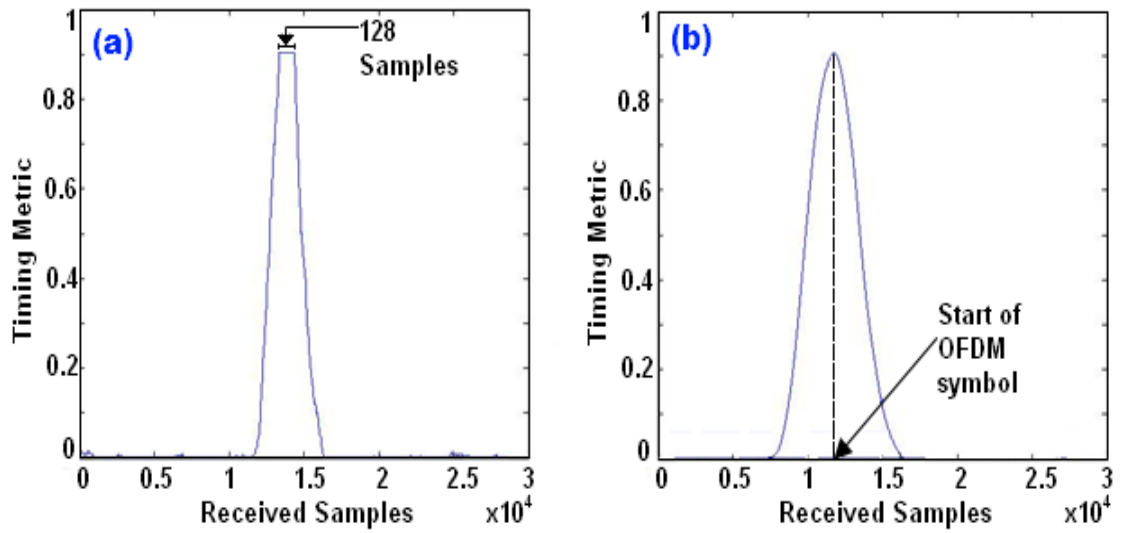


Figure 3.6. Timing metric used for OFDM symbol synchronisation: (a) Schmidl and Cox (b) Minn-Zeng Modification.

A snapshot of the experimental setup is shown in Figure 3.7 with the equalised constellation plots at various values of normalised MZM D.C. bias levels, ε (for a normalised drive level, α of 0.05) shown in Figure 3.8.

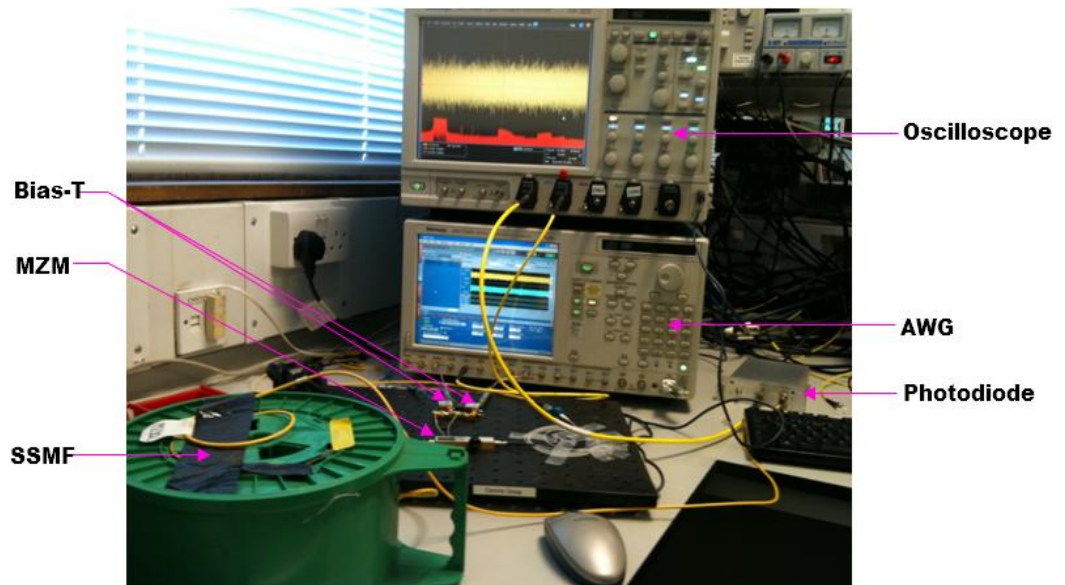


Figure 3.7. Snapshot of the DD-OOOFDM experimental setup.

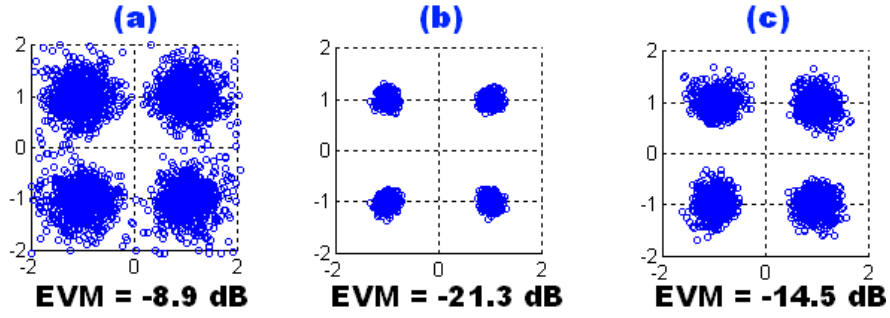


Figure 3.8. Experimental equalised 4-QAM constellations for different normalised bias levels, ε = (a) 0.27 (b) 0.5 (c) 0.69.

In the subsequent sections, a series of tests will be conducted using the simulation and experimental setups to illustrate how the MZM non-linearity influences the performance of the DD-OOFDM system. In particular, the following will be considered:

- System performance tests, concerned with illustrating the dependence of the system performance on the MZM bias and drive levels.
- System parameter variation tests which will deal with evaluating the impact of a variation in the system parameters such as the number of subcarriers and modulation format on the MZM non-linearity.
- Spectral efficiency tests which will look at operating with a reduced frequency guard band as a means to optimizing spectral efficiency for the DD-OOFDM system.

3.5 System performance tests

In this section, we investigate, with the aid of simulations and experiments, using EVM as the performance metric, how variations in the D.C. bias point and the amplitude of the drive to the MZM affect the system performance.

Using the simulation setup as shown in Figure 3.2 with the system parameters as specified in Table 3.1, a sampling rate of 12 GS/s, and a normalised MZM drive

level, α of 0.04; the value of the D.C. bias to the MZM, V_{DC} is varied from the maximum point of the optical intensity function, through the quadrature point to the null point V_{π} . For each value of normalised bias, $\varepsilon = \frac{V_{DC}}{V_{\pi}}$, the received EVM is computed.

Figure 3.9 shows the plot of the EVM variation with ε for 20-km SSF transmission. It can be seen from Figure 3.9 that the EVM first decreases (improves) with increasing values of ε because the received SNR increases. The received SNR increases because increasing ε results in an increase in the power of the OFDM sideband and a corresponding decrease in the power of the optical carrier. The EVM keeps decreasing until it gets to a point, the so-called inflection point, where the EVM is lowest. For values of ε from 0.46 to 0.56, the EVM is lower than -18 dB.

The EVM keeps decreasing until it gets to a point, the so-called inflection point, where the EVM is lowest. For values of ε from 0.46 to 0.56, the EVM is lower than -18 dB.

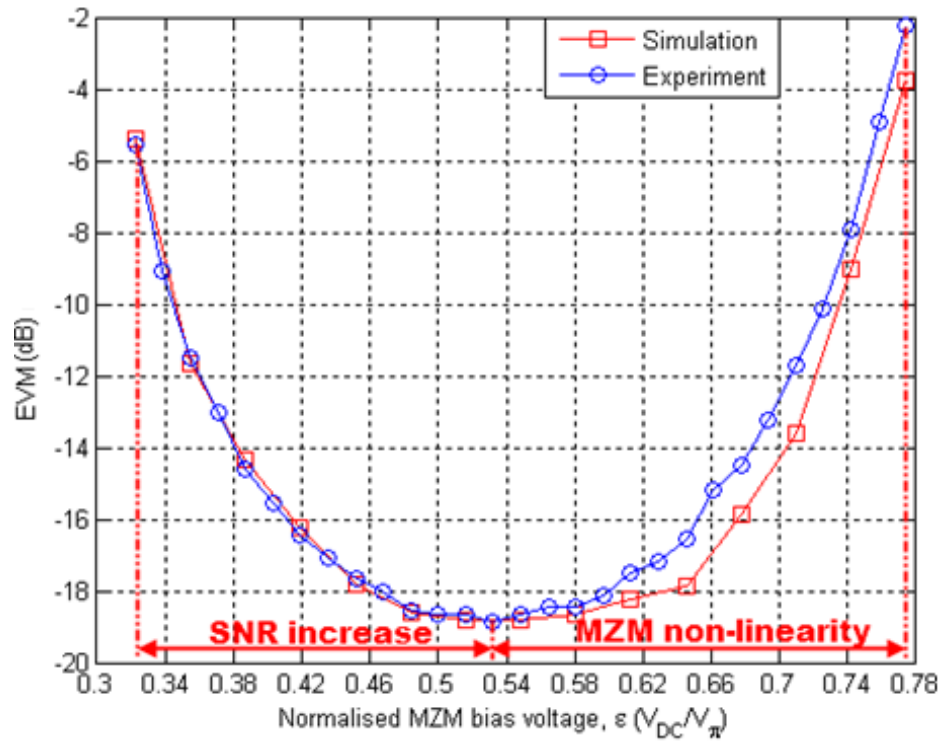


Figure 3.9. EVM vs. normalised MZM bias voltage, ε using both simulation and experimental setups.

This range of values represents the linear portion of the MZM characteristic (quadrature regime) where the EVM performance is optimum. Beyond this quadrature regime, the EVM starts to degrade with further increase in ε because of the increased influence of the MZM non-linear distortion. Hence, provided the value of ε is not increased beyond the quadrature regime where the MZM non-linearity dominates, the system performance improves.

Figure 3.9 also shows that the variation of the EVM with ε using the experimental setup as shown in Figure 3.4 validates the simulation results, with a very good agreement obtained.

Figure 3.10 shows a plot of the EVM against ε for various values of α using the simulation setup. Here, it can be seen that even though it is clear that the EVM performance degrades as ε is increased beyond the quadrature regime of the MZM, the EVM performance is still dependent on the value of α . Increasing the value of α from 0.02 initially improves the EVM performance (as shown by the dash-line curves in Figure 3.10). For higher values of α greater than 0.08, the EVM performance starts degrading (as shown by the solid-line curves in Figure 3.10). This degradation, as will be shown soon, is also due to the MZM non-linear distortion. This is because the higher the drive level, the sooner the driving OFDM signal encounters the non-linear portion of the MZM characteristics.

Next, to fully illustrate the dependence of the DD-OOFDM system performance on the drive level, the value of ε is fixed at 0.5. Then, the value of α is varied by varying the attenuation of the RVAs. For each value of α , in a similar fashion as before, the EVM is obtained. Figure 3.11 shows the variation of the EVM with α for a value of ε equal to 0.5.

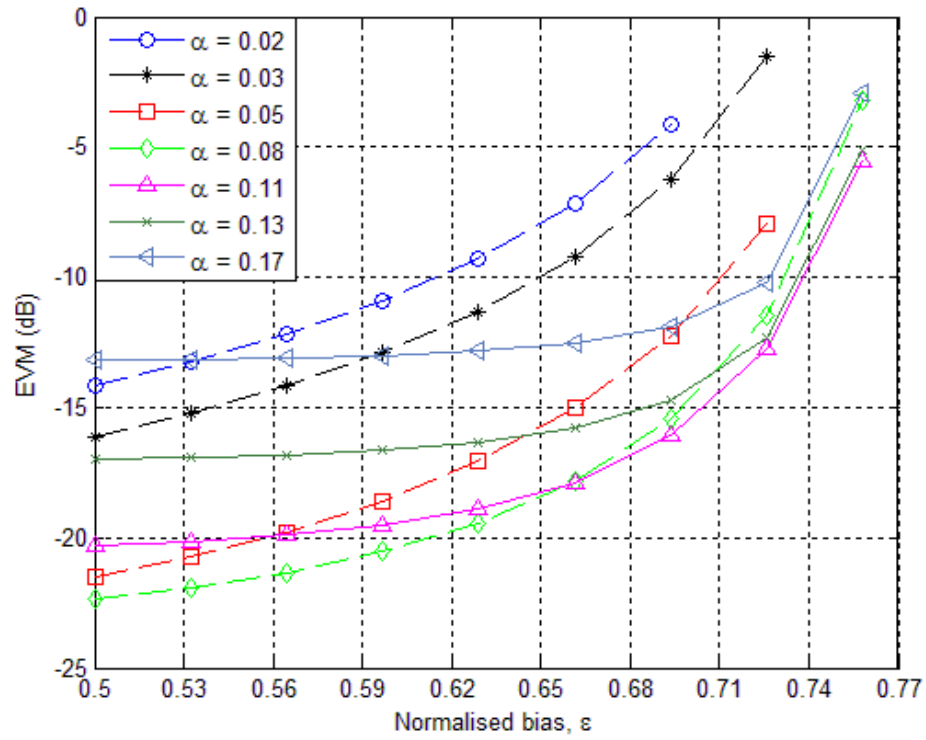


Figure 3.10. Simulated values of EVM vs. normalised bias, ε for different values of normalised drive level, α .

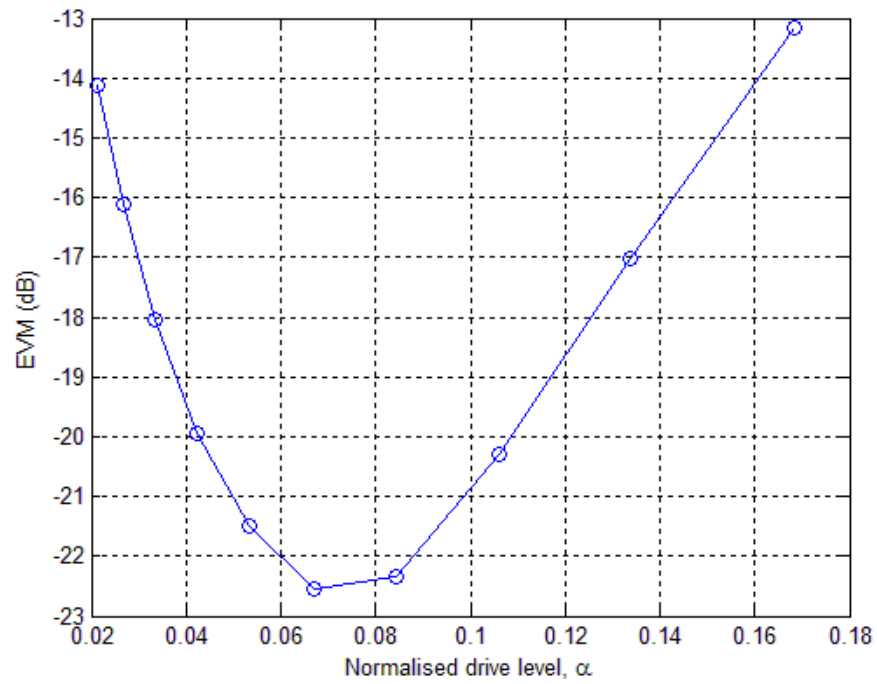


Figure 3.11. Simulated values of EVM vs. normalised drive levels, α for a normalised bias, ε of 0.5.

The simulation results in Figure 3.11 show a similar trend to that shown in Figure 3.9 with the EVM reducing up to a minimum point and then increasing, confirming that the EVM performance of the system is affected not only by the value of ε but also by the value of α .

In Figure 3.11, for very low values of α , the signal power is much lower than the noise power, resulting in low SNR, and as specified by (3.17), high EVM. Figure 3.12 (a) shows the simulated OSSB spectrum at the output of the MZM for a normalised bias level of 0.02 where it is clearly evident that at such a low value of α , the power in the optical OFDM sideband is much less than the power of the optical carrier.

As the value of α increases, the power in the OFDM sideband increases (Figure 3.12 (b)), resulting in improvement in the received SNR and consequently, reduction in the EVM and improvement in the system performance. This improvement continues until α becomes 0.08 where the EVM is optimum. For high values of $\alpha \gg 0.08$ however, the non-linear distortion terms as shown previously in (3.12) become prominent, resulting in system performance degradation.

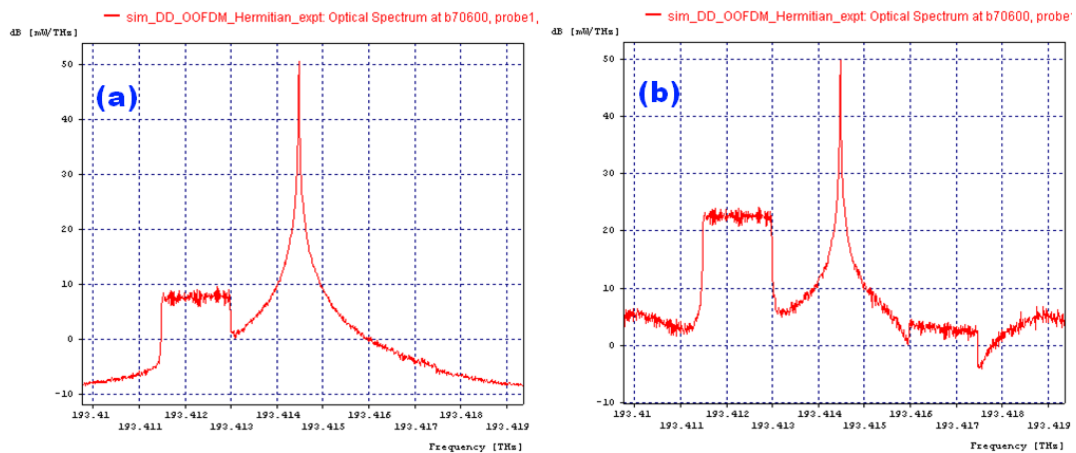


Figure 3.12. Simulated OSSB spectrum at output of MZM for (a) $\alpha = 0.02$ (b) $\alpha = 0.13$.

This is in agreement with the results shown previously in Figure 3.10. Thus, for optimum DD-OOFDM system performance, not only does the MZM bias have to be controlled to within the quadrature regime of operation but the driving amplitude still has to be chosen low enough to avoid the MZM non-linear distortion. In essence, to obtain an EVM penalty (due to the MZM non-linear distortion) of < 2 dB, α has to be ≤ 0.11 ; and ε needs to be within 0.06 of the normalised quadrature bias voltage value of 0.5.

3.6 System parameter variation tests

The investigations in this section are centred on determining the effect a variation in the number of subcarriers and modulation format has on the EVM performance of the DD-OOFDM system.

For the investigation into the system performance with respect to subcarrier number variation, the same simulation model as in section 3.3 is used with the same simulation parameters as in section 3.5 and no intentional signal clipping implemented. α is fixed at 0.11 and then ε is varied from 0.5 to 0.76 (i.e. the region dominated by the MZM non-linear distortion). The EVM is then obtained for each value of ε . This test is repeated for various numbers of subcarriers.

Figure 3.13 shows the EVM plotted against ε for a normalised drive level of 0.11 for 4, 8, 16, 32 and 64 subcarriers. Here, it can be seen that although the EVM variation with ε for the different number of subcarriers follows the same trend as discussed in section 3.5, the system performance improves with a reduction in the number of subcarriers. This improvement becomes more obvious as the value of ε increases.

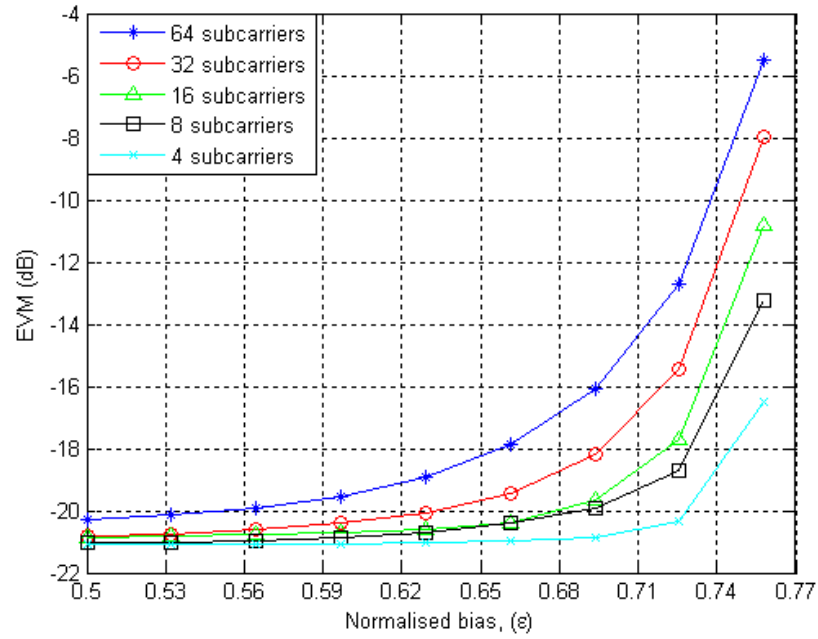


Figure 3.13. EVM vs. ϵ for different number of subcarriers.

In Figure 3.13, for a normalised bias level of 0.74, the EVM reduces from -9.4 to -12 dB and then to -14.7, -16 and -18.6 dB when the number of subcarriers reduces from 64 to 32 and then to 16, 8 and 4 subcarriers respectively. We can thus infer that the tolerance of the DD-OOFDM system to the MZM non-linearity can be improved by reducing the number of subcarriers. The reason behind this improvement can be attributed to the reduction of the non-linear impairment due to the reduction of the OFDM Peak-to-Average Power Ratio (PAPR) [119]-[121].

As stated in section 2.4.5.1, the OFDM signal is made up of a number of independently modulated subcarriers that combine constructively to give a high PAPR. This PAPR is independent on the modulation format but varies depending on the number of subcarriers [122].

Figure 3.14 shows a simulation of the Complementary Cumulative Distribution Function (CCDF) of the PAPR for the DD-OOFDM system for 1000 OFDM symbols and different modulation formats.

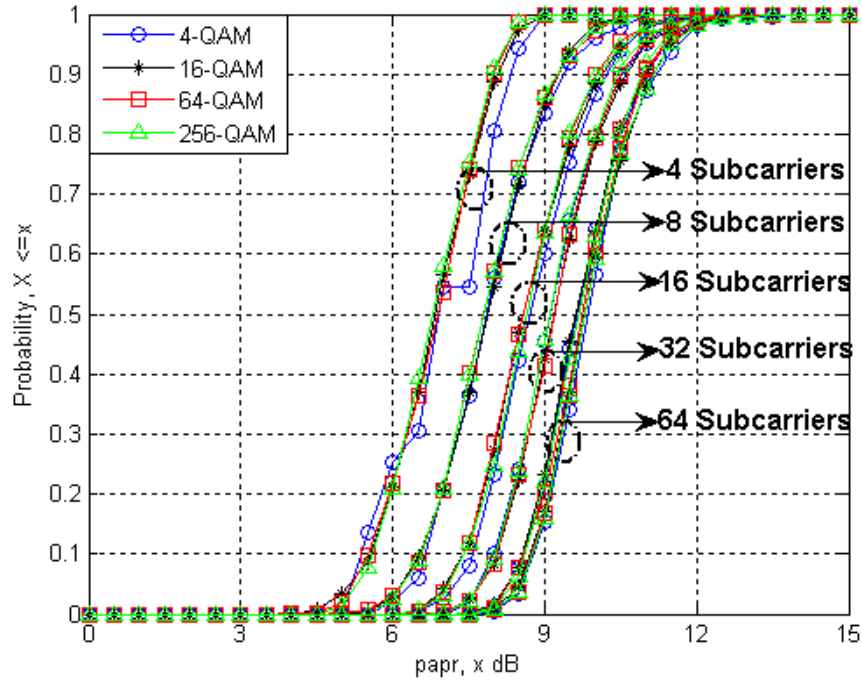


Figure 3.14. Simulated PAPR distribution for different number of subcarriers and different modulation formats.

The vertical axis of the graph is the probability that the PAPR is less than a threshold value x dB. This threshold value is the system maximum limit of the PAPR. The CCDFs of the PAPR confirm that the PAPR doesn't depend on the modulation format but decreases with a reduction in the number of subcarriers.

Figure 3.15 shows a simulation of the PAPR of the DD-OFDM system, computed using (2.46), plotted against the number of subcarriers where it can be clearly seen that the PAPR does reduce as the number of subcarriers decreases.

The results presented in Figures 3.13 – 3.15 show that the tolerance of the DD-OFDM system to the MZM non-linear distortion improves with a reduction in the number of OFDM subcarriers.

This implies that it may be desirable to minimise the number of subcarriers employed. This implication is quite interesting in the context of the usual theory that increasing the number of OFDM subcarriers is a good thing for fibre transmission.

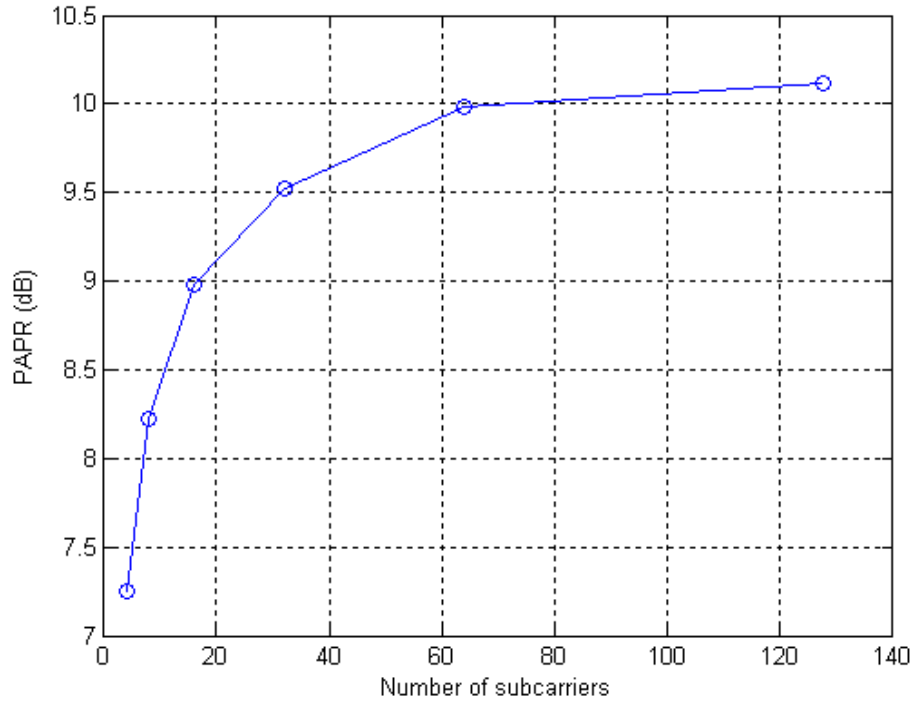


Figure 3.15. Simulated PAPR as a function of the number of subcarriers.

This is because if the cyclic prefix is excessively long relative to the number of OFDM subcarriers, a large fraction of the transmitted energy is wasted in cyclic prefix samples, resulting in a substantial power penalty. For a given cyclic prefix length, this penalty can be reduced by increasing the number of subcarriers [121].

Hence, we would like to demonstrate how the system EVM varies with SSMF length for various numbers of OFDM subcarriers in a situation where the MZM bias is in the region dominated by the MZM non-linear distortion. This would enable us to see if there is a trade-off with regards to the number of subcarriers and the SSMF length.

To demonstrate this, with the same simulation parameters, α and ϵ are kept fixed at 0.11 and 0.6 respectively. With the fibre non-linearities disabled (so chromatic dispersion is the major fibre impairment), and with the received optical

power to the photodiode kept fixed at 1 dBm, the SSMF length is varied and the EVM obtained for each fibre length. This test is repeated for the various numbers of subcarriers.

Figure 3.16 shows the variation of the EVM with the SSMF length for 4, 8, 16, 32 and 64 subcarriers using the simulation setup of Figure 3.2 with no ASE noise included. It can be seen from the figure that as the fibre length is gradually increased, the EVM starts degrading. This is because with a fixed cyclic prefix length, increase in the fibre length results in a corresponding increase in the delay spread caused by the fibre chromatic dispersion. The EVM starts degrading when the delay spread exceeds the cyclic prefix length. However, as can be seen from Figure 3.16, the rate of the EVM degradation depends on the number of OFDM subcarriers. For small fibre lengths (< 50 km), having a reduced number of subcarriers is desirable because of the greater tolerance to the MZM non-linear distortion.

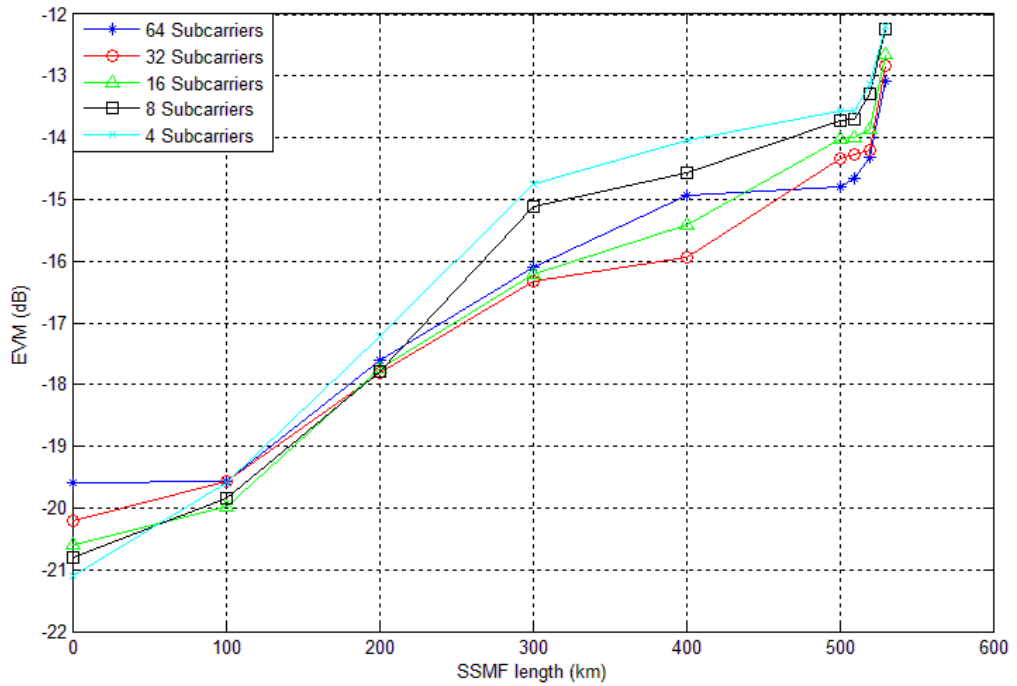


Figure 3.16. Simulated EVM degradation with SSMF length for different number of subcarriers.

At longer fibre lengths (> 450 km) however, it becomes more practical to have a higher number of subcarriers because of the power penalties caused by the pulse spreading brought about by the fibre chromatic dispersion.

The next step in our investigations is to examine the sensitivity of the OFDM signal to the MZM non-linearity for different modulation formats. To do this, the number of OFDM subcarriers is kept fixed at 64 and the modulation format is varied from 4-QAM to 64-QAM. In order to maintain the gross symbol rate of 1.5 Gbaud, and keep the signal bandwidth constant at 1.5 GHz, the gross bit rates vary between 3 Gbit/s for 4-QAM to 9 Gbit/s for 64-QAM.

For each of the modulation formats, the value of α is fixed at 0.11, ε is varied from 0.5 to 0.76; and the EVM obtained for each value of ε . Figure 3.17 shows the simulation and experimental results for the EVM variation with ε for the different modulation formats. From Figure 3.17, it can be seen that the MZM non-linearity affects the system performance more for the higher level modulation formats. For $\varepsilon = 0.5$, the EVM increases from -20.3 dB for 4-QAM to -16 dB for 64-QAM.

Since the gross symbol rate of 1.5 Gbaud is constant, the noise power for all the modulation schemes is fixed, resulting in similar SNR in the absence of the MZM non-linearity [121]. However, in the region dominated by the MZM non-linearity, the SNR now becomes signal-to-noise plus interference ratio [122]. This interference is due to the MZM non-linear distortion which becomes more severe for higher level modulation formats because the constellation points are closer to each other [123]. Figure 3.18 shows the received constellation plots for the different modulation formats for a normalised bias voltage of 0.5

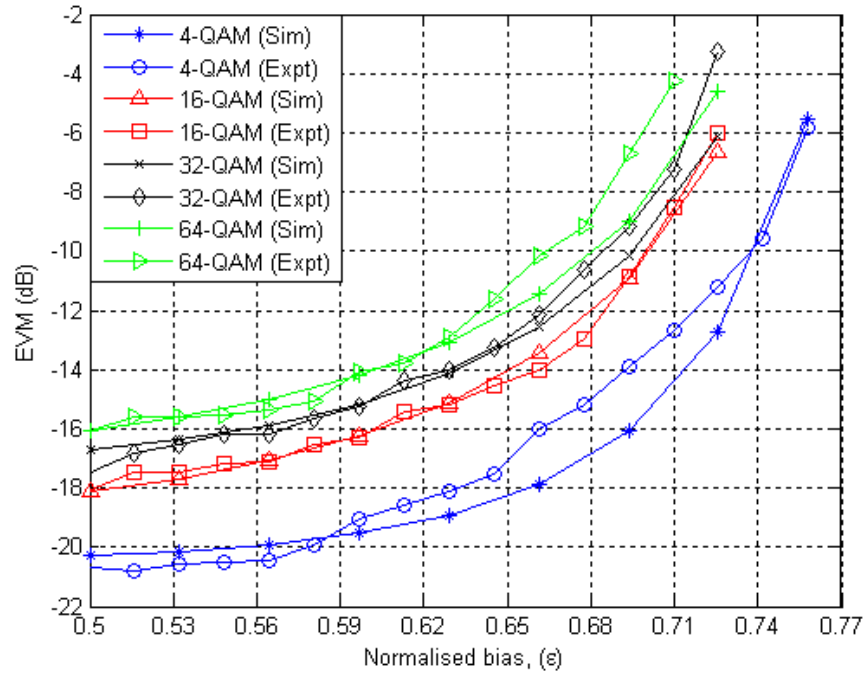


Figure 3.17. EVM vs. ϵ for different modulation formats, using both simulation and experimental setups

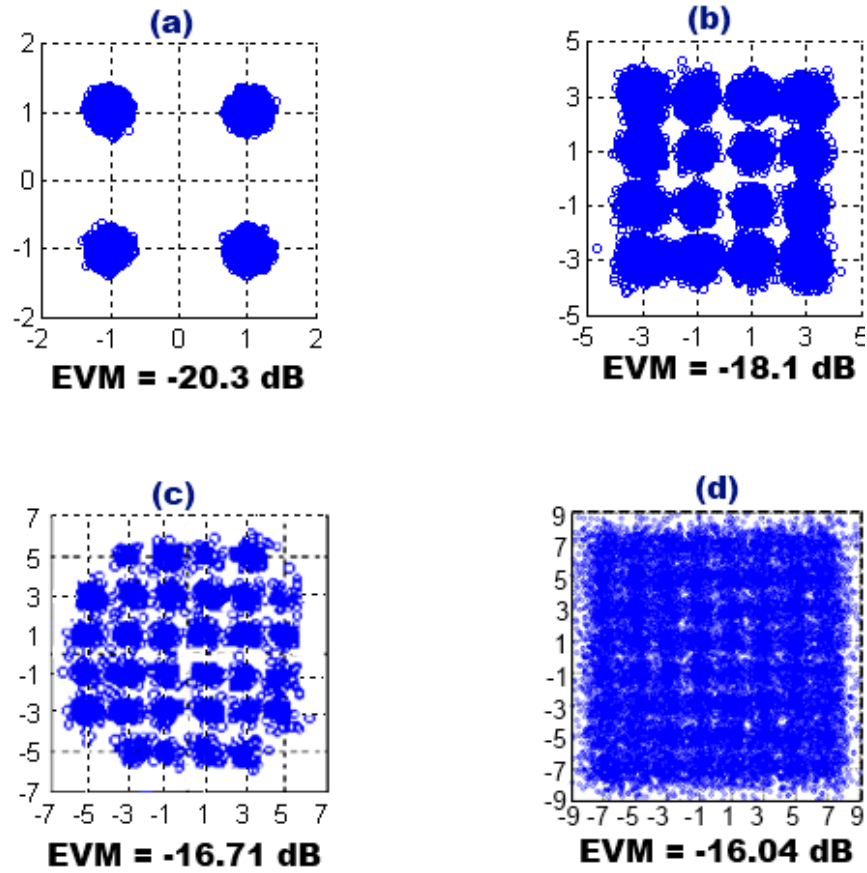


Figure 3.18. Experimental equalised constellations for different modulation formats with $\epsilon = 0.5$: (a) 4-QAM (b) 16-QAM (c) 32-QAM (d) 64-QAM

3.7 Spectral efficiency tests

In this section, the possibility of improving the spectral efficiency of DD-OOFDM systems by reduction of the width of the guard band, B_{gap} is investigated. It was stated in section 2.5.1 that to avoid significant in-band distortion from the second-order intermodulation distortion products, B_{gap} must be at least equal to the OFDM signal bandwidth, B_{SC} . The amplitude of these second-order intermodulation distortion products is dependent on the value of ε .

Figure 3.19 shows the simulated received electrical spectrum with $\alpha = 0.11$ for normalised bias voltages of 0.5 and 0.9. With $\varepsilon = 0.5$, the amplitude of the intermodulation distortion products is much less than when $\varepsilon = 0.9$.

With the intermodulation distortion products having such small amplitudes for $\varepsilon = 0.5$, it may be possible to remove a proportion of the guard band in order to improve the spectral efficiency. We therefore proceed to investigate by simulation; the impact reducing B_{gap} has on the BER performance of the DD-OOFDM system operating with a fixed value of α and for different values of ε .

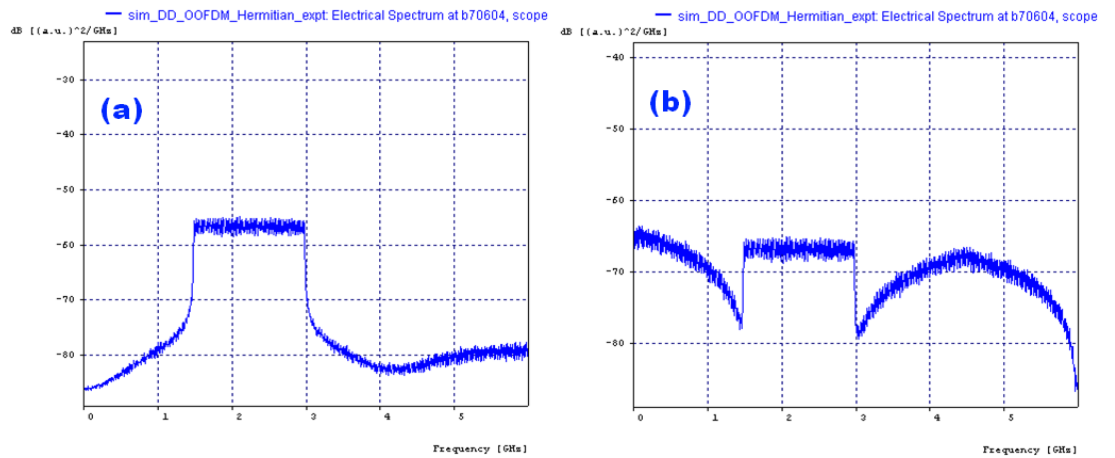


Figure 3.19. Simulated received electrical spectrum with $\alpha = 0.11$ for: (a) $\varepsilon = 0.5$ (b) $\varepsilon = 0.9$.

Figure 3.20 shows a plot of the BER against the ratio of B_{gap} to B_{SC} where it can be seen that for $\varepsilon = 0.5$, the BER is around 2.6×10^{-9} when $\frac{B_{gap}}{B_{SC}} = 0.8$. This BER remains largely unchanged as the width of the guard band is reduced. In fact, with $\frac{B_{gap}}{B_{SC}} = 0.3$, the BER is still around 1.5×10^{-8} . This is in stark contrast to when $\varepsilon = 0.7$ where the BER degrades significantly from 2.5×10^{-9} when $\frac{B_{gap}}{B_{SC}} = 0.8$ to a BER of 3.1×10^{-3} when $\frac{B_{gap}}{B_{SC}} = 0.3$. This significant BER degradation as B_{gap} is reduced for $\varepsilon = 0.7$ is due to the fact that the amplitudes of the second-order intermodulation distortion products are large enough to start causing considerable in-band distortion.

This implies that for transmission over fibre in DD-OFDM systems, with a quadrature bias, we can comfortably remove at least 50% of the guard band without a significant change in the BER performance, resulting in improvement in the spectral efficiency.

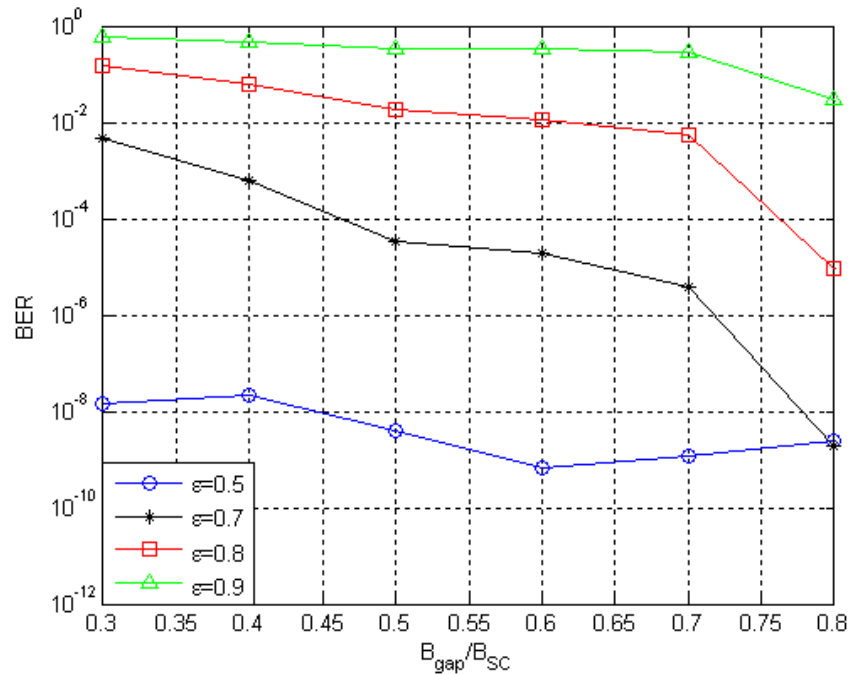


Figure 3.20. BER vs. $\frac{B_{gap}}{B_{SC}}$ for $\alpha = 0.11$ and for different values of ε .

3.8 Summary

In this chapter, the impact the non-linearity of the MZM characteristic has on the system performance of a DD-OFDM signal has been studied. With the aid of theoretical analysis, MATLAB-OptSim™ co-simulations and experiments, it has been shown that both the MZM bias point and the amplitude of the driving OFDM signal affect the system performance.

It has been found that for a fixed drive level to the MZM, provided the value of the MZM D.C. bias is not increased beyond the quadrature regime to the extent where the EVM will be degraded due to the MZM non-linear distortion, the system performance improves. Also, for a fixed value of D.C. bias, for low drive levels, the SNR is low resulting in high EVM. Increase in the drive level improves the SNR and consequently, the EVM. For exceedingly high drive levels, however, the OFDM signal suffers non-linear distortion. Thus, for optimum system performance, not only should the bias voltage be controlled to within the quadrature regime of MZM characteristics, the drive level also has to be kept sufficiently low enough to avoid the MZM non-linear distortion. Our experimental illustrations on the dependence of the EVM performance of the DD-OFDM system on the MZM bias level yielded results that closely match the simulation results.

It has also been shown that the tolerance of the DD-OFDM system to the MZM non-linearity can be improved by reducing the number of subcarriers due to the reduction of the OFDM PAPR. This improvement is however, only seen for short fibre lengths (<50 km). It has also been demonstrated that as higher level modulation formats are employed, the system performance gets more affected by the MZM non-linearity because the interference due to the MZM non-linear distortion becomes more severe.

Finally, it has been shown that with a quadrature bias, with the low level of intermodulation distortion products present, the BER remains largely unchanged for at least a 50% reduction in the guard band. Thus, the spectral efficiency in DD-OOFDM systems can be improved by reduction of the width of the guard band by at least 50% if a quadrature bias is used.

Chapter 4. Ultra-wideband (UWB) radio-over-fibre in FTTH access networks

4.1 Introduction

As stated in chapter 2, OFDM has been applied optically in access networks through UWB systems. A UWB signal is defined as any radio signal with a 10-dB bandwidth of at least 500 MHz or a fractional bandwidth of at least 0.2 [18]. The fractional bandwidth is defined as the ratio of the 10-dB bandwidth to the centre frequency of the signal and is given by:

$$BW_f = \frac{2(f_U - f_L)}{(f_U + f_L)} \quad (4.1)$$

where BW_f is the fractional bandwidth, and f_U and f_L are the upper and lower frequencies at the -10 dB emission point respectively.

In this chapter, the optical distribution of UWB signals in FTTH networks is investigated as a transparent and low-cost solution to extending the range and improving the flexibility of UWB. This chapter explores, with the aid of theoretical, simulation and experimental analysis using both EVM and BER measurements as performance metrics, how the UWB RoF system performance is limited by various parameters such as the MZM non-linearity, fibre chromatic dispersion and received optical power at the photodetector.

The chapter is organised into three sections. In section 4.2, a simulation model of a complete UWB RoF system with focus on the ECMA-368 standard using multi-band OFDM (MB-OFDM) is developed in OptSim™, and demonstrated experimentally. For both the simulation and experimental models, external modulation by an MZM is considered, and an OSSB architecture using the Hilbert Transform design is implemented to prevent sideband cancellation due to fibre

chromatic dispersion. First, the impact of the non-linearities of the MZM on the system performance of the MB-OFDM UWB RoF model is demonstrated. A two-tone intermodulation test is also simulated and compared with analytical approximations in order to explain the system performance behaviour under the influence of the third-order intermodulation distortion brought about by the MZM non-linearity. Next, the limitations brought about by fibre transmission are investigated; where simulations are performed to evaluate the maximum reach in SSMF for error-free operation for the MB-OFDM UWB RoF system. Also, the impact, if any, that fibre chromatic dispersion has on the performance of the UWB system is examined. The final investigations in this section deal with evaluating the effect of a received optical power variation on the system performance. The simulation analyses on the system performance presented in this section are validated experimentally, with a good agreement obtained between the simulation and experimental results. Finally, the chapter is concluded and summarised in section 4.3.

4.2 Simulation evaluation and experimental demonstration of MB-OFDM UWB RoF transmission

The OptSim™ simulation setup for the performance evaluation of the MB-OFDM UWB RoF system based on the point-to-point architecture of Figure 2.36 is shown in Figure 4.1. The ECMA-368 compliant MB-OFDM UWB signal with the first three sub-bands corresponding to BG #1 is generated, utilising the MATLAB-OptSim™ co-simulation functionality as previously described in section 2.7. The UWB signal complies with the no-frequency hopping schemes of TFCs 5-7 as illustrated in Table 2.4.

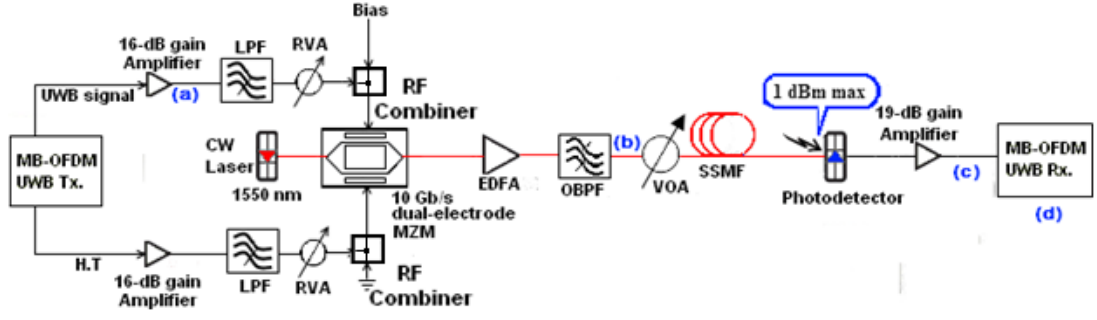


Figure 4.1. Simulation schematic of the MB-OFDM UWB transmission system. Tx.: Transmitter. HT: Hilbert Transform. LPF: Low-pass filter. CW: Continuous-wave. RVA: RF variable attenuator. MZM: Mach-Zehnder modulator. EDFA: Erbium-doped fibre amplifier. OBPF: Optical band-pass filter. VOA: Variable optical attenuator. SSMF: Standard single-mode fibre. Rx.: Receiver.

A sampling rate of 10.8 GS/s is used for the simulation and the three sub-bands are modulated using 4-QAM, each sub-band being 528-MHz wide with frequency details as listed in Table 2.3.

Since the MB-OFDM UWB signal has very wide bandwidth, out-of-band interference sources, most importantly the out-of-band leakage can cause signal degradation. The out-of-band leakage from one sub-band may cause degradation of an adjacent sub-band which would be undesirable especially in situations where different sub-bands are sent to different users. In this regard, in a practical network scenario, for satisfactory operation, the adjacent channel leakage ratio (ACLR), defined as the ratio of the power in an adjacent band to the power in the bandwidth within the main signal, should stay below -20 dB, in accordance with the ECMA-368 standard [89].

The channel bit rate per sub-band is 640 Mbit/s, providing an aggregate bit rate of 1.92 Gbit/s for the three sub-bands. This aggregate bit rate would drop to 1.44 Gbit/s (480 Mbit/s per sub-band) with the inclusion of error-correction and spreading codes. The system parameters, in accordance with the ECMA-368 standard [89], are listed in Table 4.1.

System parameter (per UWB sub-band)	Value
Subcarrier modulation format	4-QAM
FFT size	128
OFDM bandwidth	528 MHz
Number of data-carrying subcarriers	100
OFDM subcarrier frequency spacing	23.44 MHz
Information duration	242.4 ns
Cyclic prefix length (in samples)	32 (25%)
Cyclic prefix duration	60.6 ns
Guard interval duration	9.5 ns
OFDM symbol duration	312.5 ns
Channel gross bit rate	640 Mbit/s

Table 4.1. MB-OFDM UWB system parameters according to the ECMA-368 standard [89].

The generated MB-OFDM UWB signal at point (a) in Figure 4.1 is shown in Figure 4.2 (a). The Hilbert Transform design introduced in section 2.5.1.3 is used to generate the optical UWB signal. With this design, the UWB transmitter has two outputs. The first output is the real-valued UWB signal while the second output is the frequency-domain Hilbert transform of the UWB signal.

The generated UWB signals have peak-to-peak amplitudes of 1 V. These two outputs are amplified by two 16-dB amplifiers and filtered before being used to drive a 10-Gbit/s DE-MZM ($V\pi = 3.1$ V, extinction ratio = 20 dB, insertion loss = 6 dB) biased at its quadrature point.

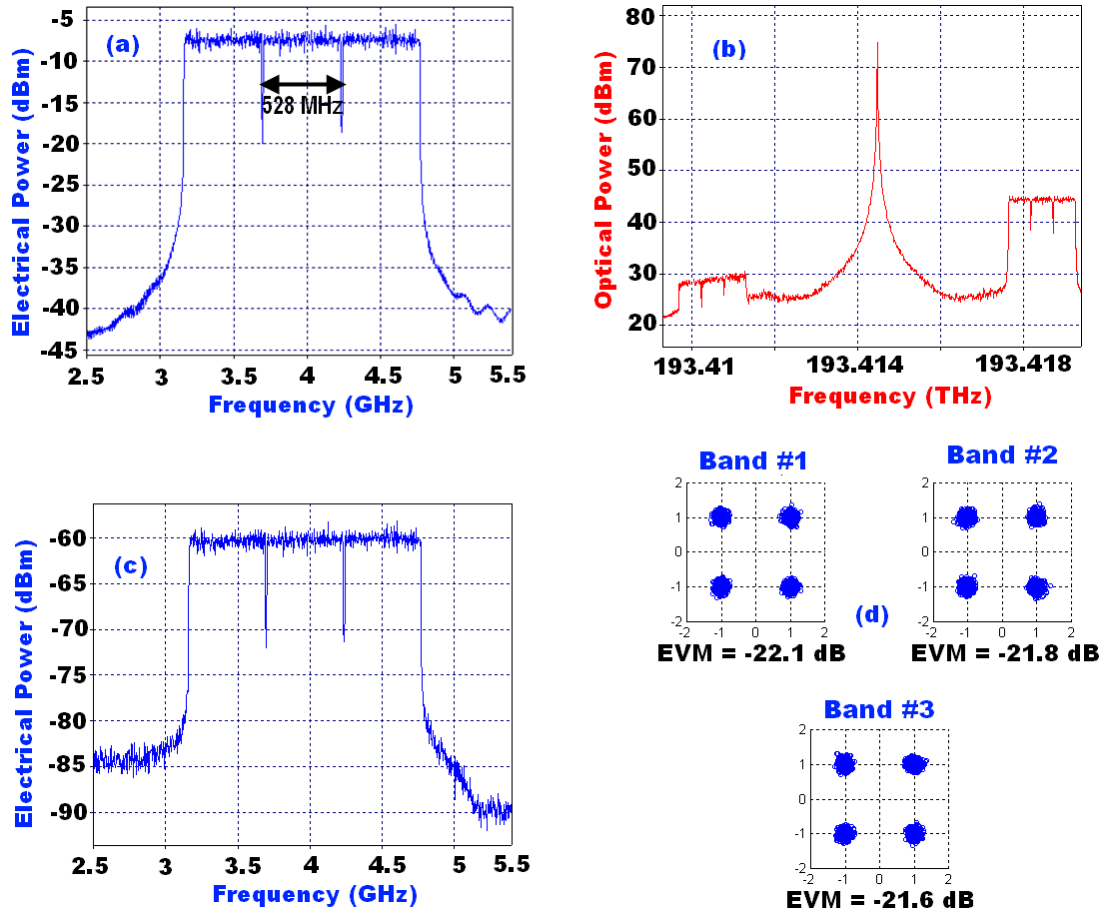


Figure 4.2. (a)-(c) Electrical and optical spectra at corresponding points in the simulation schematic shown in Figure 4.8. (d) Equalised constellation diagrams at -7 dBm UWB drive power and 1 dBm received optical power for 26-km SSMF transmission.

It is important to state at this point that the component parameters used in the simulation have been chosen to match those of the actual experimental components so as to enable the simulation results to be compared with the experimental ones.

The amplitudes of the driving UWB signals can be varied as required by tuning the attenuation of the RVAs. A CW laser with 800 kHz linewidth and centre emission wavelength of 1550 nm serves as the optical source to the MZM.

An OSSB is generated at the output of the MZM. This OSSB signal is amplified by an EDFA to compensate for the insertion loss of all optical components; filtered using an OBPF to suppress the out-of-band ASE noise, and then transmitted through various lengths of SSMF.

The OSSB spectrum of the amplified and filtered UWB signal is shown in Figure 4.2 (b). This optical UWB signal is directly detected by a photodiode with a responsivity of 0.6 A/W. A VOA is included in the setup to keep the maximum power input into the photodiode at 1 dBm. The VOA also enables the system performance to be analysed as a function of the received optical power. The photodetected UWB signal is amplified by a 19-dB amplifier (Figure 4.2 (c)) and then passed on to the UWB receiver for baseband digital signal processing. Figure 4.2 (d) shows the equalized 4-QAM constellation diagrams for a UWB drive power of -7 dBm, a SSMF length of 26 km and a received optical power of 1 dBm.

Figure 4.3 shows the experimental setup for the MB-OFDM UWB RoF system employing external modulation of a 10-Gbit/s, Fujitsu FTM7921ER DE-MZM ($V_\pi = 3.1$ V, extinction ratio = 20 dB, insertion loss = 6 dB). The same modulating MB-OFDM UWB signal, as used in the simulation setup, is generated offline in MATLAB as a single-column ASCII text file and then loaded into a Tektronix AWG7122B AWG operating at a sampling rate of 10.8 GS/s. In a similar fashion as in section 3.4, the AWG is operated in dual-output mode. The first AWG output is the UWB signal while the second output is the Hilbert transform of the UWB signal.

These two outputs are amplified by two 16-dB gain, SHF 104P amplifiers and then filtered by two 7.5-GHz, Picosecond LPFs to remove the alias components produced from the DAC conversion at the AWG. These filtered signals are then used as the electrical drives to the MZM which is biased at its quadrature point to produce an OSSB UWB signal. The optical source to the MZM is an Anritsu MG9541A tunable laser with centre emission wavelength of 1550 nm and linewidth of 800 kHz.

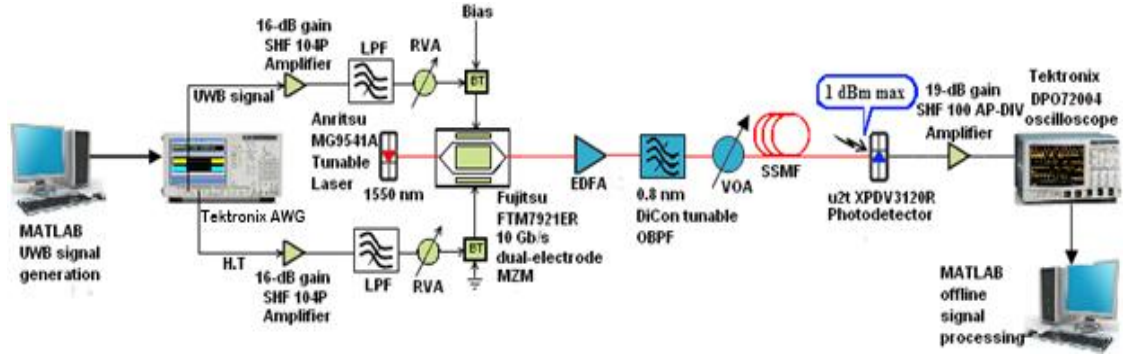


Figure 4.3. Experimental setup of the MB-OFDM UWB RoF system. HT: Hilbert Transform. LPF: Low-pass filter. RVA: RF variable attenuator. BT: Bias Tee. MZM: Mach-Zehnder modulator. EDFA: Erbium-doped fibre amplifier. OBPF: Optical band-pass filter. VOA: Variable optical attenuator. SSMF: Standard single-mode fibre

The OSSB signal generated at the output of the MZM is amplified by an EDFA and then filtered by a 0.8-nm DiCon tunable OBPF to suppress the ASE noise. Just as in the simulation setup, the filtered OSSB signal is transmitted through various lengths of SSMF with attenuation loss of 0.2 dB/km and chromatic dispersion parameter, D of 16 ps/nm/km.

The VOA is used to vary the optical attenuation to set the maximum optical power input into a u²t Photonics, XPDV3120R photodetector (0.6 A/W responsivity) at 1 dBm. After photodetection, the electrical UWB signal is amplified by a 19-dB gain, SHF-100 AP-DIV amplifier and then captured by a Tektronix DPO 72004 real-time digital sampling oscilloscope operated at 50 GS/s sampling rate. The baseband digital signal processing is performed offline in MATLAB in the same manner as demonstrated previously in section 3.4.

In the subsequent sub-sections, using the setup as shown in Figure 4.1, the impacts of the various parameters such as the MZM non-linearities, fibre transmission and received optical power on the system performance will be investigated and validated experimentally using the setup shown in Figure 4.3.

4.2.1 Impact of MZM non-linearity on system performance

For the investigation into the impact of the MZM non-linearity on the system performance, the SSMF length is fixed at 26 km. The RVAs are used to vary the amplitudes of the two driving UWB signals. For each value of driving amplitude, the corresponding drive power is measured and the VOA is adjusted to keep the input optical power to the photodetector fixed at 1 dBm. Figure 4.4 shows the variation of the EVM for the three UWB sub-bands with the UWB drive power for both the simulation and experimental models using Figures 4.1 and 4.3 respectively.

It is seen that the EVM variation with the UWB drive power follows the same trend for both the simulation and experiment with a very good agreement obtained. The EVM values for the three sub-bands improve as the UWB drive power increases from a low value. This is because of an increase in the received SNR.

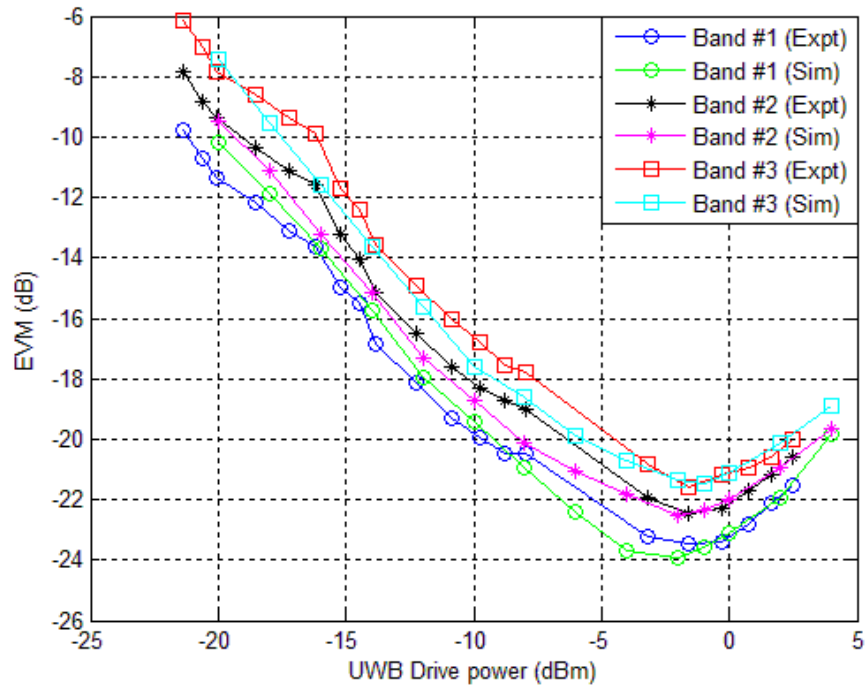


Figure 4.4. Experimental and simulated values of EVM of the three UWB sub-bands vs. UWB drive power for 26-km SSMF transmission.

This improvement in the EVM continues until the UWB drive power gets to an optimum value of -2 dBm. For UWB power levels greater than -2 dBm, the EVM starts to degrade as the distortion induced by the inherent non-linear response of the MZM becomes worse.

The measured PAPR for the UWB signal is about 15 dB. In order to fully explain the trend of the curves depicted in Figure 4.4, it is imperative to have a fuller understanding of the MZM non-linear intermodulation distortion. The third-order intermodulation (IMD3) terms are the most important in determining the severity of the degradation of the system performance due to the non-linearity of the MZM, because of their proximity to the fundamental frequency component. In this regard, a two-tone intermodulation test is simulated to help explain the impact of the MZM non-linearity on the MB-OFDM UWB RoF system.

Figure 4.5 shows the simulation setup for the two-tone test for the MB-OFDM UWB RoF system. A combination of two input RF tones at 1 and 1.004 GHz is split into two parts by an RF power splitter.

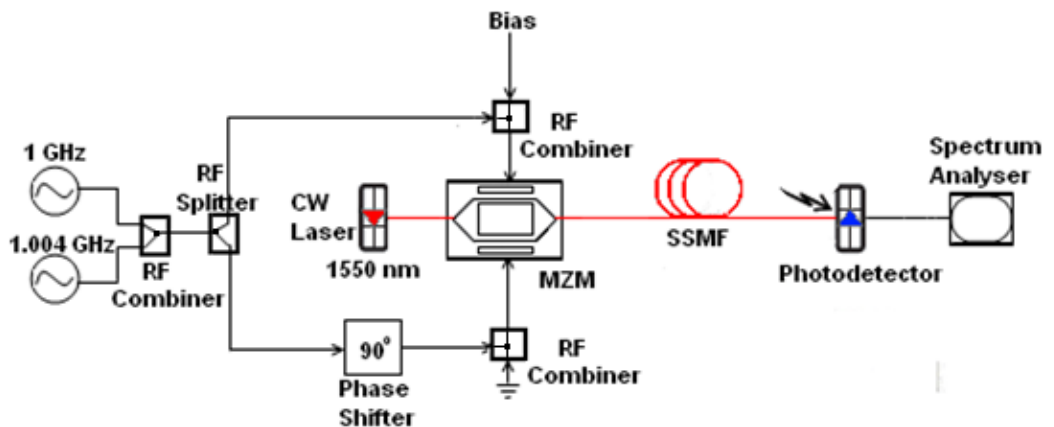


Figure 4.5. Simulation setup for the two-tone test.

One part is applied to the upper MZM electrode while the other is passed through a 90° phase shifter and used to drive the lower MZM electrode. In a similar manner as in Figure 4.1, a D.C. bias voltage is applied to the upper MZM electrode while the other D.C. terminal is grounded. The optically modulated signal is transmitted over 26 km SSMF, directly detected by the photodetector and the received electrical signal evaluated with an electrical spectrum analyser.

The amplitudes of the two RF tones are varied from a low value to a high value. For each value of RF tone amplitude, the powers of a fundamental frequency component and an IMD3 component are measured. For the two RF input tones at 1 and 1.004 GHz, the IMD3 components of significant interest to us (which are at close proximity to the fundamental frequency components) occur at 0.996 GHz i.e. $(2 \times 1 - 1.004 \text{ GHz})$ and 1.008 GHz i.e. $(2 \times 1.004 - 1 \text{ GHz})$.

Figure 4.6 shows the spectrum of the photodetected signal depicting the fundamental and IMD3 components for RF tone amplitudes equal to 1 and 3.2. As can be seen from Figure 4.6, for a low value of RF tone amplitude, the intrinsic IMD3 components at 0.996 and 1.008 GHz are quite small compared to the fundamental components at 1 and 1.004 GHz.

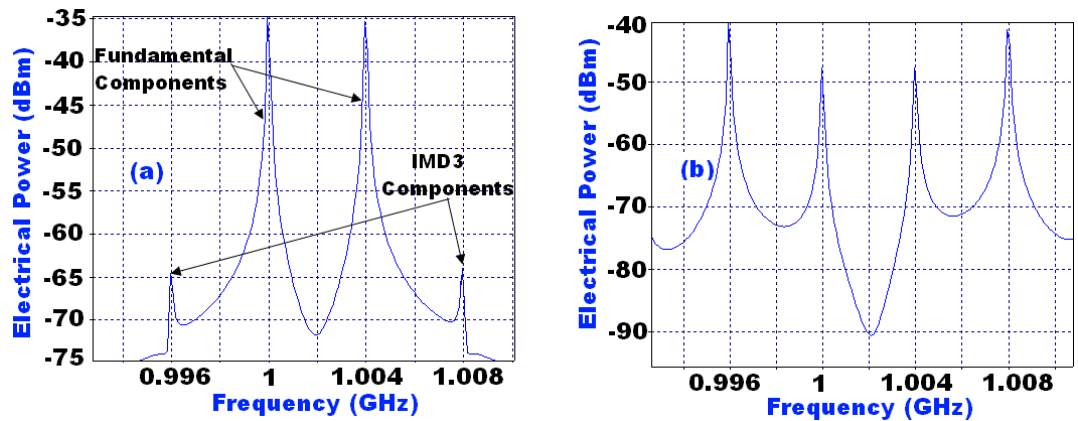


Figure 4.6. Two-tone test for 26-km SSMF transmission showing the fundamental components (1 and 1.004 GHz) and the IMD3 components (0.996 and 1.008 GHz) for: (a) RF tone amplitude of 1. (b) RF tone amplitude of 3.2.

With increase in the RF tone amplitude to 3.2, the amplitudes of the IMD3 components become higher than those of the fundamental components. For OSSB signals in direct-detection systems, the power of the fundamental frequency component P_{f1} at a frequency f_1 (1 GHz) can be approximated analytically as [124]:

$$P_{f1} = \left(10^{-\frac{\alpha L}{10}} L_{att}^2 A^2 \mathcal{R} J_0^3(\pi m_{RF}) J_1(\pi m_{RF}) \right)^2 \quad (4.2)$$

where for the simulation, $\alpha = 0.2$ dB/km is the fibre attenuation loss; $L = 26$ km is the SSMF length; $L_{att} = 0.50119$ is the attenuation of the MZM due to its insertion loss of 6 dB; $A = 8.65$ mW is the laser diode amplitude; $\mathcal{R} = 0.6$ A/W is the photodiode's responsivity; $m_{RF} = \frac{V_{RF}}{V_\pi}$ is the RF modulation index, where V_{RF} is the R.M.S voltage of the input RF tones; and $J_k(.)$ represents the Bessel function of the first kind of order k .

It should be noted that the other fundamental frequency component P_{f2} at a frequency f_2 (1.004 GHz) is the same as P_{f1} .

Similarly from [124], the power of the first IMD3 component, P_{IMD1} at a frequency of $2f_1 - f_2$ (0.996 GHz) can be approximated as:

$$P_{IMD1} = 2 \left(10^{-\frac{\alpha L}{10}} L_{att}^2 A^2 \mathcal{R} \right)^2 (D_{IM}^2 + E_{IM}^2) \quad (4.3)$$

where

$$\begin{aligned} D_{IM} = & \frac{1}{\sqrt{2}} \{ J_0^2(\pi m_{RF}) J_1(\pi m_{RF}) J_2(\pi m_{RF}) \\ & \times \left[\cos \left(\theta_{2f1} - \theta_{f2} + \frac{\pi}{4} \right) + \sin \left(\theta_{2f1-f2} - \frac{\pi}{4} \right) \right] \\ & - J_0(\pi m_{RF}) J_1^3(\pi m_{RF}) \sin \left(\theta_{f2-f1} - \theta_{f1} + \frac{\pi}{4} \right) \} \end{aligned} \quad (4.4)$$

$$\begin{aligned} E_{IM} = & \frac{1}{\sqrt{2}} \{ J_0^2(\pi m_{RF}) J_1(\pi m_{RF}) J_2(\pi m_{RF}) \\ & \times \left[\cos \left(\theta_{2f1} - \theta_{f2} - \frac{\pi}{4} \right) - \sin \left(\theta_{2f1-f2} + \frac{\pi}{4} \right) \right] \\ & - J_0(\pi m_{RF}) J_1^3(\pi m_{RF}) \sin \left(\theta_{f2-f1} - \theta_{f1} - \frac{\pi}{4} \right) \} \end{aligned} \quad (4.5)$$

$$\theta_f = \frac{\pi L D \lambda^2 f^2}{c} \quad (4.6)$$

where $\lambda = 1550$ nm is the centre emission wavelength of the laser diode, $D = 16$ ps/nm/km is the chromatic dispersion parameter of the fibre and c is the speed of light.

The powers of the fundamental and IMD3 components can be computed using (4.2)-(4.6). Figure 4.7 illustrates the computed values of the powers of the fundamental and IMD3 components as a function of the RF modulation index m_{RF} in dB. It is seen from Figure 4.7 that at low values of modulation index, the IMD3 power is much lower than that of the fundamental. As the modulation index increases, the IMD3 component increases faster than the fundamental, until at an optimum value of modulation index, the power of the IMD3 component equals that of the fundamental.

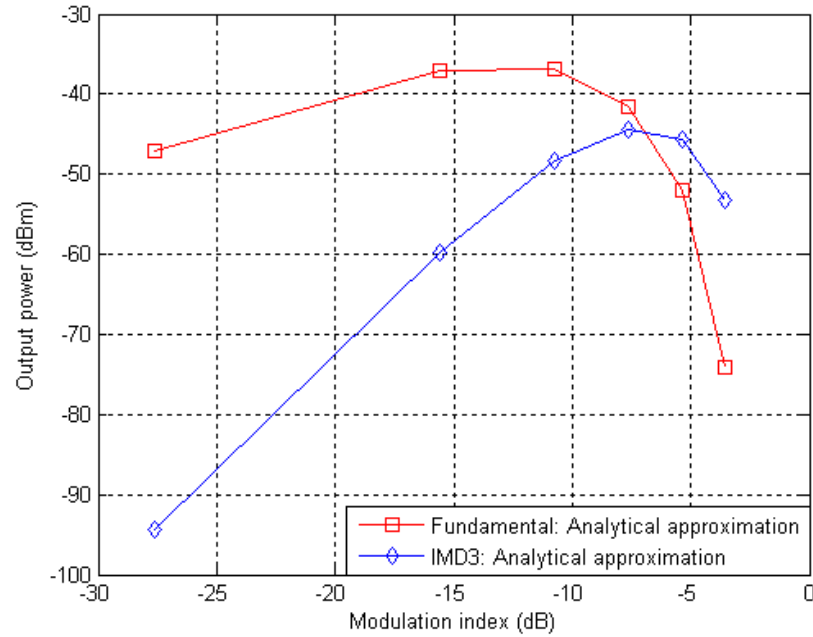


Figure 4.7. Analytical approximation showing variation of fundamental and IMD3 powers with modulation index.

For values of modulation index greater than this optimum value, the system performance starts to degrade because of the IMD3 distortion. The optimum value of the modulation index obtained from the analytical approximation, as shown in Figure 4.7, is -6.91 dB. Using the simulation setup of Figure 4.5, the variation of the output powers of the fundamental and IMD3 components with the RF modulation index can also be obtained. This variation is depicted in Figure 4.8.

Figure 4.8 shows that the results obtained from simulation follow the same trend as that obtained from the analytical approximation with a good agreement obtained at low values of modulation index. However, at higher values of modulation index, the approximation deviates from the simulation results. Consequently, the optimum modulation index obtained from simulation is -4.67 dB.

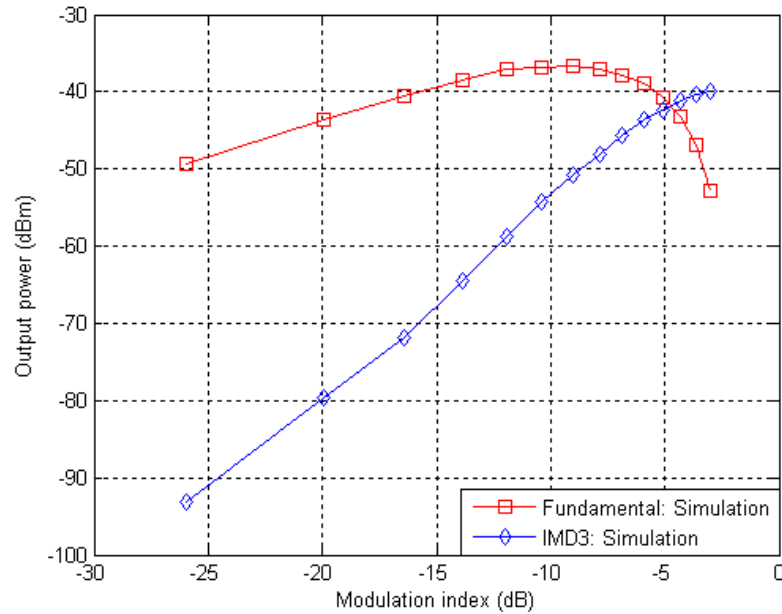


Figure 4.8. Simulation showing variation of fundamental and IMD3 powers with modulation index.

In order to relate the IMD3 simulation results depicted in Figure 4.8 to the results shown in Figure 4.4 for the MB-OFDM UWB RoF system, the variation of the received EVM with the RF modulation index is obtained with the input optical power to the photodetector kept constant at 1 dBm for each value of modulation index.

Figure 4.9 shows the variation of the EVM of the three sub-bands with the modulation index for 26-km SSMF transmission where it is apparent that the EVM of each sub-band decreases with increasing values of modulation index until the modulation index gets to the optimum value of -4.58 dB, beyond which the EVM starts to degrade.

This optimum value of modulation index is in excellent agreement with the optimum value of modulation index depicted in Figure 4.8 at which the power of the IMD3 component equals that of the fundamental component.

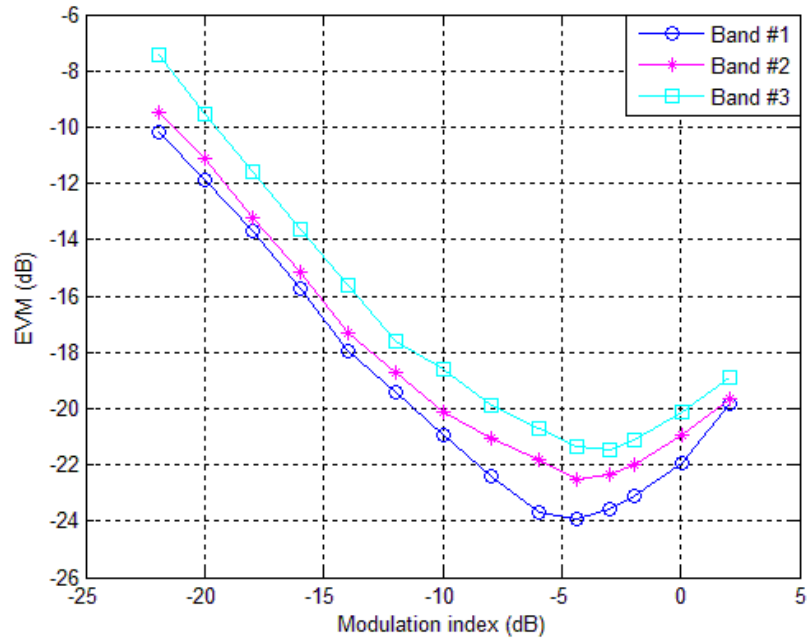


Figure 4.9. EVM of the three UWB sub-bands vs. modulation index for 26-km SSMF transmission (simulation).

4.2.2 Impact of fibre transmission on system performance

The first step in our investigations here is to evaluate the maximum reach in SSMF for error-free operation for the MB-OFDM UWB RoF system. To do this, the EDFA, OBPF and VOA in the simulation setup of Figure 4.1 are not included. The UWB drive power is fixed at the optimum value of -2 dBm and the optical power launched into the fibre is varied from -16 dBm to 4 dBm. For each value of optical launch power, the received BER is computed. Figure 4.10 shows a plot of the BER vs. the optical launch power for the three UWB sub-bands for five optical transmission cases: back-to-back, 10 km, 26 km, 50 km and 75 km of SSMF.

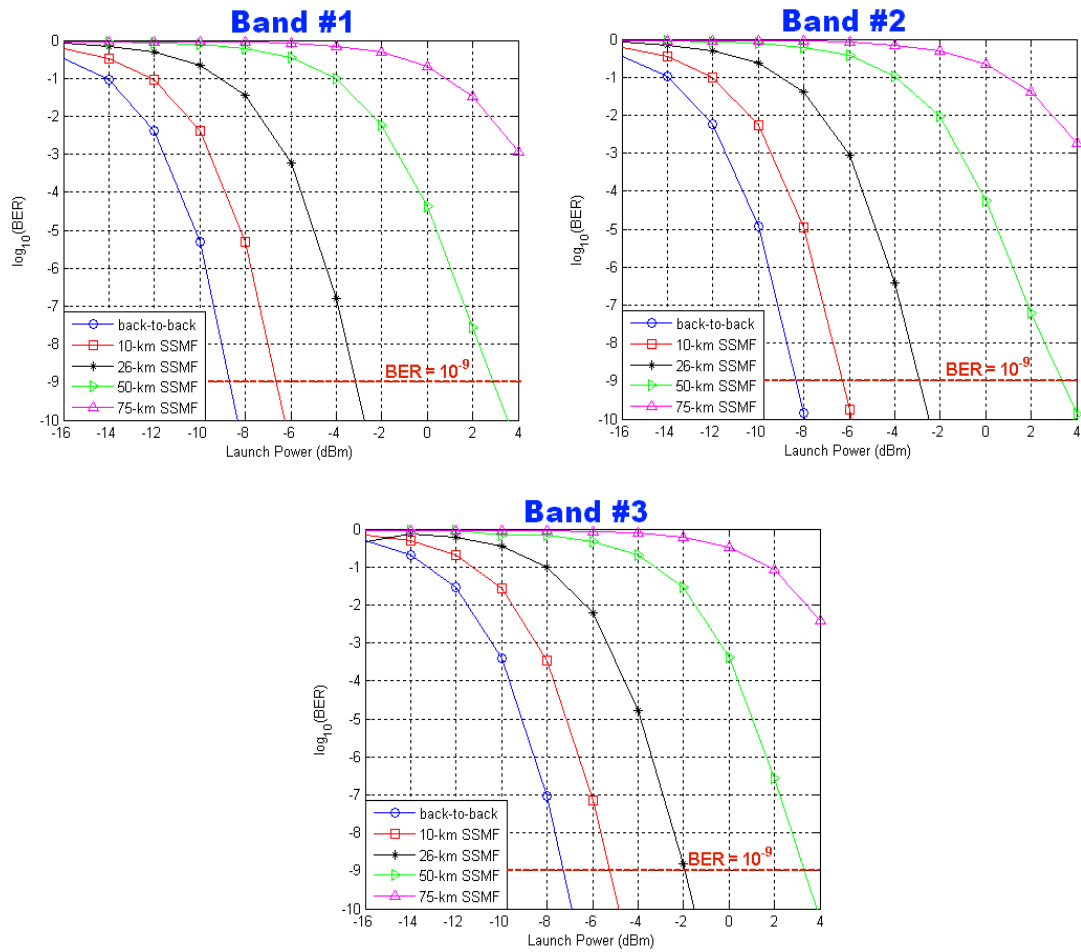


Figure 4.10. BER of the three UWB sub-bands as a function of launch power for different SSMF lengths (simulation).

It can be seen from the results presented in Figure 4.10 that for error-free operation (BER of 10^{-9}); with 4 dBm optical power launched in the fibre, the maximum SSMF reach is 50 km.

The next step is to test the robustness of the system to fibre chromatic dispersion. With the original setups as depicted in Figures 4.1 and 4.3, and with the UWB drive power still fixed at the optimum value of -2 dBm, the length of the fibre is varied from 0 to 40 km. For each fibre length, the attenuation of the VOA is tuned to keep the power input to the photodiode fixed at 1 dBm and the EVM value at the optimum UWB drive power, denoted as EVM_{opt} , is computed.

Figure 4.11 shows a plot of the measured EVM_{opt} vs. fibre length for the three UWB sub-bands for both the simulation and experiment. It can be seen that the simulation and experimental values of EVM_{opt} remain fairly constant with increasing fibre length. This asserts that the MB-OFDM UWB RoF system is robust against fibre chromatic dispersion. The reason behind this is because an OSSB architecture has been used which is resistant to the power fading caused by fibre chromatic dispersion.

Consequently, provided that the length of the delay spread caused by chromatic dispersion is less than the length of the cyclic prefix, the effect of the fibre chromatic dispersion, as demonstrated previously in section 2.7, would be to cause a rotation of each subcarrier's constellation point around the origin. This rotation can be easily reversed by making use of the one-tap equaliser in the OFDM receiver without causing any significant degradation in the value of EVM_{opt} .

Figure 4.12 shows the equalised constellation (experiment) for optimum UWB drive power operation for all subcarriers in sub-band 2 for different fibre lengths, confirming that EVM_{opt} doesn't degrade with increasing fibre length.

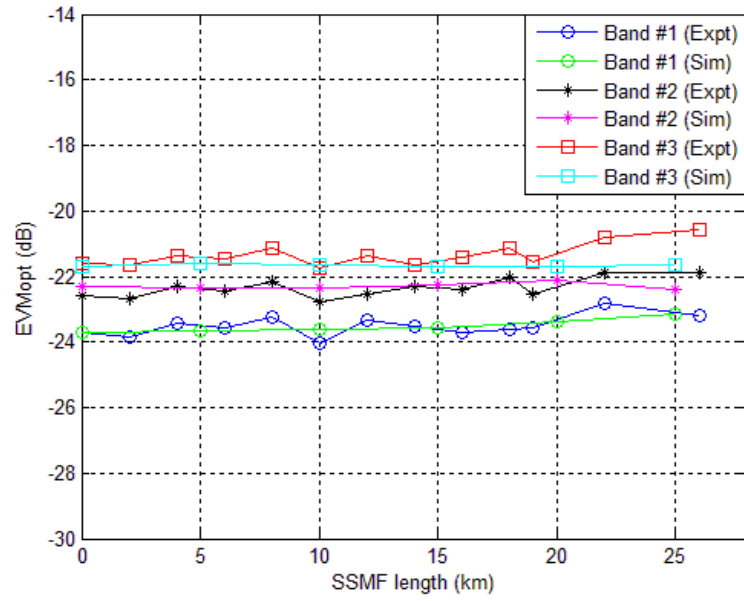


Figure 4.11. EVM_{opt} vs. fibre length for the three UWB sub-bands.

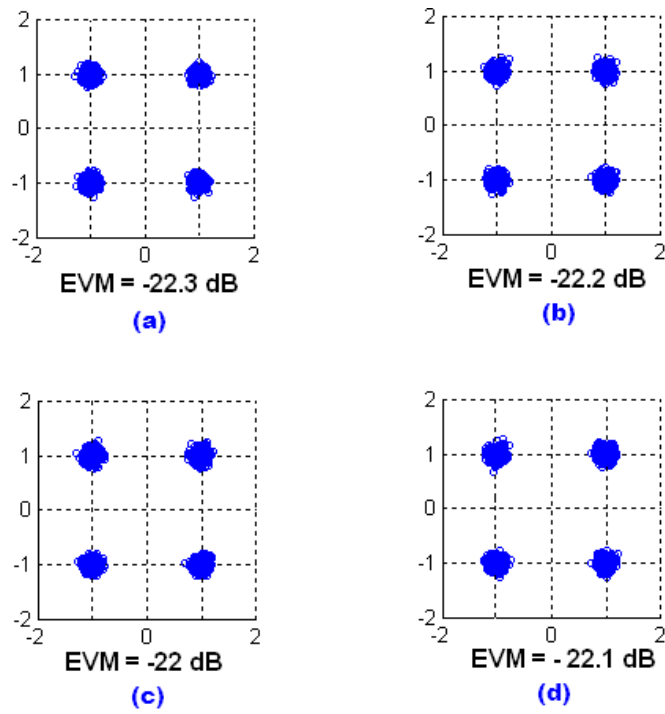


Figure 4.12. Sub-band 2 equalised constellation for different fibre lengths: (a) 2 km. (b) 4 km. (c) 18 km. (d) 22 km.

4.2.3 Impact of received optical power on system performance

To illustrate the effect of the received optical power on system performance, the system is operated with a drive power of -2 dBm to yield EVM_{opt} . The received optical power to the photodetector is then varied by tuning the attenuation of the VOA. Figure 4.13 shows the EVM variation of the three UWB sub-bands with the received optical power for optical back-to-back, 4, 10, 19 and 26 km SSMF transmission for both the simulation and the experiment.

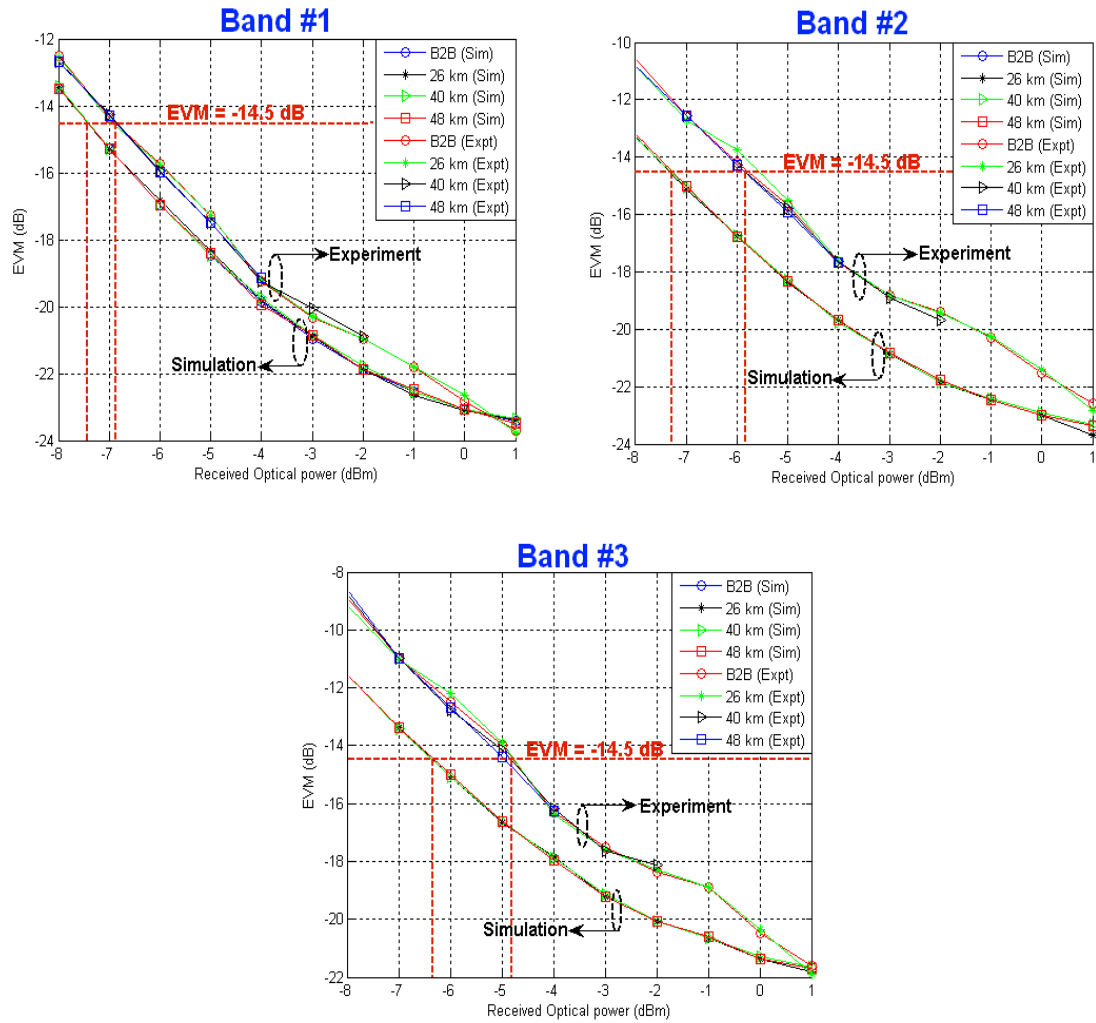


Figure 4.13. EVM of the three UWB sub-bands vs. received optical power.

It is obvious from Figure 4.13 that the EVM improves with increasing received optical power. The EVM is limited by electrical noise at low received power. Increasing the received optical power improves the EVM due to an increase in the received SNR.

According to [22], the total system EVM can be expressed as:

$$EVM^2 = (EVM_0^2) + \frac{1}{SNR} \quad (4.7)$$

where EVM_0 is the EVM induced by phase distortion and SNR is the received signal-to-noise ratio. Since EVM_0 is independent of optical power, it is clear from (4.7) that the EVM improves with increasing received optical power, in agreement with the results shown in Figure 4.13.

Considering an EVM threshold of -14.5 dB as specified by the ECMA-368 standard [89], the optical receiver sensitivities for successfully recovering the three UWB sub-bands are -7.43, -7.28 and -6.35 dBm for sub-bands #1, 2 and 3 respectively for the simulation; and -6.86, -5.82 and -4.81 dBm for sub-bands #1, 2 and 3 respectively for the experiment. Figure 4.13 also shows confirms the system is robust against fibre chromatic dispersion, with hardly any power penalty obtained for the various fibre lengths used.

4.3 Summary

In this chapter, the distribution of ECMA-368 compliant MB-OFDM UWB signals in FTTH networks has been investigated by both experiment and simulation. The impact of various parameters including UWB drive power, RF modulation index of the MZM, fibre distribution and received optical power on the system performance has been demonstrated with the aid of theoretical analysis, simulation

and experimental studies. For the investigations, an OSSB architecture has been utilised and BER and EVM measurements used as the performance metric.

It is shown that the system performance is limited by low SNR at low values of UWB drive power (and RF modulation index) and by the MZM non-linearity at high values of UWB drive power (and RF modulation index). The results of the two-tone intermodulation analysis show that at low values of RF modulation index, the power of the fundamental components is much higher than that of the IMD3 components. Increase in the RF modulation index results in the IMD3 components increasing faster than that of the fundamental. At an optimum value of modulation index (-6.91 dB by analytical approximation and -4.67 dB by simulation), the power of the IMD3 component equals that of the fundamental. For values of modulation index greater than the optimum, the IMD3 distortion dominates and the system performance starts to degrade. The simulations also confirm that at a modulation index of -4.58 dB, the EVM performance of the MB-OFDM UWB RoF system is optimum, showing a good agreement with the simulation results of the two-tone test. Increase in the modulation index beyond -4.58 dB results in system performance degradation.

It has been shown with the aid of simulations that for error-free operation (BER of 10^{-9}); with 4 dBm optical power launched in the fibre, the maximum SSMF reach is 50 km. Also, when the optimum EVM, EVM_{opt} is used, provided the length of the cyclic prefix is greater than the length of the delay spread, transmission over fibre is not limited by fibre chromatic dispersion. This is because an OSSB architecture which is resistant to the power fading caused by chromatic dispersion. In addition, it is found that the EVM performance degrades with reduction in received optical power due to reduction in the received SNR.

For all the tests on the system performance of the UWB RoF system, a good agreement between the simulation and experimental results is obtained.

Chapter 5. MB-OFDM UWB RoF operation in the 60-GHz band

5.1 Introduction

Since the 60-GHz band is wider and less restricted in terms of power limits than the frequency band allocated for UWB, this chapter looks at MB-OFDM UWB operation in the 60-GHz band as an interesting solution for the RoF delivery of multi-Gbit/s signals to end-users in FTTH access networks. This FTTH application scenario was first proposed and demonstrated by M. Beltran, et al. in [125] using a directly-modulated VCSEL.

As stated in section 2.6.3, a couple of international standards such as ECMA-387, IEEE 802.15.3c, WirelessHD and WiGig have been recently launched to support multi-Gbit/s communications in the 60-GHz band. Single-chip solutions based on the WirelessHD standard have already been integrated into consumer electronic products including TVs, laptop and desktop computers, digital cameras, and set-top boxes [99], [126] for uncompressed HD video applications. Likewise, the development of cheap single-chip CMOS prototypes [127] based on the ECMA-387 standard for high data rate UWB operation in the 60-GHz band [100] also presents opportunities for UWB to be introduced in a wide range of products including PC peripherals, consumer electronic products and even in devices with board space restrictions like mobile phones [125].

These ECMA-387 single-chip prototypes have been used in 60-GHz radios for demonstrations showing high-speed file transfer for data and image files as well as 1080i uncompressed video streaming [127]. Consequently, if these single-chip 60-GHz radios are used as transmitters in the access points of a FTTH access network

like that shown in Figure 2.36, multi-Gbit/s UWB signals could be delivered over the common FTTH access network to a variety of UWB-enabled CPEs.

Transition of UWB to the 60-GHz band for such an application scenario also gives an opportunity for the UWB transmission reach to be further extended by increasing the EIRP from -41.3 dBm/MHz to 13 dBm/MHz as permitted in the 60-GHz band [109]. In addition, the uneven frequency response of 60-GHz systems can easily be compensated for by using a simple OFDM one-tap equaliser. These advantages, coupled with the fact that the unlicensed bandwidth available in the 60-GHz band is comparable to the 7.5 GHz UWB bandwidth, make MB-OFDM UWB operation in the 60-GHz band quite an interesting consideration.

This chapter reviews and experimentally demonstrates four techniques for enabling MB-OFDM UWB RoF operation in the 60-GHz band. These techniques are classified in terms of the underlying modulation/detection principles employed, namely IM-DD and optical heterodyne detection (OHD).

The first three techniques fall under the IM-DD category but differ in the way intensity modulation is carried out. In each of these three techniques, the modulating MB-OFDM UWB signal drives a different type of non-linear component – a laser, a MZM and a mixer. We experimentally demonstrate that the system performance of the various techniques is limited by the first major non-linear component encountered by the driving UWB signal. We also illustrate the limitations imposed on the three techniques by fibre distribution.

The fourth technique falls under the OHD category and utilises uncorrelated optical heterodyne mixing of an OSSB UWB signal with another free-running unmodulated laser in a broadband photodiode and envelope detection to achieve reduced overall system complexity by avoiding any analogue frequency/phase-

locking mechanism or high-frequency electro-optic and RF devices. We demonstrate analytically that this technique is robust to laser phase noise. We also demonstrate experimentally the impacts of fibre distribution and wireless transmission on the system performance.

The structure of this chapter is as follows: in section 5.2, the three IM-DD techniques for generating the 60-GHz MB-OFDM UWB signal are introduced and their respective system performances, evaluated experimentally. Section 5.3 compares the three IM-DD techniques in terms of transmission performance, cost and complexity. Section 5.4 introduces the OHD technique, where it is demonstrated analytically that this technique is, in principle, capable of avoiding the laser phase noise effects at baseband. We also experimentally demonstrate, using the OHD technique proposed system, the successful transmission of a 60-GHz MB-OFDM UWB signal over SSMF and a further wireless channel. In section 5.5, we present a novel pre-distortion technique for compensating the MZM non-linearity, and apply this technique in a MB-OFDM UWB system. Finally, the conclusions are drawn in section 5.6.

5.2 60-GHz MB-OFDM UWB generation by IM-DD

In this section, three transmission techniques for generating the 60-GHz MB-OFDM UWB signal based on IM-DD are reviewed and experimentally demonstrated. These three techniques all differ in terms of the first non-linear component that is driven by the MB-OFDM UWB signal and in the way up-conversion to the 60-GHz band is achieved.

The first two techniques are based on optical frequency up-conversion using optical frequency multiplication (OFM). In OFM, high-order optical harmonics are generated at the output of an external modulator (like an MZM) which is driven by a

low RF sinusoidal signal because of the non-linear response of the external modulator. Consequently, mm-wave signals can be generated by the beating of any two high-order optical harmonics and/or the beating of any high-order optical harmonics with the optical carrier in a broadband photodiode as demonstrated in [128] – [135]. Technique #1 utilises a directly-modulated DFB laser for electro-optical conversion, in cascade with a high-bandwidth MZM (used for optical frequency up-conversion). The electrical drive to the MZM is a 15-GHz LO (frequency-multiplied by two). Thus, 60-GHz mm-wave generation is achieved by the beating of the optical harmonics at $f_c + 30$ and $f_c - 30$ GHz at the photodiode, where f_c is the centre emission frequency of the optical carrier. Technique #2 is essentially the same as technique #1, but utilises an externally-modulated, low-bandwidth MZM for electro-optical conversion.

The third technique is based on electrical frequency up-conversion by mixing the MB-OFDM UWB signal with a high RF sinusoidal signal. This technique utilises only a high-bandwidth MZM, externally modulated by the MB-OFDM UWB signal that has been electrically up-converted to 60-GHz. This technique has been previously used to transport multi-Gbit/s OFDM signals at 60 GHz over very short SSMF lengths [136], [137].

The three techniques are illustrated in the high-level diagram shown in Figure 5.1, where it can be seen that there is a different arrangement of devices for each technique. In each technique, the MB-OFDM UWB signal drives a different type of non-linear device - a DFB laser, a MZM and a mixer. It is envisaged that it is the first non-linear component encountered by the driving UWB signal that will dominate the distortion in the RF path. After 60-GHz mm-wave generation, the three techniques all use the same device setup for data delivery, detection and recovery.

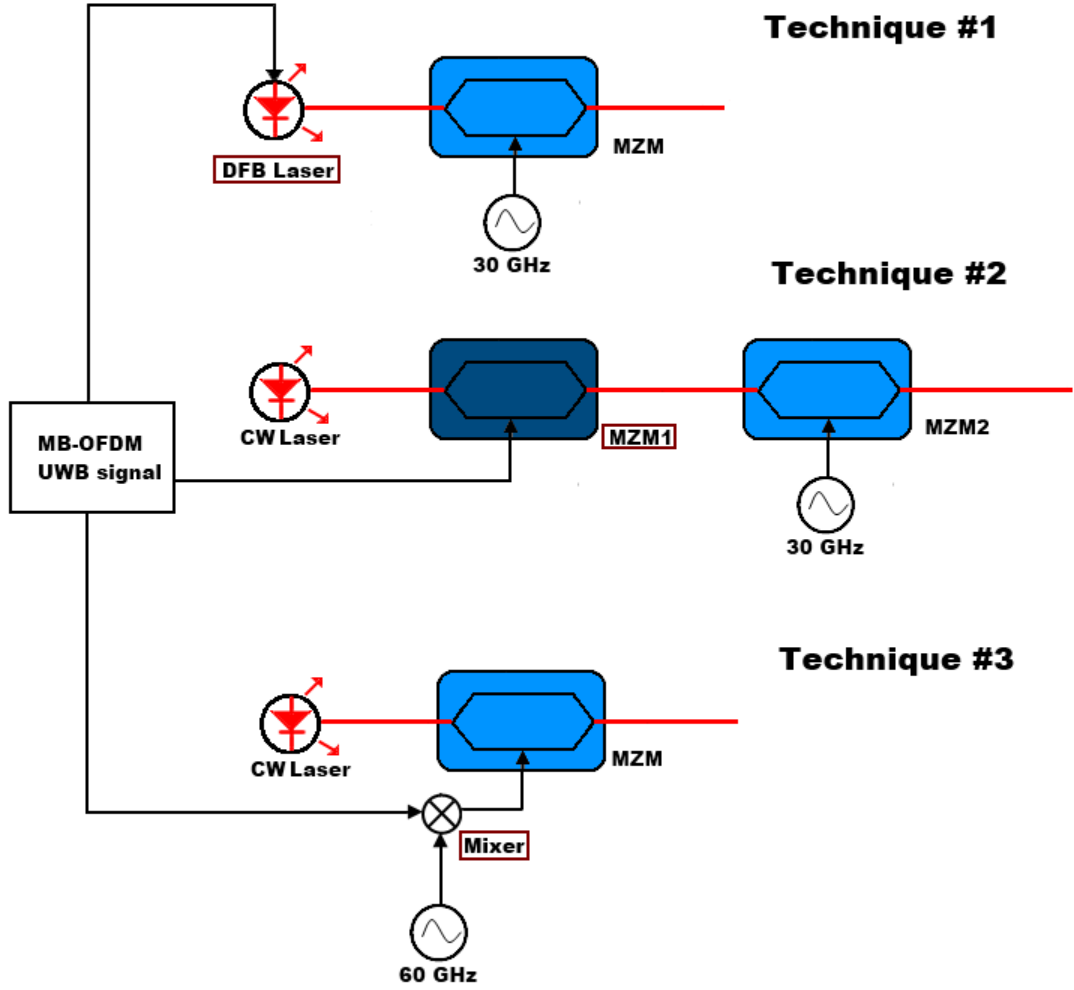


Figure 5.1. High-level diagram showing the three IM-DD techniques for 60-GHz MB-OFDM UWB generation. DFB: Distributed feedback. CW: Continuous Wave. MZM: Mach-Zehnder modulator.

This section begins with a theoretical analysis of mm-wave generation using the three IM-DD transmission techniques. The impact of various parameters including device non-linearity (i.e. laser, MZM and mixer), laser bias current, temperature, LO power, received optical power and chromatic dispersion on the system performance of the three techniques are then investigated experimentally.

It should be noted that the system parameter being investigated is dependent on the devices included in the setup of that particular transmission technique. However, for all the techniques under review, the system performance is evaluated at a bit rate of 3.84 Gbit/s, using EVM measurements as the performance metric.

5.2.1 Technique #1 (DFB laser + MZM)

The first technique for mm-wave generation is shown schematically in Figure 5.2. The first non-linear device encountered by the MB-OFDM UWB signal is a DFB laser. The optical signal modulation is therefore obtained by direct modulation of the current of the DFB laser by the UWB signal at an IF frequency. Ignoring the chirp of the laser, the optical field after the direct modulation can be expressed as [3], [138]:

$$E_{laser}(t) = \left(A_o \sqrt{1 + \alpha \operatorname{Re}(s_B(t) \cdot e^{j\omega_{IF}})} \right) \cdot e^{j\omega_o t} \quad (5.1)$$

$$m \equiv \alpha \sqrt{\sum_{k=-\frac{N_{sc}}{2}+1}^{\frac{N_{sc}}{2}} |c_k|^2} \quad (5.2)$$

where A_o is the instantaneous power of the optical MB-OFDM UWB signal; α is a scaling constant to set an appropriate optical modulation index m to minimise the clipping noise [3]; $s_B(t)$ is the baseband OFDM signal as given in (3.4); ω_{IF} is the angular IF frequency for up-converting the baseband OFDM signal to passband; ω_o is the angular centre emission frequency of the DFB laser; and c_k is the transmitted information symbol for the k th OFDM subcarrier.

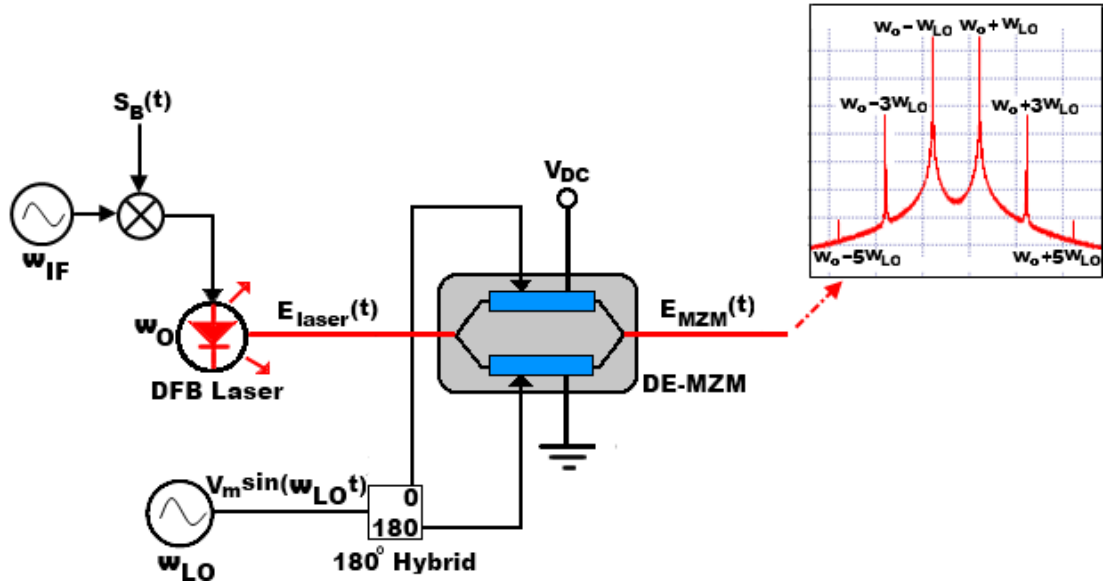


Figure 5.2. Schematic layout of technique #1. DFB: Distributed feedback. DE-MZM: Dual-electrode Mach-Zehnder modulator. Inset: optical spectrum at the output of the DE-MZM.

The optical MB-OFDM UWB signal at the output of the DFB laser serves as the optical source to a DE-MZM biased at its null-point to generate a DSB-SC signal. An RF sinusoid with amplitude V_M and angular frequency of ω_{LO} is applied to a 180° electrical hybrid. It is important to note that ω_{LO} is half the desired mm-wave frequency of operation.

The two outputs of the 180° electrical hybrid directly drive the two electrodes of the DE-MZM. A D.C. bias, V_{DC} is applied to one of the DE-MZM electrodes while the other electrode is grounded.

Consequently, the drive voltages can be expressed as:

$$V_{mod1}(t) = V_M \sin(\omega_{LO} t) + V_{DC} \quad (5.3)$$

$$V_{mod2}(t) = V_M \sin(\omega_{LO} t + \pi) \quad (5.4)$$

If the insertion loss of the DE-MZM is neglected, and the extinction ratio is assumed to be infinite, utilising (2.12), the optical field at the DE-MZM output can be expressed as:

$$E_{MZM}(t) = \frac{E_{laser}(t)}{2} \left\{ e^{j\frac{\pi}{V_{\pi}}V_M \sin(\omega_{LO}t + \pi)} + e^{j\frac{\pi}{V_{\pi}}V_M \sin(\omega_{LO}t)} \cdot e^{j\frac{\pi}{V_{\pi}}V_{DC}} \right\} \quad (5.5)$$

$$= \frac{E_B(t)}{2} e^{j\omega_o t} \left\{ e^{j\frac{\pi}{V_{\pi}}V_M \sin(\omega_{LO}t + \pi)} + e^{j\frac{\pi}{V_{\pi}}V_M \sin(\omega_{LO}t)} \cdot e^{j\frac{\pi}{V_{\pi}}V_{DC}} \right\} \quad (5.6)$$

where

$$E_B(t) = \left(A_o \sqrt{(1 + \alpha \operatorname{Re}(s_B(t) \cdot e^{j\omega_{IF}}))} \right) \quad (5.7)$$

To achieve a null-point bias, $V_{DC} = V_{\pi}$. Consequently, (5.6) reduces to:

$$E_{MZM}(t) = \frac{E_B(t)}{2} e^{j\omega_o t} \left\{ e^{jm_{LO} \sin(\omega_{LO}t + \pi)} - e^{jm_{LO} \sin(\omega_{LO}t)} \right\} \quad (5.8)$$

where m_{LO} is the RF modulation index, given by:

$$m_{LO} = \frac{\pi V_M}{V_{\pi}} \quad (5.9)$$

Applying the Jacobi-Anger expansion [139]-[141],

$$e^{jx \sin \theta} = \sum_{n=-\infty}^{\infty} J_n(x) e^{jn\theta} \quad (5.10)$$

where $J_n(x)$ is the Bessel function of the first kind of order n . Applying (5.10) in (5.8), the optical field at the output of the DE-MZM becomes:

$$E_{MZM}(t) = \frac{E_B(t)}{2} e^{j\omega_o t} \left\{ \sum_{n=-\infty}^{\infty} J_n(m_{LO}) e^{j(n\omega_{LO}t + n\pi)} - \sum_{n=-\infty}^{\infty} J_n(m_{LO}) e^{j(n\omega_{LO}t)} \right\} \quad (5.11)$$

$$= \frac{E_B(t)}{2} e^{j\omega_o t} \left\{ \sum_{n=-\infty}^{\infty} J_n(m_{LO}) e^{j(n\omega_{LO}t + \frac{n\pi}{2})} \left(e^{j(\frac{n\pi}{2})} - e^{-j(\frac{n\pi}{2})} \right) \right\} \quad (5.12)$$

$$= jE_B(t) \left\{ \sum_{n=-\infty}^{\infty} J_n(m_{LO}) \sin\left(\frac{n\pi}{2}\right) e^{j[(\omega_o + n\omega_{LO})t + \frac{n\pi}{2}]} \right\} \quad (5.13)$$

For $0 < m_{LO} < \pi$, the Bessel function $J_n(m_{LO})$ for $n \geq 1$ decreases with increasing values of n . For example, $J_1\left(\frac{\pi}{2}\right)$, $J_3\left(\frac{\pi}{2}\right)$, $J_5\left(\frac{\pi}{2}\right)$, and $J_7\left(\frac{\pi}{2}\right)$ are 0.5668, 0.0690, 0.0022, and 3.3851×10^{-5} , respectively. Therefore, the optical sidebands

with Bessel functions higher than $J_5(m_{LO})$ can be ignored. Consequently, (5.13) reduces to

$$\begin{aligned} E_{MZM}(t) = E_B(t) \{ & -J_1(m_{LO}) e^{j(\omega_o + \omega_{LO})t} + J_1(m_{LO}) e^{j(\omega_o - \omega_{LO})t} \\ & -J_3(m_{LO}) e^{j(\omega_o + 3\omega_{LO})t} + J_3(m_{LO}) e^{j(\omega_o - 3\omega_{LO})t} \\ & -J_5(m_{LO}) e^{j(\omega_o + 5\omega_{LO})t} + J_5(m_{LO}) e^{j(\omega_o - 5\omega_{LO})t} \} \end{aligned} \quad (5.14)$$

Equation (5.14) shows that the optical spectrum at the output of the DE-MZM is carrier-suppressed, and all the even-order sidebands are eliminated, leaving only the odd-order optical sidebands as shown in the inset of Figure 5.2. The beating of the first-order sidebands at $(\omega_o + \omega_{LO})$ and $(\omega_o - \omega_{LO})$ with themselves on a square-law photodiode would result in frequency doubling, producing a strong RF signal at $2\omega_{LO}$.

Figure 5.3 shows the experimental setup for this technique employing a directly-modulated HP LSC2500 DFB laser. The modulating MB-OFDM UWB signal, with a frequency span from 1 GHz to 2.584 GHz as shown in Figure 5.3 (a), comprises three 16-QAM sub-bands, each with a bandwidth of 528 MHz.

Each sub-band has 128 subcarriers, of which, 100 are data tones, 12 are pilots for carrier and phase tracking, 10 are guard tones and the remaining 6 are null tones. An FFT size of 128 and a cyclic prefix length of 32 samples per band are used for each sub-band. Consequently, the symbol duration of each band is 312.5 ns, resulting in a bit rate per band of 1.28 Gbit/s and an aggregate bit rate of 3.84 Gbit/s.

The MB-OFDM UWB system parameters used in all the experiments in this chapter are listed in Table 5.1.

System parameter (per UWB sub-band)	Value
Subcarrier modulation format	16-QAM
FFT size	128
OFDM bandwidth	528 MHz
Number of data-carrying subcarriers	100
OFDM subcarrier frequency spacing	23.44 MHz
Information duration	242.4 ns
Cyclic prefix length (in samples)	32 (25%)
Cyclic prefix duration	60.6 ns
Guard interval duration	9.5 ns
OFDM symbol duration	312.5 ns
Gross bit rate	1.28 Gbit/s

Table 5.1. 60-GHz MB-OFDM UWB system parameters.

The time-domain samples of the MATLAB-generated MB-OFDM UWB signal are then loaded into a Tektronix AWG7122B AWG operating at a sampling rate of 10.8 GS/s. The real-valued MB-OFDM UWB signal is amplified by a 19-dB gain, SHF 600 APP amplifier and passed through a Picosecond 7.5-GHz LPF to remove the high frequency aliasing products formed from the DAC process at the AWG.

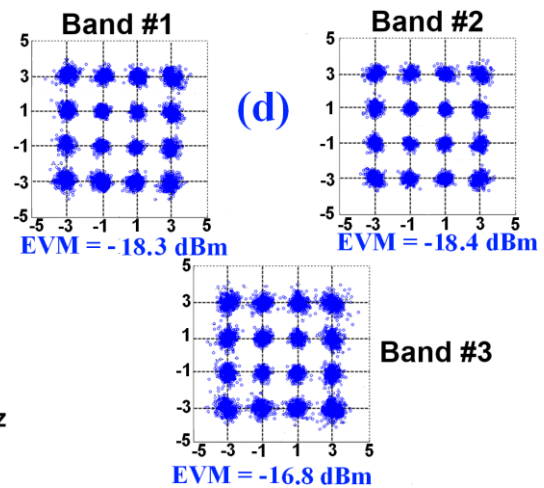
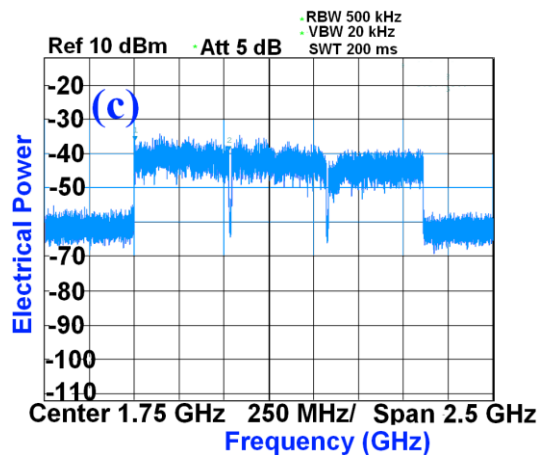
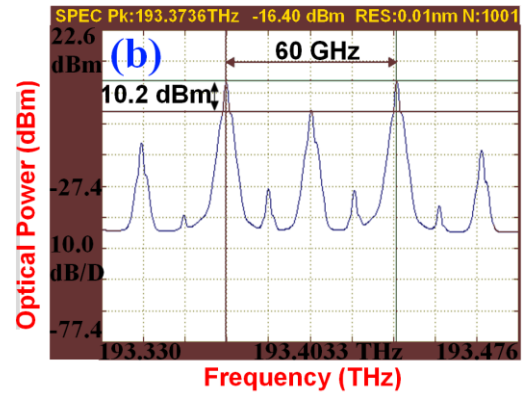
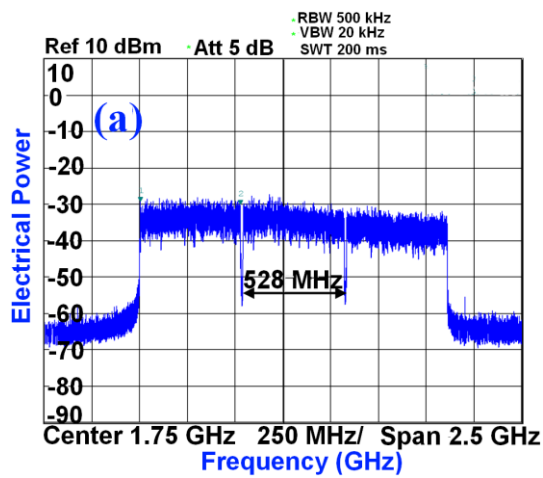
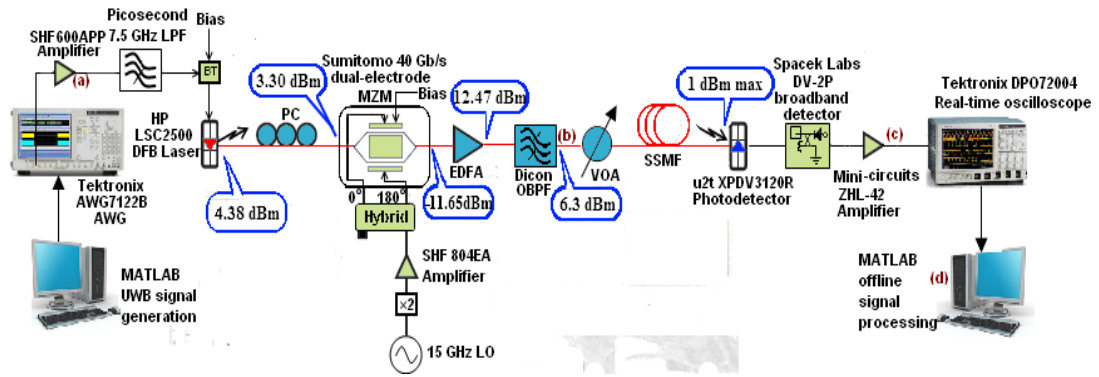


Figure 5.3. Experimental setup for technique #1. AWG: Arbitrary Waveform Generator. LPF: Low-Pass Filter. BT: Bias Tee. PC: Polarisation Controller. MZM: Mach-Zehnder Modulator. LO: Local Oscillator. EDFA: Erbium-Doped Fibre Amplifier. OBPF: Optical Band-Pass Filter. VOA: Variable Optical Attenuator. SSMF: Standard Single Mode Fibre. Insets (a) – (c): Electrical and optical spectra at corresponding points in the experimental setup. Inset (d): Equalised back-to-back constellation diagrams at 1 dBm received optical power.

The low-pass filtered MB-OFDM UWB signal is then used to directly modulate the DFB laser. Optical frequency up-conversion to the 60-GHz band is achieved by using the modulated optical signal as the optical source to a Sumitomo 40-Gbit/s DE-MZM. The input optical power to the DE-MZM is 3.30 dBm. The DE-MZM has an insertion loss of 6 dB and an extinction ratio of 20 dB. The DE-MZM D.C. bias is set to the half-wave switching voltage, V_{π} of -1 V to generate an optical DSB-SC signal.

A 15-GHz LO signal, frequency multiplied by two, is amplified by an SHF 804 EA amplifier providing 20 dB gain and applied to a 180° hybrid connected to the arms of the DE-MZM. The optical DSB-SC signal is further amplified by an EDFA to compensate for the insertion loss of all optical components and then a DiCon tunable OBPF with bandwidth of 0.8 nm is used for suppression of the ASE noise. The filtered optical DSB-SC signal is shown in Figure 5.3 (b), with the first-order sidebands spaced 60 GHz apart from themselves.

The optical signal is then sent through various lengths of SSMF with a loss due to attenuation of 0.2 dB/km and D of 16ps/nm/km. A VOA is used to maintain a maximum of 1 dBm input to a u²t Photonics, XPDV3120R photodetector with 70 GHz bandwidth and slope efficiency of 0.6 A/W. After photodetection, down-conversion straight to baseband is achieved using a Spacek Labs, DV-2P waveguide broadband detector. The down-converted electrical MB-OFDM UWB signal is amplified by a 30-dB gain, Mini-Circuits ZHL-42 amplifier (Figure 5.3 (c)).

A Tektronix DPO 72004, 20-GHz, 50-GS/s real-time digital sampling oscilloscope is then used to capture the signal. The oscilloscope is operated at a sampling rate of 25 GS/s and the baseband digital signal processing is performed offline in MALAB. Figure 5.3 (d) shows the equalized optical back-to-back 16-QAM

constellation diagrams with their corresponding EVM values at a received optical power of 1 dBm.

In the subsequent sub-subsections, using the setup as shown in Figure 5.3, the impacts of the various parameters such as laser non-linearity, laser bias current, temperature, LO power, chromatic dispersion and received optical power at the photodetector on the system performance will be investigated.

5.2.1.1 Impact of laser non-linearity

For the investigation into the impact of the DFB laser non-linearity, electrical attenuators are used to vary the amplitude of the driving UWB signal to the DFB laser for optical back-to-back transmission. For each value of driving amplitude, the corresponding drive power is measured and the VOA is adjusted to keep the input optical power to the photodetector fixed at 1 dBm.

Figure 5.4 shows the variation of the EVM for the three bands with the UWB drive power for laser bias currents of 40, 60 and 80 mA. It is evident that the EVM first reduces with increasing values of drive power because the received SNR increases. At high power levels, the EVM starts to degrade due to clipping of the high amplitude peaks in the lower half of the UWB signal because of the non-linearity of the laser characteristics. The lower the bias current, the sooner the UWB signal encounters the laser non-linearity and the lower the value of the drive power at which the minimum EVM is obtained (P_{opt}). P_{opt} is -6.2, -2.2 and 3.4 dBm for bias currents of 40, 60 and 80 mA respectively.

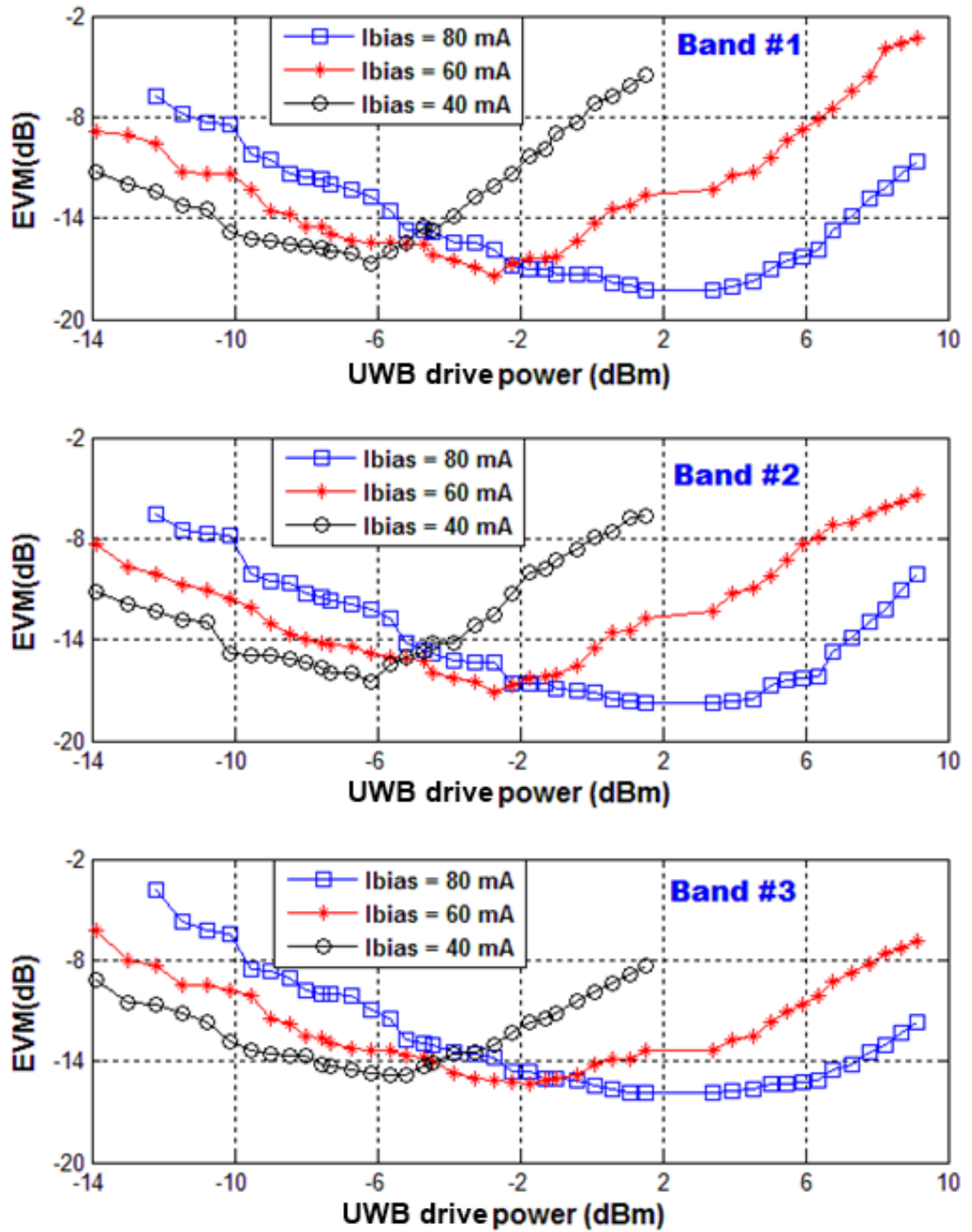


Figure 5.4. EVM vs. UWB drive power for different bias currents for the three UWB sub-bands.

5.2.1.2 Impact of laser bias current

We keep the laser temperature fixed at 20°C and operate the system with the LO power and UWB drive power fixed at 24 dBm and 3.4 dBm respectively. Next, the bias current is varied from 35 to 110 mA. Figure 5.5 shows that the EVM for all

the bands improves as the bias is increased. This is because at low bias currents close to the laser's threshold current of 16 mA, the non-linearity of the laser limits the system performance since there is no stimulated light output below the threshold current. Increase in the bias current results in operation in the linear portion of the laser's L-I characteristics, implying an increase in the laser output power and consequently, EVM improvement.

At bias currents greater than 80 mA, the EVM performance begins to degrade due to saturation of the photodetector. Hence, even with operation in the laser's linear regime, the laser bias current should not be increased to the point where photodetector saturation occurs.

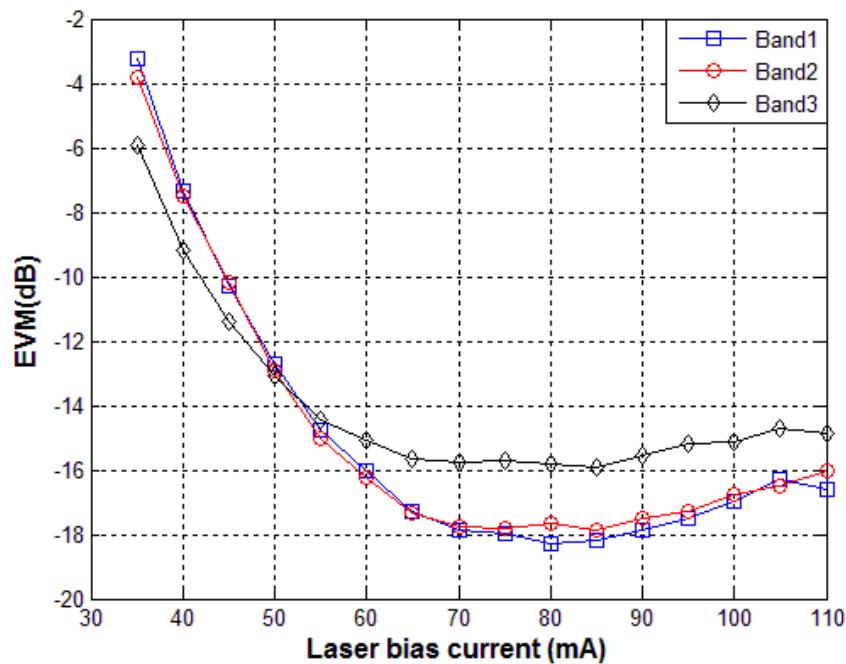


Figure 5.5. EVM vs. laser bias current for the three UWB sub-bands.

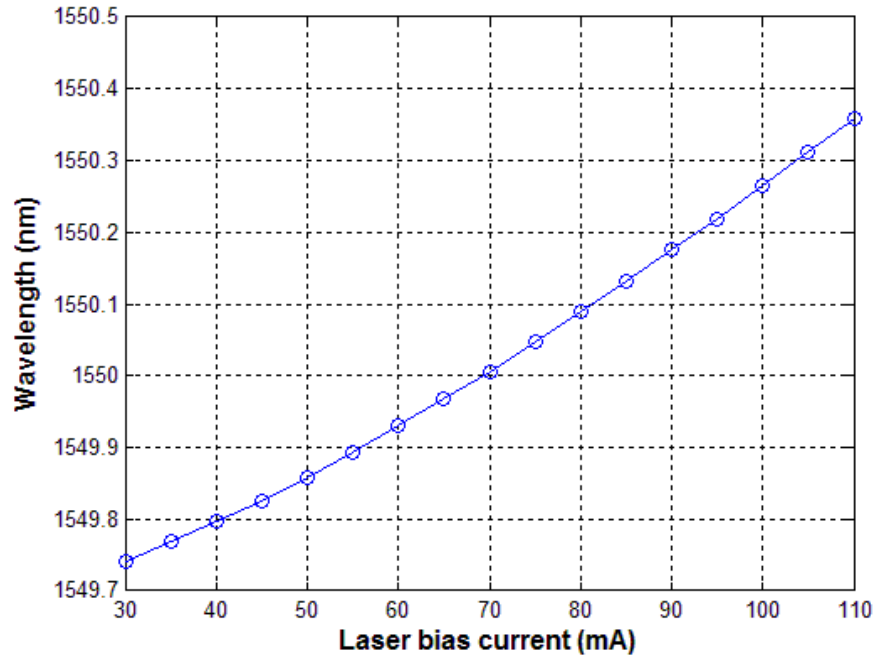


Figure 5.6. DFB laser wavelength drift with bias current.

Wavelength drift also occurs with laser bias current changes as shown in Figure 5.6 (from 1549.75 nm at 30 mA to 1550.35 nm at 110 mA). Since the bandwidth of the OBPF is 0.8 nm, this drift would necessitate continuous OBPF tuning. To circumvent this, the optical network can be made reconfigurable as proposed in [142] by using EVM fluctuations of OFDM edge tones to detect the wavelength drift to allow for automatic wavelength reassignment.

5.2.1.3 *Impact of operating temperature*

For this investigation, the UWB drive power and laser bias current are fixed at 3.4 dBm and 80 mA respectively to yield the minimum EVM as shown in Figures 5.4 and 5.5. The operating temperature is then varied from 20 to 55 °C and the EVM measured for each temperature.

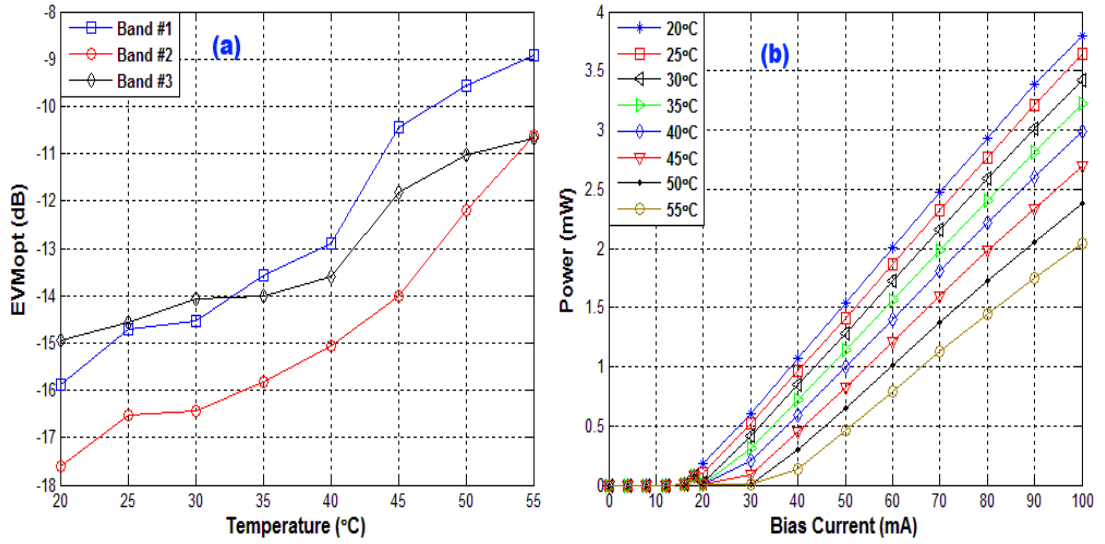


Figure 5.7. (a) EVM degradation with increase in operating temperature (b) laser output optical power vs. bias current for different operating temperatures.

Figure 5.7 (a) shows that the EVM degrades with increase in temperature. This is because as seen in Figure 5.7 (b), for a fixed bias current, as the temperature increases, the output power of the laser decreases (for a bias current of 80 mA, the laser output power decreases from 3 to 1.5 mW as the temperature increases from 20 to 55 °C). This decrease in output power results in a reduction in the SNR and consequently, an increase in the EVM.

5.2.1.4 Impact of LO power

With the same optimum bias and drive conditions as in the preceding subsection and with the received optical power kept constant at 1 dBm, the LO power is varied to see its impact on the EVM performance. Figure 5.8 shows the plot of the EVM vs. the LO power for optical back-to-back transmission, with the EVM improving with increasing LO power. For values of LO power greater than 24 dBm however, the EVM then starts to degrade.

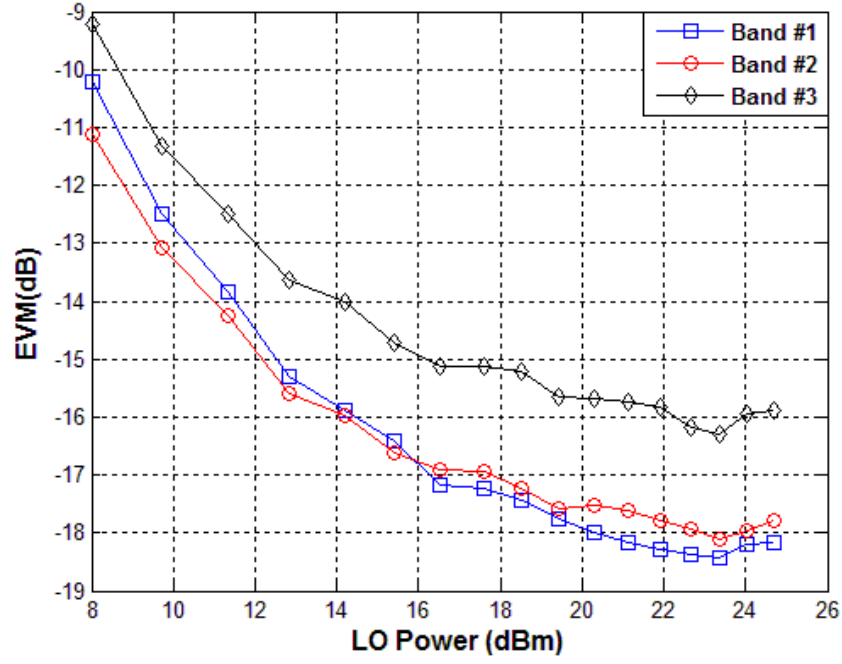


Figure 5.8. EVM vs. LO power for the three UWB sub-bands.

This trend can easily be explained by referring back to (5.14), where it can be inferred that the amplitudes of the first-order sidebands are proportional to the value of the RF modulation index, m_{LO} which in turn is dependent on the LO power. Since these sidebands beat at the photodetector to yield the UWB signal in the 60-GHz band, the higher the LO power, the higher their amplitudes and the better the received SNR and EVM. For $0 < m_{LO} < \left(\frac{\pi}{2}\right)$, the Bessel function $J_1(m_{LO})$ increases with increasing values of m_{LO} . However, for values of $m_{LO} > \left(\frac{\pi}{2}\right)$, $J_1(m_{LO})$ starts decreasing as m_{LO} increases. For example, $J_1\left(\frac{\pi}{4}\right)$, $J_1\left(\frac{\pi}{2}\right)$, and $J_1(\pi)$ are 0.3632, 0.5668, and 0.2846, respectively. This is why the EVM first improves with increasing LO power up to a point, before it starts to degrade.

5.2.1.5 Impacts of received optical power and fibre transmission

The values of the laser bias, drive, and LO power are fixed at 80 mA, 3.4 dBm and 24 dBm respectively to yield the minimum EVM. Using sub-band #2 as the

test band, the attenuation of the VOA is varied to enable the received optical power to be varied considering back-to-back, 5, 12 and 16 km SSMF transmissions. Figure 5.9 shows the EVM improving with an increase in the received optical power because of an increase in the received SNR. The optical receiver sensitivity at an EVM of -17 dB is -4.2 dBm for optical back-to-back transmission. The receiver sensitivity worsens at longer fibre spans due to progressive EVM degradation induced by chromatic dispersion.

In order to explain the cause of the system's susceptibility to degradation caused by the fibre chromatic dispersion, let us consider the inset of Figure 5.10 which shows a magnified view of the optical spectrum at the output of the DE-MZM as illustrated previously in the inset of Figure 5.2. As can be seen from the inset of Figure 5.10, each optical sideband is in itself an optical DSB-C signal, with upper wavelength sidebands (USB1, USB2) and lower wavelength sidebands (LSB1, LSB2).

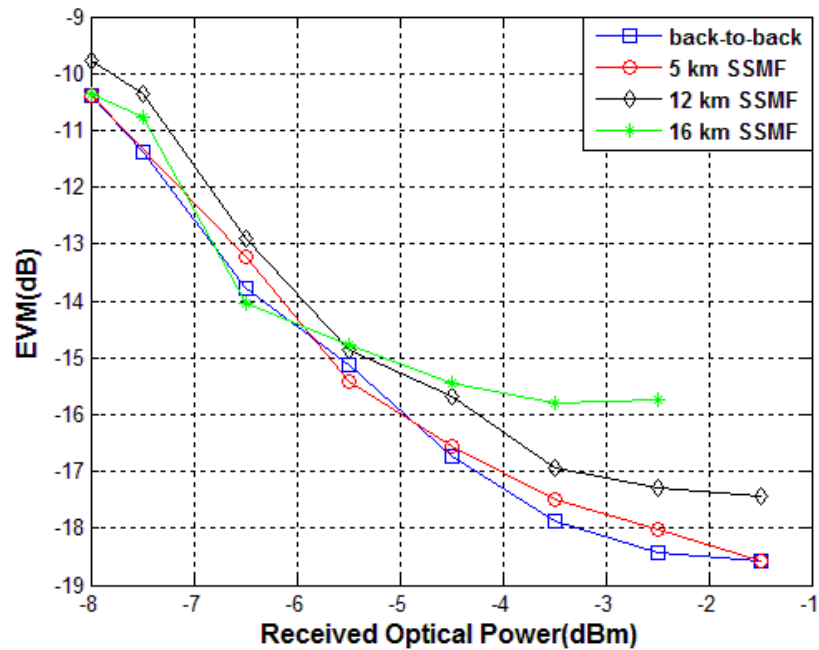


Figure 5.9. Sub-band #2 EVM vs. received optical power for different SSMF lengths.

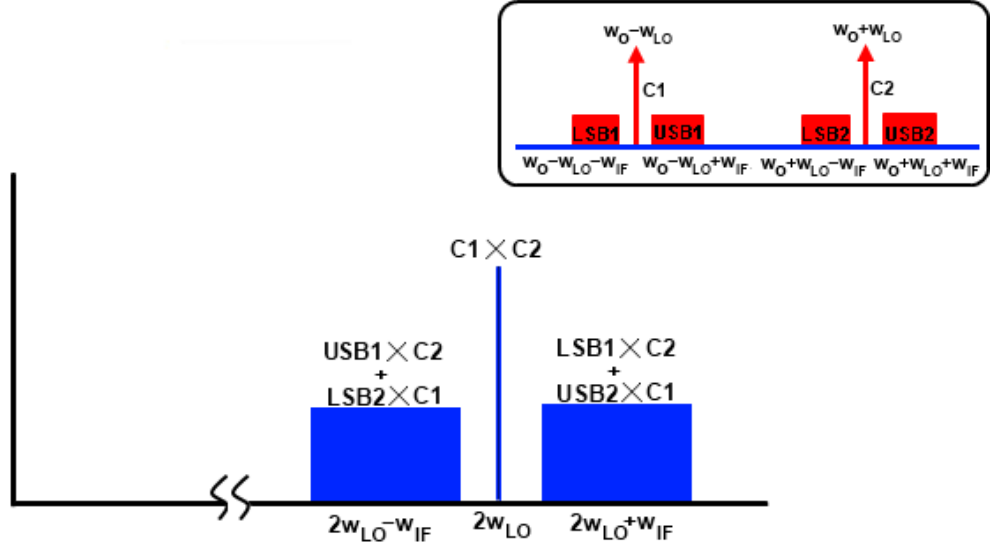


Figure 5.10. Photodetected spectrum for technique #1. Inset: Magnified view of the optical spectrum at the output of the DE-MZM, considering only the first-order optical sidebands.

Considering only the frequency components of interest to us after square-law photodetection (i.e. those around $2\omega_{LO}$), we can clearly see from Figure 5.10 that the frequency terms at $(2\omega_{LO} + \omega_{IF})$ and $(2\omega_{LO} - \omega_{IF})$ are obtained from the superimposition of two beating terms $(LSB1 \times C2) \& (USB2 \times C1)$ and $(USB1 \times C2) \& (LSB2 \times C1)$, respectively.

Consequently, the generated mm-wave is susceptible to power fading from chromatic dispersion. Improving the chromatic dispersion of this system would necessitate very precise optical filtering to remove USB1 and/or USB2; or LSB1 and/or LSB2, which would require precise wavelength control of both the filter and the source.

Figure 5.11 shows the down-converted UWB signal at point (c) in Figure 5.3 for optical back-to-back and 16-km SSMF transmission where it can be confirmed that there is progressive signal deterioration, and hence EVM degradation at longer fibre lengths due to dispersion-induced fading.

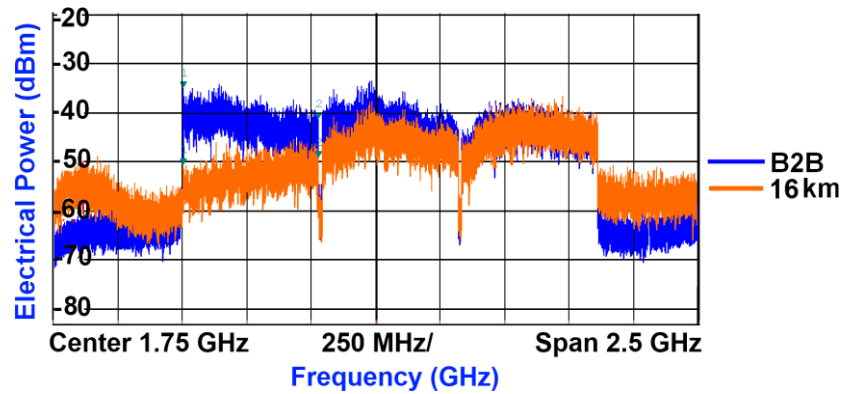


Figure 5.11. Down-converted UWB signal spectra, showing signal deterioration at longer SSMF lengths.

The nature of this EVM degradation is illustrated in Figure 5.12 which shows an OptSim™ simulation of the received EVM of sub-band #2 at 1 dBm received optical power for SSMF spans ranging from 0 to 20 km. An apparent “fading cycle” of 16 km is observed. This trend of EVM degradation is quite similar to the power degradation when an un-modulated RF signal at 1.75 GHz is transmitted instead of the UWB signal. In Figure 5.12, the RF power degradation is computed to be the difference between the measured RF power at the end of the fibre span and the measured RF power at 0 km.

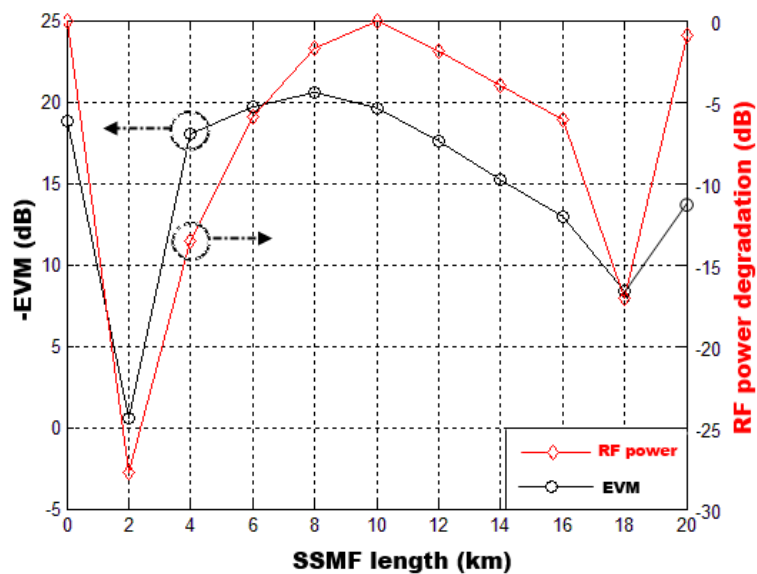


Figure 5.12. Simulation of EVM degradation of sub-band#2 and RF power degradation of a 1.75 GHz signal with increasing fibre lengths.

5.2.2 Technique #2 (Cascaded MZMs)

This technique is quite similar to the technique presented in section 5.2.1, the difference being that the MB-OFDM UWB signal drives a low-bandwidth DE-MZM (DE-MZM1) as opposed to the direct modulation of technique #1. Using external modulation with DE-MZM1 allows an OSSB signal to be easily generated for better robustness to chromatic dispersion which couldn't be achieved with technique #1. In a similar manner as in technique #1, a high-bandwidth DE-MZM (DE-MZM2) is used for optical up-conversion of the MB-OFDM UWB signal to the 60-GHz band. The schematic for this technique is shown in Figure 5.13.

A lightwave from a laser operating in continuous wave mode serves as the optical source to DE-MZM1. The MB-OFDM UWB signal at an IF frequency is passed through a 90° electrical hybrid, and the outputs of the hybrid are used to drive the two electrodes of DE-MZM1 which is biased at its quadrature point to yield an OSSB signal.

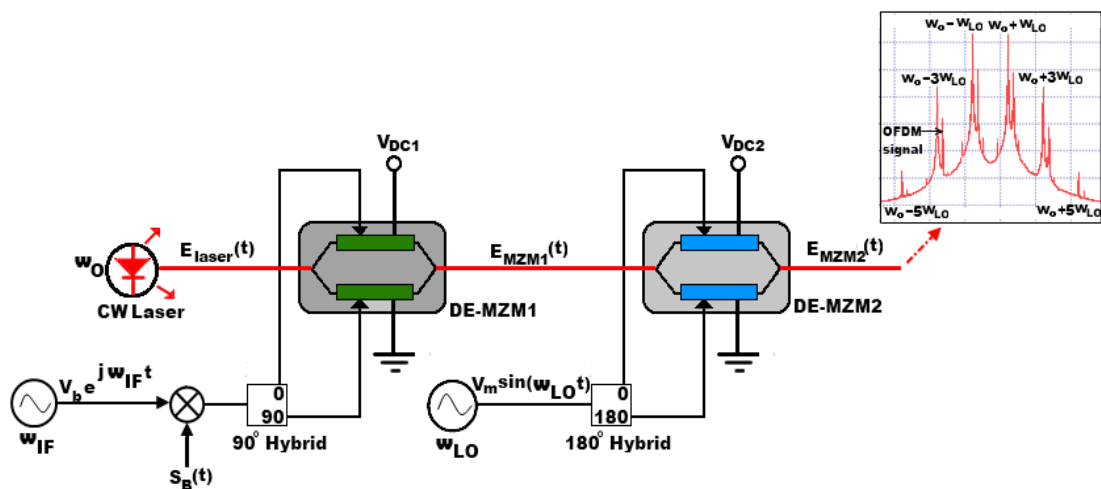


Figure 5.13. Schematic layout of technique #2. CW: Continuous wave.

A D.C bias, V_{DC1} is applied to the top electrode while the bottom electrode is grounded. In this case, the drive voltages applied to DE-MZM1 can be expressed as:

$$V_{mod1}(t) = \text{Re}\{s_B(t).V_b e^{j\omega_{IF}t}\} + V_{DC1} \quad (5.15)$$

$$V_{mod2}(t) = \text{Re}\{s_B(t).V_b e^{j(\omega_{IF}t + \frac{\pi}{2})}\} \quad (5.16)$$

In this analysis, the insertion losses of both DE-MZM1 and DE-MZM2 are ignored. Also, the extinction ratios of both MZMs are assumed to be infinite. Consequently, from (2.12), the optical field at the output of DE-MZM1 can be expressed as:

$$E_{MZM1}(t) = \frac{E_{laser}(t)}{2} \left\{ e^{j\frac{\pi}{V_{\pi1}} \text{Re}\{s_B(t).V_b e^{j(\omega_{IF}t + \frac{\pi}{2})}\}} + e^{j\frac{\pi}{V_{\pi1}} \text{Re}\{s_B(t).V_b e^{j\omega_{IF}t}\}} \cdot e^{j\frac{\pi}{V_{\pi1}} V_{DC1}} \right\} \quad (5.17)$$

$$E_{laser}(t) = (\sqrt{2P}).e^{j\omega_o t} \quad (5.18)$$

where P is the optical power of the CW laser, V_b is the amplitude of the RF sinusoid used to upconvert the MB-OFDM UWB signal to an IF frequency, and all other constants are as defined previously in section 5.2.1.

For a quadrature-point bias, $V_{DC1} = \frac{V_{\pi1}}{2}$. Making use of this, and substituting (5.18) in (5.17), and the optical field at the output of DE-MZM1 can be written as:

$$E_{MZM1}(t) = \left(\sqrt{\frac{P}{2}} \right) e^{j\omega_o t} \left\{ e^{jm_{LO1} \text{Re}\{s_B(t)e^{j(\omega_{IF}t + \frac{\pi}{2})}\}} + j e^{jm_{LO1} \text{Re}\{s_B(t)e^{j\omega_{IF}t}\}} \right\} \quad (5.19)$$

where m_{LO1} is the RF modulation index of DE-MZM1, given by:

$$m_{LO1} = \frac{\pi V_b}{V_{\pi1}} \quad (5.20)$$

$$E_{MZM1}(t) = \left(\sqrt{\frac{P}{2}} \right) e^{j\omega_o t} \{s_1(t)\} \quad (5.21)$$

where

$$s_1(t) = e^{jm_{LO1}.Re\{s_B(t)e^{j(\omega_{IF}t+\frac{\pi}{2})}\}} + je^{jm_{LO1}.Re\{s_B(t)e^{j\omega_{IF}t}\}} \quad (5.22)$$

$$= e^{jm_{LO1}\left(\sum_{k=-\frac{N}{2}+1}^{\frac{N}{2}} |c_k| \cos([\omega_{IF}+\omega_{f_k}]t+\frac{\pi}{2})\right)} + je^{jm_{LO1}\left(\sum_{k=-\frac{N}{2}+1}^{\frac{N}{2}} |c_k| \cos([\omega_{IF}+\omega_{f_k}]t)\right)} \quad (5.23)$$

The optical signal at the output of DE-MZM1 serves as the optical source to DE-MZM2 which is biased at its null-point to generate a DSB-SC signal. An RF sinusoid with amplitude V_M and angular frequency of ω_{LO} is applied to a 180° electrical hybrid. The two outputs of the 180° electrical hybrid directly drive the two electrodes of DE-MZM2. A D.C. bias, V_{DC2} is applied to one of the electrodes of DE-MZM2 while the other electrode is grounded.

In a similar vein as in technique #1, the drive voltages to DE-MZM2 can be expressed as:

$$V_{mod1}(t) = V_M \sin(\omega_{LO}t) + V_{DC2} \quad (5.24)$$

$$V_{mod2}(t) = V_M \sin(\omega_{LO}t + \pi) \quad (5.25)$$

The optical field at the output of DE-MZM2 can be expressed as:

$$E_{MZM2}(t) = \frac{E_{MZM1}(t)}{2} \left\{ e^{j\frac{\pi}{V_{\pi2}}V_M \sin(\omega_{LO}t+\pi)} + e^{j\frac{\pi}{V_{\pi2}}V_M \sin(\omega_{LO}t)} \cdot e^{j\frac{\pi}{V_{\pi2}}V_{DC2}} \right\} \quad (5.26)$$

$$= \left(\sqrt{\frac{P}{2}} \right) \cdot \left(\frac{s_1(t)}{2} \right) e^{j\omega_o t} \{ e^{jm_{LO2} \sin(\omega_{LO}t+\pi)} - e^{jm_{LO2} \sin(\omega_{LO}t)} \} \quad (5.27)$$

where m_{LO2} is the RF modulation index of DE-MZM2, given by:

$$m_{LO2} = \frac{\pi V_M}{V_{\pi2}} \quad (5.28)$$

Substituting (5.28) and the Jacobi-Anger expansion of (5.10) in (5.27), we have:

$$E_{MZM2}(t) = j \left(\sqrt{\frac{P}{2}} \right) s_1(t) \cdot \left\{ \sum_{n=-\infty}^{\infty} J_n(m_{LO2}) \cdot \sin\left(\frac{n\pi}{2}\right) \cdot e^{j[(\omega_o+n\omega_{LO})t+\frac{n\pi}{2}]} \right\} \quad (5.29)$$

where $J_n(x)$ is the Bessel function of the first kind of order n .

Ignoring optical sidebands with Bessel functions higher than $J_5(m_{LO2})$, (5.29) reduces to:

$$E_{MZM2}(t) = \left(\sqrt{\frac{P}{2}}\right) s_1(t) \cdot \{-J_1(m_{LO2}) e^{j(\omega_o + \omega_{LO})t} + J_1(m_{LO2}) e^{j(\omega_o - \omega_{LO})t} \\ -J_3(m_{LO2}) e^{j(\omega_o + 3\omega_{LO})t} + J_3(m_{LO2}) e^{j(\omega_o - 3\omega_{LO})t} \\ -J_5(m_{LO2}) e^{j(\omega_o + 5\omega_{LO})t} + J_5(m_{LO2}) e^{j(\omega_o - 5\omega_{LO})t}\} \quad (5.30)$$

Equation (5.30) is in agreement with (5.14) in the sense that the optical spectrum at the output of DE-MZM2, as shown in the inset of Figure 5.13, is carrier suppressed and contains only odd-order optical sidebands. Each optical sideband is in itself an OSSB signal. Frequency doubling would therefore be obtained by the beating of the first-order sidebands at $(\omega_o + \omega_{LO})$ and $(\omega_o - \omega_{LO})$ with themselves on a square-law photodiode to produce a MB-OFDM UWB signal centred at $2\omega_{LO}$.

Figure 5.14 shows the experimental setup for technique #2. This time, the AWG is operated in dual-output mode but also at a sampling rate of 10.8 GS/s. The first AWG output is the same MB-OFDM UWB signal at an IF frequency as used in section 5.2.1 while the second output is the MB-OFDM UWB signal, phase shifted by 90° by making use of the frequency-domain Hilbert Transform. These two outputs are amplified by two 19-dB gain, SHF 600 APP amplifiers and filtered by two Picosecond 7.5-GHz LPFs before being used to drive a Fujitsu MZM ($V\pi=3.1$ V) biased at its quadrature point. An Anritsu MG9541A tunable laser with centre emission wavelength of 1550 nm serves as the optical source for the MZM. Consequently, an OSSB signal (Figure 5.14 (a)) is generated at the output of the Fujitsu MZM. This, as we will later demonstrate, allows for better chromatic dispersion resistance without having to resort to using fibre Bragg gratings (FBGs) for optical filtering as used by G. H. Nguyen et al. in [143].

Optical up-conversion to the 60-GHz band is achieved in a similar vein as in technique #1 by using the modulated optical signal as the optical source for the Sumitomo 40-Gbit/s DE-MZM, biased at its null point to generate an optical DSB-SC signal. This optical DSB-SC signal, with the first-order sidebands spaced 60 GHz apart is shown in Figure 5.14 (b).

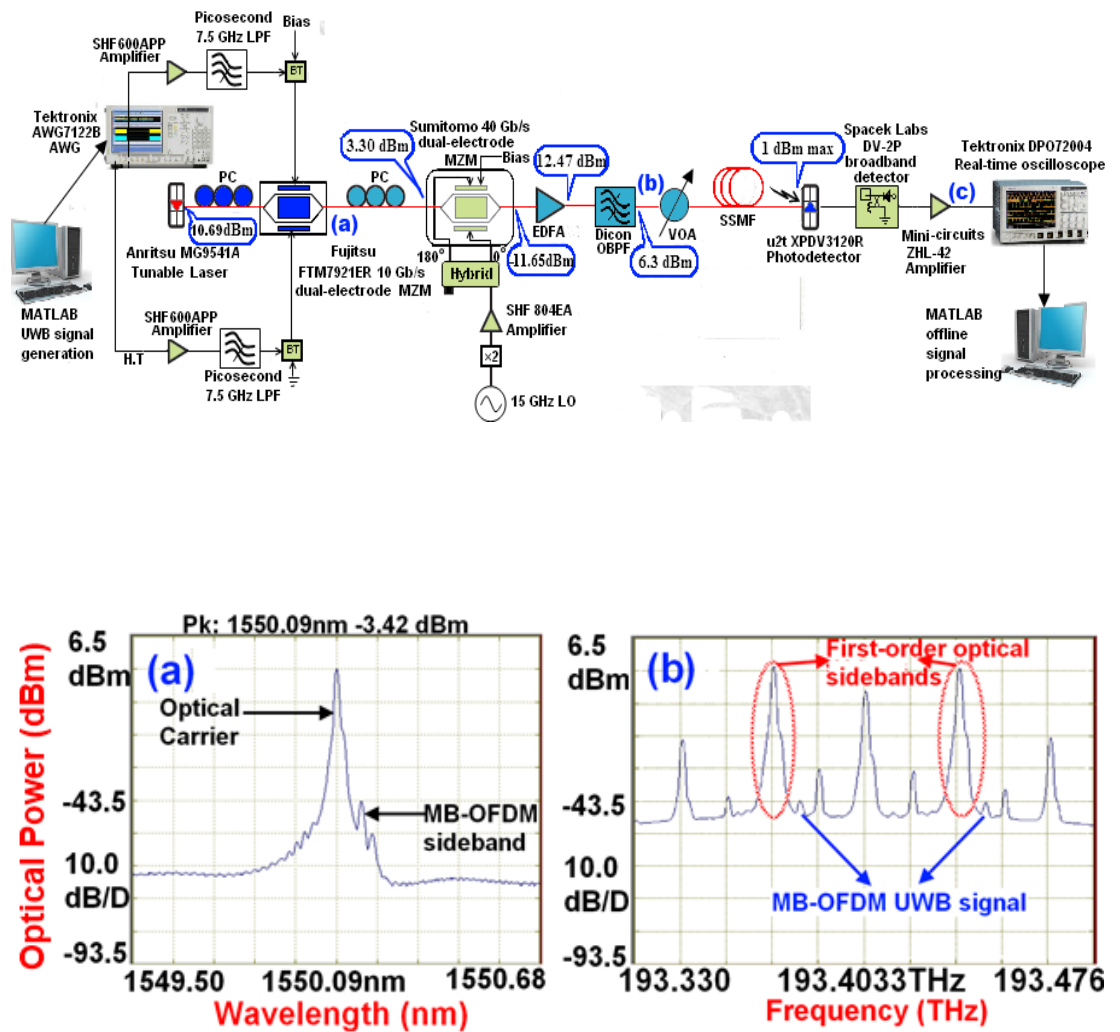


Figure 5.14. Experimental setup for the cascaded MZMs Technique. AWG: Arbitrary Waveform Generator. H.T: Hilbert Transform. LPF: Low-Pass Filter. BT: Bias Tee. PC: Polarisation Controller. MZM: Mach-Zehnder Modulator. LO: Local Oscillator. EDFA: Erbium-Doped Fibre Amplifier. OBPF: Optical Band-Pass Filter. VOA: Variable Optical Attenuator. SSMF: Standard Single Mode Fibre. Insets (a) – (b): Optical spectra at corresponding points in experimental setup.

To ensure a fair comparison with technique #1, the input optical power to the Sumitomo MZM is also kept fixed at 3.30 dBm for this technique. This necessitates having the tunable laser operate at a higher output power (10.69 dBm) than the DFB laser (4.38 dBm) to compensate for the insertion loss of the Fujitsu MZM. Fibre transmission, data detection and baseband digital processing are done in exactly the same way as in technique #1, using exactly the same devices.

In the subsequent sub-subsections, using the setup as shown in Figure 5.14, the impacts of the various parameters such as MZM non-linearity, LO power, chromatic dispersion and received optical power at the photodetector on the system performance will be illustrated.

5.2.2.1 *Impact of MZM non-linearity*

The investigation into the impact of the non-linearity of the Fujitsu MZM (DE-MZM1) is two-fold. The first investigation focuses on the variation of the UWB drive power to DE-MZM1 while the second investigation focuses on the variation of the D.C. bias voltage to DE-MZM1.

In a similar vein as in section 5.2.1.1, variation of the UWB drive power is achieved with the aid of electrical attenuators. For each value of driving amplitude, the corresponding drive power is measured and the VOA is adjusted to keep the input optical power to the photodetector fixed at 1 dBm. Figure 5.15 shows the plot of the measured values of the EVM versus the UWB drive power for optical back-to-back transmission, where as expected, the EVM performance is limited by low SNR at low drive powers and by non-linear distortion of DE-MZM1 at high drive powers, with the minimum EVM obtained at a drive power of -1.7 dBm for the three UWB sub-bands.

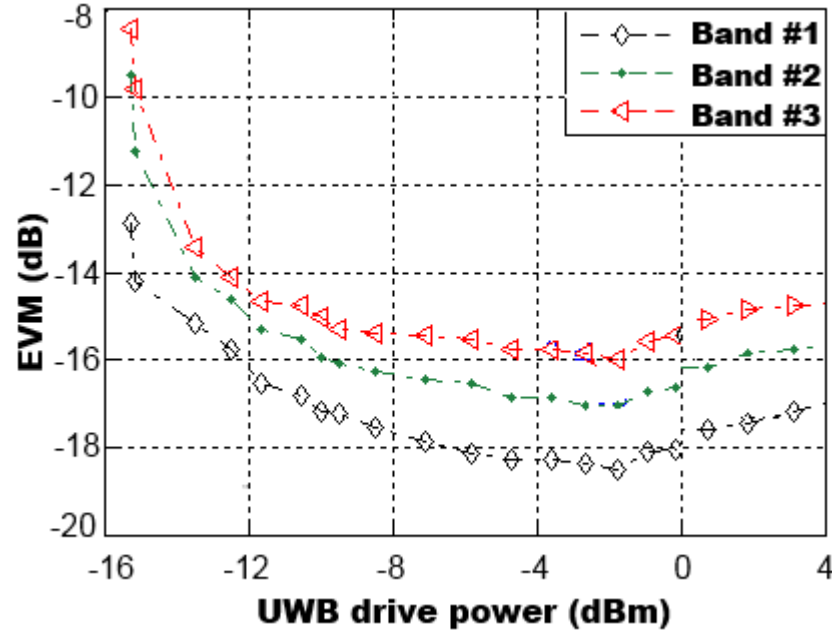


Figure 5.15. EVM vs. UWB drive power for the three UWB sub-bands.

For the investigation into the impact of the D.C. bias voltage to DE-MZM1, with the UWB drive power and LO power kept fixed at -1.7 and 24 dBm respectively, the D.C. bias voltage of the Fujitsu MZM (DE-MZM1) is varied in order to find the optimum EVM. Figure 5.16 shows the EVM variation with the normalised D.C. bias voltage of DE-MZM1 $\left(V_{DC1}/V_{\pi1}\right)$.

It can be seen that the EVM first improves with increasing D.C. bias voltage (because of improvement in the received SNR) up to an inflection point, beyond which the EVM starts to degrade because of the non-linear distortion induced by DE-MZM1. Since DE-MZM1 is the same Fujitsu MZM that was employed for the experiments in chapter 3, it is not surprising to see that the results of Figure 5.16 are in excellent agreement with that of Figure 3.9, showing that the EVM performance is optimum when the normalised bias is within the linear portion of DE-MZM1's characteristics (for normalised bias voltage within the range of 0.46 to 0.56).

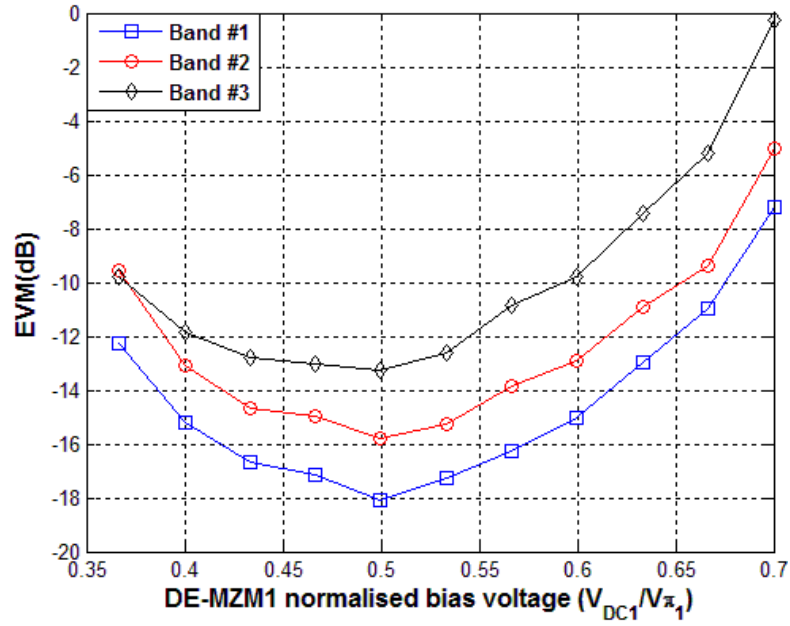


Figure 5.16. EVM vs. normalised bias voltage of DE-MZM1.

Beyond this quadrature regime, the EVM starts to degrade with further increase in the normalised bias voltage because of the increased influence of the non-linear distortion of DE-MZM1.

5.2.2.2 Impact of LO power

With the values of the UWB drive power and normalised D.C. bias voltage of DE-MZM1 kept fixed at -1.7 dBm and 0.5 respectively in order to yield the optimum EVM, the LO power is varied to see its impact on the EVM performance.

Figure 5.17 shows the plot of the EVM vs. the LO power for optical back-to-back transmission, with the EVM improving with increasing LO power, showing good agreement with the results presented in section 5.2.1.4 for technique #1. This is because in a similar manner as for technique #1, the amplitudes of the first-order sidebands that beat at the photodiode, as seen from (5.30), are dependent on the LO power.

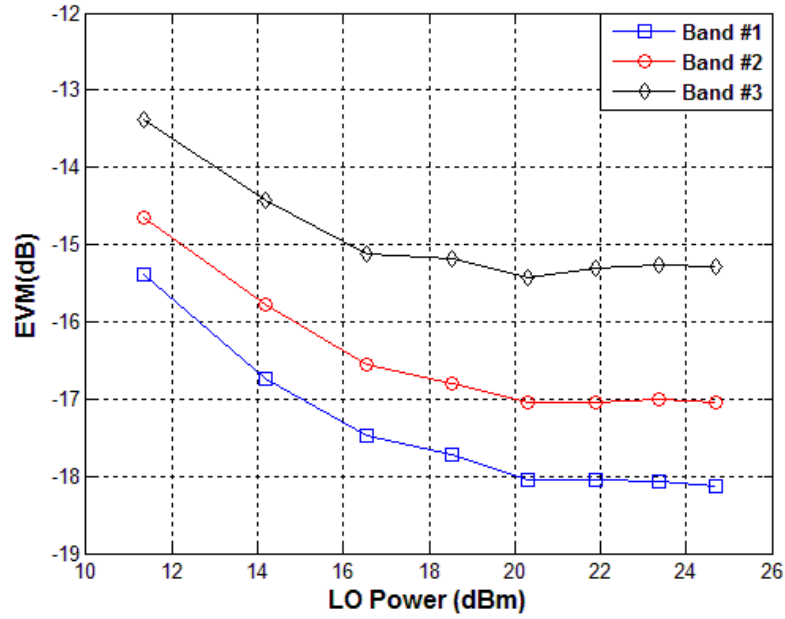


Figure 5.17. EVM vs. LO power for the three UWB sub-bands.

5.2.2.3 Impacts of received optical power and fibre transmission

The values of DE-MZM1 normalised bias voltage, drive and LO power are fixed at 0.5, -1.7 dBm and 24 dBm respectively to yield the minimum EVM. Using sub-band #2 as the test band, for various SSMF lengths, the received optical power is varied by tuning the attenuation of the VOA. Figure 5.18 shows that as expected, the EVM improves with increase in the received optical power. The optical receiver sensitivity at an EVM of -17 dB is -4.6 dBm for optical back-to-back transmission.

Unlike technique #1 however, this sensitivity does not degrade with increasing fibre lengths, implying technique #2 is robust against fibre chromatic dispersion. In a similar manner as in technique #1, the robustness of the system to fibre chromatic dispersion can be explained by considering the inset of Figure 5.19 which shows the optical spectrum at the output of DE-MZM2, considering only the first-order optical sidebands.

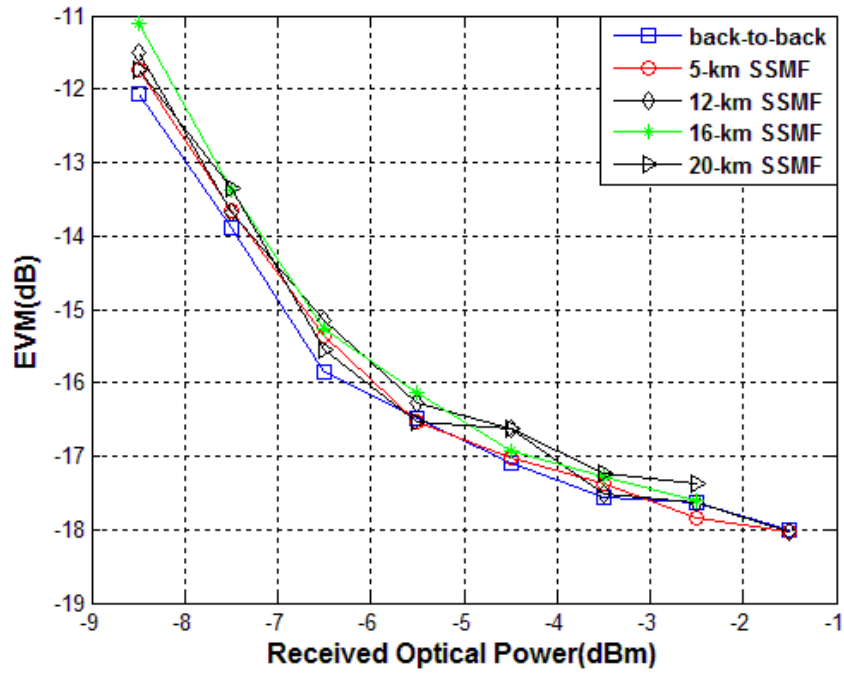


Figure 5.18. Sub-band #2 EVM vs. received optical power for different SSMF lengths.

Here, we can clearly see that each optical sideband is an OSSB signal, with only upper (or lower) wavelength sidebands USB1, USB2 (or LSB1, LSB2); depending on which optical sideband of DE-MZM1 is suppressed.

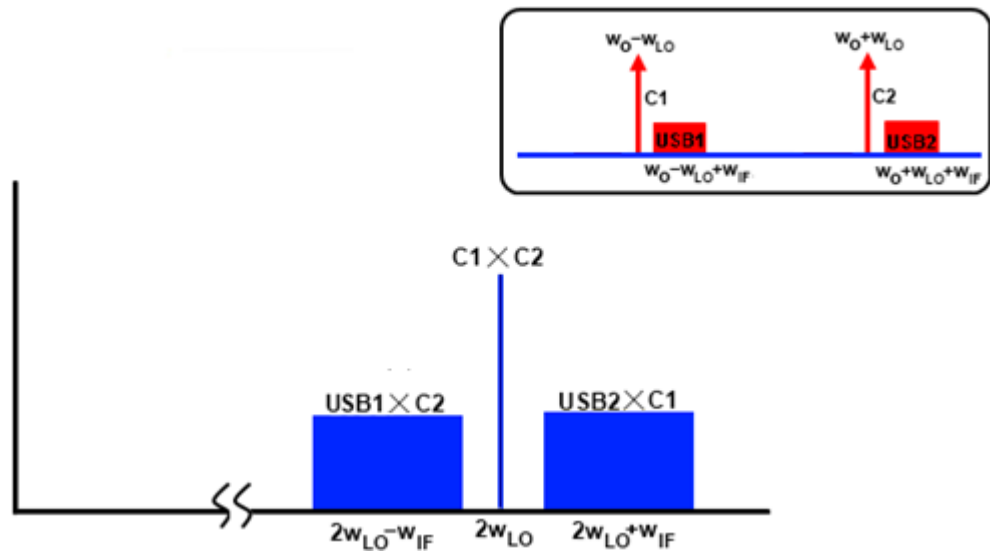


Figure 5.19. Photodetected spectrum for technique #2. Inset: Magnified view of the optical spectrum at the output of the DE-MZM2, considering only the first-order optical sidebands.

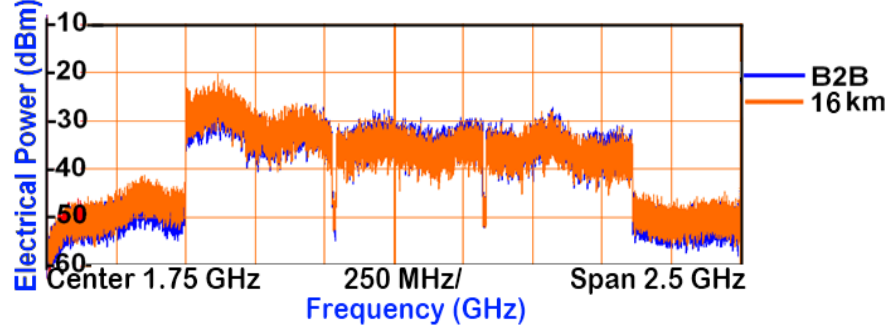


Figure 5.20. Down-converted UWB signal spectra, showing robustness to chromatic dispersion.

This implies that after square-law photodetection, the frequency terms at $(2\omega_{LO} + \omega_{IF})$ and $(2\omega_{LO} - \omega_{IF})$ are obtained from only one beating term ($USB2 \times C1$) and ($USB1 \times C2$), respectively. This is the reason why technique #2 demonstrates robustness to chromatic dispersion.

Figure 5.20 shows the down-converted UWB signal at point (c) in Figure 5.14 for optical back-to-back and 16-km SSMF transmission where it can be confirmed that there is no signal deterioration at longer fibre lengths.

5.2.3 Technique #3 (Electrical frequency up-conversion using mixer)

This technique is different to the afore-mentioned techniques in the sense that up-conversion to the 60-GHz band is achieved electrically, by mixing the MB-OFDM UWB signal with a 60-GHz sinusoidal signal. So, the mixer is the first non-linear device encountered by the UWB signal. The 60-GHz MB-OFDM UWB signal then serves as the electrical drive to a high-bandwidth MZM biased at its quadrature point.

A lightwave from a laser operating in continuous wave mode serves as the optical source to the MZM. The schematic for this technique is shown in Figure 5.21.

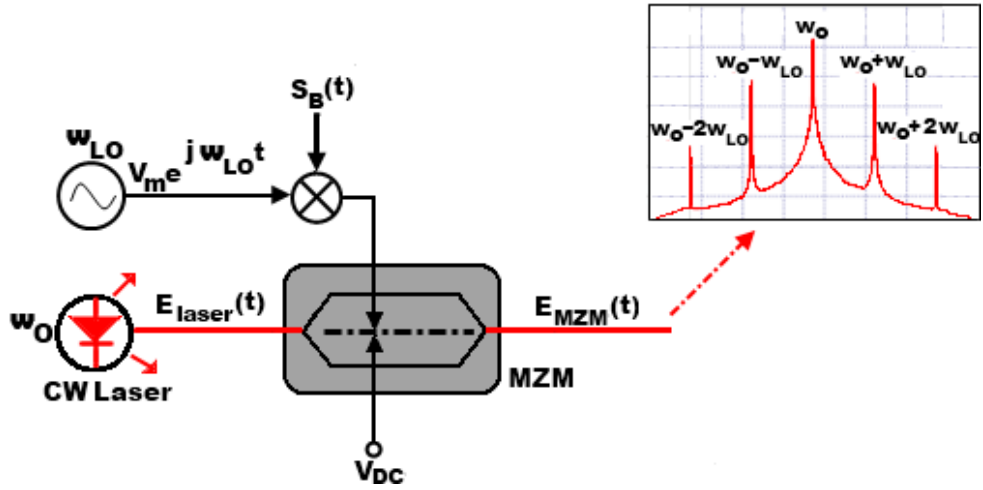


Figure 5.21. Schematic layout of technique #3. CW: Continuous wave. MZM: Mach-Zehnder modulator. Inset: optical spectrum at the output of the MZM.

It is important to note that because of the unavailability of actual 90° electrical hybrids that can operate at 60-GHz, we have been unable to implement OSSB modulation with this technique to combat fibre chromatic dispersion fading. Consequently, with this limitation, DSB-C modulation is used.

If the MZM is operated in the push-pull mode, the optical field at the output of the MZM with an ideal extinction ratio assumed, and with the insertion losses of the MZM ignored, can be expressed as [144], [145]:

$$E_{MZM}(t) = E_{laser}(t) \cos \left\{ \frac{\pi}{2} \left[\frac{V_{mod}(t)}{V_\pi} \right] \right\} \quad (5.31)$$

where $E_{laser}(t)$ and $V_{mod}(t)$ represent the output optical field of the laser and the drive voltage to the MZM, given respectively, by:

$$E_{laser}(t) = (\sqrt{2P}) \cdot \cos(\omega_o t) \quad (5.32)$$

$$V_{mod}(t) = \text{Re}\{s_B(t) \cdot V_m e^{j\omega_{LO} t}\} + V_{DC} \quad (5.33)$$

where P is the optical power of the laser, V_m and ω_{LO} are the amplitude and angular frequency of the RF sinusoid used to up-convert the MB-OFDM UWB signal to an RF frequency, and all other constants are as defined previously in section 5.2.1. It is

important to note that for this technique, ω_{LO} is the desired mm-wave frequency of operation.

Substituting (5.32) and (5.33) in (5.31), we have:

$$E_{MZM}(t) = (\sqrt{2P}) \cos \left\{ \frac{\pi}{2} \left[\frac{V_{DC}}{V_{\pi}} + \frac{V_m}{V_{\pi}} \text{Re}\{s_B(t) \cdot e^{j\omega_{LO}t}\} \right] \right\} \cdot \cos(\omega_o t) \quad (5.34)$$

$$\text{Re}\{s_B(t) \cdot e^{j\omega_{LO}t}\} = \sum_{k=-\frac{N_{sc}}{2}+1}^{\frac{N_{sc}}{2}} |C_k| \cos(\omega_{LO} + \omega_{f_k})t \quad (5.35)$$

For a quadrature bias, $V_{DC} = \frac{V_{\pi}}{2}$. Consequently, the output optical field can be rewritten as:

$$E_{MZM}(t) = (\sqrt{2P}) \cos \left\{ \frac{\pi}{4} + \frac{m_{RF}}{2} \sum_{k=-\frac{N_{sc}}{2}+1}^{\frac{N_{sc}}{2}} |C_k| \cos(\omega_{LO} + \omega_{f_k})t \right\} \cdot \cos(\omega_o t) \quad (5.36)$$

$$= (\sqrt{P}) \cos(\omega_o t) \cdot \left\{ \cos \left[\frac{m_{RF}}{2} \sum_{k=-\frac{N_{sc}}{2}+1}^{\frac{N_{sc}}{2}} |C_k| \cos(\omega_{LO} + \omega_{f_k})t \right] - \sin \left[\frac{m_{RF}}{2} \sum_{k=-\frac{N_{sc}}{2}+1}^{\frac{N_{sc}}{2}} |C_k| \cos(\omega_{LO} + \omega_{f_k})t \right] \right\} \quad (5.37)$$

where m_{RF} is the phase modulation index, which corresponds to m_{LO} of (5.10).

Applying the Jacobi-Anger expansion [139]-[141],

$$\cos[x \cos \theta] = J_0(x) + 2 \sum_{n=1}^{\infty} (-1)^n J_{2n}(x) \cos(2n\theta) \quad (5.38)$$

and

$$\sin[x \cos \theta] = -2 \sum_{n=1}^{\infty} (-1)^n J_{2n-1}(x) \cos[(2n-1)\theta] \quad (5.39)$$

Using (5.38) and (5.39) in (5.37), and letting

$$C_{RF} = \frac{m_{RF}}{2} \quad (5.40)$$

Equation (5.37) reduces to:

$$\begin{aligned} E_{MZM}(t) = (\sqrt{P}) \cdot & \left\{ J_0(C_{RF}) \cos(\omega_o t) \right. \\ & + 2 \sum_{n=1}^{\infty} (-1)^n J_{2n}(C_{RF}) \sum_{k=-\frac{N_{sc}}{2}+1}^{\frac{N_{sc}}{2}} |C_k| \cos[2n((\omega_{LO} + \omega_{f_k})t)] \cos(\omega_o t) \\ & + 2 \sum_{n=1}^{\infty} (-1)^n J_{2n-1}(C_{RF}) \sum_{k=-\frac{N}{2}+1}^{\frac{N}{2}} |C_k| \cos[(2n-1)((\omega_{LO} + \omega_{f_k})t)] \cos(\omega_o t) \left. \right\} \quad (5.41) \end{aligned}$$

Ignoring the high-order Bessel functions, (5.41) can be further simplified as:

$$\begin{aligned} E_{MZM}(t) = (\sqrt{P}) \cdot & \left\{ J_0(C_{RF}) \cos(\omega_o t) \right. \\ & - J_1(C_{RF}) \sum_{k=-\frac{N_{sc}}{2}+1}^{\frac{N_{sc}}{2}} |C_k| \cos[(\omega_o + \omega_{LO} + \omega_{f_k})t] \\ & - J_1(C_{RF}) \sum_{k=-\frac{N_{sc}}{2}+1}^{\frac{N_{sc}}{2}} |C_k| \cos[(\omega_o - \omega_{LO} - \omega_{f_k})t] \\ & - J_2(C_{RF}) \sum_{k=-\frac{N_{sc}}{2}+1}^{\frac{N_{sc}}{2}} |C_k| \cos[(\omega_o + 2\omega_{LO} + 2\omega_{f_k})t] \\ & \left. - J_2(C_{RF}) \sum_{k=-\frac{N_{sc}}{2}+1}^{\frac{N_{sc}}{2}} |C_k| \cos[(\omega_o - 2\omega_{LO} - 2\omega_{f_k})t] \right\} \quad (5.42) \end{aligned}$$

The first term in (5.42) is the optical carrier, the second and third terms represent the first-order optical sidebands, while the remaining two terms represent the second-order optical sidebands, as shown in the inset of Figure 5.21. The beating

of the first-order sidebands with the optical carrier on a photodetector would result in the superimposition of two RF signals at ω_{LO} which may constructively or destructively interfere, depending on the phase shift induced by chromatic dispersion.

Figure 5.22 shows the experimental setup for this technique. The MB-OFDM UWB signal at an IF frequency is generated by the AWG which is operated at a sampling rate of 10.8 GS/s. The UWB signal is electrically up-converted to the 60-GHz band by mixing it with a 30 GHz LO signal frequency multiplied by two (using an active multiplier). The up-converted mm-wave UWB signal at the output of the mixer is amplified by a 30-dB gain HPA and used as the electrical drive to a high-bandwidth Sumitomo MZM. The UWB signal is electrically up-converted to the 60-GHz band by mixing it with a 30 GHz LO signal frequency multiplied by two (using an active multiplier). The up-converted mm-wave UWB signal at the output of the mixer is amplified by a 30-dB gain HPA and used as the electrical drive to a high-bandwidth Sumitomo MZM.

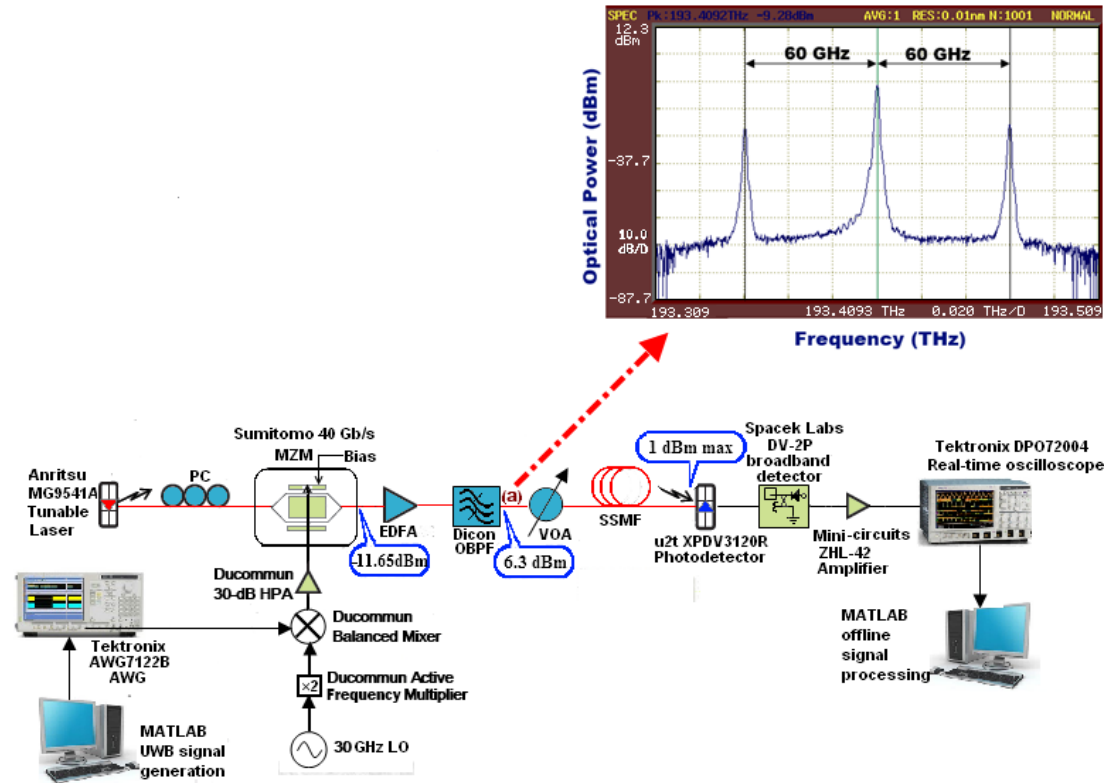


Figure 5.22. Experimental setup of technique #3. AWG: Arbitrary Waveform Generator. PC: Polarisation controller. HPA: High-power amplifier. MZM: Mach-Zehnder modulator. EDFA: Erbium-doped fibre amplifier. OBPF: Optical band-pass filter. VOA: Variable optical attenuator. SSMF: Standard single-mode fibre. Inset: Optical spectrum at point (a) in the experimental setup.

The optical source to the MZM is a tunable laser with linewidth of 800 kHz and centre emission wavelength of 1550 nm. Although the MZM used to modulate the optical signal is specified for 40 Gbit/s, it has reasonable performance around 60 GHz. The MZM is biased at its quadrature point, resulting in an optical DSB-C signal, which is amplified by an EDFA and filtered for ASE noise suppression. The optical DSB-C signal with the first-order sidebands spaced 60-GHz apart from the optical carrier is shown in the inset of Figure 5.22. Fibre transmission, data detection and baseband digital processing is done in exactly the same way as in techniques #1 and #2 using exactly the same devices.

In the subsequent sub-subsections, using the setup as shown in Figure 5.22, the impacts of the various parameters such as mixer non-linearity, LO power, chromatic dispersion and received optical power at the photodetector on the system performance will be investigated.

Before proceeding with the experiments, it is important to highlight, at this stage, some of the mixer characteristics that will influence the experimental investigations. The mixer used in the experiment employs high-performance GaAs Schottky beamlead diodes which enable very good performance with a moderate LO pumping level [146]. The “mixing” process takes place due to the switching response of the diodes’ I-V curves to the LO signal [147].

For an “ideal” single-diode (unbalanced) mixer as shown in Figure 5.23 (a), the possible mixer output products after up-conversion are governed by the relation:

$$f_{RF} = nf_{LO} \pm f_{IF} \quad n \text{ odd} \quad (5.43)$$

where f_{RF} , f_{LO} and f_{IF} represent the centre frequencies of the RF, LO and IF signals respectively and n is an integer that assumes odd values only.

For such an “ideal” single-diode mixer, the LO power is significantly stronger than the IF, so the transconductance of the diode is affected only by the LO [147]. It is also assumed that the diode switches instantaneously as shown in Figure 5.23 (b). However for realistic diode mixers, the diode I-V characteristics demonstrate some “turn-on” transition as shown in Figure 5.23 (c). In addition, the IF signal will affect the transconductance of the diode to a certain extent, regardless of how small the IF signal is. Consequently, additional unwanted mixing products called “spurs” are produced at the RF output because of a combination of the realistic IV-characteristics and the transconductance modulation by the IF signal. As a result, for practical single-diode mixers, output products at the RF port are governed mathematically by [147], [148]:

$$f_{RF} = kf_{LO} \pm mf_{IF} \quad (5.44)$$

where k and m are both integers, and all other terms are as defined previously in (5.43).

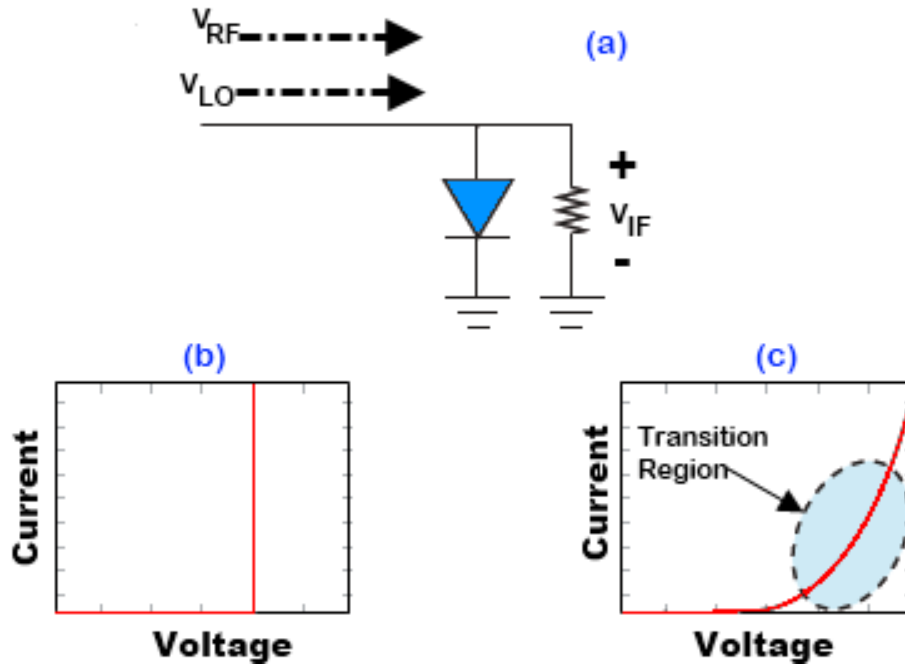


Figure 5.23. (a) Single-diode mixer. I-V Characteristics for (b) ideal diode (c) practical Schottky diode [147].

Equation (5.44) shows that all possible harmonic mixing components are present at the RF output of practical single-diode mixers. However, in balanced diode mixers, which make use of 180° hybrid junctions, in addition to inter-port isolation being provided (i.e. LO-to-RF, RF-to-IF, and LO-to-IF), it is also possible to suppress between 50-100% of the spurious interference [147], [149].

The mixer used in the experiment is a single-balanced diode mixer which is illustrated schematically in Figure 5.24. With the LO applied to the 180° port of the hybrid, the spurious terms that contain the even-order harmonic LO products will be suppressed (i.e. $2f_{LO} \pm mf_{IF}, 4f_{LO} \pm mf_{IF}, \dots$). However, the spurious terms that contain the odd-order harmonic LO products still remain (i.e. $f_{LO} \pm mf_{IF}, 3f_{LO} \pm mf_{IF}, \dots$).

It is also important to note that the LO signal which is fed into the mixer is not a “pure” single tone. This is because the unavailability of a 60-GHz signal generator has made us resort to frequency multiplication of a 30-GHz LO. Hence, harmonics of the LO signal are also produced at the output of the active frequency multiplier. Depending on the value of f_{IF} and the width of the IF signal, the spurious image term at $f_{LO} + 2f_{IF}$ may be quite close, or may in some cases, overlap with the desired RF signal at $f_{LO} + f_{IF}$, creating substantial interference.

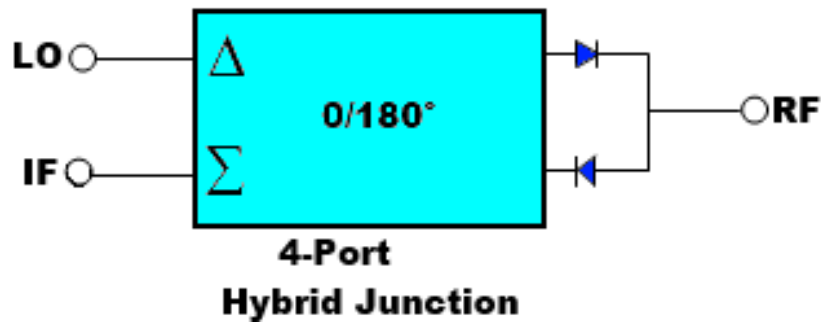


Figure 5.24. Single-balanced diode mixer

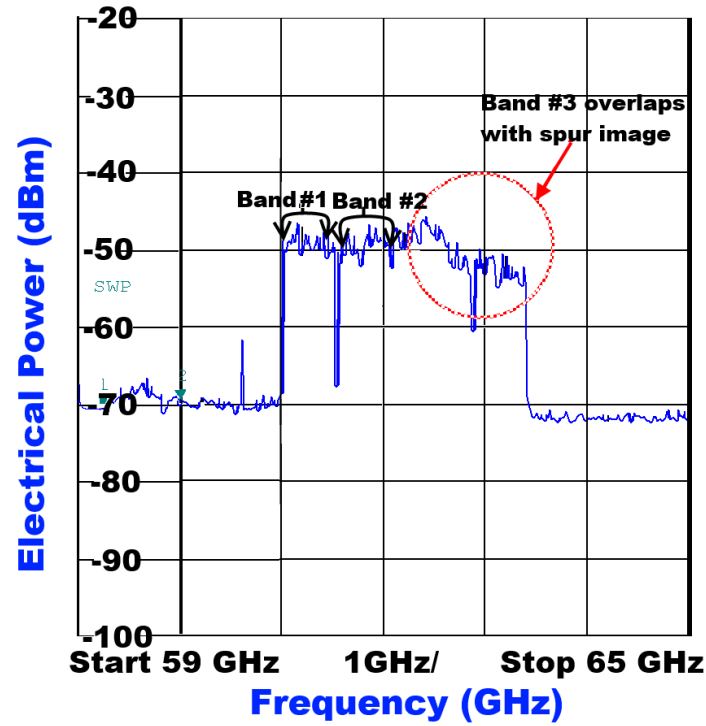


Figure 5.25. Spurious image term overlapping with desired RF signal.

In the case where there is overlap, filtering of the undesired spurious component would be impossible. Considering our UWB signal which spans from 1 GHz to 2.584 GHz, the desired RF signal after up-conversion to 60 GHz would be centred at 61.792 GHz and span from 61 to 62.584 GHz.

There would also be a spurious image term centred at 63.584 GHz which as can be seen in Figure 5.25, would be quite close and create substantial interference with sub-band #3 of the desired RF UWB signal. As a result, only UWB sub-band#2 is transmitted for the experiment investigations in this section.

5.2.3.1 Impact of IF power

The first step in our experimental investigations is to optimise the IF stage of the RoF system for the highest received SNR prior to fibre transmission. Consequently, with an optical back-to-back connection, and with the LO power fixed

at 0 dBm, the IF power to the single-balanced mixer is varied by attenuating the output of the AWG. Figure 5.26 shows the variation of the EVM of sub-band #2 with the IF power to the mixer for a received optical power of 1 dBm, where it can be seen that the EVM improves as the IF power increases from a low value up to -14.8 dBm, beyond which the EVM starts to degrade.

The reason for this trend is that for low IF powers, the mixer operates linearly with a constant conversion loss. So, with fixed LO power, increasing the IF power would result in a corresponding increase in the power of the RF signal, resulting in an increase in the received SNR and a corresponding improvement in the EVM.

However, for large IF powers, the mixer starts deviating from the linear behaviour, and the conversion loss starts increasing. This is referred to as mixer compression.

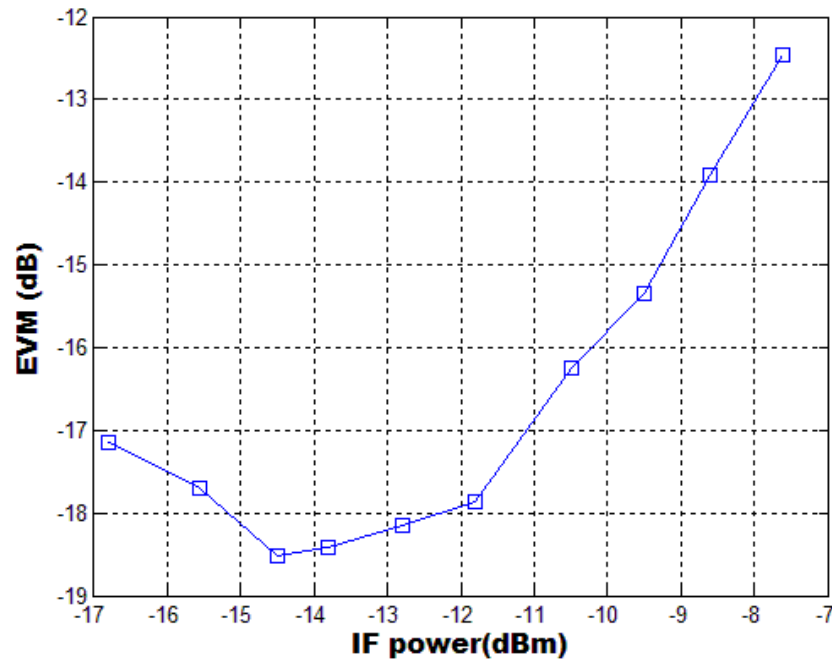


Figure 5.26. Sub-band #2 EVM vs. IF power.

As described previously, when the mixer operates linearly, the diode switching action is completely dominated by the LO. However, with sufficient increase in the IF signal power, the diode switching action is compromised by the IF signal and the diodes get partially turned on by the IF signal. In addition to increase in the conversion loss, this also results in increased spurious performance, increased levels of intermodulation distortion [147], and consequently, EVM degradation.

5.2.3.2 *Impact of LO power*

With the IF power to the mixer fixed at -14.8 dBm, and with an optical back-to-back connection, the LO power to the mixer is varied and the EVM computed. Figure 5.27 shows the variation of the EVM of sub-band #2 with the LO power for a received optical power of 1 dBm.

For low LO powers, the LO feed-through at the mixer's RF port is minimised but the mixer's conversion loss and noise figure are poor, resulting in poor system performance. Increase in the LO power results in improvement in the mixer noise figure, resulting in improvement in the EVM, up to an optimum LO power of 0 dBm.

For LO powers higher than this optimum, the mixer noise figure starts to degrade again, resulting in EVM degradation. The reason why the mixer noise figure degrades when the LO power is too high is that with a very high LO power, the LO signal becomes almost a square-shaped signal [150].

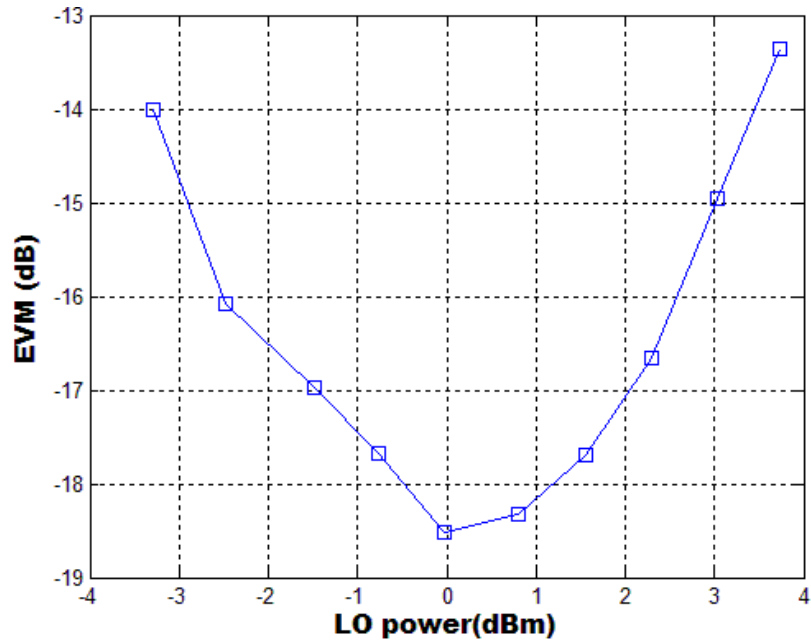


Figure 5.27. Sub-band #2 EVM vs. LO power.

A square-shaped signal contains additional harmonics not present in a pure sinusoid signal. These additional harmonics add additional noise to the RF signal which further degrades the signal noise figure.

5.2.3.3 *Impacts of received optical power and fibre transmission*

Since both sidebands of the optical signal were transmitted, chromatic dispersion-induced fading of the generated 60-GHz carrier after SSMF transmission is expected. In order to investigate the nature of the fading and the impact it has on the system performance, the IF and LO powers are kept at -14.8 and 0 dBm respectively to yield the optimum EVM, then the UWB signal is transmitted over various SSMF lengths and the EVM of the received signal computed for different received optical powers. Figure 5.28 shows the EVM variation of sub-band #2 with the received optical power for different SSMF lengths, where it can be seen that as expected, the EVM improves with increasing received optical power for the different SSMF lengths.

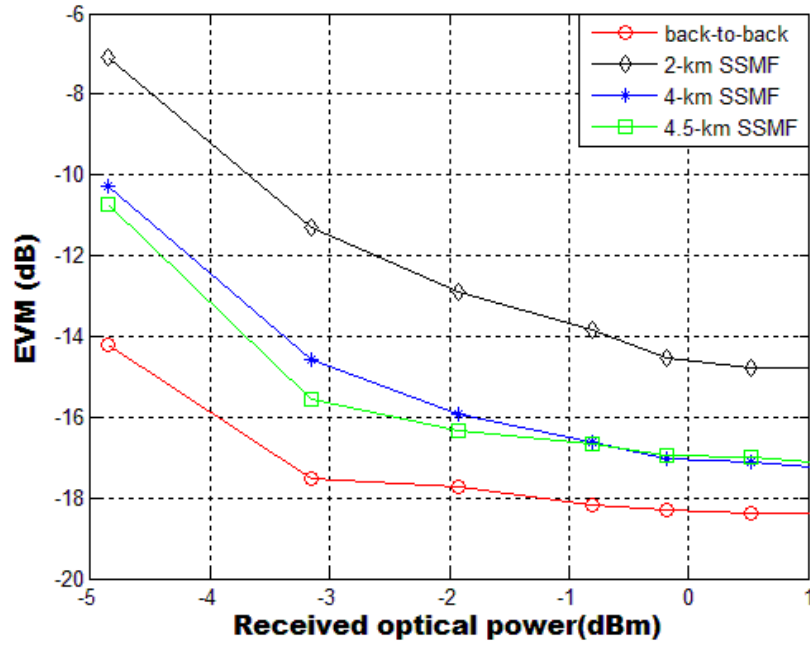


Figure 5.28. Sub-band #2 EVM vs. received optical power for different SSMF lengths.

A more interesting observation is that for 1 dBm received optical power; a power penalty of 3.6 dB is observed after just 2-km SSMF transmission because of the severe dispersion-induced fading suffered by the UWB signal. This is because in accordance with (2.34), the lengths of SSMF at which the power cancellation of the RF signal due to chromatic dispersion occurs will be very small because of the high frequencies involved. The power penalty then improves to 1.1 dB and 1.2 dB for 4-km and 4.5-km SSMF transmissions respectively, indicating the UWB signal has started recovering from fading at these lengths.

In a similar manner as in section 5.2.1.5, a detailed study of the trend of the EVM degradation has also been conducted by observing the EVM of the UWB signal at 1 dBm received optical power for SSMF spans ranging from 0 to 5 km, with a length resolution of 250 m. As shown in Figure 5.29, an apparent “fading cycle” of around 2 km is observed. This “fading cycle” is quite similar to that of an unmodulated RF signal at 61.75 GHz when optical DSB-C transmission is used.

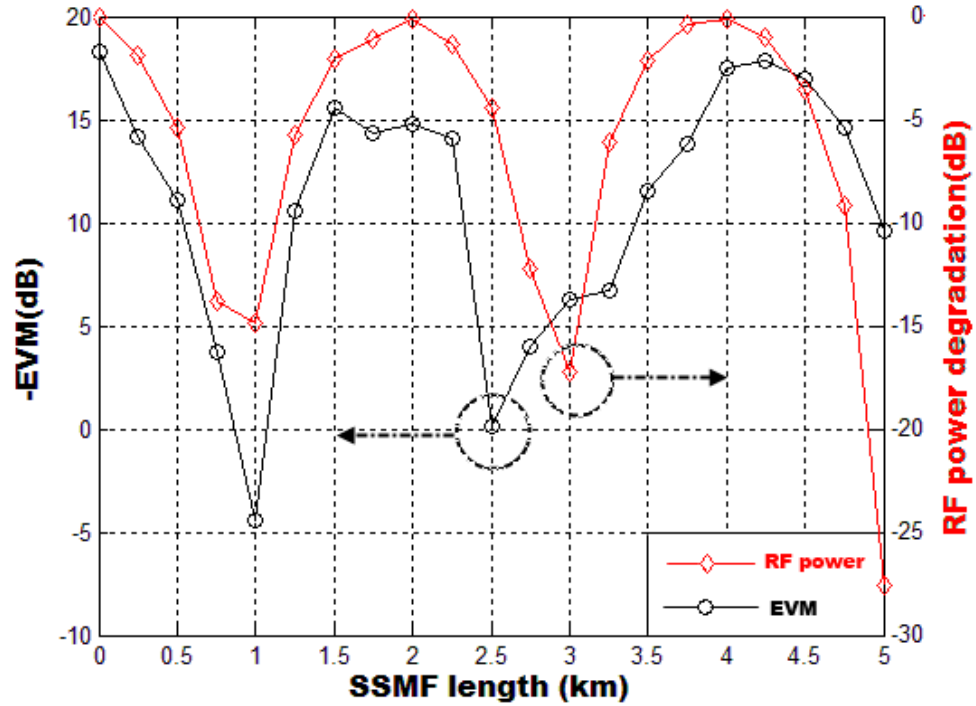


Figure 5.29. EVM degradation for UWB signal and RF power degradation for a 61.75 GHz signal at 1 dBm received optical power when optical DSB-C transmission is used.

It should be highlighted again that the chromatic dispersion fading experienced when using this technique can be eliminated by employing OSSB modulation. However, this would necessitate either having a 90-degree electrical hybrid that can operate at 60 GHz or using optical filtering to remove one of the sidebands. The required devices to achieve this were either not available to us or would add complexity to the system.

5.3 Comparison of the IM-DD transmission techniques

The three IM-DD transmission techniques differ in either the principle used to modulate the optical carrier (i.e. direct or external modulation) or the methods used for up-conversion to the 60-GHz band (optical up-conversion or electrical mixing). Also, in the three different implementations, the electrical UWB signal drives a different type of non-linear device. These differences therefore lead to

different behaviours during light propagation, implying there will be differences in the signals produced both in the optical and electrical domain after photodetection.

Despite this, we have tried to compare the three techniques as fairly as possible by using the same modulating signal with the same modulation format and ensuring that the optical power at the output of the 40-Gbit/s MZM as well as the optical power into the VOA for all the techniques were kept at -11.65 and 6.3 dBm respectively. Also, the sampling rates used for both the AWG and the digital sampling oscilloscope were the same for all the techniques. Down-conversion of the mm-wave UWB signal to baseband, as well as the baseband digital signal processing were all carried out in the same way, with the same devices. Table 5.2 shows the comparison of the three transmission techniques based on transmission performance, cost and complexity.

Technique #1 requires just one DE-MZM and does not require 60-GHz electrical and electro-optical devices like technique #3. It therefore has the simplest and cheapest architecture out of all the three techniques.

With optimum laser bias and operating temperature values of 80 mA and 20°C respectively, it is found that technique #1 can tolerate higher signal driving amplitudes than the other two techniques before non-linear distortion sets in. However, since the laser is the device that is driven by the MB-OFDM UWB signal, technique #1 may be disadvantaged by the limited modulation bandwidth of the laser used if the bandwidth of the driving signal is too wide. In addition, due to difficulties in precise optical filtering of one of the optical sidebands (which would require precise wavelength control of both the filter and the laser source); the desired UWB signal at the RF frequency is obtained by the superimposition of two beating terms.

	Technique #1	Technique #2	Technique #3
Up-conversion Scheme	Optical	Optical	Electrical
First non-linear device encountered by UWB signal	DFB laser	DE-MZM	Mixer
Number of MZMs	1	2	1
Fading cycle	16 km	–	2 km
Optical receiver sensitivity for back-to-back tx.	-4.2 dBm (EVM threshold of -17 dB)	-4.6 dBm (EVM threshold of -17 dB)	-3.3 dBm (EVM threshold of -17 dB)
Optimum UWB drive power for minimum EVM	3.4 dBm at 80 mA bias current. (Minimum EVM is -18.1 dB)	-1.7 dBm. (Minimum EVM is -18.2 dB)	-14.8 dBm. (Minimum EVM is -18.5 dB)
Advantages	Simple architecture. Lowest cost. Can accommodate higher drive powers before device non-linearity is encountered (5.1 dBm more drive power than technique #2 and 18.2 dBm more drive power than technique #3).	Best EVM performance at low drive powers (for -8 dBm drive power, EVM is -17.8 dB as compared to -11.8 dB and -13 dB for techniques #1 and #3 respectively). Impressive robustness against fibre chromatic dispersion.	Simple architecture.
Disadvantages	Limited by laser modulation bandwidth. Suffers chromatic dispersion fading, though not as severe as technique #3. A power penalty of 11 dB obtained after 18-km SSMP transmission.	Complex architecture. Requires extra optical power to compensate for insertion loss of DE-MZM1.	Requires quite expensive, high-bandwidth devices; not cost-effective. Severely hindered by chromatic dispersion fading; only suitable for short-distance applications. A 7.2 dB power penalty is obtained after just 500 m SSMP

Table 5.2. Comparisons of the three IM-DD transmission techniques.

Consequently, this technique suffers some chromatic dispersion-induced fading though not as severe as technique #3. A fading “cycle” of 16 km is observed with a power penalty of 11 dB obtained after 18-km SSMF transmission.

Technique #2 is quite similar to technique #1 in terms of optical up-conversion architecture but requires two DE-MZMs as opposed to all the other techniques that use just one DE-MZM. So, technique #2 is relatively more complex than the other techniques. Also, the complexity of this technique is further slightly increased by the need for OSSB modulation to be done with the first MZM, which would require an additional 90° electrical hybrid (or a frequency-domain Hilbert Transform). This however results in a system that is robust to fibre chromatic dispersion fading because only one beating term at the photodetector produces the desired mm-wave UWB signal. Technique #2 also demonstrates the best performance at low UWB drive powers. For an UWB drive power of -8 dBm, the EVMs obtained for techniques #1, #2 and #3 are -11.8 dB, -17.8 dB and -13 dB respectively. To match the other two techniques and keep the optical power into the 40-Gbit/s MZM fixed at 3.30 dBm, the CW laser used in this technique had to operate at a higher output power (10.69 dBm) than the DFB laser of technique #1 (4.38 dBm) to compensate for the insertion loss of the first MZM.

Though technique #3 is simple and also requires only one DE-MZM, there are several drawbacks that limit the system performance. Firstly, it requires high-frequency electrical and electro-optical devices (MZM, LOs, and mixer) for its implementation which will drive the cost up. In addition, because of the non-availability of some of the required high-frequency components, we have been forced to compromise and use alternatives. For instance, the MB-OFDM UWB signal is processed at 60 GHz, but the DE-MZM is specified for 40 Gbit/s. We have

also used a 30 GHz LO, frequency multiplied by 2 to generate the 60-GHz carrier. Although the system performance using these alternatives is still acceptable to a certain degree, there are resulting impairments (e.g. the additional harmonics generated by the active frequency multiplier) that have limited the system performance.

Secondly, despite the simple architecture, technique #3 requires very careful adjustments of the IF and LO powers to the mixer. The results obtained with this technique show that the mixer strongly dominates the distortion in the RF path with the system performance hampered by the spurious interference from the harmonics produced by the mixer. In our case, these spurs caused interference with the desired UWB signal in the 60-GHz band, forcing us to transmit only one UWB sub-band. To avoid increased levels of intermodulation distortion and spurious performance, the IF power (i.e. UWB drive power) and the LO power to the mixer must be kept sufficiently low enough. Consequently, with technique #3, the UWB drive power at which the minimum EVM is obtained is far less than the other techniques. This implies that the UWB signal experiences non-linear distortion much earlier with technique #3 than with the other two techniques (minimum EVM is obtained at 3.4, -1.7 and -14.8 dBm for techniques #1, #2 and #3 respectively).

Thirdly, by virtue of the fact that DSB-C modulation is employed and because of the high frequencies involved, technique #3 is also more severely impacted by fibre chromatic dispersion fading than all the other techniques. A fading “cycle” of 2 km is observed, with a 7.2 dB power penalty obtained after just 500 m SSMF transmission (for a received optical power of 1 dBm). In fact, after 1 km transmission, the UWB signal cannot be recovered. This makes technique #3 suitable only for very short distances, possibly restricted to in-building applications only.

5.4 60-GHz MB-OFDM UWB generation by OHD

This technique achieves all-optical up-conversion by utilising uncorrelated optical heterodyne mixing of an OSSB MB-OFDM UWB signal with a free-running CW laser in a broadband photodiode. The frequency offset between the two uncorrelated optical sources that beat at the photodiode is 60 GHz. In contrast to the numerous existing heterodyne mixing implementations in literature that require optical injection locking or complex optical phase-locked loops e.g. [151]-[153], this proposed technique utilises envelope detection to avoid laser phase noise effects at baseband, thus obviating signal control techniques, resulting in a very simple and cost-effective transmission system.

Both optical sources are tunable lasers that utilize thermo-electric cooler (TEC) modules to ensure wavelength stability and accuracy throughout their tuning ranges. Using such lasers guarantees that the beat term falls within the 60-GHz band.

It is well-known that the phase noise of the carrier generated by the beating of two uncorrelated optical sources on a photodetector significantly degrades the detection performance of the transmission system. This phase noise may manifest itself in the broadening of the spectral linewidth. In the absence of phase noise, the photodetected electrical signal at an IF frequency can be detected by extracting a carrier reference from it, followed by coherent demodulation. However, in the presence of phase noise, a carrier-recovery circuit might have difficulties in tracking rapid phase variations, resulting in degradation of the detection performance. Alternatively, these phase-noise effects can be avoided at baseband by utilizing a self-homodyning receiver [154] or an envelope detector with sufficient IF bandwidth [155].

The proposed system utilizes square-law envelope detection at the customer unit to down-convert the mm-wave wireless signal straight to baseband. Envelope detection is preferred over self-homodyning because it is cheaper and has been shown to provide better sensitivity [156]. Consequently, this proposed OHD technique significantly simplifies the optical mm-wave generation and data recovery as it doesn't require any high-bandwidth electro-optical device at the central office or high-frequency LOs at either the central office or the customer unit; or optical phase-locking techniques to generate the mm-wave wireless signal. This means that mm-wave independence is achieved, provided the frequency separation between the two optical sources is within the bandwidth of the broadband photodiode.

Figure 5.30 shows the schematic for this technique. One laser (signal laser) is used as the optical source to a low-bandwidth DE-MZM which is modulated by the MB-OFDM UWB signal. The phase fluctuations of the signal laser $\phi_1(t)$, as characterized by the Wiener-Lévy process, has zero mean and a variance of $2\pi\beta|t|$, where β is the two-sided 3-dB laser linewidth of Lorentzian power density spectrum [157].

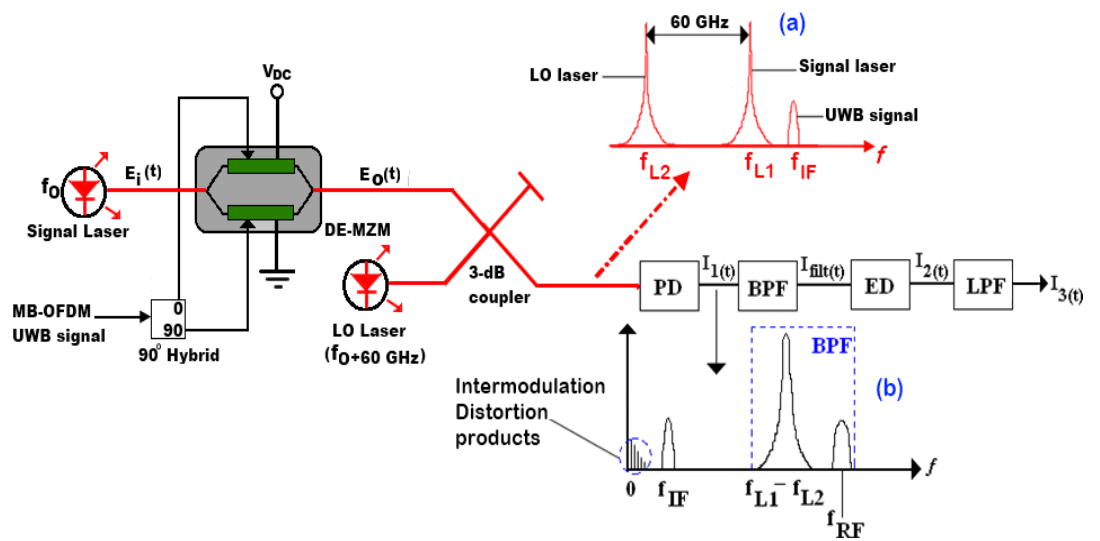


Figure 5.30. Schematic layout of OHD technique. MZM: Mach-Zehnder modulator. LO: Local Oscillator. PD: Photodetector. BPF: Band-pass filter. ED: Envelope detector. LPF: Low-pass filter. Inset (a) Combined optical spectra. Inset (b) Photodetected signal spectra.

To introduce this phase fluctuation, the optical field at the output of the MZM is multiplied by the noisy carrier $e^{j\phi_1(t)}$, which is the laser phase noise. Consequently, the field of the optical UWB signal at the output of the MZM in the presence of the signal laser phase noise can be written as:

$$E_{1p}(t) = e^{j(2\pi f_{L1}t + \phi_1(t))} + e^{j(2\pi[f_{L1} + f_{IF}]t + \phi_1(t))} \cdot \sum_{k=-\frac{N_{sc}}{2}+1}^{\frac{N_{sc}}{2}} C_k e^{j2\pi f_k t} \quad (5.45)$$

where f_{L1} , f_{IF} , N_{sc} and f_k are the centre frequency of the signal laser, the carrier frequency of the UWB signal, the number of OFDM subcarriers and the frequency of the k th subcarrier.

In a similar vein, the optical field at the output of the second laser (LO laser), in the presence of the LO laser phase noise, $e^{j\phi_2(t)}$ can be expressed as:

$$E_{2p}(t) = e^{j(2\pi f_{L2}t + \phi_2(t))} \quad (5.46)$$

where f_{L2} is the centre frequency of the LO laser. The two optical signals are combined in the optical coupler resulting in the optical signal spectra shown in inset (a) of Figure 5.30.

For simplicity, we have neglected both the fibre and wireless channels in this analysis. The generated photocurrent, $I_1(t)$, at the output of the square-law photodetector is:

$$I_1(t) = \mathcal{R} \left\{ \left(E_{1p}(t) + E_{2p}(t) \right) \cdot \left(E_{1p}(t) + E_{2p}(t) \right)^* \right\} \quad (5.47)$$

where \mathcal{R} is the responsivity of the photodetector and the superscript " * " carries out the complex conjugation operation. After some algebraic manipulations, it is easy to show that (5.47) can be expressed as:

$$\begin{aligned}
I_1(t) = \mathcal{R} \bigg\{ & 2 + \left[\left(\sum_{k=-\frac{N_{SC}}{2}+1}^{\frac{N_{SC}}{2}} C_k \cos(2\pi f_k t) \right)^2 + \left(\sum_{k=-\frac{N_{SC}}{2}+1}^{\frac{N_{SC}}{2}} C_k \sin(2\pi f_k t) \right)^2 \right] \\
& + \left[2 \sum_{k=-\frac{N_{SC}}{2}+1}^{\frac{N_{SC}}{2}} C_k \cos(2\pi [f_{IF} + f_k] t) \right] + [2 \cos(\epsilon_1(t))] \\
& + \left[2 \sum_{k=-\frac{N_{SC}}{2}+1}^{\frac{N_{SC}}{2}} C_k \cos(\epsilon_2 + 2\pi f_k t) \right] \bigg\} \quad (5.48)
\end{aligned}$$

where

$$\epsilon_1(t) = 2\pi[f_{L1} - f_{L2}]t + (\phi_1(t) - \phi_2(t)) \quad (5.49)$$

$$\epsilon_2(t) = 2\pi f_{RF}t + (\phi_1(t) - \phi_2(t)) \quad (5.50)$$

and

$$f_{RF} = f_{L1} - f_{L2} + f_{IF} \quad (5.51)$$

The first term in (5.48) is a D.C. component. The second term represents the second-order inter-modulation distortion products. The third term is a copy of the MB-OFDM UWB signal centred at a frequency of f_{IF} . The fourth term is an RF carrier at a frequency of $(f_{L1} - f_{L2})$, obtained from the beating of the two optical carriers with themselves. The final term is the desired MB-OFDM UWB signal at the RF frequency of f_{RF} . It is seen that the last two terms have random phase deviations of $(\phi_1(t) - \phi_2(t))$. If $\phi_1(t)$ and $\phi_2(t)$ have spectral densities represented by η_1 and η_2 rps²/Hz respectively, these last two terms will have spectral densities of $(\eta_1 + \eta_2)$ rps²/Hz, resulting in a 3-dB linewidth equal to the sum of the linewidths of the signal and LO lasers [155]. All the terms in (5.48) are illustrated in the photodetected signal spectra shown in inset (b) of Figure 5.30, with the increased linewidths of the last two terms clearly evident. The BPF shown in Figure 5.30

removes the undesired components, leaving only the last two terms in (5.48). The filtered electrical signal, $I_{filt}(t)$ is down-converted by passing it through the envelope detector. Assuming an ideal square-law envelope detector, the down-converted signal $I_2(t)$ is written as:

$$I_2(t) = |I_{filt}(t)|^2 \quad (5.52)$$

$$= 4\mathcal{R}^2 \left\{ \cos(\epsilon_1(t)) + \sum_{k=-\frac{N_{sc}}{2}+1}^{\frac{N_{sc}}{2}} C_k \cos(\epsilon_2 + 2\pi f_k t) \right\}^2 \quad (5.53)$$

After filtering $I_2(t)$ with the LPF, the higher-frequency components in (5.53) are eliminated, leaving the baseband signal, $I_3(t)$.

$$I_3(t) = 4\mathcal{R}^2 \left\{ \sum_{k=-\frac{N_{sc}}{2}+1}^{\frac{N_{sc}}{2}} C_k \cos(2\pi[f_{IF} + f_k]t) \right\} \quad (5.54)$$

Equation (5.54) shows that no laser phase noise terms remain. This implies that the proposed technique is, in principle, capable of avoiding the laser phase noise effects at baseband. In addition, the system will be robust against chromatic dispersion because as shown in inset (b) of Figure 5.30, the desired UWB signal at the RF frequency is obtained by the beating of only two optical components, i.e. one optical carrier and the optical UWB sideband.

The cost and complexity of this technique can also be further driven down by employing a DFB laser for direct-modulation of the UWB signal instead of external modulation with the MZM, provided the UWB signal is within the modulation bandwidth of the DFB laser.

One concern with this technique is the long-term stability of the optical sources which can be obtained if the sources utilise TEC modules to ensure wavelength stability and accuracy. However, with this technique, down-conversion

of the mm-wave UWB signal to baseband will still be possible as long as the drift (if any) of the received signal is within the bandwidth of the envelope detector.

The experimental setup of technique #3 is shown in Figure 5.31. The UWB signal is generated offline in MATLAB and then loaded into the AWG operating at a sampling rate of 10.8 GS/s. The outputs of the AWG (i.e. the UWB signal and its Hilbert Transform) are amplified by two 16-dB gain, RF amplifiers and then filtered by two 7.5-GHz, LPFs. These filtered signals (Figure 5.32 (a)) are then used as the electrical drives to the same Fujitsu 10-Gbit/s DE-MZM used in section 5.2.2, biased at its quadrature point.

The optical source to the DE-MZM is a tunable laser with linewidth of 800 kHz and centre emission wavelength of 1549.51 nm. An OSSB is thus generated at the output of the MZM. This OSSB signal is combined in a 3-dB optical coupler with another CW signal emitted from another tunable laser with linewidth of 100 kHz and centre emission wavelength of 1550 nm. The frequency difference between the two optical sources is chosen to yield the desired 60-GHz mm-wave carrier frequency.

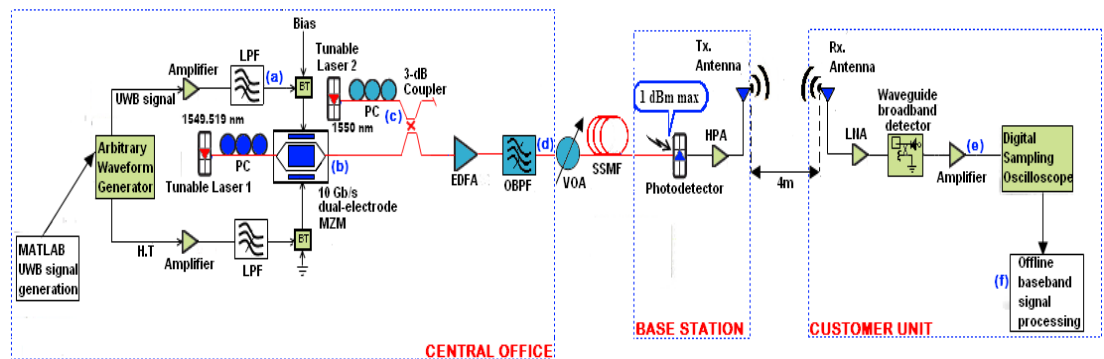


Figure 5.31. Experimental setup of OHD technique. H.T: Hilbert transform. LPF: Low-pass filter. BT: Bias tee. PC: Polarisation controller. MZM: Mach-Zehnder modulator. EDFA: Erbium-doped fibre amplifier. OBPF: Optical band-pass filter. VOA: Variable optical attenuator. SSMF: Standard single-mode fibre. HPA: High-power amplifier. Tx.: Transmit. Rx.: Receive. LNA: Low-noise amplifier.

A polarisation controller ensures maximum coupling of the two optical signals is achieved. The combined optical signals are then amplified by an EDFA before being filtered using a 0.8-nm, tunable OBPF to suppress the out-of-band ASE noise. The optical spectrum of the filtered and combined signals is shown in Figure 5.32 (b). The optical signals are then transmitted through various lengths of SSMF fibre. A VOA is used to maintain a maximum of 1 dBm input to the 70-GHz broadband photodetector located at the base station. After photodetection, the 60-GHz UWB signal is amplified by a 30-dB gain, high-power amplifier (HPA) before being applied to an antenna for up to 4-m wireless transmission. Both the antennas used in the experimental setup are dual-reflector Cassegrain antennas with frequency range of 50-75 GHz, 30-dBi gain and 3-dB beam width of 3.1° .

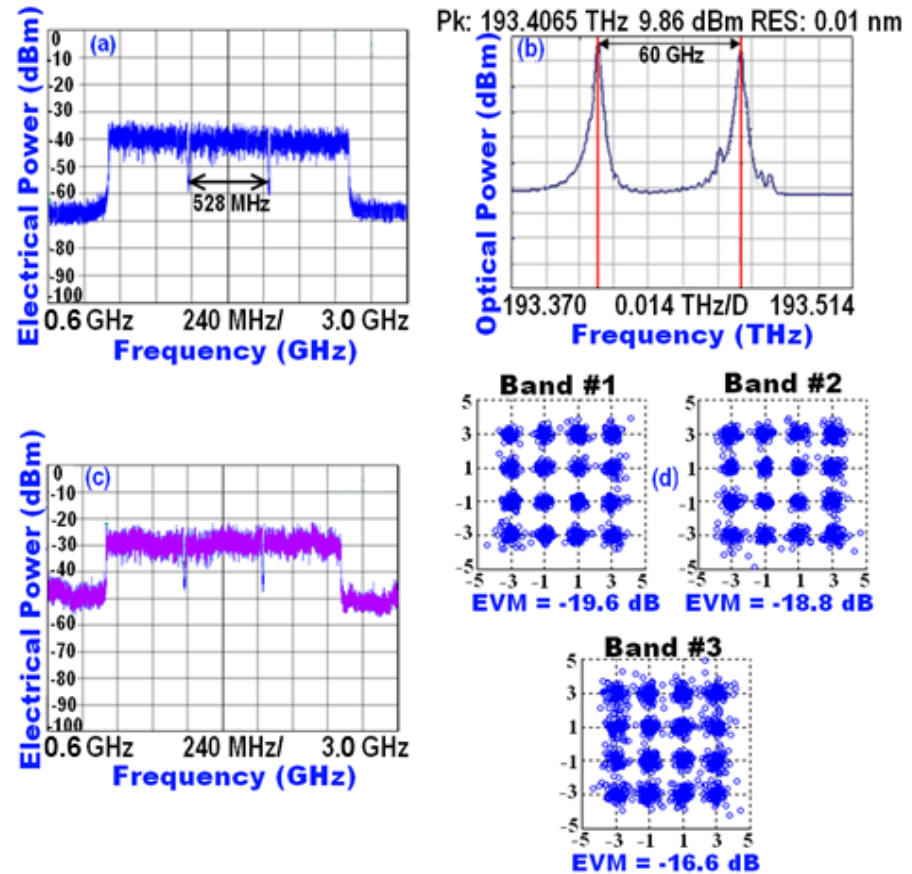


Figure 5.32. (a)-(c) Electrical and optical spectra at corresponding points in experimental setup (shown in Figure 5.21). (d) Equalized constellation diagrams at 1 dBm received optical power for 26-km SSMF and 2-m wireless transmission.

At the customer unit, the received wireless 60-GHz MB-OFDM UWB signal is amplified by a 30-dB gain, low-noise amplifier (LNA). Down-conversion of the mm-wave UWB signal is achieved by linearly detecting its envelope using the waveguide broadband detector (DV-2P) in WR-15 waveguide from Spacek Labs Inc. The down-converted signal is further amplified by a 30-dB gain amplifier with a frequency range of 0.7-4.2 GHz (Figure 5.32 (c)) and then captured by the real-time oscilloscope operated at a sampling rate of 50 GS/s. Figure 5.32 (d) shows the equalized 16-QAM constellation diagrams for a SSMF length of 26 km, received optical power of 1 dBm and a 2-m wireless channel.

A drawback of this technique has to do with the limitations of the envelope detection. This is primarily because the input to the envelope detector has to be properly band-pass filtered around the desired signal to avoid the simultaneous demodulation of unwanted signal components. There could also be additional problems if, because of the wavelength drift of the optical sources, part of the desired received signal drifts out of the bandwidth of the BPF. This is because for the proposed technique to be successful in avoiding the phase noise effects at baseband, the last two terms of (5.48) have to be fed into the envelope detector so the phase noise terms cancel out. Another concern is that the IF bandwidth of the envelope detector has to be sufficiently large enough for the signal to be down-converted.

In the proposed system, the HPA, Cassegrain antennas, and the LNA are all band-limited to within 50-75 GHz, ensuring that signal components outside this frequency range are “filtered” off and will not be transmitted. Hence, we didn’t have to resort to using a mm-wave BPF (which was not available). In addition, by utilising optical sources that have TEC modules, wavelength stability is guaranteed, resulting in negligible drift of the received signal. Finally, the IF bandwidth of the envelope

detector is around 5 GHz, sufficiently large enough for down-converting the UWB signal to baseband. This would allow the envelope detector to operate with data rates as high as 6.6 Gbit/s (i.e. a 3 dB bandwidth which is at least 75% of the data rate), and act as a maximum likelihood demodulator at that data rate [158].

In the subsequent sub-subsections, using the setup as shown in Figure 5.31, the impacts of the various parameters such as wireless distance and received optical power at the photodetector on the system performance will be illustrated.

5.4.1 Impacts of received optical power and fibre transmission

In a similar vein as in sections 5.2.1.5, 5.2.2.3 and 5.2.3.3, the system performance is tested for a variation of the received optical power at a bit rate of 3.84 Gbit/s by tuning the attenuation of the VOA. The peak-to-peak amplitudes of the UWB signals from the AWG are optimised to yield the highest SNR prior to fibre transmission and the wireless distance kept fixed at 2.4 m.

Figure 5.33 shows the EVM variation of the three UWB sub-bands with the received optical power for five optical transmission cases: back-to-back, 10 km, 26 km, 37 km and 48 km of SSMF, with the EVM improving with increasing received optical power, as expected. Figure 5.33 also shows that the system is robust against fibre chromatic dispersion, with hardly any power penalty obtained for the various fibre lengths used. Transmission over longer fibre spans is therefore possible but would be dependent on the available amplification power budget.

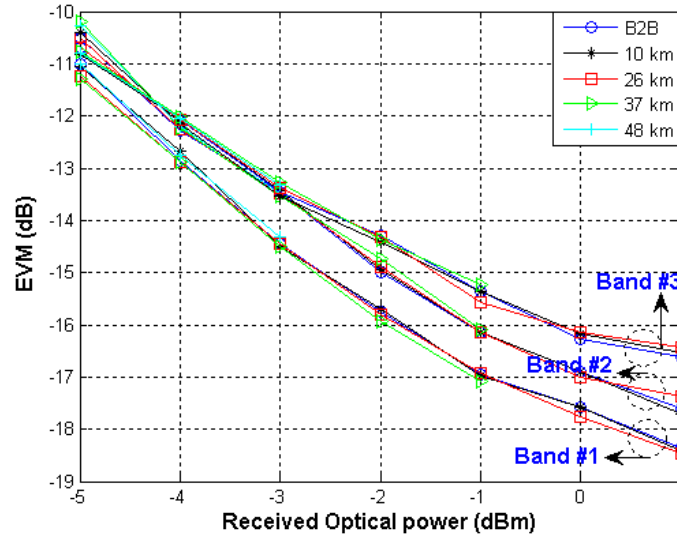


Figure 5.33. EVM of the three UWB sub-bands as a function of received optical power for a fixed wireless distance of 2.4 m and different SSMF lengths.

5.4.2 Impact of wireless transmission

Figure 5.34 shows the wireless experimental setup. The transmit antenna is mounted on a movable base attached to a trolley, while the receive antenna is mounted on a fixed metal base. The photodetector and the HPA are attached to the transmit antenna, while the LNA and the envelope detector are attached to the receive antenna. The distance between the two antennas is measured with the aid of scale rulers connected end-to-end as shown in Figure 5.34.

For the investigation into the impact of the wireless transmission, the fibre length is fixed at 26 km and with all other parameters constant, the wireless distance is varied from 2 to 4 m by carefully moving the transmit antenna away from the receive antenna.

In accordance with Friis transmission formula, the FSPL at distances of 2 and 4 m can be computed using (2.30). In this case,

$$f = \sqrt{(f_{min} \cdot f_{max})} \quad (5.55)$$

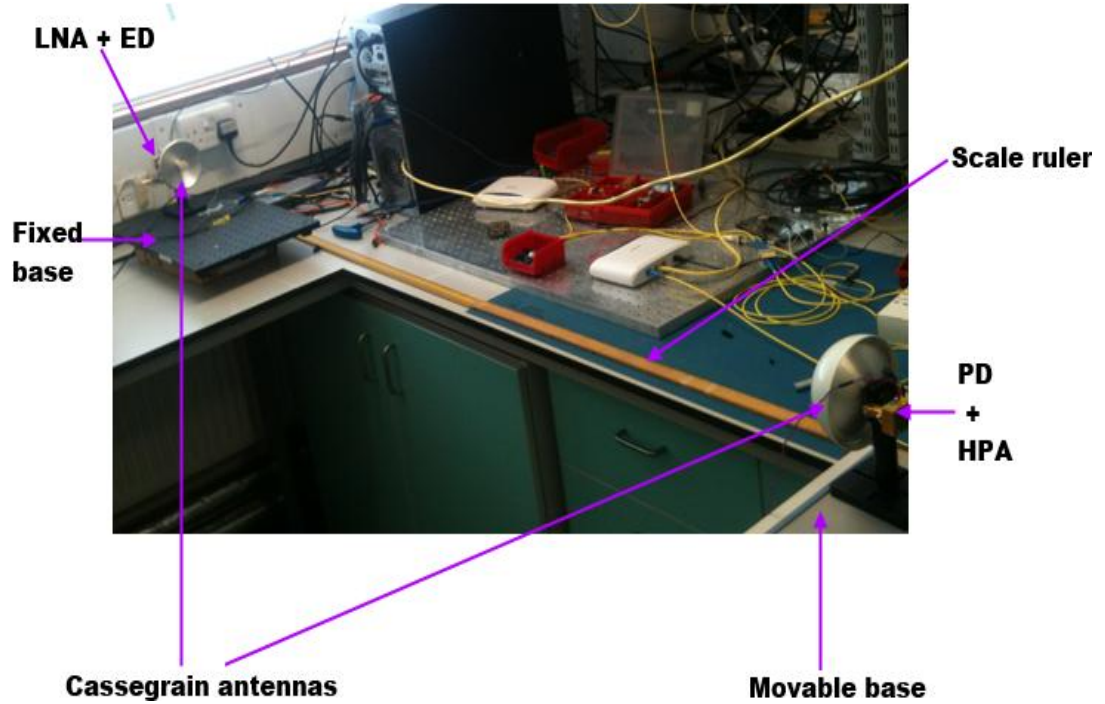


Figure 5.34. Wireless experimental setup. LNA: Low-noise amplifier. ED: Envelope detector. PD: Photodetector. HPA: High-power amplifier.

where $f_{min} = 61$ GHz and $f_{max} = 62.584$ GHz represent the lower and upper cut-off frequencies for the MB-OFDM UWB signal in the 60-GHz band.

Substituting $f = 61.79$ GHz into (2.30), the corresponding values of the FSPL at wireless distances of 2 and 4 m are 74.3 dB and 80.3 dB respectively.

As a result of this FSPL, extra amplification (as compared to having a cable link) would be required for wireless transmission. This amplification is provided by both the HPA and LNA. The EVM is obtained for several wireless distances between 2 and 4m. In addition, the wireless link is replaced with just a single coaxial cable connection between the photodetector and the envelope detector, and the EVM obtained as before.

Figure 5.35 shows the variation of the EVM with the wireless distance where it can be seen that the EVM performance degrades with longer wireless distances due to increase in the FSPL, in agreement with (2.30).

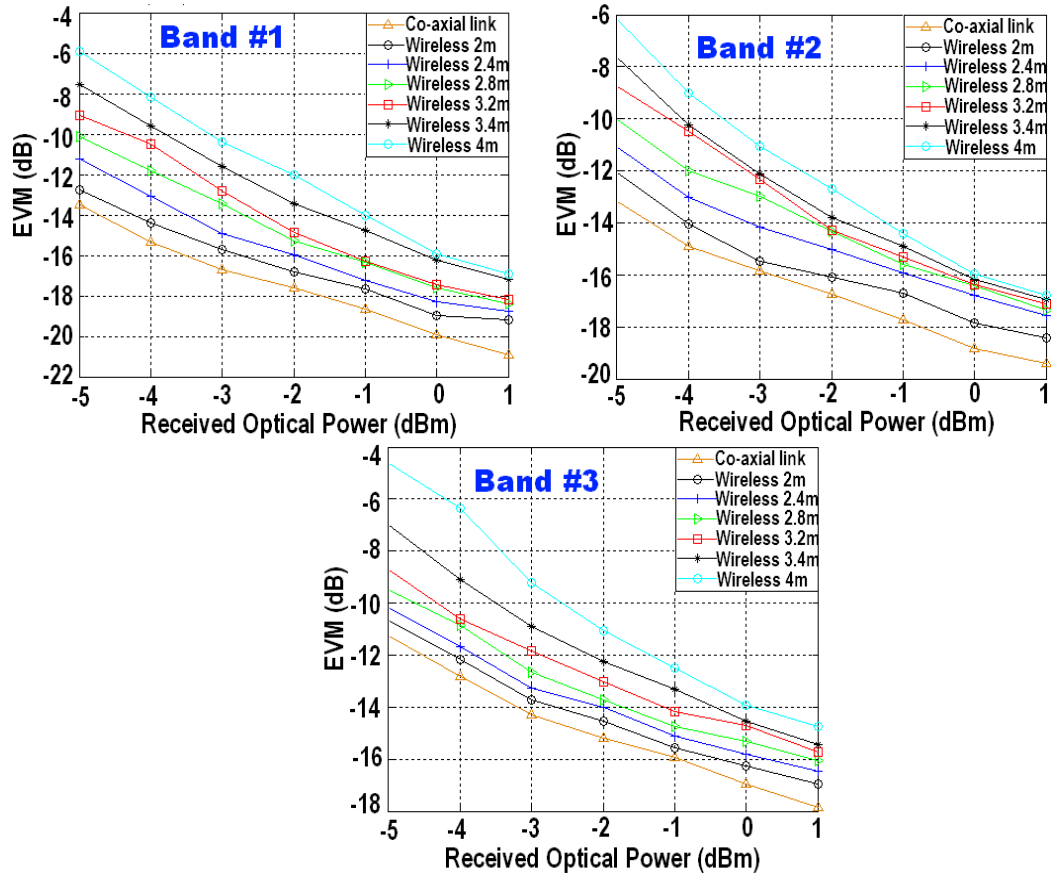


Figure 5.35. EVM as a function of received optical power for a fixed SSMF length of 26 km and different wireless distances (direct coaxial link also included).

5.5 MZM non-linearity compensation using pre-distortion

For majority of the experimental work considered in the previous sections and chapters, the OFDM signals have modulated the lightwave using MZMs. However, as illustrated by the experimental investigations in those sections, the performance of the various RoF systems that utilise these MZMs for electro-optical conversion is strongly dependent on the non-linear distortion induced by the MZMs at high modulation indexes (or drive powers). As stated in section 2.4.5.1, OFDM signals, due to their multi-carrier nature, have a high PAPR. This PAPR, as we demonstrated in section 3.6, is independent of the modulation format employed but increases with the number of OFDM subcarriers used.

The high PAPR required is a challenge in optical communications because MZMs, as shown in section 3.2, have non-linear, peak-limited power transfer characteristics. So, at high modulation indexes, the high amplitude peaks of the OFDM signal start to be clipped due to the MZM non-linearity. Reducing the operating range of the MZM to accommodate the high peaks of the OFDM signal may necessitate optical amplification at the transmitter because of the power efficiency penalty incurred.

PAPR-reduction techniques, including selective mapping, interleaving and partial transmit sequence, which are well known in RF communications, have been recently applied in optical OFDM transmission systems [159]. However, these algorithms introduce undesired effects at the transmitter such as a significant amount of redundancy and coding overhead [160] - [162] and increased computational complexity. An increase in the coding overhead would necessitate a corresponding increase in the sampling rate so as to maintain the bit rate, implying faster DACs would be required. On the other hand, increased computational complexity at the transmitter is not desirable at the speeds at which optical systems are designed to operate [163], [164].

This section focuses on applying digital pre-distortion to the MB-OFDM UWB signals as a linearisation technique to compensate for the MZM non-linearity and improve system performance at high modulation indexes. Previous studies on digital pre-distortion for MZM non-linearity compensation have been focused on CO-OFDM systems [164], [165].

Recently, a digital pre-distorter for direct-detection UWB signals was proposed and simulated in [166]. However, in the expression for the output voltage of the proposed pre-distorter in [166], for the purpose of simplicity and ease of

evaluation, the product of the square of the electrical field at the MZM input and the photodiode responsivity was made equal to 2. Also, the D.C. offset voltage at which maximum transmission is obtained was assumed to be 0. These assumptions will not be consistent in actual MZMs.

In this section, we propose and experimentally demonstrate, for the first time to our knowledge, a digital pre-distortion technique for MZM non-linearity compensation in direct-detection MB-OFDM UWB systems which is valid for any single-electrode MZM.

5.5.1 Digital pre-distorter model

If a single-electrode MZM is operated in the push-pull mode, and the D.C. offset voltage at which maximum transmission is obtained is not assumed to be 0, the relationship between the output and input optical fields of the MZM with the insertion loss neglected, as given in (5.31) can be re-written as:

$$E_o(t) = E_i(t) \cos \left\{ \frac{\pi}{2} \left[\frac{V_{mod}(t) - V_{on}}{V_\pi} \right] \right\} \quad (5.56)$$

where V_{on} is the D.C. offset voltage at which maximum transmission is obtained and all other constants are as defined previously in section 5.2.3.

Consequently, by taking the square of the modulus of the output optical field $E_o(t)$, the power transfer function of the MZM can be obtained as:

$$\frac{P_o(t)}{P_i(t)} = \cos^2 \left(\frac{\pi(V_{mod} - V_{on})}{2V_\pi} \right) \quad (5.57)$$

$$= \frac{1}{2} \left(1 + \cos \left\{ \frac{\pi(V_{mod} - V_{on})}{V_\pi} \right\} \right) \quad (5.58)$$

The mitigation of the MZM non-linearity is achieved by using a digital pre-distorter with a transfer characteristic which is the inverse of the MZM power

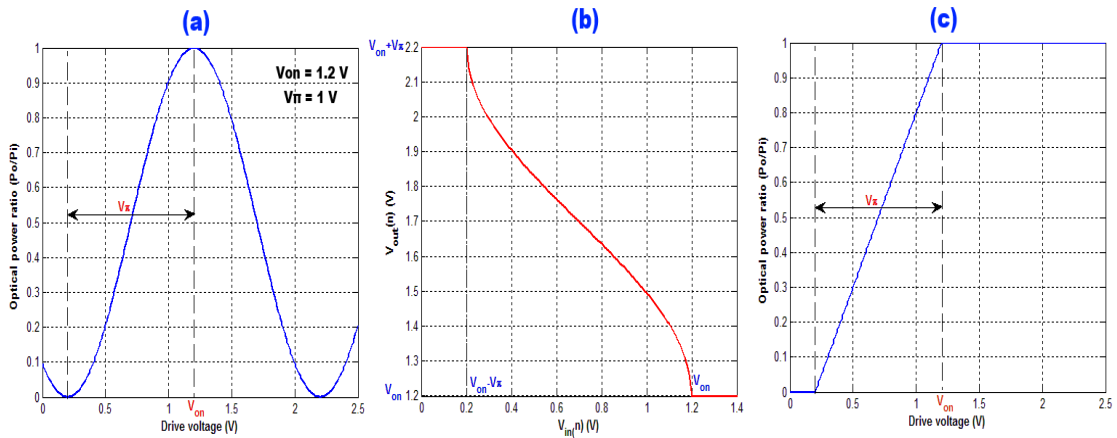
transfer characteristic in (5.58). After some algebraic manipulations, it is easy to show that the pre-distortion transfer function can be expressed as:

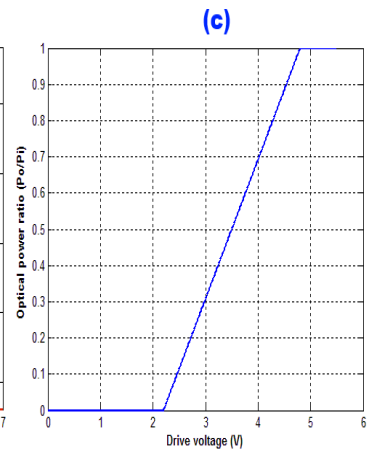
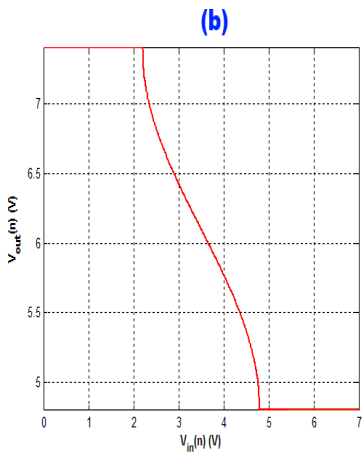
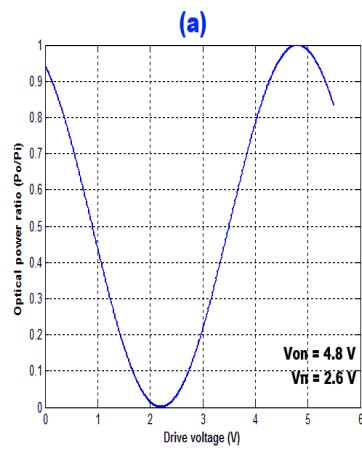
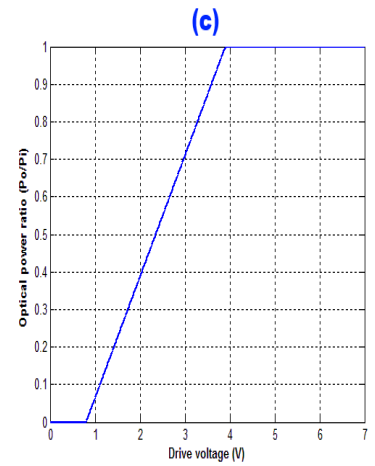
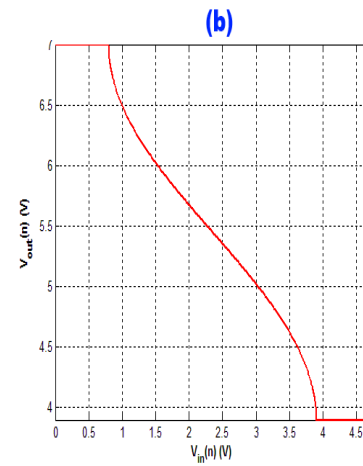
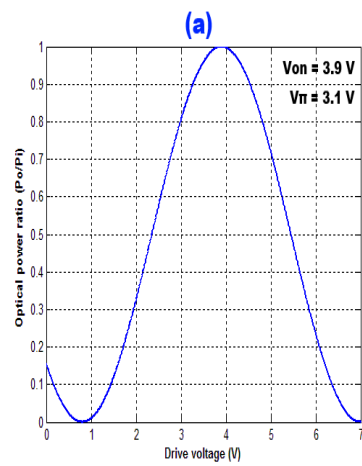
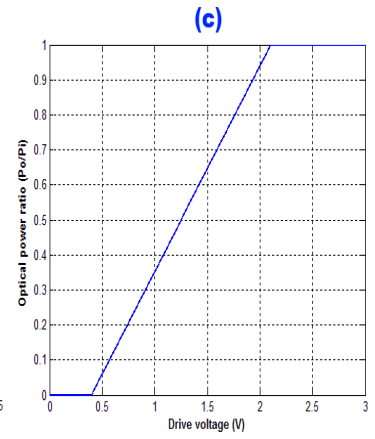
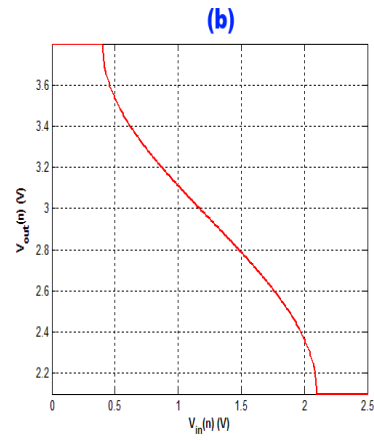
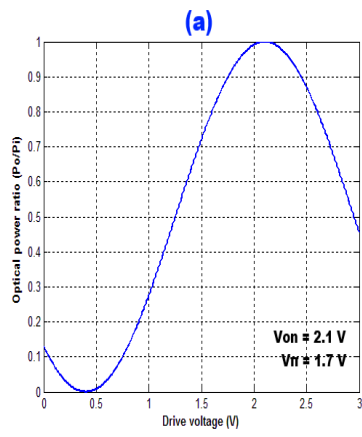
$$V_{out}(n) = \left[\frac{V_{\pi}}{\pi} \cdot \cos^{-1} \left(\frac{2\{V_{in}(n) - (V_{on} - V_{\pi})\}}{\max_n |V_{in}(n)| - (V_{on} - V_{\pi})} - 1 \right) \right] + V_{on} \quad (5.59)$$

where $V_{out}(n)$ and $V_{in}(n)$ are the digital output and input voltages of the pre-distorter respectively.

Since a $\cos^{-1}(\)$ function is defined for argument values between -1 and 1, the value of $V_{out}(n)$ is restricted between V_{on} and $(V_{on} + V_{\pi})$. A combination of the pre-distortion function in (5.59) with the MZM power transfer function in (5.58) results in a linear relationship between the MZM optical intensity and the drive voltage as shown in Figures 5.36 (a)-(c).

Figure 5.36 (c) shows that the region of the MZM response which can be linearised by the digital pre-distorter is limited. Linearisation occurs over the range from $(V_{on} - V_{\pi})$ to V_{on} . The transmission is hard-limited when the drive voltage is outside this range. The results shown in Figure 5.36 also confirm that the pre-distortion function in (5.59) is valid for single-electrode MZMs with different combinations of V_{π} and V_{on} .





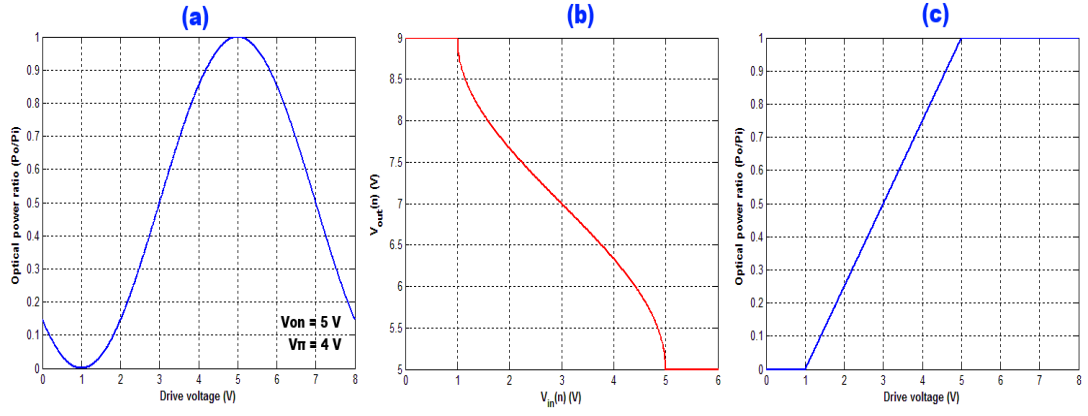


Figure 5.36. (a) MZM Power transfer characteristics (b) Pre-distorter transfer characteristics (c) Compensated transfer characteristics for different values of V_{on} and V_{π} : 1.2 V and 1 V; 2.1 V and 1.7 V; 3.9 V and 3.1 V; 4.8 V and 2.6 V; 5 V and 4 V.

5.5.2 Experimental setup and results for digital pre-distortion

To evaluate the improvement brought about by digital pre-distortion in RoF applications, an experiment is performed based on MB-OFDM UWB RoF transmission. Figure 5.37 shows the experimental setup of the MB-OFDM UWB optical transmission system with digital pre-distortion. The MB-OFDM UWB signal with the first sub-band of band group #1 is generated off-line in MATLAB. This sub-band is 528 MHz wide, centred at a frequency of 3.432 GHz and modulated with 16-QAM. 128 OFDM subcarriers are used and the OFDM symbol duration is 312.5 ns, giving a gross bit rate of 1.28 Gbit/s.

The generated real-valued UWB signal is then passed to the digital pre-distorter to compensate for the non-linearity of the MZM by making use of the transfer function depicted in (5.59). Since the UWB signal is generated offline in MATLAB, the pre-distortion transfer function is also implemented offline in MATLAB. In this case, in (5.59), $V_{in}(n)$ is the generated MB-OFDM UWB signal while $V_{out}(n)$ represents the compensated MB-OFDM UWB signal. Although we have implemented the pre-distortion transfer function offline in MATLAB, in future,

a more practical implementation of the pre-distortion function could be based on look-up tables like those used in [167] and [168] for fibre dispersion compensation.

The MZM used for the experiment is a JDS Uniphase 10-Gbit/s single-electrode amplitude modulator having a 4.5 dB insertion loss, half-wave switching voltage V_{π} of 1.7 V and a V_{on} of 2.1 V. The compensated transfer characteristics of this MZM have already been shown in Figure 5.36.

The time-domain samples of the compensated UWB signal are saved as a single-column ASCII text file and loaded into a Tektronix AWG7122B AWG operating at a sampling rate of 12 GS/s. The filtered UWB signal is then amplified by a 40-dB gain, SHF 84P amplifier. A Picosecond 7.5 GHz LPF is used to filter the alias terms produced from the DAC process at the AWG. The filtered MB-OFDM UWB signal (inset (a) of Figure 5.37) is then used to drive the MZM, biased at its quadrature point.

An RVA placed at the output of the filter enables the RF modulation index of the MZM to be varied. An Anritsu MG9541A tunable laser with centre emission wavelength of 1550 nm and 9.47 dBm output optical power serves as the optical source to the MZM.

The optical DSB-C signal generated at the output of the MZM is amplified by an EDFA to compensate for the insertion loss of all optical components and then a 0.8 nm DiCon tunable OBPF is used to suppress the out-of-band ASE noise.

The filtered optical DSB-C signal as shown in inset (b) of Figure 5.37 is transmitted through 20-km SSMF. A VOA is used to vary the optical attenuation to set the maximum optical power input into a u²t Photonics, XPDV3120R photodetector at 1 dBm.

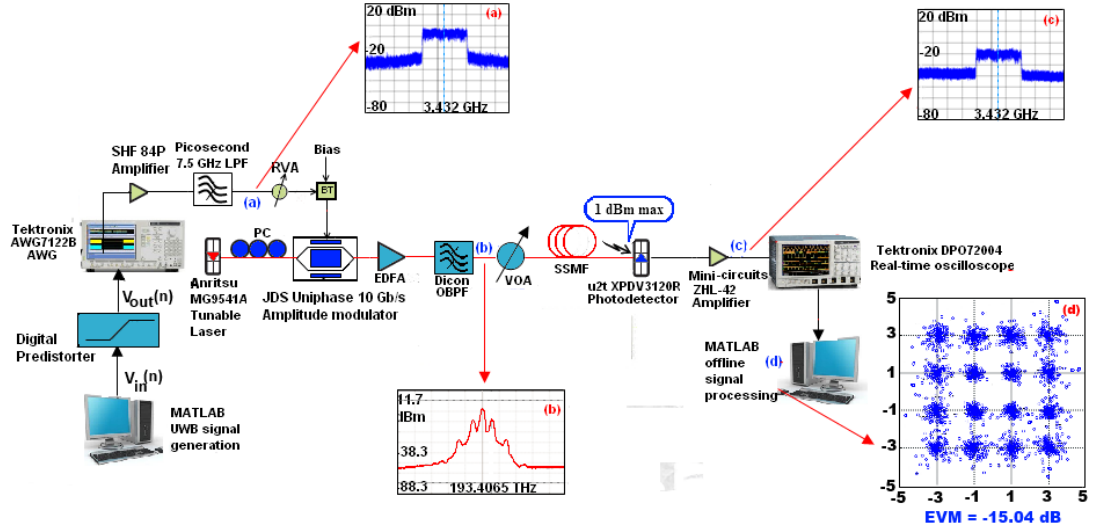


Figure 5.37. Experimental setup for digital pre-distortion. AWG: Arbitrary waveform generator. LPF: Low-pass filter. RVA: RF variable attenuator, BT: Bias tee. PC: Polarization controller. EDFA: Erbium-doped fibre amplifier. OBPF: Optical band-pass filter. VOA: Variable optical attenuator. SSMF: Standard single-mode fibre. Insets (a) – (c): Electrical and optical spectra at corresponding points in the experimental setup. Inset (d): Constellation diagram after 20-km SSMF transmission and at 1 dBm received optical power.

After photodetection, the electrical UWB signal is amplified by a Mini-circuits ZHL-42 amplifier providing 30 dB gain (inset (c) of Figure 5.37) and then captured by a Tektronix DPO 72004 real-time digital sampling oscilloscope operated at a sampling rate of 25 GS/s. Baseband digital signal processing is as usual performed offline in MATLAB. Inset (d) of Figure 5.37 shows the equalised constellation after 20-km SSMF transmission and at 1 dBm received optical power.

For our investigations, the performance of the compensated MB-OFDM UWB signal is compared with that of the uncompensated one, using EVM measurements as the performance metric. With the received optical power held constant at 1 dBm, the UWB drive power is varied by varying the attenuation of the RVA.

Figure 5.38 shows the variation of the EVM with the drive power for 20-km SSMF transmission.

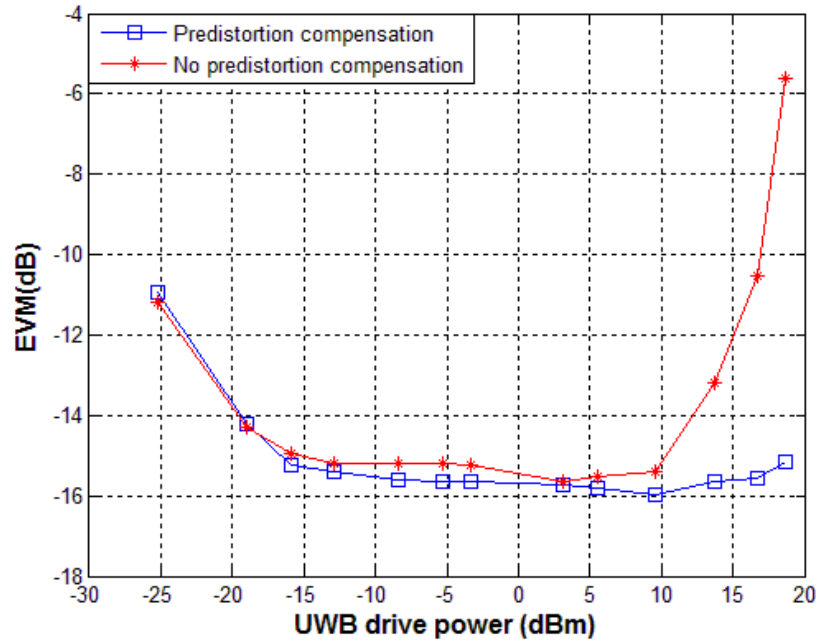


Figure 5.38. EVM vs. UWB drive power: with/without digital pre-distortion compensation.

It can be seen that in accordance with the results presented in the previous chapters, with low values of drive power, the system performance is limited by low SNR, resulting in poor EVM performance. The EVM improves as the drive power is increased but at higher drive powers, the EVM starts to increase as the system performance is degraded due to the MZM non-linear distortion. However, a significant improvement in the EVM at higher drive powers occurs when pre-distortion is applied, permitting higher driving signal amplitudes to be used. The EVM is still less than -15 dB for drive powers up to 18 dBm, around a 9 dB improvement when compared to the uncompensated case.

Also, the optimum drive power for which the minimum EVM is obtained increases when pre-distortion is applied. Without pre-distortion, the optimum drive power is 3 dBm. This optimum drive power increases to 10 dBm when pre-distortion is applied.

5.6 Summary

In this chapter, MB-OFDM UWB operation in the license-free 60-GHz band has been reviewed. Four techniques for up-converting the MB-OFDM UWB signal to the 60-GHz band have been discussed. These techniques have been classified in terms of the underlying modulation/detection principles employed, into intensity modulation – direct detection (IM-DD) and optical heterodyne detection (OHD) techniques. The first three techniques are based on IM-DD while the last technique is based on OHD. For the IM-DD techniques, the MB-OFDM UWB signal drives a different non-linear component – a DFB laser, a DE-MZM and a mixer. The first two IM-DD techniques utilise OFM using either the DFB laser or low-bandwidth DE-MZM for electro-optical conversion, in cascade with a high-bandwidth DE-MZM driven by a 30-GHz LO. The third IM-DD technique achieves mm-wave generation by electrically mixing the MB-OFDM UWB signal with a 60-GHz LO.

Theoretical analyses of the mm-wave generation using the three IM-DD techniques have also been provided in this chapter. For all the techniques, the performance of the 60-GHz MB-OFDM RoF signal in the presence of various parameters including device non-linearities, bias currents and voltages, drive and LO power levels, received optical power and fibre chromatic dispersion has been comprehensively investigated, using EVM measurements as the performance metric. The optimum values for these system parameters have also been demonstrated. It has been shown that the distortion in the RF path is dominated by the first major non-linear component encountered by the driving UWB signal.

The three IM-DD techniques have also been compared in terms of cost, complexity and system performance, especially with regards to fibre transmission. It has been found that technique #1 is the cheapest and simplest to implement.

Technique #3, although having a simple architecture, is disadvantaged by the need for high-bandwidth electrical and electro-optical devices which will drive the cost up. On the other hand, technique #2 requires 2 DE-MZMs and an additional 90° electrical hybrid, making it more complex than techniques #1 and #3.

Technique #2 is robust against fibre chromatic dispersion while techniques #1 and #3 are not; though the fibre transmission distance with technique #3 is more severely limited by chromatic dispersion than technique #1. A fading cycle of 16 km and 2 km is obtained for techniques #1 and #3 respectively.

Techniques #1 and #2 while similar in principle, demonstrate slightly different performances with technique #2 demonstrating superior performance to technique #1 at low drive powers. However, technique #1 demonstrates better robustness to non-linear intermodulation distortion than technique #2.

The OHD technique utilises uncorrelated optical heterodyning with envelope detection to achieve all optical mm-wave generation and detection, without having to resort to using complex optical phase-locked loops or high-frequency microwave sources. Using the proposed OHD technique, multiple wide-band 16-QAM OFDM channels have been successfully transmitted over 48-km SSMF without any chromatic dispersion compensation and a further 4-m wireless distance. The system also demonstrates impressive robustness to phase noise and fibre chromatic dispersion, the only limitation imposed in fibre distribution being the available amplification power budget.

Finally, we have proposed the use of digital pre-distortion to mitigate the MZM non-linear distortion for direct-detection MB-OFDM UWB over fibre transmission systems. Performance analysis shows an increased tolerance to the amplitude of the applied UWB signal as well as increase in the optimum drive power

when pre-distortion is employed. It is observed that for drive powers up to 18 dBm, the EVM is still less than -15 dB when digital pre-distortion is applied, almost a 9 dB improvement when compared to the uncompensated case.

Chapter 6. Concluding remarks and future work

6.1 Thesis summary

Optical OFDM is a fast-progressing and vibrant research field in optical communications. This thesis has investigated the development and implementation of different techniques that apply optical OFDM for multi-Gbit/s communications in the access network. With the aid of mathematical modelling as well as simulation and experimental demonstrations using BER and EVM measurements as figures of merit, the bulk of the work for this thesis has been focused on evaluating the performance of various DD-OOFDM systems which are degraded by various impairments including device non-linearities, adverse operating conditions, electrical and optical power levels, and fibre chromatic dispersion. This investigation has been carried out on various DD-OOFDM architectures in different frequency bands ranging from baseband to millimetre-wave. In addition to performance evaluation, the results of the investigation have enabled us to obtain the optimum parameter values as well as observe the limitations imposed in fibre distribution for all of the considered DD-OOFDM systems.

Finally, system performance improvement of the optical OFDM systems by MZM non-linearity impairment compensation using digital pre-distortion has been considered. Although digital pre-distortion for MZM non-linearity compensation has been carried out in previous studies by various researchers [164], [165], the focus has been on CO-OFDM systems. We have proposed and experimentally demonstrated a novel digital pre-distorter for DD-OOFDM systems which is valid for any single-electrode MZM.

6.2 Main contributions of this thesis

The main contributions of this thesis are as follows:

The evaluation of the system performance of an ECMA-368 compliant MB-OFDM UWB system.

- With focus on the ECMA-368 standard, simulations coupled with experimental validation have been presented to demonstrate the feasibility of using OFDM-based UWB RoF techniques to provide multi-Gbit/s connectivity for bandwidth-intensive applications such as HD audio and video content delivery in FTTH networks.
- Measurements have been taken to evaluate the maximum fibre reach for error-free operation (BER of 10^{-9}) for the MB-OFDM UWB system. It has been established that with 4 dBm optical power launched in the fibre, for error-free operation, the maximum SSMF reach for MB-OFDM UWB is 50 km.
- The effects of various parameters including the UWB drive power, chromatic dispersion and received optical power on the MB-OFDM UWB system have been investigated. In addition, for an OSSB-modulated MZM, an optimum modulation index of -4.58 dB has been established for the MB-OFDM UWB RoF system.

The applicability of the 60-GHz band for MB-OFDM UWB operation.

- The applicability of the license-free 60-GHz band for MB-OFDM UWB operation has been explored. We have analytically illustrated and experimentally demonstrated three techniques based on IM-DD for generating a 60-GHz MB-OFDM UWB signal. In each of these three techniques, the modulating MB-OFDM UWB signal drives a different type of non-linear component – a laser, a MZM and a mixer.

- A comparative study of the three IM-DD techniques based on transmission performance, chromatic dispersion robustness, cost and complexity has been presented. We have experimentally demonstrated that the system performance of the various techniques is limited by the first major non-linear component encountered by the driving UWB signal.

- A simple 60-GHz MB-OFDM UWB RoF system employing a combination of uncorrelated optical heterodyning and envelope detection has been proposed. Mathematical analysis has demonstrated that the proposed system is capable of avoiding the laser phase noise effects at baseband.

Proof-of-concept experimental demonstration of the proposed system have also been carried out for the successful transmission of a 3.84 Gbit/s, 16-QAM MB-OFDM UWB signal over up to 48-km standard single-mode fibre and a further 4-m wireless channel.

In particular, it has been established that photonic millimetre-wave signal generation and detection can be achieved without the need for complex optical phase-locked loops and high-frequency microwave sources.

The evaluation of the system performance of a DD-OOOFDM baseband system in the presence of MZM non-linear distortion.

- It has been shown that the system performance of DD-OOOFDM in the presence of the MZM non-linear distortion can be improved by proper biasing and selection of appropriate drive to the MZM. In particular, to obtain an EVM penalty (due to the MZM non-linear distortion) of < 2 dB the normalised MZM drive level has to be ≤ 0.11 ; and the normalised MZM D.C. bias level needs to be within 0.06 of the normalised quadrature bias voltage value of 0.5.

- Simulation and experimental investigations have shown that to improve the tolerance to the MZM non-linear distortion, it would be beneficial to reduce the number of subcarriers (due to reduction of the system PAPR), or employ lower level modulation formats. It has also been shown that the benefit of operating with a reduced number of subcarriers applies only if the length of fibre is < 50 km. For longer fibre lengths > 450 km however, it would be more practical to operate with a large number of subcarriers because of the power penalties caused by the pulse spreading brought about by the fibre chromatic dispersion.
- It has been demonstrated that by operating at a quadrature bias, the spectral efficiency of the DD-OFDM system can be improved by reducing the width of the guard band by at least 50%. This is because of the low level of intermodulation distortion products present at quadrature bias.

Digital pre-distortion in DD-OFDM systems.

- A novel digital pre-distorter with a transfer characteristic which is the inverse of the MZM power transfer characteristics has been proposed for mitigating MZM non-linear distortion in DD-OFDM systems. In addition, the proposed distorter is valid for any single-electrode MZM with any combination of V_{on} and V_{π} .
- Experimental demonstration of this digital pre-distortion technique in a MB-OFDM UWB RoF system has shown an increased tolerance to the amplitude of the applied UWB signal as well as increase in the optimum drive power when pre-distortion is employed. It has also been observed that for drive powers up to 18 dBm, the EVM is still less than -15 dB when digital pre-distortion is applied, almost a 9 dB improvement when compared to the uncompensated case.

6.3 Future work

A number of further areas for investigation are suggested as a result of the work carried out during this Ph.D., including:

- Bi-directional MB-OFDM UWB RoF transmission is an obvious next stage. If the same optical wavelength is used in the bi-directional transmission, the impacts of impairments such as Rayleigh back scattering and stimulated Brillouin on the system performance would be important investigations.
- In order to further save cost for potential future mass deployment of 60-GHz MB-OFDM UWB RoF systems based on the proposed OHD technique, the optical heterodyning of two DFB lasers can be considered, instead of using a laser and a MZM. It is envisaged that since the proposed OHD technique avoids the laser noise effects as baseband, the non-narrow linewidth of such DFB lasers would not be a serious detriment to system performance.
- The combined optical access and wireless transmission of uncompressed HD video in the 60-GHz band using the IM-DD or OHD techniques can also be considered.
- Extend the digital pre-distortion technique for a conventional DE-MZM and evaluate the operational limit of the pre-distortion technique.

References

- [1] A. J. Lowery, L. Dui and J. Armstrong, "Orthogonal frequency division multiplexing for adaptive dispersion compensation in long haul WDM systems," in *Proc. OFC/NFOEC 2006*, pp. 1-3, paper PDP39.
- [2] I. B. Djordjevic and B. Vasic, "Orthogonal frequency division multiplexing for high-speed optical transmission," *Opt. Exp.*, vol. 14, no. 9, pp. 3767-3775, Apr. 2006.
- [3] W. Shieh, and I. B. Djordjevic, *OFDM for optical communications*. Academic Press, Oct. 29, 2009.
- [4] W. Shieh, X. Yi, and Y. Tang, "Transmission experiment of multi-gigabit coherent optical OFDM systems over 1000km SSMF fibre," *Electron. Lett.*, vol. 43, no. 3, pp. 183-184, Feb. 2007.
- [5] D. R. Goff, and K. S. Hansen, *Fiber optic reference guide: a practical guide to communications technology*. Focal Press, Mar. 15, 2002.
- [6] H. Bulow, F. Buchali, and A. Klekamp, "Electronic dispersion compensation," *J. Lightw. Technol.*, vol. 26, no. 1, pp. 158 - 167, Jan. 2008.
- [7] A. Ali, H. Paul, J. Leibrich, W. Rosenkranz, and K-D. Kammeyer, "Optical biasing in direct detection optical-OFDM for improving receiver sensitivity," in *Proc. OFC/NFOEC 2010*, pp. 1-3, paper JThA12.
- [8] J. K. K. Rhee, S. J. Lim, and M. Kserawi, "All optical OFDM transmission systems," in *Proc. ACP 2011*, pp. 1-6.
- [9] K. Yonenaga, *et al.*, "100 Gbit/s all-optical OFDM transmission using 4x25 Gbit/s optical duobinary signals with phase-controlled optical sub-carriers," in *Proc. OFC/NFOEC 2008*, pp. 1-3, paper JThA48.
- [10] K. Lee, T. T. Chan, and J. K. Rhee, "All optical discrete Fourier transform processor for 100 Gbps OFDM transmission," *Opt. Exp.*, vol. 16, no. 6, pp. 4023-4028, Mar. 2008.
- [11] K. Takiguchi, M. Oguma, T. Shibata, and H. Takahashi, "Optical OFDM demultiplexer using silica PLC based optical FFT circuit," in *Proc. OFC/NFOEC 2009*, pp. 1-3, paper OWO3.
- [12] Y. K. Huang, D. Qian, R. E. Saperstein, P. N. Ji, N. Cvijetic, L. Xu, and T. Wang, "Dual-polarization 2x2 IFFT/FFT optical signal processing for 100-Gb/s QPSK-PDM all-optical OFDM," in *Proc. OFC/NFOEC 2009*, pp. 1-3, paper OTuM4.
- [13] Y. K. Huang, R. Saperstein, and T. Wang, "All-optical OFDM transmission with coupler-Based IFFT/FFT and pulse interleaving," in *Proc. LEOS 2008*, pp. 408-409, paper TuFF2.
- [14] A. Caballero, *et al.*, "High capacity 60 GHz and 75-110 GHz band links employing all-optical OFDM generation and digital coherent detection," *J. Lightw. Technol.*, vol. 30, no. 1, pp. 147-155, Jan. 2012.

- [15] Y. K. Huang, *et al.*, "Transmission of spectral efficient super-channels using all-optical OFDM and digital coherent receiver technologies," *J. Lightw. Technol.*, vol. 29, no. 24, pp. 3838-3844, Dec. 2011.
- [16] N. Cvijetic, "OFDM for next-generation optical access networks," *J. Lightw. Technol.*, vol. 30, no. 24, pp. 384-398, Feb. 2012.
- [17] R. Llorente, *et al.*, "Optical distribution of OFDM and impulse-radio UWB in FTTH networks," in *Proc. OFC/NFOEC 2008*, pp. 1-3, paper JWA109.
- [18] Federal Communications Commission, "Revision of part 15 of the Commission's rules regarding ultra-wideband transmission systems," FCC, Washington, DC, Tech. Rep. FCC 02-48, Apr. 2002.
- [19] T. Lunttila, S. Iraji, and H. Berg, "Advanced coding schemes for a multiband OFDM ultrawideband system towards 1 Gbps," in *Proc. CCNC 2006*, pp. 553-557.
- [20] K. M. Strohm, R. Schneider, and J. Wenger, "KOKON: A joint project for the development of 79 GHz automotive radar sensors," in *Proc. IRS 2005*, pp. 1526-1529.
- [21] A. Paller, *et al.*, "First results from car-to-car and car-to-infrastructure radio channel measurements at 5.2 GHz," in *Proc. PIMRC 2007*, pp. 1-5.
- [22] M. N. Sakib, *et al.*, "Impact of optical transmission on multiband OFDM ultra-wideband wireless system with fiber distribution," *J. Lightw. Technol.*, vol. 27, no. 18, pp. 4112-4123, Sep. 2009.
- [23] S-K. Yong, P. Xia, and A. V. Garcia, *60 GHz-technology for Gbps WLAN and WPAN: from theory to practice*. John Wiley & Sons Ltd, Dec. 1, 2010.
- [24] Corning Inc., "Broadband technology overview," white paper, Jun. 2005.
- [25] T. Koonen, "Fiber to the home/fiber to the premises: what, where, and when?," *Proc. IEEE*, vol. 94, no. 5, pp. 911-934, May 2006.
- [26] N. J. Frigo, *et al.*, "Demonstration of performance-tiered modulators in a WDM PON with a single shared source," in *Proc. ECOC 1995*, pp. 441-444.
- [27] N. J. Frigo, P. P. Iannone, and K. C. Reichmann, "Spectral slicing in WDM passive optical networks for local access," in *Proc. ECOC 1998*, pp. 119-120.
- [28] D. K. Jung, *et al.*, "Wavelength-division-multiplexed passive optical network for FTTx," in *Proc. OECC 2005*, pp. 380-381, paper 7A3-6.
- [29] R. Ramaswami, K. N. Sivarajan, and G. H. Sasaki, *Optical networks: a practical perspective*. Morgan Kaufmann Publishers, Jul. 16, 2009.
- [30] A. Ng'oma, "Radio-over-fibre technology for broadband wireless communication systems," Ph.D. thesis, Technische Universiteit Eindhoven, Jun. 2005.
- [31] D. Wake, and K. Beachman, "A novel switched fibre distributed antenna system," in *Proc. ECOC 2004*, vol. 5, pp. 132-135.
- [32] H. T. Friis, "A note on a simple transmission formula," *Proc. IRE*, vol. 34, no. 5, pp. 254-256, May 1946.
- [33] Unlocking the capacity of optical communications, UNLOC. [Online]. Available: <http://www.unloc.net/> [Accessed Jun. 24, 2013].

- [34] G. H. Smith, D. Novak, and Z. Ahmed, "Overcoming chromatic-dispersion effects in fiber-wireless systems incorporating external modulators", *IEEE Trans. Microw. Theory Tech.*, vol. 45, no. 8, pp. 1410-1415, Aug. 1997.
- [35] U. Gliese, S. Norskov, and T. N. Nielsen, "Chromatic dispersion in fiber-optic microwave and millimetre-wave links", *IEEE Trans. Microw. Theory Tech.*, vol. 44, no. 10, pp. 1410-1415, Oct. 1996.
- [36] B. Pal, *Frontiers in guided wave optics and optoelectronics*. InTech, Feb. 1, 2010.
- [37] J. Capmany, and D. Novak, "Microwave photonics combines two worlds," *Nat. Phot.*, vol. 1, pp. 319-330, Jun. 2007.
- [38] CommScope Inc in-building wireless solutions [Online]. Available: http://docs.commscope.com/Public/InBuilding_Wireless_Solutions_Brochure.pdf/ [Accessed Jun. 24, 2013].
- [39] CommScope Inc solutions by market [Online]. Available: <http://www.commscope.com/systimax/eng/solutions/index.html> [Accessed Jun. 24, 2013].
- [40] N. J. Gomes, P. P. Monteiro, and Atilio Gameiro, *Next generation wireless communications using radio over fiber*. John Wiley & Sons, Aug. 15, 2012.
- [41] M. Tur, L. Yaron, and O. Raz, "Photonic technologies for antenna beamforming," in *Proc. OFC/NFOEC 2011*, pp. 1-3, paper OThA6.
- [42] R. Rotman, S. Rotman, W. Rotman, O. Raz, and M. Tur, "Wideband RF beamforming: the Rotman lens vs. photonic beamforming," in *Proc. APS 2005*, vol. 2B, pp. 23–26.
- [43] B. Vidal, M. A. Piqueras, and J. Martí, "Multibeam photonic beamformer based on optical filters," *Electron. Lett.*, vol. 42, no. 17, pp. 980–981, Aug. 2006.
- [44] L. Yaron, R. Rotman, S. Zach, and M. Tur, "Photonic beamformer receiver with multiple beam capabilities," *IEEE Photon. Technol. Lett.*, vol. 22, no. 23, pp. 1723-1725, Dec. 2010.
- [45] J. L. Corral, J. Martí, J. M. Fuster, and R. I. Laming, "True time-delay scheme for feeding optically controlled phased-array antennas using chirped-fiber gratings," *IEEE Photon. Technol. Lett.*, vol. 9, no. 11, pp. 1529–1531, Nov. 1997.
- [46] M. Y. Chen, H. Subbaraman, and R. T. Chen, "Photonic crystal fiber beamformer for multiple x-band phased-array antenna transmissions," *IEEE Photon. Technol. Lett.*, vol. 20, no. 5, pp. 375-377, Mar. 2008.
- [47] R.-J. Essiambre, G. Kramer, P. J. Winzer, G. J. Foschini, and B. Goebel, "Capacity limits of optical fiber networks," *J. Lightw. Technol.*, vol. 28, no. 4, pp. 662–701, Feb. 2010.

- [48] S. L. Jansen, I. Morita, T. C. W. Schenk, and H. Tanaka, "121.9-Gb/s PDM-OFDM transmission with 2-b/s/Hz spectral efficiency over 1000 km of SSMF," *J. Lightw. Technol.*, vol. 27, no. 3, pp. 177–188, Jan. 2009.
- [49] W. Shieh, Q. Yang, and Y. Ma, "107 Gb/s coherent optical OFDM transmission over 1000-km SSMF fiber using orthogonal band multiplexing," *Opt. Exp.*, vol. 16, no. 9, pp. 6378–6386, Apr. 2008.
- [50] A. Sano, *et al.*, "No-guard-interval coherent optical OFDM for 100-Gb/s long-haul WDM transmission," *J. Lightw. Technol.*, vol. 27, no. 16, pp. 3705–3713, Aug. 2009.
- [51] T. Keller and L. Hanzo, "Adaptive multicarrier modulation: A convenient framework for time-frequency processing in wireless communications," *Proc. IEEE*, vol. 88, no. 5, pp. 611–640, May 2000.
- [52] R. V. Nee, and R. Prasad, *OFDM for wireless multimedia communications*. Artech House Publishers, Dec. 31, 1999.
- [53] R. W. Chang, "Synthesis of band-limited orthogonal signals for multichannel data transmission," *Bell System Technical Journal*, vol. 55, pp. 1775–1796, 1966.
- [54] S. B. Weinstein, and P. M. Ebert, "Data transmission by frequency division multiplexing using the discrete Fourier transform," *IEEE Trans. Commun. Technol.*, vol. 19, no. 5, pp. 628–634, Oct. 1971.
- [55] D. H. Bailey, and P. N. Swartztrauber, "The fractional Fourier transform and applications," *Society for Industrial and Applied Mathematics Review*, vol. 33, no. 3, pp. 389–404, Sep. 1991.
- [56] J. Armstrong, "OFDM for optical communications," *J. Lightw. Technol.*, vol. 27, no. 3, pp. 189–204, Feb. 2009.
- [57] B. Goebel, "PAPR reduction techniques for coherent optical OFDM transmission," in *Proc. ICTON 2009*, pp. 1–4, paper Mo.B2.4.
- [58] W. Shieh, H. Bao, and Y. Tang, "Coherent optical OFDM: theory and design", *Opt. Exp.*, vol. 16, no. 2, pp. 842–859, Jan. 2008.
- [59] S. L. Jansen, "Coherent optical 25.8-Gb/s OFDM transmission over 4160-km SSMF," *J. Lightw. Technol.*, vol. 26, no.1, pp. 6–15, Jan. 2008.
- [60] B. J. C. Schmidt, A. J. Lowery, and J. Armstrong, "Experimental demonstrations of electronic dispersion compensation for long-haul transmission using direct-detection optical OFDM", *J. Lightw. Technol.*, vol. 26, no. 1, pp. 196–202, Jan. 2008.
- [61] A. J. Lowery, "Improving sensitivity and spectral efficiency in direct-detection optical OFDM systems," in *Proc. OFC/NFOEC 2008*, pp. 1–3, paper OMM4.
- [62] W. Shieh, and C. Athaudage, "Coherent optical orthogonal frequency division multiplexing," *Electron. Lett.*, vol. 42, no. 10, pp. 587–589, May 2006.
- [63] X. Liu, *et al.*, "Transmission of a 448-Gb/s reduced-guard-interval CO-OFDM signal with a 60-GHz optical bandwidth over 2000 km of ULAF and five 80-GHz-grid ROADMs," in *Proc. OFC/NFOEC 2010*, pp. 1–3, paper PDPC2.

- [64] S. Chandrasekhar, X. Liu, B. Zhu, and D. W. Peckham, "Transmission of a 1.2-Tb/s 24-carrier no-guard-interval coherent OFDM superchannel over 7200-km of ultra-large-area fiber," in *Proc. ECOC 2009*, pp. 1-2, paper PD2.6.
- [65] X. Yi, N. K. Fontaine, R. P. Scott, and S. J. Ben Yoo, "Tb/s coherent optical OFDM systems enabled by optical frequency combs," *J. Lightw. Technol.*, vol. 28, no. 14, pp. 2054–2061, Jul. 2010.
- [66] M. Luo, *et al.*, "4 × 1.93 Tbit/s 8-PSK DFT-S coherent optical OFDM transmission over 2240 km SSMF," *Electron. Lett.*, vol. 48, no. 23, pp. 1484-1486, Nov. 2006.
- [67] M. Cvijetic, *coherent and nonlinear lightwave communications*. Boston, MA: Artech House, Dec. 1996.
- [68] G. Colavolpe, T. Foggi, E. Forestieri, and M. Secondini, "Impact of phase noise and compensation techniques in coherent optical systems," *J. Lightw. Technol.*, vol. 29, no. 18, pp. 2790-2800, Sep. 2011.
- [69] X. Yi, W. Shieh, and Y. Tang, "Phase estimation for coherent optical OFDM," *IEEE Photon. Technol. Lett.*, vol. 19, no. 12, pp. 919–921, Jun. 2007.
- [70] X. Liu, *et al.*, "3 485-Gb/s WDM transmission over 4800 km of ULAF and 12 100-GHz WSSs using CO-OFDM and single coherent detection with 80-GS/s ADCs," in *Proc. OFC 2011*, pp. 1-3, paper JThA037.
- [71] Q. Zhuge, C. Chen, and D. V. Plant, "Dispersion-enhanced phase noise effects on reduced-guard-interval CO-OFDM transmission," *Opt. Exp.*, vol. 19, no. 5, pp. 4472–4484, Feb. 2011.
- [72] Q. Zhuge, M. H. Morsy-Osman, and D. V. Plant, "Low overhead intra-symbol carrier phase recovery for reduced-guard-interval CO-OFDM," *Opt. Exp.*, vol. 31, no. 8, pp. 1158–1169, Apr. 2013.
- [73] D. Breuer, *et al.*, "Opportunities for next-generation optical access," *IEEE Commun. Mag.*, vol. 49, no. 2, pp. 17–24, Feb. 2011.
- [74] J. Kani, "Next-generation PONs: An operator's view," in *Proc. ECOC 2009*, pp. 1-2, paper 5.7.4.
- [75] P. Iannone and K. Reichmann, "Optical access beyond 10 Gb/s PON," in *Proc. ECOC 2010*, pp. 1-2, paper Tu.B.3.1.
- [76] D. Breuer, R. Hülsermann, C. Lange, T. Monath, and E. Weis, "Architectural options and challenges for next generation optical access," in *Proc. ECOC 2010*, pp. 1-2, paper Mo.2.B.1.
- [77] D. Qian, J. Hu, P. Ji, T. Wang and N. Cvijetic, "10-Gb/s OFDMA-PON for delivery of heterogeneous services," in *Proc. OFC/NFOEC 2008*, pp. 1-3, paper OWH4.
- [78] L. Xiu, D. Qian, J. Hu, W. Wei and T. Wang, "OFDMA-based passive optical networks (PON)," in *Proc. LEOSST 2008*, pp. 159-160, paper TuE3.1.
- [79] D. Qian, N. Cvijetic, H. Junqiang and T. Wang, "A novel OFDMA-PON architecture with source-free ONUs for next-generation optical access Networks," *IEEE Photon. Technol. Lett.*, vol. 21, no. 17, pp. 1265-1267, Sep. 2009.
- [80] C. W. Chow, *et al.*, "WDM extended reach passive optical networks using OFDM-QAM," *Opt. Exp.*, vol. 16, no. 16, pp. 12096-12101, Aug. 2008.

- [81] D. Qian, N. Cvijetic, H. Junqiang and W. Ting, "40-Gb/s MIMO-OFDM-PON using polarization multiplexing and direct-detection," in *Proc. OFC/NFOEC 2009*, pp. 1-3, paper OMV3.
- [82] T. Duong, *et al.*, "Experimental demonstration of 10 Gb/s upstream transmission by remote modulation of 1 GHz RSOA using adaptively modulated optical OFDM for WDM-PON single fibre architecture," in *Proc. ECOC 2008*, pp. 1-2, paper Th.3.F.1.
- [83] W. Wei, *et al.*, "PONIARD: A Programmable Optical Networking Infrastructure for Advanced Research & Development of Future Internet," *J. Lightw. Technol.*, vol. 27, no. 3, pp. 233-241, Feb. 2009.
- [84] EU FP7 Project, ACCORDANCE (A Converged Copper-Optical-Radio OFDMA-based access Network with high Capacity and Flexibility): Deliverable 5.4 (D5.4) [Online]. Available: <http://ict-accordance.eu> [Accessed Jul. 10, 2013].
- [85] K. Kanonakis, *et al.*, "An OFDMA-based optical access network architecture exhibiting ultra-high capacity and wireline-wireless convergence," *IEEE Commun. Mag.*, vol. 50, no. 8, pp. 71-78, Aug. 2012.
- [86] R. Kohno, "State of arts in ultra wideband (UWB) wireless technology and global harmonization," in *Proc. EMC 2004*, vol. 2, pp. 1093-1099, Oct. 2004.
- [87] R. Llorente, *et al.*, "Optical distribution of OFDM and impulse-radio UWB in FTTH networks," in *Proc. OFC/NFOEC 2008*, pp. 1-3, paper JWA109.
- [88] Multi-Band OFDM physical layer proposal for IEEE 802.15 Task Group 3a IEEE P802.15 Working Group for WPAN, 2004.
- [89] European Computer Manufacturers' Association, "High rate ultra wideband PHY and MAC standard," Ecma International Std. ECMA-368, Dec. 2008.
- [90] W. P. Siriwongpairat, W. Su, M. Olfat, and K. J. R. Liu, "Multiband-OFDM MIMO coding framework for UWB communication systems," *IEEE Trans. Signal Process.*, vol. 54, no. 1, pp. 214-224, Jan. 2006.
- [91] A. Stephan, J-F. Helard, and B. Uguen, "MIMO UWB systems based on linear precoded OFDM for home gigabit applications," in *Proc. GLOBECOM 2008*, pp. 1-6.
- [92] V. P. Tran, and A. Sibille, "Spatial multiplexing in UWB MIMO communications," *Electron. Lett.*, vol. 42, no. 16, pp. 931-932, Aug. 2006.
- [93] A. Tyagi, and R. Bose, "A new distance notion for PPAM space-time trellis codes for UWB MIMO communications," *IEEE Trans. Commun.*, vol. 55, no. 7, pp. 1279-1282, Jul. 2007
- [94] T. Kaiser, F. Zheng, and E. Dimitrov, "An overview of ultra-wide-band systems with MIMO," *Proc. IEEE*, vol. 97, no. 2, pp. 285-312, Feb. 2009.
- [95] C-C. Chong, F. Watanabe, and H. Inamura, "Potential of UWB technology for the next generation wireless communications," in *Proc. ISSSTA 2006*, pp. 422-429.
- [96] WiMedia Alliance. (January 2009). Regulatory Status. [Online]. Available: <http://www.wimedia.org> [Accessed Jan. 21, 2013].

- [97] S. K. Yong, and C-C. Chong, "An overview of multigigabit wireless through millimeter wave technology: potentials and technical challenges," *EURASIP J. Wireless Commun. and Netw.*, vol. 2007, article ID 78907, pp. 1-10, 2007.
- [98] M. Matin, *Ultra wideband communications: novel trends – system, architecture and implementation*. InTech, Jul. 27, 2011.
- [99] WirelessHD, LLC. [Online]. Available: <http://www.wirelesshd.org> [Accessed Jan. 21, 2013].
- [100] European Computer Manufacturers' Association, "High rate 60 GHz PHY, MAC and PAL standard," Ecma International Std. ECMA-387, Dec. 2010.
- [101] "802.15.3c-2009, IEEE Standard for Information technology - Telecommunications and information exchange between systems - local and metropolitan area networks – specific requirements. Part 15.3: wireless medium access control (MAC) and physical layer (PHY) Specifications for high rate wireless personal area networks (WPANs) Amendment 2: Millimeter-wave-based alternative physical layer extension," Oct. 2009.
- [102] Wireless Gigabit Alliance. [Online]. Available: <http://wirelessgigabitalliance.org> [Accessed Jan. 21, 2013].
- [103] R. C. Daniels, and R. W. Heath, "60 GHz wireless communications: emerging requirements and design considerations," *IEEE Veh. Technol. mag.*, vol. 2, no. 3, pp. 41-50, Sept. 2007.
- [104] A. C. Valdez, "Analysis of atmospheric effects due to atmospheric oxygen on a wideband digital signal in the 60 GHz band," Master's thesis, Virginia Polytechnic Institute and State University, 2001.
- [105] F. Giannetti, M. Luise, and R. Reggiannini, "Mobile and personal communications in 60 GHz band: A survey," *Wireless Pers. Commun.*, vol. 10, no.2, pp. 207-243, 1999.
- [106] A. Ng'oma, and M. Sauer, "Radio-over-fiber technologies for high data rate wireless applications," in *Proc. SARNOFF 2009*, pp. 1-6.
- [107] Federal Communications Commission, "Operation within the band 57–64 GHz," FCC, Rep. FCC 15.255, Oct. 2002.
- [108] Industry Canada, "Low-power licence-exempt radiocommunication devices (All frequency bands):Category I Equipment," IC RSS-210, Jun. 2007.
- [109] European Telecommunications Standards Institute, "60 GHz multiple-Gigabit WAS/RLAN systems," ETSI Std. EN 302 567, Rev. 1.1.1, Mar. 2009.
- [110] Australian Communications and Media Authority, "Radiocommunications (low interference potential devices) class licence 2000," ComLaw F2011C00543, Jul. 2011.
- [111] Association of Radio Industries and Businesses, "Millimeter-wave data transmission equipment for specified low power radio station (ultra high speed wireless LAN system)," ARIB, STD-T74 v1.1, Nov. 2005.

- [112] OptSim™ Product Overview [Online]. Available: <http://www.rsoftdesign.com/products.php?sub=System+and+Network&itm=OptSim> [Accessed Apr. 2, 2013].
- [113] R. Papannareddy, *Lightwave communication systems: a practical perspective*. Penram International Publishing (India) Pvt. Ltd., 2004.
- [114] RSoft design group, Inc., *Optsim user guide*, 2009.
- [115] K. Cho, and D. Yoon, "On the general BER expressions of one- and two-dimensional amplitude modulations," *IEEE Trans. Commun.*, vol. 50, no. 7, pp. 1074-1080, Jul. 2002.
- [116] R. A. Shafik, M. S. Rahman, and A. H. M. R. Islam, "On the extended relationships among EVM, BER and SNR as performance metrics," in *Proc. ICECE 2006*, pp. 408-411.
- [117] H. Minn, M. Zeng, and V. K. Bhargava, "On timing offset estimation for OFDM systems," *IEEE Commun. Lett.*, vol. 4, no. 7, pp. 242-244, Jul. 2000.
- [118] T. M. Schmidl, and D. C. Cox, "Robust frequency and timing synchronization for OFDM," *IEEE Trans. Commun.*, vol. 45, no. 12, pp. 1613-1621, Dec. 1997.
- [119] H. Taga, "A theoretical study of OFDM system performance with respect to subcarrier numbers," *Opt. Exp.*, vol. 17, no. 21, pp. 18638-18642, Oct. 2009.
- [120] G. L. Stüber, *Principles of Mobile Communication*. Springer, Jan. 1, 2001.
- [121] D. J. F. Barros, "Orthogonal frequency-division multiplexing for optical communications," Ph.D. thesis, Stanford University, Sep. 2001.
- [122] J. James, P. Shen, A. Nkansah, X. Ling, and N. J. Gomes, "Nonlinearity and noise effects in multi-level signal millimetre-wave over fiber transmission using single and dual wavelength modulation," *IEEE Trans. Microw. Theory Tech.*, vol. 58, no. 11, pp. 3189-3198, Nov. 2010.
- [123] W. Rosenkranz, A. Ali, and J. Leibrich, "Design considerations and performance comparison of high-order modulation formats using OFDM," in *Proc. ICTON 2010*, pp. 1-4, paper Tu.D1.3.
- [124] T-S. Cho, and K. Kim, "Effect of third-order intermodulation on radio-over-fiber systems by a dual-electrode Mach-Zehnder modulator with ODSB and OSSB signals," *J. Lightw. Technol.*, vol. 24, no. 5, pp. 2052-2058, May 2006.
- [125] M. Beltran, et al., "Performance of a 60-GHz D.C.M-OFDM and BPSK-impulse ultra-wideband system with radio-over-fiber and wireless transmission employing a directly-modulated VCSEL," *IEEE J. Sel. Areas Commun.*, vol. 29, no. 6, pp. 1295-1302, Jun. 2011.
- [126] T. S. Rappaport, J. N. Murdock, and F. Gutiérrez, "State of the art in 60-GHz integrated circuits and systems for wireless communications," *Proc. IEEE*, vol. 99, no. 8, pp. 1390 – 1436, Aug. 2011.
- [127] "ECMA publishes 60 GHz standard," Press release, Dec. 2008. [Online]. Available:

- <http://www.ecma-international.org/news/PressReleases/PREcma%20publishes%2060%20GHz%20Standard.htm> [Accessed Jan. 21, 2013].
- [128] M. Larrode, A. Koonen, J. Vegas, and A. Ng'oma, "Bidirectional radio-over-fiber link employing optical frequency multiplication," *IEEE Photon. Technol. Lett.*, vol. 18, no. 1, pp. 241–243, Jan. 2006.
- [129] M. Larrode, A. Koonen, and J. Olmos, "Fiber-based broadband wireless access employing optical frequency multiplication," *IEEE J. Sel. Top. Quantum Electron.*, vol. 12, no. 4, pp. 875 – 881, Jul. 2006.
- [130] M. Larrode, A. Koonen, and J. Olmos, "Overcoming modal bandwidth limitation in radio-over-multimode fiber links," *IEEE Photon. Technol. Lett.*, vol. 18, no. 22, pp. 2428–2430, Nov. 2006.
- [131] A. Ng'oma, A. Koonen, I. Tafur, H. Boom, and G. Khoe, "Using optical frequency multiplication to deliver a 17 GHz 64 QAM modulated signal a simplified radio access unit fed by multimode fiber," in *Proc. OFC 2005*, pp. 1-3, Paper OWB2.
- [132] M. Larrode, A. Koonen, J. Olmos, E. Verdurmen, and J. Turkiewicz, "Dispersion tolerant radio-over-fiber transmission of 16 and 64 QAM radio signals at 40 GHz," *IEEE Electron. Lett.*, vol. 42, no. 15, pp. 872–874, Jul. 2006.
- [133] M. Mohamed, X. Zhang, B. Hraimel, and K. Wu, "Efficient photonic generation of millimeter-waves using optical frequency multiplication in radio-over-fiber systems," in *Proc. MW 2007*, pp. 179-182, Paper Th.-4.20.
- [134] B. Hraimel, R. Kashyap, X. Zhang, J. Yao, and K. Wu, "Large signal analysis of fiber dispersion effect on photonic up-conversion in radio over fiber link using dual electrode Mach-Zehnder external modulator," in *Proc. SPIE 2006*, pp. 1-12, vol. 63432L.
- [135] M. Mohamed, X. Zhang, B. Hraimel, and K. Wu, "Analysis of frequency quadrupling using a single Mach-Zehnder modulator for millimeter-wave generation and distribution over fiber systems," *Opt. Exp.*, vol. 16, no. 14, pp. 10786-10802, Jul. 2008.
- [136] A. Ng'oma, et al., "21 Gbps OFDM wireless signal transmission at 60 GHz using a simple IMDD radio-over-fiber system," in *Proc. OFC 2010*, pp. 1-3, Paper OTuF4.
- [137] W.-J. Jiang, et al., "Simple 14- Gb/s short-range radio-over-fiber system employing a single-electrode MZM for 60-GHz wireless applications," *J. Lightw. Technol.*, vol. 28, no. 16, pp. 2238-2246, Aug. 2010.
- [138] G. P. Agrawal, *Fiber-optic communication systems*. John Wiley & Sons, Ltd, Jun. 24, 2002.
- [139] D. Colton, and R. Kress, *Inverse acoustic and electromagnetic scattering theory, (Applied Mathematical Sciences)*. Springer, Oct. 25, 2012.
- [140] A. A. M. Cuyt, V. Petersen, B. Verdonk, H. Waadeland, and W. B. Jones, *Handbook of continued fractions for special functions*. Springer, Apr. 22, 2008.

- [141] M. Abramowitz and I. A. Stegun, *Handbook of mathematical functions: with formulas, graphs, and mathematical tables*. Dover Books on Mathematics, Jun. 1, 1965.
- [142] M. P. Thakur, *et al.*, “First demonstration of secure, AWG performance interrogation using OFDM edge-tones on WDM access networks,” in *Proc. ECOC 2010*, pp. 1-3, paper Tu.3.B.
- [143] G. H. Nguyen, V. Dobremez, B. Cabon, and Y. L. Guennec, “Optical techniques for up-conversion of MB-OFDM signals in 60 GHz band using fiber bragg grating,” in *Proc. ICC 2009*, pp. 1-5, 2009.
- [144] M. Seimetz, *High-order modulation for optical fiber transmission*. Springer, Jun. 23, 2009.
- [145] C. T. Lin, J. Chen, S. P. Dai, P. C. Peng, and S. Chi, “Impact of nonlinear transfer function and imperfect splitting ratio of MZM on optical up-conversion employing double sideband with carrier suppression modulation,” *J. Lightw. Technol.*, vol. 26, no. 15, pp. 2449-2459, Aug. 2008.
- [146] Ducommun Technologies, “FDB series balanced mixers,” [Online]. Available: <http://www.ducommun.com/pdf/FDB-Series.pdf> [Accessed Jan. 26, 2013].
- [147] F. Marki, and C. Marki, “Mixer basics primer: A tutorial for RF & microwave mixers,” [Online]. Available: http://www.markimicrowave.com/menus/appnotes/mixer_basics_primer.pdf [Accessed Jan. 26, 2013].
- [148] G. Breed, “The mathematics of mixers: basic principles,” [Online]. Available: http://www.highfrequencyelectronics.com/Archives/Jan11/HFE0111_Tutorial.pdf [Accessed Jan. 26, 2013].
- [149] Miteq, “Balanced Schottky diodes ,” [Online]. Available: http://www.miteq.com/docs/MITEQ_Mixer_Question_Answers.pdf [Accessed Feb. 26, 2013].
- [150] S. Farahani, *ZigBee wireless networks and transceivers*. Newnes, Apr. 8, 2011.
- [151] R. P. Braun, G. Grosskopf, D. Rohde, F. Schmidt, and G. Walf, “Fiber-optic millimeter-wave generation at 64 GHz and spectral efficient data transmission for mobile communications,” in *Proc. OFC 1998*, pp. 17-18, Paper TuC4.
- [152] J. P. Yao, “Microwave photonics,” *J. Lightw. Technol.*, vol. 27, no. 3, pp. 314-335, Feb. 2009.
- [153] I. Aldaya, G. Campuzano, and G. Castanon, “Generation of OFDM signals in the 60 GHz band using the sideband injection locking technique for radio over fiber,” in *Proc. ICTON 2012*, pp. 1-4, Paper Tu.P.18.

- [154] A. H. M. R. Islam, *et al.*, “Millimeter-wave radio-over-fiber system based on heterodyned unlocked light sources and self-homodyned RF receiver,” *IEEE Photon. Technol. Lett.*, vol. 23, no. 8, pp. 459-461, Apr. 2011.
- [155] G. J. Foschini, L. J. Greenstein, and G. Vannucci, “Noncoherent detection of coherent lightwave signals corrupted by phase noise,” *IEEE Trans. Commun.*, vol. 36, no. 3, pp. 306-314, Mar. 1988.
- [156] I. G. Insua, D. Plettemeier, and C. G. Schäffer, “Simple remote heterodyne radio-over-fiber system for gigabit per second wireless access,” *J. Lightw. Technol.*, vol. 28, no. 16, pp. 2289-2295, Aug. 2010.
- [157] L. Tomba, “On the effect of Wiener phase noise in OFDM systems,” *IEEE Trans. Commun.*, vol. 46, no. 5, pp. 580–583, May 1998.
- [158] J. M. Wozencraft and I. M. Jacobs, “Principles of Communication Engineering,” Wiley & Sons, 1965.
- [159] L. Nadal, *et al.*, “Comparison of peak power reduction techniques in optical OFDM systems based on FFT and FHT,” in *Proc. ICTON 2011*, pp. 1-4, paper We.A1.5.
- [160] B. S. Krongold, and D. L. Jones, “PAR reduction in OFDM via active constellation extension,” *IEEE Trans. Broadcast.*, vol. 49, no. 3, pp. 258–268, Sep. 2003.
- [161] S. Sezginer and H. Sari, “OFDM peak power reduction with simple amplitude predistortion,” *IEEE Commun. Lett.*, vol. 10, no. 2, pp. 65–67, Feb. 2006.
- [162] C. Ciochina, F. Buda, and H. Sari, “An analysis of OFDM peak power reduction techniques for WiMAX systems,” in *Proc. ICC 2006*, vol. 10, pp. 4676–4681.
- [163] J. Tellado, *Multicarrier Modulation with Low PAR: Applications to DSL and Wireless*. Boston: Kluwer Academic, Sep. 30, 2000.
- [164] D. J. Barros, *et al.*, “Optical modulator optimization for orthogonal frequency-division multiplexing,” *J. Lightw. Technol.*, vol. 27, no. 13, pp. 2370-2378, Jul. 2009.
- [165] Y. Tang, *et al.*, “Coherent optical OFDM transmitter design employing predistortion,” *IEEE Photon. Technol. Lett.*, vol. 20, no. 11, pp. 954-956, Jun. 2008.
- [166] Vidak Vujičić, *et al.*, “Predistortion technique for mitigating the Mach-Zehnder modulator nonlinearity effect in DD-OFDM-UWB optical transmission systems,” in *Proc. ICTON 2011*, pp. 1-4, paper Tu.A5.5.
- [167] R. I. Killey, P. M. Watts, V. Mikhailov, M. Glick, and P. Bayvel, “Electronic dispersion compensation by signal predistortion using digital processing and a dual-drive Mach-Zehnder modulator,” *IEEE Photon. Technol. Lett.*, vol. 17, no. 3, pp. 714-716, Mar. 2005.
- [168] R. I. Killey, P. M. Watts, M. Glick, and P. Bayvel, “Electronic dispersion compensation by signal predistortion,” in *Proc. OFC/NFOEC 2006*, pp. 1-3, paper OWB3.